

**Tilt-To-Length Coupling in LISA
Pathfinder:
Model, Data Analysis and Take-Away
Messages for LISA**

Von der Fakultät für Mathematik und Physik
der Gottfried Wilhelm Leibniz Universität Hannover

zur Erlangung des akademischen Grades

**Doktorin der Naturwissenschaften
Dr. rer. nat.**

genehmigte Dissertation von

Marie-Sophie Hartig, M.Sc.

Hannover 2022

Referent: Prof. Dr. Gerhard Heinzl
Institut für Gravitationsphysik, Leibniz Universität Hannover

Korreferent: Prof. Dr. Guido Müller
Department of Physics, University of Florida

Korreferent: Dr. David Robertson
Institute for Gravitational Research, University of Glasgow

Tag der Promotion: 19. May 2022

In der vorliegenden Arbeit wurden gegenüber der am 18. März 2022 bei der Fakultät für Mathematik und Physik der Leibniz Universität Hannover eingereichten Version an vereinzelten Stellen kleine Änderungen im Sinne eines besseren Verständnisses vorgenommen.

Abstract

In the mid-2030s, the laser interferometer space antenna (LISA) is planned to be launched and will be the first gravitational wave detector in space. One of the major noise sources in LISA will be tilt-to-length (TTL) coupling, i.e. the coupling of lateral and angular spacecraft motion into the interferometric readout.

Likewise, TTL coupling was a significant noise in LISA's technology demonstrator mission LISA Pathfinder (LPF), operating from March 2016 until the end of June 2017 with a performance that exceeded the expectations. During this mission, TTL coupling was the main noise contributor between 20 and 200 mHz. It was successfully subtracted via a fit model in post-processing. However, each analytical model existing at that time failed to describe the TTL coupling consistently. The lack of such a physical model limited the ability to minimise the TTL noise via realignments of the optical system a priori.

Therefore, I present in this thesis, on the one hand, a detailed description of the TTL mechanisms in general cases and a derivation of the corresponding analytical equations if possible. On the other hand, I interpret these findings for the LPF case, followed by an analysis of the TTL noise during this mission.

The analytical models introduced in the first part describe TTL coupling in general interferometric detectors. This analysis covers geometric and non-geometric TTL coupling contributions from lateral and angular jitter of either a mirror or a receiving system. The models can be applied to different interferometric setups modelling the found TTL noise and developing strategies for the TTL coupling suppression. The model predictions have been verified in simulation and, in the case of LPF, by the comparison to data taken during the mission.

In particular, the new LPF TTL model successfully describes how the measured coupling depends on the alignment of the test masses hosted by the LPF satellite and, therefore, how they could have been realigned for an optimal TTL suppression. Also, the TTL coupling coefficients match the results from the fit used during the LPF mission in a TTL coupling experiment. Based on this data, I present how a comparable physical model can be derived using the fit results.

In addition, the long-term analysis shows that TTL coupling is not stable over the entire mission duration. The individual TTL contributors are affected by a small distortion of the optical bench and its components, mainly due to temperature changes. However, the TTL coupling provides an additional measure for the actual alignment of the full optical system.

In summary, I demonstrate within this thesis that modelling TTL noise in space interferometers while complex is possible. Likewise, this result boosts our confidence that the suppression techniques planned for LISA will enable the successful gravitational wave measurement.

Keywords: Laser Interferometry, Tilt-To-Length Coupling, LISA Pathfinder

Contents

Abstract	I
List of Figures	V
List of Tables	VII
List of Boxes	VIII
List of Acronyms	IX
1 Introduction	1
I General Information	3
2 Space-Based Laser Interferometers	5
2.1 Laser Interferometer Space Antenna	5
2.2 LISA Pathfinder	8
2.3 Other Space-Based Interferometers	13
3 The Interferometric Readout	15
3.1 Power Detection for Two Interfering Beams	15
3.2 Interferometric Signals	17
4 Introduction to Tilt-To-Length Coupling	23
4.1 Angular and Lateral Tilt-To-Length Coupling	23
4.2 Geometric and Non-Geometric Tilt-To-Length Coupling	25
4.3 Tilt-To-Length Coupling in this Work	25
4.4 Tilt-To-Length Coupling in other Works	26
II Tilt-To-Length Coupling: Model and Suppression	27
5 Analytical Modelling of Tilt-To-Length Coupling	29
5.1 Geometric Tilt-To-Length Coupling	29
5.2 Non-geometric Tilt-To-Length Coupling	43
5.3 Cancellations in the Full Longitudinal Path Length Signal	62
5.4 Summary of the Tilt-To-Length Coupling Effects	66
6 Tilt-To-Length Suppression Strategies	69
6.1 Suppression by Design, Alignment or Subtraction	69
6.2 Suppression Strategies in Space Interferometers	71

III	Tilt-To-Length Coupling Analysis for LISA Pathfinder	77
7	Tilt-To-Length Coupling Models for LISA Pathfinder	79
7.1	The Tilt-To-Length Coupling Fit Model	79
7.2	The Analytical Tilt-To-Length Coupling Model	81
8	Analysis of the Long Cross-Talk Experiment	97
8.1	The Cross-Talk Experiments in LISA Pathfinder	97
8.2	Modelling Tilt-To-Length Noise with the Fit Approach	99
8.3	Modelling Tilt-To-Length Noise with the Analytical Model	105
8.4	Comparison of Both Models	107
8.5	Adaptions of the Fit Model	110
8.6	Extraction of a Tilt-To-Length Model from the Fit Results	114
8.7	Application of Second-Order Models	114
8.8	Noise Contributors	118
8.9	Injections in the α_1 -Readout	119
8.10	Summary of the Model Analysis	120
9	Test Mass Realignments during the Mission	123
9.1	Engineering Days	123
9.2	Further Realignments of the Test Masses	129
10	Long-Term Analysis of the TTL Coefficients	133
10.1	Characterisation of the Coupling Coefficients' Stability	134
10.2	Stresses and Relaxations	136
10.3	Analysis of the Angular Readouts	136
10.4	Analysis of the Long-Term Spot Positions	141
10.5	Summary of the Long-Term Coupling Coefficient Stability	144
IV	Outlook and Conclusion	145
11	Take-Away Messages for LISA	147
11.1	Modelling Tilt-To-Length Coupling	147
11.2	Subtraction of Tilt-To-Length Coupling	147
11.3	Back-Up: Coefficient Calibration Scheme	148
11.4	The Test Mass Interferometer Readout	149
12	Summary	151
	Appendices	153
A	GRACE Follow-On	155
A.1	Mission and Instrument	155
A.2	Tilt-To-Length Coupling in GRACE-FO	156
B	Further Analytical Approaches	159
B.1	Longitudinal Displacement Strategies	159
B.2	Intuitive Approach: Signal Cancellation for Identical Beams	162
B.3	Tilt-Dependency of the Beam Parameters	165
C	Code: Derivation of Analytical TTL Formulas for LPF	167

C.1 Derivation of Optical Path Length Differences and Beam Walk	167
C.2 Derivation of the Non-Geometric Longitudinal Path Length Signal	173
C.3 LISA Pathfinder Optical Parameters	173
D LISA Pathfinder Data Analysis	175
D.1 The Long Cross-Talk Experiment	175
D.2 Long-Term Analysis	187
Bibliography	189
Project Documents	195
Complete List of Publications	197
Acknowledgements	199
Curriculum Vitae	201

List of Figures

2.1	LISA orbit	6
2.2	LISA S/C constellation	7
2.3	Timeline of the LISA Pathfinder mission	9
2.4	LISA Pathfinder performance	10
2.5	The four interferometers in LISA Pathfinder	11
2.6	LISA Pathfinder’s drag-free attitude control system	12
3.1	Gaussian beam profile	18
3.2	Quadrant photodiode	20
4.1	Angular and lateral TTL coupling	24
5.1	Lever arm TTL coupling	30
5.2	Pitch and yaw rotations	31
5.3	Angular piston TTL coupling	33
5.4	Lateral piston TTL coupling	34
5.5	Receiver angular TTL coupling	37
5.6	Receiver lateral TTL coupling	38
5.7	Notation of longitudinal and lateral offsets of the centre of rotation	38
5.8	Transmissive component’s TTL coupling	40
5.9	Transformation of beam coordinates into detector coordinates	44
5.10	Beam parameter TTL coupling	46
5.11	Amplitude profiles of two shifted and tilted Gaussian beams	47
5.12	Detector coordinate system	48
6.1	TTL suppression via imaging systems	70
6.2	LPF Performance before and after realignment	72
6.3	LPF Performance before and after subtraction	73
7.1	LPF: the x12-interferometer	82
7.2	LPF: beam walk on the second test mass	83
7.3	LPF: analytical length signals	86
7.4	LPF: full LPS and its contributors	86
7.5	LPF: comparison of LPS for SEPDs and QPDs	87
7.6	LPF: comparison of the LPS with and without inserted nominal alignments	88
7.7	LPF: accuracy of the analytical model	89
8.1	LXE: performance of the fit model (1st and 12th sub-experiment)	100
8.2	LXE: correlations in the fit model (1st and 12th sub-experiment)	100
8.3	LXE: fitted coupling coefficients	102
8.4	Noise run mid-February 2017: fitted coupling coefficients	103
8.5	Noise run mid-February 2017: histograms of the fitted coupling coefficients	104
8.6	LXE: performance of the analytical model (1st and 12th sub-experiment)	107
8.7	LXE: comparison of the fitted and analytical coupling coefficients	108

8.8	LXE: comparison of the coupling coefficients for variants of the fit model	111
8.9	LXE: comparison of the fitted and analytical coupling coefficients split for y - and z -injections	112
8.10	LXE: performance of the second-order analytical model (1st and 12th sub-experiment)	115
8.11	LXE: performance of the second-order fit model (1st and 12th sub-experiment) .	116
8.12	LXE: second-order fit coefficients	116
8.13	LXE: performance of the extended second-order fit model (1st and 12th sub-experiment)	117
8.14	LXE: noise contributors (1st and 12th sub-experiment)	119
8.15	LXE: o_1 -readout (1st and 12th sub-experiment)	119
8.16	LXE: o_1 -readout for the single injections during the 1st sub-experiment	120
8.17	LXE: o_1 -readout for the single injections during the 2nd sub-experiment	120
9.1	Engineering days: fitted coupling coefficients	125
9.2	Noise contributors before and after the engineering days	127
9.3	Engineering days: analytical modelling of the realignment noise	128
9.4	Engineering days: noise prediction for analytically derived realignment angles . .	129
9.5	Noise contributors during the noise run prior to the realignments	130
9.6	Noise contributors in the noise runs after each realignment step	130
10.1	Fitted coupling coefficients during the entire mission duration	135
10.2	Temperature changes in LPF	135
10.3	Mean angular readouts related to the fitted coupling coefficients	137
10.4	Spot positions changes at the reference interferometer	142
10.5	Sketch of a distorted optical bench	142
A.1	GRACE Follow-On setup	156
A.2	GRACE Follow-On optical bench setup	157
B.1	Longitudinal test mass shifts	160
B.2	Beam properties at arbitrary detector point	162
D.1	LXE: performance of the fit model	175
D.2	LXE: correlations in the fit model	176
D.3	LXE: performance of the analytical model	177
D.4	LXE: performance of the fit model without the stiffness terms	178
D.5	LXE: performance of the fit model without the residual longitudinal S/C accelerations	179
D.6	LXE: performance of the fit model with additional angular stiffness terms	180
D.7	LXE: performance of the fit model split up for experiments with y - and z -injections	181
D.8	LXE: performance of the second-order analytical model during the LXE	182
D.9	LXE: performance of the second-order fit model	183
D.10	LXE: performance of the extended second-order fit model	184
D.11	LXE: noise contributors	185
D.12	LXE: o_1 -readout	186
D.13	Spot positions in all interferometers	188

List of Tables

3.1	Gaussian beam parameters	19
5.1	Geometric TTL parameters	32
5.2	Summary of angular TTL coupling effects	67
5.3	Summary of lateral TTL coupling effects	67
7.1	LPF: stability of coefficients in the non-geometric analytical model depending on the single beam parameter uncertainties	91
7.2	LPF: stability of coefficients of the complete analytical model depending on the single beam parameter uncertainties	91
7.3	LPF: error estimate of coefficients of the complete analytical model	92
8.1	The short cross-talk experiment	98
8.2	The long cross-talk experiment	99
8.3	Estimated errors of the fit coefficients	105
9.1	The engineering days	124
9.2	Set-points to optimise the cross-talk suppression	124
9.3	Engineering days: comparison of set-points and analytical predictions	126
9.4	Coupling coefficients prior, in between and after the test mass realignments	129
10.1	Coupling coefficients after test mass realignments and after LXE	133
10.2	Mean angular readouts before and during the cooldown	138
10.3	Coupling coefficients prior and during and after the cooldowns	138
10.4	Mean angular readouts before and after the test mass realignments	139
10.5	Coupling coefficients prior and after the test mass realignments	140
C.1	LISA Pathfinder parameters	174
D.1	Timespans for the TTL coefficient fit	187

List of Boxes

4.1	Angular and lateral TTL coupling	24
5.1	Lever arm effect	30
5.2	Angular piston effect	33
5.3	Lateral piston effect	34
5.4	Angular receiver jitter	37
5.5	Lateral receiver jitter	38
5.6	Transmissive components	40
5.7	Beam parameter TTL coupling	46
5.8	Static beam offsets	47
5.9	Angular jitter induced beam walk on the detector	50
5.10	Lateral jitter induced beam walk on the detector	53
5.11	Tilts of the reference beam	54
5.12	Detector geometry TTL coupling	61
5.13	Detector tilt TTL coupling	64
7.1	TTL noise in LPF: The fit model	79
7.2	TTL noise in LPF: The analytical model	93

List of Acronyms

AP	arithmetic mean phase.
ASD	amplitude spectral density.
CoM	centre of mass.
CoR	centre of rotation.
DFACS	drag-free attitude control system.
DMU	data management unit.
DOF	degree of freedom.
DOY	day of the year.
DPS	differential power sensing.
DRS	disturbance reduction system.
DWS	differential wavefront sensing.
ED	engineering days.
ESA	European Space Agency.
FIOS	fibre injector optical subassembly.
GRACE-FO	Gravity Recovery and Climate Experiment Follow-On.
GRS	gravitational reference sensor.
LISA	Laser Interferometer Space Antenna.
LPF	LISA Pathfinder.
LPS	longitudinal path length signal.
LRI	laser ranging instrument.
LTP	LISA technology package.

LTPDA	LISA technology package data analysis.
LXE	long cross-talk experiment.
OB	optical bench.
OMS	optical metrology system.
OPD	optical path length difference.
OPL	optical path length.
PD	photodiode.
PoD	point of detection.
PoR	point of reflection.
QPD	quadrant photodetector.
S/C	spacecraft.
SEPD	single-element photodiode.
TDI	time-delay interferometry.
TM	test mass.
TTL	tilt-to-length.
UTC	coordinated universal time.

Chapter 1

Introduction

Since the first gravitational wave detection in 2015, ground-based laser interferometers have become important detectors for cosmic events. In the next decade, their measurement band will be extended to lower frequencies by space-based interferometers like the Laser Interferometer Space Antenna (LISA). These new detectors come along with a number of new possibilities but also technological challenges and different types of noises. One of these is the unwanted coupling of angular and lateral jitter into the interferometric measurements, called tilt-to-length (TTL) coupling.

TTL coupling was a major noise source in the technology demonstrator LISA Pathfinder (LPF) and will likely be it also in LISA. This coupling demands a strategy to suppress the noise by design or alignment. In LPF, TTL noise was not suppressed by design but was reduced by realignment. The residuals were then fully subtracted in data post-processing. For this subtraction, a model has been used, which relied on fitting linear coupling coefficients to the measured angular and lateral jitter. However, the prior realignment was necessary for the successful subtraction at all frequencies. Also, this fit model did not provide a physical explanation of the underlying mechanisms and had to be recomputed regularly to account for long-term changes within the setup.

These drawbacks could have been overcome with an analytical model providing a subtraction model for the entire mission duration. Further, such a model could have been used for a justified realignment of the interferometric setup to reduce the coupling of TTL noise. The simplified analytical TTL model available during the LPF mission did not explain the full measured coupling noise. Therefore, I will derive in this thesis an analytical TTL model accounting for all coupling mechanisms present in LPF and - to some extent - beyond. My modelling includes all geometric effects as well as the analysis of coupling terms related to the detector and wavefront properties assuming general-astigmatic Gaussian beams.

I will apply the derived analytical model and the fit model used in the LPF mission to the data of a cross-talk experiment performed during the LPF mission and dedicated to analysing the present TTL coupling. With this analysis, I can show that both models succeed in subtracting the induced TTL noise.

Due to the good suppression performance of the analytical model, I will use it to analyse the realignment at the beginning of the mission. While the simplified analytical model available at that time failed in consistently describing which realignments should have been applied for complete suppression of the TTL coupling, my model predicts different realignments recommendations, which I assume to provide a better TTL coupling suppression. Additionally, I will

analyse the long-term behaviour of the coupling coefficients. The analytical model can explain big parts of the visible drifts and jumps of the coefficients yielding an explanation of the stability of the latter.

From the successful analysis of the LPF data, I can extrapolate several takeaway messages for the TTL coupling in LISA. The expected TTL coupling in both missions is not directly comparable since they deviate in several aspects. These are, for example, the usage of lenses and curved mirrors as well as the flat-top beams in LISA, which are not the scope of this work. However, the application of an analytical model has been proven successful for the first time in space-based laser interferometers. Also, my analysis manifests several challenges regarding the suppression of TTL coupling. These are the limitations of the subtraction scheme for large TTL noise, drifts of the coupling coefficients in long time scales and the effect of temperature changes. Moreover, my findings boost our confidence that, if recalibrations are necessary for LISA, these can be done based on the daily data.

The presented work is divided into four parts. I will first provide some general information for the reader's convenience. So, I will introduce the space-based laser interferometers discussed in this writing. Moreover, I will explain how the interferometric readout is derived analytically and which signals will be computed in the missions. Also, I will introduce TTL coupling and its origins in general and define what I will analyse here and what has been presented previously in other works.

The second part of this thesis covers a detailed analysis of TTL coupling. There, I will model TTL coupling analytically in the most general cases. This modelling will be divided into the geometric, i.e. corresponding to path length differences of the beam axes, and non-geometric, i.e. wavefront and detector geometry related, coupling contributions. These cancel each other in some specific cases. On the other hand, the characteristics I derive here can be used to intentionally suppress or counteract TTL coupling by design, realignment or subtraction. Therefore, I will extrapolate suppression strategies from my analytical TTL coupling models. Furthermore, I will present the additional strategies probed successful in experiments or applied in LPF or LISA.

In the third part of this work, I will apply the analytical TTL model to the LPF setup and compare the corresponding model with the linear fit model used in the mission. In particular, I will compare the subtraction performance and coupling coefficients of these models for the data of a cross-talk experiment and show that both succeed in subtracting the injected TTL noise. Further, I will analyse the correlations within the fit by adapting the model and extending both models to account also for the second-order TTL noise. Moreover, I will compare the single noise contributors during this cross-talk experiment which, on the one hand, affect the performance of the fit model and, on the other hand, give us insights into the noise contributors that are the least suppressed by the alignment during that time of the mission. Finally, both models will be used to analyse the realignments performed in an early mission stage and the long-time behaviour of the coupling coefficients.

I will elaborate in the last part what we learn from the LPF TTL analysis for the upcoming LISA mission. With this, I aim to contribute to current TTL investigations.

Part I

General Information

Chapter 2

Space-Based Laser Interferometers

In the last six and a half years, ground-based laser interferometers [1, 2, 3, 4] have proven to detect gravitational wave signals successfully. From the first detection [5], they revealed unexpected pieces of information about the universe and its massive objects. Moreover, third-generation observatories with significantly improved sensitivities will extend the current measurement band to lower frequencies in the following decades [6, 7, 8]. However, these ground-based detectors will always be limited at lower frequencies by the available space, the gravity gradient noise on Earth and the suspension systems necessary to suppress seismic noise. Therefore, several space-based observatories have been proposed which overcome the limits of the ground-based interferometers. In the following, I will introduce the space interferometers LISA and LPF and give a rough overview of the additionally planned missions.

2.1 Laser Interferometer Space Antenna

The Laser Interferometer Space Antenna (LISA) [9] was chosen as European Space Agency (ESA)'s L3 mission in 2017. It will be the first space-based gravitational wave detector with a proposed launch in the mid-2030s. It is expected to measure gravitational wave signals of diverse heavy sources (Sec. 2.1.1). This will be achieved based on the technology tests with LPF (see Sec. 2.2): it will measure the distances between pairs of free-falling test masses which are covered by separated drag-free spacecraft (S/C) (Sec. 2.1.2). This measurement scheme will make LISA sensitive at the frequency range from 10^{-4} Hz to 0.1 Hz (Sec. 2.1.3). While LISA's nominal science mode is set to four years, an extension up to ten years is possible [9].

2.1.1 Science case

The low-frequency range covered by LISA gives access to a series of undetected cosmic sources. In its sensitivity band lie heavier and more eccentric binary systems than ever detected on ground. Also, LISA will have the potential to discover new astrophysical systems or cosmological sources [9].

Moreover, the sensitivity range of LISA enables us to observe the evolution of binary systems starting from their formation. In our close neighbourhood, the antenna will cover compact binary systems within the Milky Way. At far distances, it will monitor the origin, growth and merge of massive black holes. In particular, the detection of black hole binary systems within LISA's sensitivity range will allow us to test our current understanding of the general theory of

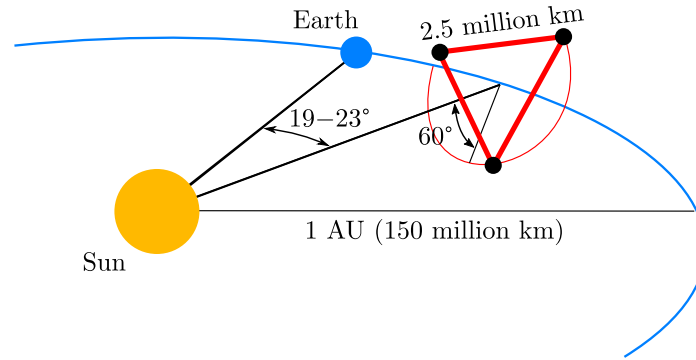


Figure 2.1: The LISA orbit. LISA will consist of three S/C forming a triangle of 2.5 million kilometre arm length. This constellation will follow the Earth on an Earth-like orbit. Figure reproduced from [9].

relativity [9].

LISA will reveal some of the earliest history of our universe measured today. Further, it will probe the expansion rate of the universe. Another goal of the space antenna will be the detection of the stochastic gravitational wave background of cosmological origin and the following implications for TeV-scale particle physics [9].

In summary, the all-sky monitor LISA will be the first-ever space-based gravitational wave observatory to study the universe.

2.1.2 Constellation

LISA will consist of three S/C exchanging laser beams forming an approximately equilateral triangle of 2.5 million km arm length. It will follow Earth at a distance of more than 50 million km (see Fig. 2.1). Since each satellite will follow its own stable orbit around the sun, the arm length will change over time and the angles between the laser arms will be subject to continuous breathing. The laser light transmitted will have a wavelength of 1064 nm and a power of a few Watts. Only a fraction of this beam, i.e. a few 100 pW, will enter the receiving S/C by a telescope of 30 cm radius [9].

Each S/C will contain two optical benches and associated test masses. Since the test masses will be much quieter than their hosting S/C, they provide the geodesic reference system for the measurements. Therefore, the gravitational wave signal will be derived from the distance changes between the pairs of test masses along the three arms. For this scientific measurement, the signals of three interferometers will be combined. First, the long-arm interferometer (also named differently, e.g., science interferometer) will measure the distance changes between two far optical benches, see Fig. 2.2. Additionally, test mass interferometers will measure the distance variation between the optical bench and the test mass at each end of the arm. These three lengths will then be combined to the full signal on ground. Every optical bench will contain a third interferometer, the reference interferometer, which will track the relative frequency noise of the two local lasers [9, 10].

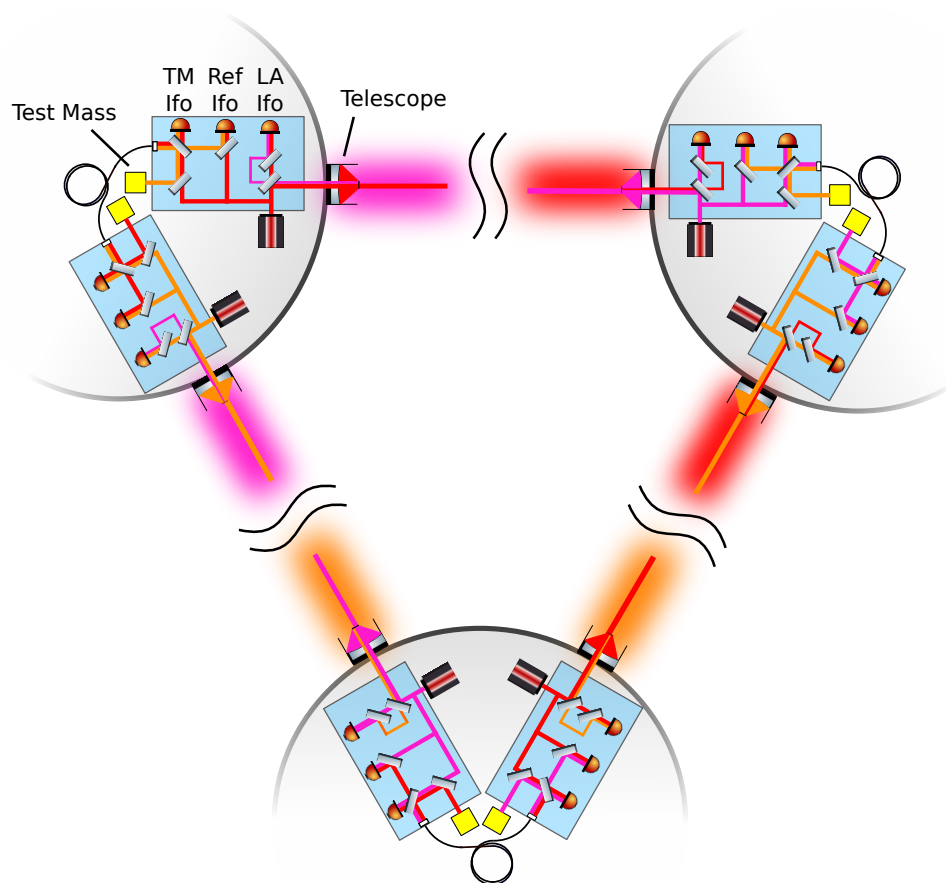


Figure 2.2: Simplified sketch of the constellation of the LISA S/C. Each S/C is equipped with two test masses and associated optical benches. The optical benches host three interferometers: the long-arm interferometer (labelled ‘LA Ifo’) measuring the distance changes between two S/C, the test mass interferometer (‘TM Ifo’) measuring the distance changes between the test mass and the respective optical bench, and the reference interferometer (‘Ref Ifo’) serving as a differential frequency reference. The three involved beams at each optical bench (two local beams and the received beam) are shown in different shades of red.

2.1.3 Performance requirements

In order to detect the gravitational wave signals of the sources listed in Sec. 2.1.1, LISA needs to measure distance changes between the pairs of test masses of the order of picometres up to nanometres in the Millihertz regime. These test masses will follow their geodesic trajectories with sub-femto- $g/\sqrt{\text{Hz}}$ spurious acceleration, as proven in the LISA Pathfinder mission [11]. The test mass orbits will yield variations of the distances between the test masses of several 10000 km. However, these variations have little effect on the low-frequency measurements since they happen at a frequency of months. Furthermore, the orbital movement will induce relative velocities between the S/C being measurable via the Doppler shifts of up to 15 MHz [9, 10].

Apart from the macroscopic test mass movements, residual noises such as pointing and jitter noise will couple into the measurements. These will be reduced by an accurate design and further subtracted in post-processing, as I will explain in Sec. 6.2.2. Altogether, the single test mass accelerations are required to stay below

$$S_{\text{acc}}^{1/2} \leq 3 \frac{\text{fm}}{\text{s}^2 \sqrt{\text{Hz}}} \sqrt{1 + \left(\frac{0.4 \text{ mHz}}{f}\right)^2} \sqrt{1 + \left(\frac{f}{8 \text{ mHz}}\right)^4} \quad (2.1)$$

at frequencies f between $100 \mu\text{Hz}$ and 0.1 Hz . The goal is to reach this sensitivity even for frequencies between $20 \mu\text{Hz}$ and 1 Hz . At the same frequency ranges, the total displacement noise along one LISA arm must stay below

$$S_{\text{IFO}}^{1/2} \leq 10 \frac{\text{pm}}{\sqrt{\text{Hz}}} \sqrt{1 + \left(\frac{2 \text{ mHz}}{f}\right)^4}. \quad (2.2)$$

These sensitivity requirements yield further requirements, e.g., for the S/C angular jitter and test mass lateral displacement [9].

2.1.4 Major noise contributors

Without suppression, the laser frequency noise will be the largest noise contributor in LISA. While laser frequency noise would cancel for equal arm lengths, it will be delayed differently due to the unequal propagation distance between two sets of S/C. In order to suppress this noise, independent readouts of the phase-differences are combined with proper delays referring to the Doppler-shifts accumulated along the respective LISA arm. This technique is called time-delay interferometry (TDI) [12].

Every S/C contains its own clock. Since the combination of the signals measured at different S/C relies on the accuracy of these clocks, any timing jitter couples into the signal. Therefore, clock-noise is a major noise contributor and needs to be suppressed in post-processing [13, 14].

Another crucial noise source in LISA is the tilt-to-length coupling, which is the central element of this thesis.

2.2 LISA Pathfinder

Since LISA will be the first gravitational wave detector in space, it carries several new instruments and technologies that cannot be sufficiently tested on the ground. Therefore, the European Space Agency (ESA) launched the precursor mission LISA Pathfinder (LPF) for the

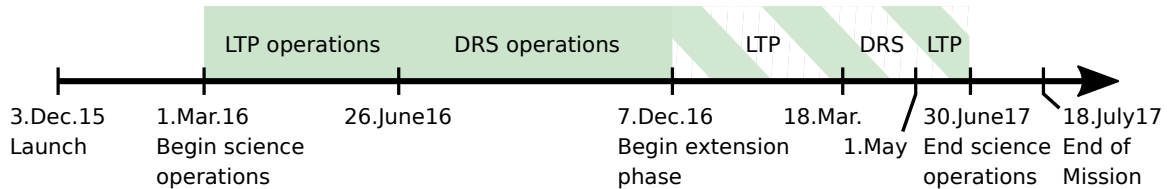


Figure 2.3: Timeline of the LPF mission, launched at the 3rd December 2015. The nominal mission operation phase of the LISA technology package (LTP) started at the 1st of March 2016. It was followed by NASA’s disturbance reduction system (DRS) operations using different thrusters. Between the 7th of December 2016 and LPF’s shut down at the 30th of June 2017, the mission extension phase took place including both LTP and DRS operations [17, 18].

first in-flight tests of low-frequency gravitational wave detection technology [15]. LPF was a technology validation mission demonstrating that the nearly free fall of test masses is feasible. Consisting of only one satellite that hosts two test masses, its interferometer arm was too short to be sensitive for gravitational waves. Further, the LISA requirements were relaxed to $S_{\Delta g, \text{LPF}}^{1/2} \leq 30 \text{ fm s}^{-2} \text{ Hz}^{-1/2}$ at 1 mHz. However, LPF was sensitive to the differential accelerations of the test masses. It demonstrated the precise readout of the relative test mass motions required for LISA [16].

2.2.1 Performance

Launched on the 3rd of December 2015 from Kourou (French Guiana), LPF was sent to the Lagrange point L1, where it was brought into science mode on the 1st of March 2016 (Fig. 2.3). In the following nominal phase, LPF outperformed its original requirements achieving already the LISA requirements at frequencies above 10 mHz, see Fig. 2.4. Between 1 mHz and 10 mHz it reached a sensitivity of $S_{\Delta g, \text{LPF}}^{1/2} \simeq (5.57 \pm 0.04) \text{ fm s}^{-2} \text{ Hz}^{-1/2}$, i.e. more than a factor of 5 below the LPF and only a factor of 1.4 above the LISA requirement [11].

This first science phase was followed by NASA operations taking place from the 26th of June until the 7th of December 2016. Thereupon, the mission extension phase started featuring a even better performance. Above 2 mHz, LPF reached $S_{\Delta g, \text{LPF}}^{1/2} \simeq (1.74 \pm 0.05) \text{ fm s}^{-2} \text{ Hz}^{-1/2}$, i.e. it stayed well below the LISA requirements. Also at lower frequencies LPF met the requirements, reaching $S_{\Delta g, \text{LPF}}^{1/2} \simeq (6 \pm 1) \times 10 \text{ fm s}^{-2} \text{ Hz}^{-1/2}$ at 20 μHz [19]. The extension phase ended on the 18th of July 2017 and the whole satellite was switched off [11].

During the entire mission duration, satellite motion coupled into the measurements at frequencies between 20 and 200 mHz (see, e.g., the bump of the red curve in Fig. 2.4) [11] and had to be subtracted in post-processing. We refer to this noise as TTL coupling, which is the central theme of this work. I will further discuss the LPF TTL coupling in Sec. 6.2.1.

2.2.2 Control and measurement schemes

LPF contained two quasi-cubic test masses made of a gold-platinum alloy, each situated within an electrode housing. The test masses were 376 mm apart (surface to surface) and an optical bench was placed in between. This constellation mimics one LISA arm shrinking it down to a couple of decimetres. A heterodyne interferometric readout provided the distance changes of the two test masses [20].

In order to measure the level of free fall and possible misalignments of its test masses, LPF con-

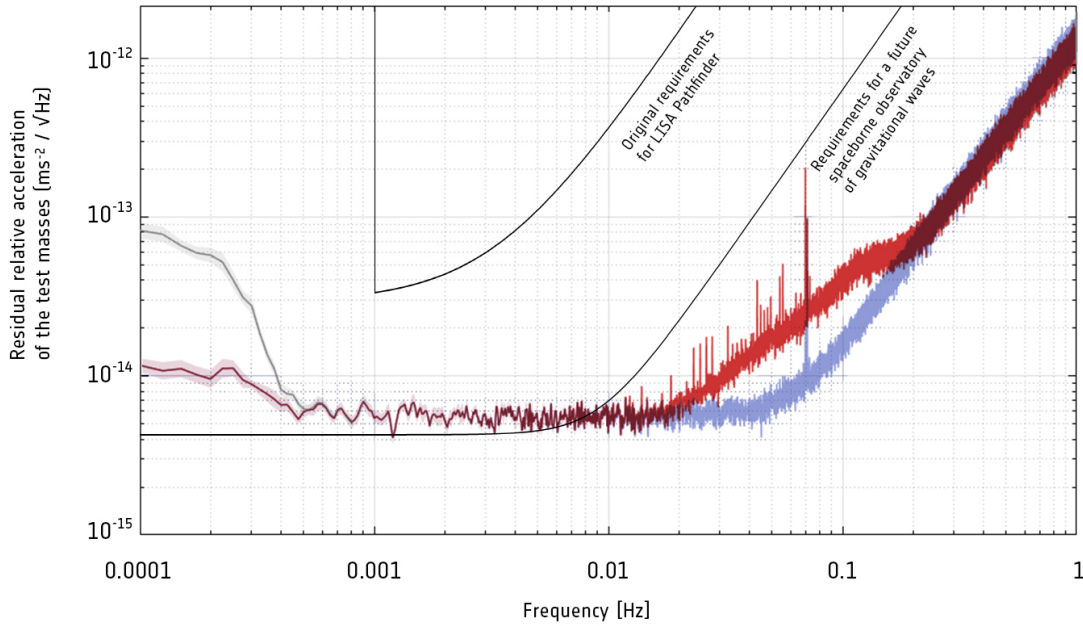


Figure 2.4: The amplitude spectral density (ASD) of Δg during the nominal LPF operation phase. Gray: Measurement of the ASD averaged over 6.5 days, starting at the 8th of April 2016. Red: ASD of the same measurements after subtraction of centrifugal forces (dominant at low frequencies). Blue: ASD of the same measurements after further subtraction of the cross-talk of S/C motion. Figure credit: [11]

tained two primary sensors, the optical metrology system (OMS) and the gravitational reference sensor (GRS) [16, 20].

The laser source, laser modulator, optical components, phasemeter and the processing computer together formed the OMS. It measured the relative displacement of the two test masses along the x -axis and additionally their differential angular orientation via differential wavefront sensing (DWS). LPF's optical bench included, therefore, four different interferometers [16, 20, 21]:

1. The x12-interferometer: Measured the interference signal of a local reference beam and a measurement beam that was reflected at both test masses. It determined the relative distance changes between the test masses, i.e. the main science signal, and their relative angles.
2. The x1-interferometer: Measured the interference signal of a local reference beam and a measurement beam that was reflected only at the first test mass. It determined the relative displacement of the S/C with respect to this test mass and their relative angular alignment.
3. The reference interferometer: Provided a reference phase signal. This signal was subtracted from the other signals.
4. The frequency interferometer: Measured the laser frequency noise. This signal was used to stabilise the laser.

All four interferometers are shown in Fig. 2.5. My subsequent work, in particular, the data analysis in Sec. III builds on the readouts of the x1- and the x12-interferometer.

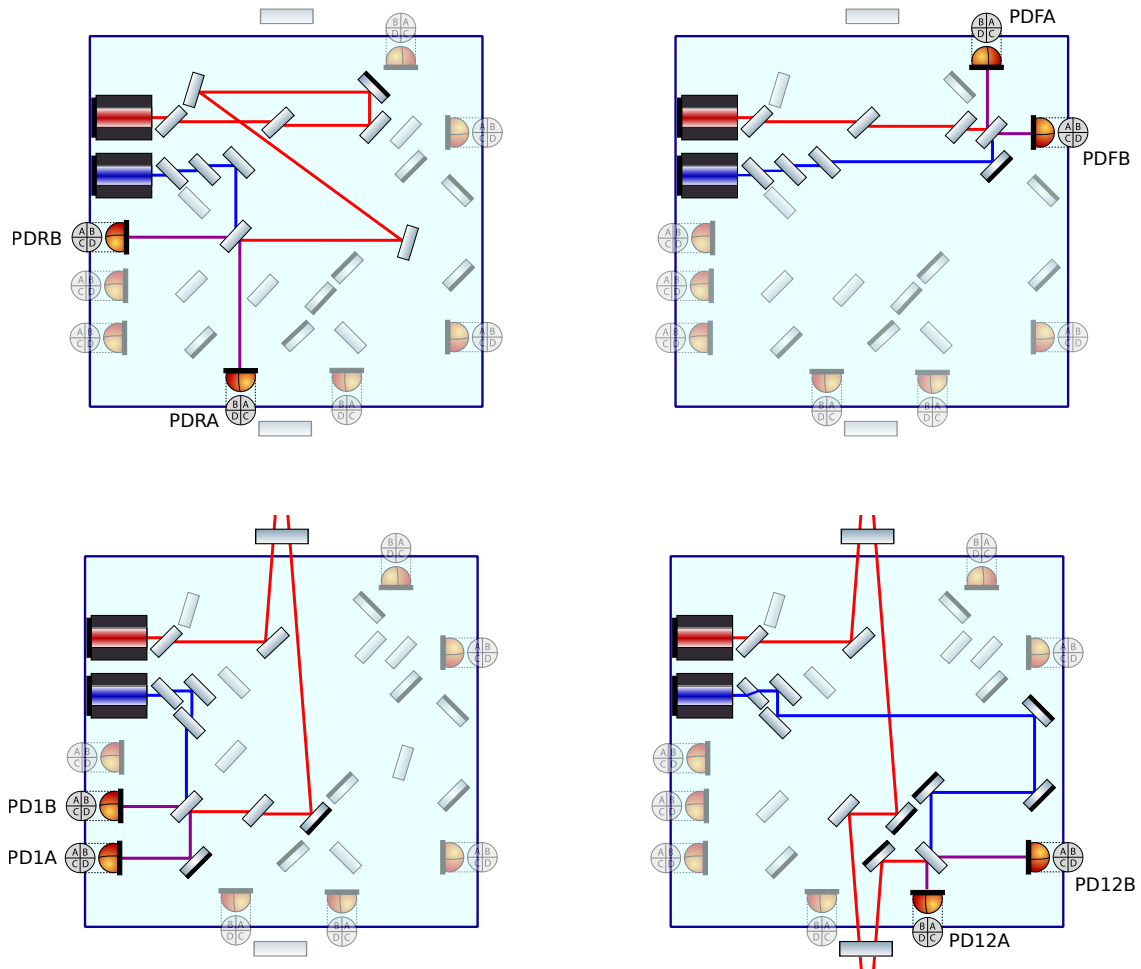


Figure 2.5: The four interferometers in LPF. The measurement beam is shown in red and the reference beam in blue. Top-left: reference interferometer. Top-right: frequency interferometer. Bottom-left: x1-interferometer. Bottom-Right: x12-interferometer.

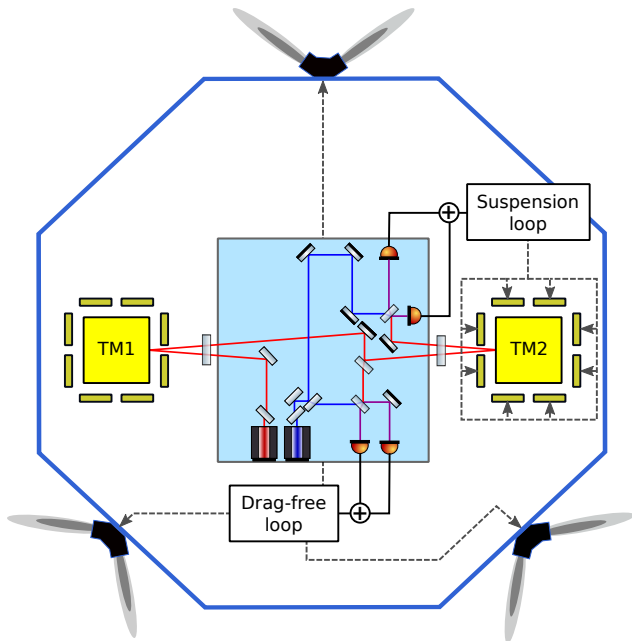


Figure 2.6: Schematic of LISA Pathfinder and its drag-free attitude control system. Drag-free control loop: The measurement of the x_1 -interferometer was used to correct the S/C alignment via the thrusters. Suspension loop: The measurement of the x_2 -interferometer was used for the correction of the alignment of the second test mass via its surrounding electrodes.

The data of the four interferometers is processed by the data management unit (DMU). It produces the desired longitudinal path length signal (LPS) and DWS readouts. These measurements are then communicated to other systems, e.g., the drag-free attitude control system (DFACS) described below [16].

The GRS was, on the one hand, a sensing and, on the other hand, also an actuation system. It consisted of the two test masses, the electrode housing and the front-end electronics. Electrodes mounted on the housing measured all six degrees of freedom of both test masses (i.e. the shifts of the first test mass in all directions, the shifts of the second test mass orthogonal to the measurement axis and rotations of the first test mass around the measurement axis). Additionally, another set of electrodes was used to apply forces on the test masses to correct their positions and alignments. The LPF mission has shown that the OMS is five orders of magnitude less noisy than the GRS [20].

Further, a control scheme was used to minimise the undesired influence of the hosting S/C on the test masses (TMs), i.e. the DFACS [22], see Fig. 2.6: The first test mass, TM1, was not controlled along the sensitive x -axis. The S/C was then forced by the DFACS to follow TM1. Therefore, the relative position of TM1 was determined via the x_1 -interferometer first and, second, the necessary thrust strength was deduced and applied to the satellite via the micro-Newton thrusters. This continuous control scheme was called the drag-free loop. The second test mass, TM2, followed TM1 accordingly. Its relative position was obtained using the x_2 -interferometer readout additionally. The electrostatic force actuator of the second electrode housing corrected then its position and alignment. Since the forces and torques applied to TM2 are well known, they could be subtracted in post-processing to estimate the level of free fall of this test mass. Additionally, the electrostatic force was applied at a frequency below the LPF measurement band minimising its impact on the acceleration measurement. This control scheme was called the suspension loop [20, 22].

2.2.3 Δg and its contributors

The main observable during the LPF mission was the test masses' residual acceleration noise Δg . It describes not only the actual differential acceleration of the test masses along their

optical axis $\Delta\ddot{x}$ but additionally depends on forces acting on the test masses or the S/C and the coupling of S/C motion into the readout.

The free-fall accelerations of the test masses are described by

$$g_1 = \ddot{x}_1 + \omega_1^2(x_1 - x_{\text{SC}}), \quad (2.3)$$

$$g_2 = \ddot{x}_2 + \omega_2^2(x_2 - x_{\text{SC}}) - g_c. \quad (2.4)$$

Thereby, x_i and \ddot{x}_i denote the displacement and acceleration of the respective test mass or S/C. The acceleration of the test masses depended on their alignment with respect to S/C due to stiffnesses ω_i^2 , which are different for both test masses. These force gradients act like a spring with a negative spring constant. They depend on gravitational, electrostatic and magnetic forces. Since the satellite was balanced for a minimal gravitational force experienced by the test masses at their optimal position, a slight offset pulled them further away towards the centre of the S/C. This gravitational force was larger than the electrostatic contribution, which originates from changes of the acting electrostatic force due to position changes of the respective test mass. Finally, g_c describes the estimated forces applied on TM2, i.e. to make it follow the S/C and thus the TM1 motion [17, 20].

Let us consider first a perfectly aligned system. To distinguish the residual acceleration noise in this case from the accelerations measured in slightly misaligned systems, it is denoted here Δg_x . It equals the differential accelerations of the two test masses, i.e.

$$\Delta g_x = g_2 - g_1 \quad (2.5)$$

$$= \ddot{x}_2 + \omega_2^2(x_2 - x_{\text{SC}}) - g_c - \ddot{x}_1 - \omega_1^2(x_1 - x_{\text{SC}}) \quad (2.6)$$

Using the readout of the x1- and x12-interferometer, $o_{12} = x_2 - x_1$ and $o_1 = x_1 - x_{\text{SC}}$, and the differential stiffness $\Delta\omega_{12}^2 = \omega_2^2 - \omega_1^2$, which characterises how the S/C motion couples into Δg , Eq. (2.6) transforms to

$$\Delta g_x = \ddot{o}_{12} + \omega_2^2 o_{12} + \Delta\omega_{12}^2 o_1 - g_c. \quad (2.7)$$

In summary, the differential acceleration Δg_x of a perfectly aligned system can be calculated via the x1- and x12-interferometer readout, the prior computed stiffnesses and the control forces acting on TM2 [17, 20].

For misaligned systems, further forces and noises contribute to Δg . First, the cross-talk of S/C motion coupled in all degrees of freedom into the measurement, g_{xtalk} . This contribution relates to the TTL coupling which I will describe in Sec. 5 and discuss for LPF in Sec. 6.2.1. Second, since LPF was a rotating reference frame, its rotations introduce inertial forces, g_{rot} that coupled into the measurements along the optical (x -) axis. These inertial forces were, on the one hand, the centrifugal force g_Ω depending on the S/C velocity Ω and, on the other hand, the Euler force $g_{\dot{\Omega}}$ originating from rotational accelerations of the S/C. Altogether we find [11, 17, 20]

$$\Delta g = \Delta g_x + g_{\text{xtalk}} + g_{\text{rot}}. \quad (2.8)$$

2.3 Other Space-Based Interferometers

Laser interferometers are not only used to measure gravitational waves. Since 2018 the satellites of the mission Gravity Recovery and Climate Experiment Follow-On (GRACE-FO), a mission to map the Earth's gravity field, measure their distance variations via a laser ranging instrument (LRI) [23, 24]. I provide further information about GRACE-FO in App. A.

Additional to LISA, there are a couple of additional laser interferometric missions planned to be launched into space within the next decades. Besides proposals for interferometers on the surface on the Moon [P4, 25] that could potentially bridge parts of the sensitive gap between LISA and the Earth-based interferometers, further space-based laser interferometers are investigated by different space agencies. Prominent examples are the Chinese TianQin and Taiji [26, 27, 28, 29] missions which are planned to be launched in the 2030s and hence could operate at the same time as LISA. Another proposed mission is the DECI-hertz Gravitational wave Observatory (DECIGO) by the Japan Aerospace Exploration Agency [30, 31, 32]. It is supposed to measure gravitational wave signals in the deci-Hertz regime parallel to the other space-based interferometers in the 2030s.

These missions will likely face similar challenges as LISA. Thus the discussion of the TTL noises below likely also becomes relevant for them.

Chapter 3

The Interferometric Readout

Laser interferometry relies on the measurement of changes in the interference signal produced by two superimposed laser beams. Not only gravitational waves but also various noise sources affect the interference pattern by changing the path length, beam direction or point of detection at the detector of one of the beams. In this section, I will explain what the photodiodes (PDs) measure and how we extract the desired information from this measurement.

3.1 Power Detection for Two Interfering Beams

In interferometric setups, photodiodes are used to measure the power of the incoming laser light. If more than one beam impinges at the detector, we detect interference between the involved beams. In this case, the power of both beams either adds up constructively, or we measure less light when the beams interfere destructively. In most ideal laser interferometers, only two beams interfere. However, due to unwanted reflections of fractions of the beams, also ghost beams propagate to the photodiode's surface.

Within this thesis, I will consider the ideal case of two interfering beams. Their detected power equals the intensity distribution integrated over the detector surface, i.e.

$$P = \int_{\text{PD}} dS I. \quad (3.1)$$

The intensity, on the other hand, depends on the beams' wavefront properties, i.e. their shape and orientation. In particular, phase differences between them affect the intensity distribution constructively or destructively. Mathematically, the intensity is described via the electric field equations of the beams,

$$E_b(t) = A_b \exp(-i \Phi_b + i \omega_b t), \quad (3.2)$$

where A_b denotes the amplitude and Φ_b the phase of the respective beam (b). The electric field oscillates over time at the angular speed ω_b . The intensity is proportional to the squared absolute electrical field of a beam. So the intensity of the interfering beams equals the squared absolute sum of both electrical fields,

$$I \simeq |E_{b1} + E_{b2}|^2. \quad (3.3)$$

In classical Michelson interferometers, both beams are affected by gravitational waves. However, in space-based laser interferometers like LISA and LPF the beam carrying information about

length changes interferes with a local beam. Any variations of that local beam are kept to a minimum and it serves as a reference. Therefore, we call it the reference beam (r). The other beam, tracking the variations in the system, is called the measurement beam (m). In the following, I will assume an interference of these two beams and hence get

$$I \simeq |E_m + E_r|^2 . \quad (3.4)$$

Inserting Eq. (3.2) via (3.4) into Eq. (3.1), we derive

$$\begin{aligned} P(t) &= \int_{\text{PD}} dS I \\ &\stackrel{(3.4)}{=} \int_{\text{PD}} dS |E_m(t) + E_r(t)|^2 \\ &\stackrel{(3.2)}{=} \int_{\text{PD}} dS (A_m^2 + A_r^2) \left[1 + \frac{2A_r A_m}{A_m^2 + A_r^2} \cos(-\Delta\Phi + \omega_{\text{het}}t) \right] \\ &\equiv \int_{\text{PD}} dS \bar{I} [1 + c_I \cos(-\Delta\Phi + \omega_{\text{het}}t)] \end{aligned} \quad (3.5)$$

with the average intensity and the corresponding local contrast

$$\bar{I} = A_m^2 + A_r^2 , \quad (3.6)$$

$$c_I = \frac{2A_m A_r}{A_m^2 + A_r^2} \quad (3.7)$$

[33, 34]. Both values can experimentally be derived via the minimal and maximal intensities, see [35]. The phase difference $\Delta\Phi$ equals the difference between the phases of measurement and reference beam, i.e.

$$\Delta\Phi = \Phi_m - \Phi_r . \quad (3.8)$$

Analogously we define the differential angular frequency

$$\omega_{\text{het}} = \omega_m - \omega_r . \quad (3.9)$$

While the differential frequency would be zero in homodyne interferometers, a frequency offset ω_{het} is added in heterodyne interferometers. This heterodyne frequency is much smaller than the original frequency, i.e. $\omega_{\text{het}} \ll \omega_{m,r}$. However, it adds a time-dependent term to the measured power. The signal is, therefore, encoded in the deviations of the power fluctuations. Heterodyne interferometers are usually used in space-based interferometers like GRACE-FO and LISA. In these missions, the distance between two S/C varies over time due to their orbital properties causing time-varying Doppler shifts and hence a continuously drifting differential frequency.

Mind that the intensity I , the contrast c_I and the phase Φ are local properties. By evaluating the final integral in Eq. (3.5), we find

$$P \equiv \bar{P} [1 + c \cos(-\phi + \omega_{\text{het}}t)] , \quad (3.10)$$

where \bar{P} denotes the mean power, c is the contrast on the whole photodiode surface and ϕ gives the detected phase [33, 34].

Build on this preparatory work, I will introduce the different signals processed by the detector in the next section.

3.2 Interferometric Signals

We typically define four different types of signals characterising the phase changes, the beam's relative orientation and centres of incidence, and the quality of the signal [33]. Within this work, the primary focus lies on the first one, the LPS. It contains not only the information about gravitational wave signals but is also affected by the TTL coupling, which will be introduced below. However, in experiments, the other three signals are also needed to characterise the observed coupling.

3.2.1 The longitudinal path length signal

The longitudinal path length signal (LPS) [33, 34] is a measure of phase differences. It converts for a continuous detector the measured phase into a length signal via

$$\text{LPS} = \frac{1}{k} \phi, \quad (3.11)$$

where $k = 2\pi/\lambda$ is the wavenumber depending on the wavelength λ of the beams. This holds for homodyne interferometers as well as for heterodyne interferometers, where the heterodyne frequency is sufficiently small against the laser frequency f , i.e. $f_{\text{het}} \ll f$, such that

$$k \approx k_1 = \frac{2\pi}{\lambda_1} \approx \frac{2\pi}{\lambda_2} = k_2. \quad (3.12)$$

The interferometers in LPF fulfilled this requirement [36]. In order to obtain the phase ϕ from the measured power in Eq. (3.10) a phase demodulation was applied in LPF [33]. This phase demodulation was based on a discrete Fourier transform. Here, we perform the analytical equivalent for the continuous time-interval of one oscillation cycle: An integration of the power multiplied with a cosine and sine function of the heterodyne frequency respectively gives two non-time-dependent products,

$$Q_1 = \frac{1}{\pi} \int_0^{2\pi} d(\omega_{\text{het}} t) \cos(\omega_{\text{het}} t) \cdot P(\omega_{\text{het}} t) = \bar{P} c \cos(\phi), \quad (3.13)$$

$$Q_2 = \frac{1}{\pi} \int_0^{2\pi} d(\omega_{\text{het}} t) \sin(\omega_{\text{het}} t) \cdot P(\omega_{\text{het}} t) = -\bar{P} c \sin(\phi). \quad (3.14)$$

With this we can compute the phase via

$$\phi = -\arctan\left(\frac{Q_2}{Q_1}\right). \quad (3.15)$$

Mathematically, we achieve the same result when integrating over the complex product of the electrical fields of the two beams and set the time dependency to zero [34],

$$\begin{aligned} Q &= \int_{\text{PD}} dS 2E_m E_r^* |_{t=0} \\ &= \int_{\text{PD}} dS 2A_m A_r \exp(-i \Delta\Phi) \\ &= \int_{\text{PD}} dS \bar{I} c_I \exp(-i \Delta\Phi) \\ &= \bar{P} c \exp(-i \phi). \end{aligned} \quad (3.16)$$

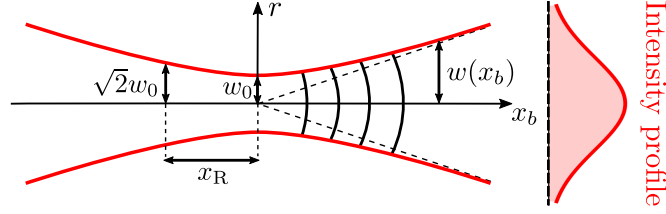


Figure 3.1: Profile of a Gaussian beam. The beam has a waist size w_0 defining the Rayleigh range x_R . It propagates in x_b -direction constantly increasing its radial width $w(x_b)$ and the radius of curvature $R(x_b)$ of the circle segments. The intensity profile of the beam along a radial cross-section has a Gaussian distribution. It becomes flatter at larger distances from its waist position.

Hence the phase ϕ is the negative argument of Q , i.e.

$$\phi = -\arg(Q). \quad (3.17)$$

Moreover, we see that

$$Q = Q_1 + i Q_2 \quad (3.18)$$

and therefore

$$\phi = -\arctan\left(\frac{\Im(Q)}{\Re(Q)}\right). \quad (3.19)$$

For our analytical derivations, the formalism (3.16) is easier to implement. Therefore, it is used for the computation following in Sec. 5. In this section, I will compute the LPS for a setup with two interfering local Gaussian beams based on [34]. This scenario describes the interference observed in LPF. Also, in ground-based laboratories, this is a common case since all unclipped and undisturbed propagating laser beams are Gaussian beams, i.e. their intensity profile has a Gaussian distribution, see Fig. 3.1.

Although Gaussian beams are in the literature usually described for propagation in z -direction, I will assume a propagation in x -direction throughout this thesis. This axis is the sensitive axis in LPF. The amplitude and phase of Gaussian beams are then given by

$$A_b = E_{0b} \frac{w_{0b}}{w(x_b)} \exp\left[\frac{-r_b^2}{w(x_b)^2}\right], \quad (3.20)$$

$$\Phi_b = \frac{k r_b^2}{2R(x_b)} - \zeta(x_b) + k x_b. \quad (3.21)$$

A summary of all parameters is given in Tab. 3.1. A necessary assumption for our analytical computations is that the beam parameter-dependent spot sizes $w(x_b)$, radii of curvature $R(x_b)$ and Gouy phases $\zeta(x_b)$ are identical for all points on the detector [34]. This is usually the case since they are nearly unaffected by small misalignments. We, therefore, compute Q by

$$Q = \int_{\text{PD}} dS \ 2 E_{0m} E_{0r} \frac{w_{0m} w_{0r}}{w(x_m) w(x_r)} \exp\left[\frac{-r_m^2}{w(x_m)^2} + \frac{-r_r^2}{w(x_r)^2}\right] \cdot \exp\left[-i k \left(\frac{r_m^2}{2R(x_m)} - \frac{r_r^2}{2R(x_r)}\right) + i(\zeta(x_m) - \zeta(x_r)) - i k(x_m - x_r)\right]. \quad (3.22)$$

We refer to the function Q as the complex amplitude. Its representation for Gaussian beams (3.22) will be used in Sec. 5.2 for the analytical derivation of the signal changes due to TTL coupling.

Name	Symbol	Description
wavenumber	$k = 2\pi/\lambda$	spacial frequency
beam index	$b \in \{m, r\}$	indicates if the parameter belongs to the measurement (m) or reference (r) beam
mean amplitude	E_0	-
radial distance	$r = \sqrt{y^2 + z^2}$	distance to the beam ray
distance from waist	x_b	defined in propagation direction
Rayleigh range	$x_R = \pi w_0^2/\lambda$	distance from waist at which the area of the cross section is doubled
radius of curvature	$R(x_b) = x_b[1 + (x_b/x_R)^2]$	characterises the curvature of the wavefront
waist size	w_0	radius of the beam at its waist
beam width	$w(x_b) = w_0\sqrt{1 + (x_b/x_R)^2}$	beam radius at the distance from waist x_b
Gouy phase	$\zeta(x_b) = \arctan(x_b/x_R)$	phase accumulated by the beam in the near field
angular frequency	ω	-

Table 3.1: Parameters defining the electrical field of Gaussian beams.

3.2.2 The contrast

The contrast [33] (compare Sec. 3.1) describes the relative difference between the maximum and the minimum power at the detector,

$$c = \frac{P_{\max} - P_{\min}}{P_{\max} + P_{\min}}. \quad (3.23)$$

It is, therefore, a measure for the quality of the measurements. The optimal contrast is $c = 1$. An accurate measurement becomes difficult if the contrast is low, as power fluctuations are less characteristic. We can compute the contrast using the complex amplitude Q and the measured power P via

$$c = \frac{\sqrt{Q_1^2 + Q_2^2}}{\bar{P}} = \frac{|Q|}{\bar{P}}, \quad (3.24)$$

where

$$\bar{P} = \frac{1}{2\pi} \int_0^{2\pi} d(\omega_{\text{het}}t) P. \quad (3.25)$$

3.2.3 The differential power sensing signal

While the LPS and the contrast can be derived for any detector, we have to consider quadrant photodetectors (QPDs) for the following signals. QPDs consist of four sensitive surfaces separated by an insensitive cross slit, see Fig. 3.2. These four measurements can hence be combined to new signals. One of them is the differential power sensing (DPS) signal [33]. It indicates the position of the beam's amplitude centroid on the detector. It combines the power measurements of the single segments. If the power is larger on one segment, this indicates that the beam has been shifted in this direction. We distinguish between the horizontal and the vertical DPS

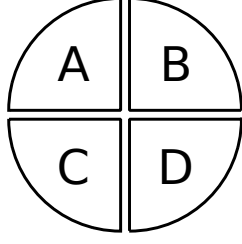


Figure 3.2: Quadrant photodiode. The four sensitive surfaces are labelled A, B, C and D (standard labelling when viewing from the front, i.e. in direction of the propagating beam). The cross slit between these regions is insensitive.

signal,

$$\text{DPS}_h = \frac{\bar{P}_{\text{right}} - \bar{P}_{\text{left}}}{\bar{P}_{\text{right}} + \bar{P}_{\text{left}}} = \frac{\bar{P}_B + \bar{P}_D - \bar{P}_A - \bar{P}_C}{\bar{P}_A + \bar{P}_B + \bar{P}_C + \bar{P}_D}, \quad (3.26)$$

$$\text{DPS}_v = \frac{\bar{P}_{\text{up}} - \bar{P}_{\text{down}}}{\bar{P}_{\text{up}} + \bar{P}_{\text{down}}} = \frac{\bar{P}_A + \bar{P}_B - \bar{P}_C - \bar{P}_D}{\bar{P}_A + \bar{P}_B + \bar{P}_C + \bar{P}_D}. \quad (3.27)$$

The average powers P_i are derived like in Eq. (3.25) for the power measured in the respective detector quadrant. The DPS signal was used in LPF for the first realignment of the beams. Note that the horizontal DPS signal was defined there the opposite way [TN1], i.e. $\text{DPS}_h = \frac{\bar{P}_{\text{left}} - \bar{P}_{\text{right}}}{\bar{P}_{\text{right}} + \bar{P}_{\text{left}}}$. However, I stay with the definition above, which corresponds to the detectors coordinate system, which I will introduce below and is currently used in simulations for LISA [37].

3.2.4 The differential wavefront sensing signal

The differential wavefront sensing (DWS) signal [33, 38] is an important signal in the characterization of TTL coupling. It measures the relative angle between the two incoming beams. Precisely, it compares the measured phases on the four quadrants and computes a horizontal and vertical differential phase,

$$\text{DWS}_h = \phi_{\text{right}} - \phi_{\text{left}}, \quad (3.28)$$

$$\text{DWS}_v = \phi_{\text{up}} - \phi_{\text{down}}. \quad (3.29)$$

The horizontal DWS signal DWS_h represents the differential yaw angle and the vertical DWS signal DWS_v gives the differential pitch angle. There are different methods to compute the left, right, top and bottom phases. In LPF, these phases were computed following the formalism (3.15) given the power measured at the investigated quadrants, cf. (3.5). E.g., the phase ϕ_{left} is defined as

$$\begin{aligned} \phi_{\text{left}} &= -\arctan \left[\frac{\int_0^{2\pi} d(\omega_{\text{het}} t) \sin(\omega_{\text{het}} t) \int_{A,C} dS I}{\int_0^{2\pi} d(\omega_{\text{het}} t) \cos(\omega_{\text{het}} t) \int_{A,C} dS I} \right] \\ &= -\arctan \left[\frac{\int_0^{2\pi} d(\omega_{\text{het}} t) \sin(\omega_{\text{het}} t) (\int_A dS I + \int_C dS I)}{\int_0^{2\pi} d(\omega_{\text{het}} t) \cos(\omega_{\text{het}} t) (\int_A dS I + \int_C dS I)} \right] \\ &= -\arctan \left[\frac{\bar{P}_A c_A \sin(\phi_A) + \bar{P}_C c_C \sin(\phi_C)}{\bar{P}_A c_A \cos(\phi_A) + \bar{P}_C c_C \cos(\phi_C)} \right]. \end{aligned} \quad (3.30)$$

Analogously we get

$$\phi_{\text{right}} = -\arctan \left[\frac{\bar{P}_B c_B \sin(\phi_B) + \bar{P}_D c_D \sin(\phi_D)}{\bar{P}_B c_B \cos(\phi_B) + \bar{P}_D c_D \cos(\phi_D)} \right], \quad (3.31)$$

$$\phi_{\text{up}} = -\arctan \left[\frac{\bar{P}_A c_A \sin(\phi_A) + \bar{P}_B c_B \sin(\phi_B)}{\bar{P}_A c_A \cos(\phi_A) + \bar{P}_B c_B \cos(\phi_B)} \right], \quad (3.32)$$

$$\phi_{\text{down}} = -\arctan \left[\frac{\bar{P}_C c_C \sin(\phi_C) + \bar{P}_D c_D \sin(\phi_D)}{\bar{P}_C c_C \cos(\phi_C) + \bar{P}_D c_D \cos(\phi_D)} \right]. \quad (3.33)$$

Like the DPS signal, the horizontal DWS signal was defined with an opposite sign in LPF. In order to make this work best applicable for future analysis, for instance, in the context of LISA, the definition above is used throughout this work.

Chapter 4

Introduction to Tilt-To-Length Coupling

One of the major noise sources in space-based laser interferometers is tilt-to-length (TTL) coupling [11, 39, 40, 41, 42]. It originates from lateral and rotational jitter of reflective surfaces inside the S/C, e.g. test masses, but also of the S/C itself. However, TTL coupling can appear not only in space interferometers but also in laboratory experiments. Any measurement of the interference signal of laser beams where one of the beams reflects at a misplaced or jittering surface or is received by a jittering optical bench (OB) can potentially be affected by this noise.

4.1 Angular and Lateral Tilt-To-Length Coupling

We refer to the path length signal changes due to angular and lateral jitter as TTL coupling. Angular jitter of a component can affect the path length signal in various ways, as I will discuss in Sec. 5. These are rotations of the beam paths – in vacuum or air, but also within transmissive optical components – and rotations of components into or out of the beam path, see Fig. 4.1. The rotations change the beam’s path lengths as well as their points of incidence and wavefront properties at the detector.

Lateral TTL also falls under the term TTL coupling since it only occurs at tilted surfaces, as I will show in Sec. 5. By shifting a component in a direction that is not parallel to its reflecting or detecting surface, the beam path to the component gets elongated or shortened. Additionally, the beam’s point of detection, i.e. the point where the beam axis meets the detector surface, changes due to the lateral shift, see Fig. 4.1. Given a laterally jittering receiving system (discussed in Sec. 5), the detector surface itself jitters with respect to the received beam. In this case, the measured signal would change even if the beam path stays unchanged. The phase changes are induced here by the mismatch of the interfering wavefront due to the shift. I introduce the TTL changes due to wavefront mismatches in the following subsection.

Summary box 4.1 | Angular and lateral TTL coupling

Angular and lateral jitter induce TTL coupling.

Via tilting a reflective component, the beam path after the reflection also gets rotated, leading to a path length change. Additionally, the beam accumulates additional or reduced path lengths due to the shifted point of reflection.

A shift of a rotated component changes the point of reflection, yielding an elongated or shortened path length.

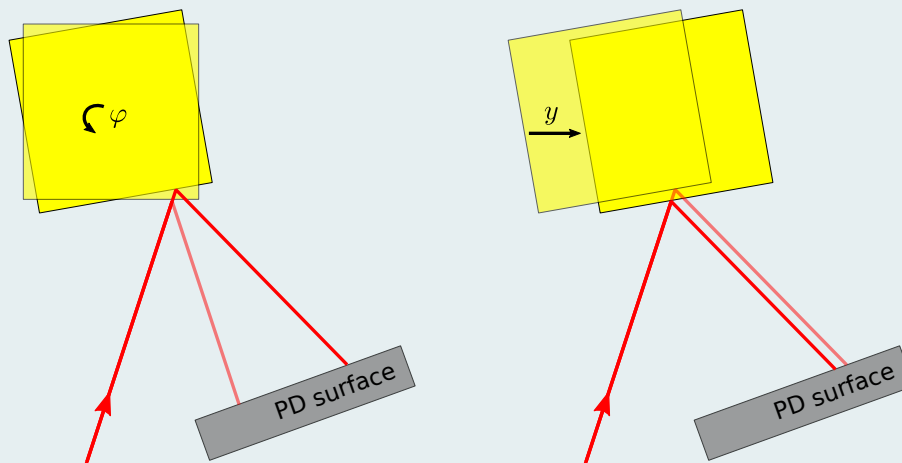


Figure 4.1: Angular (left) and lateral (right) TTL coupling depicted for a reflection at a jittering test mass. The original path and test mass alignment are shown in light colours.

4.2 Geometric and Non-Geometric Tilt-To-Length Coupling

While laser interferometers are built to measure distance changes between two objects, the TTL coupling disturbs this measurement quantity. So, the angular or lateral jitter of one of the beams with respect to the detector affects, on the one hand, its path and, therefore, its geometric path length and, on the other hand, the interference pattern on the detector. We refer to length changes of the beam axis as geometric TTL coupling [P3] and to all additional effects due to the wavefront properties and the detector geometry as non-geometric TTL coupling [P2].

The geometric TTL coupling is independent of the beam types. It arises when the beam jitters angularly with respect to the detector surfaces. In experimental setups, these rotations can be applied directly to the beam itself or indirectly via the jitter of a component, e.g. a test mass or a receiving system. It is possible to suppress such geometric TTL coupling by dedicated imaging systems [39, 43]. Furthermore, lateral jitter of a test mass, thereby moving into or out of the beam path, creates geometric TTL coupling.

Although dominant in many interferometers not using imaging systems, the geometric TTL coupling does not describe the measured phase difference alone. Additionally, wavefront related coupling terms alter the signal. These are different for every beam type and further depend on aberrations of the wavefronts [40] and the beam diffractions [37]. Also, the non-geometric TTL coupling depends on the detector geometry. The photodiodes' sensitive surfaces are of limited size, feature in the case of QPDs an insensitive cross slit making the beams clip at the detector borders, or suffer from arbitrary detector errors. All these detector properties alter the measured signal. Moreover, the signal itself can be defined differently when using QPDs. This choice for a signal definition further alters the measured TTL noise.

4.3 Tilt-To-Length Coupling in this Work

In this work, I differentiate, on the one hand, between geometric and non-geometric and, on the other hand, between angular and lateral TTL coupling.

In terms of geometric TTL coupling (Sec. 5.1), I investigate how the beam axis' path length changes for angular and lateral jitter of reflecting surfaces, e.g. test masses. We find TTL coupling due to jitter of the test masses relative to the S/C in LPF (Sec. 6.2.1) and in the test mass interferometer of LISA (Sec. 6.2.2). Furthermore, I will describe the TTL coupling due to the jitter of a receiving system, as we find it in the long-arm interferometer of LISA where the beam received from a far S/C interferes with a local beam (Sec. 6.2.2). Additionally, I discuss the TTL effect of planar transmissive components, i.e. windows or transmissive beamsplitters. While a beam exits a component with planar surfaces at the same angle as it enters the latter, its refraction angle depends on the alignment of the incoming angle. Transmissive components, therefore, change the optical path length of a tilted refracting beam. This is different for components with curved surfaces, e.g. lenses. However, the analytical description of the TTL coupling in lens systems is not the content of this work.

As introduced above, non-geometric TTL coupling (Sec. 5.2) depends on the beams types interfering, i.e. their wavefronts properties. I focus in this work on the analytical description of TTL coupling for Gaussian beams as we find them in LPF and also the test mass interferometer of LISA. The expected non-geometric signal contribution will be derived depending on the beam parameters and their alignment with respect to each other and to the detector surface. Thereby, I neglect possible wavefront aberrations such as defocus, astigmatism, coma, trefoil or spherical

aberrations. Also, the diffraction of the beams due to clipping at apertures along the beam path will not be covered here.

Besides the beams' wavefront properties, the non-geometric TTL coupling also depends on the detector geometry. I will describe the effect of the detector alignment and the shape of its sensitive areas on the coupling signal. In particular, I compare the expected coupling for single-element photodiodes (SEPDs) and QPDs. The latter allow for different signal definitions. In this work, I use the so-called LPF signal definition [36] as it was used during the LPF mission.

4.4 Tilt-To-Length Coupling in other Works

The analytical derivation of geometric and non-geometric TTL coupling presented in this work builds on previously published findings: Schuster et al. investigate in [44] the TTL coupling for a simplified case featuring Gaussian beams with equal beam parameters or planar waves. Moreover, it has been shown previously that the LPS cancels for Gaussian beams in some special cases [33, 44] which I reconsider in the upcoming discussion (Sec. 5.3). Relevant geometric TTL coupling effects have also been defined in [35, 37, 45].

As mentioned above, geometric TTL coupling is dominant in many interferometers. One possibility to suppress geometric coupling is given by dedicated imaging systems. These change the beam path depending on the respective angular and lateral alignment. A suitable alignment can, therefore, minimise the geometric TTL coupling at the detector. Contrary to LPF, in the LISA mission, imaging systems will be used to minimise the TTL coupling in the test mass interferometer [39] as well as the long-arm interferometer [43]. Dedicated experiments with 2- and 4-lens imaging systems have proven to meet the LISA requirements [39, 43].

However, the minimisation of TTL coupling by imaging systems is limited. On the one hand, the alignment of the imaging systems is likely not perfect, resulting in residual geometric TTL coupling and, on the other hand, non-geometric TTL coupling still enters the signal. Therefore, it has been investigated in [43] how the lateral alignment of the used QPD induces further coupling, thereby counteracting the residual TTL noise.

Another relevant difference within LPF and LISA are the beam types at the LISA long-arm interferometer. There, a local Gaussian beam will interfere with the received beam, which will be a fraction of the beam transmitted by a far S/C. This received beam will no longer be Gaussian but can be approximated by a flat-top beam [43]. So, it will be clipped by the telescope and, therefore, further suffers from diffraction. Schuster investigated in [37] the TTL noise from a diffracted beam imaged by a lens system onto the detector plane. Since the diffraction changes the interference pattern, it also affects the TTL coupling noise.

Besides diffraction, the beams' wavefronts are likely suffering from aberrations in the form of defocus, astigmatism, coma, trefoil or spherical aberrations. These aberrations can take any form but are usually small in laboratory setups. For beams propagating far distances as between the LISA satellites, they can become more significant. Thus, they will likely yield TTL coupling in the LISA long-arm interferometers [40, 41].

In every interferometer using QPDs, different LPS definitions can be applied to compute the full signal. Within this work, I use the LPF signal. A comparison of further signal definitions can be found in [36].

Part II

Tilt-To-Length Coupling: Model and Suppression

Chapter 5

Analytical Modelling of Tilt-To-Length Coupling

In this chapter, I will mathematically derive how TTL coupling changes the LPS. I divide the TTL effects into geometric [P3, 36] and non-geometric [P2, 36], i.e. wavefront and detector geometry related effects. In several cases, this separation is beneficial. So optical path length differences (OPDs) are often assumed to be dominant. However, lens systems (i.e. imaging systems) can be used to suppress significant parts of the geometric effects [39, 46]. In this case, the non-geometric TTL coupling becomes dominant. I will provide here analytical formulas describing the geometric and non-geometric noise contributors for angular and lateral jitter coupling. Moreover, I will show some cases where geometric and non-geometric coupling terms cancel each other.

The analytical work presented in this chapter, particularly the non-geometric TTL analysis, builds on the methods described in [33, 34, 36]. The working principle of the lever arm and the piston effect has been previously introduced in [37]. Here, I present a comprehensive analysis of the geometric and non-geometric TTL effects coupling into LPF and beyond. Wherever possible, I provide analytical equations describing these effects in two- and three-dimensional setups. The key findings have been published in [P3, P2].

5.1 Geometric Tilt-To-Length Coupling

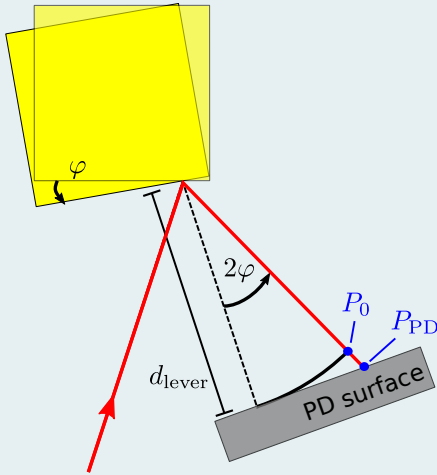
The geometric TTL coupling [P3] describes the phase changes due to the path length change of the beam axis. Thereby, we also account for optical effects that would directly affect this length measurement, for example, transmissions through optical components of a different material as the surrounding medium. Respectively, we refer to the measured length of the beam axis also as the optical path length (OPL).

I divide my analysis here for four independent effects that add up to the full geometric coupling. The first two are the lever arm and the piston effect, described in Sec. 5.1.1. Both originate from the jitter of a reflective test mass relative to the optical bench, such as in LPF. In Sec. 5.1.2 I will explain the coupling of a receiving S/C jitter relative to the beam path. This coupling occurs if the beam originates from a first OB and is then received by a second one which jitters with respect to the beam. We find such coupling, for instance, for the long-arm interferometer of LISA or in GRACE-FO. The fourth geometric coupling I discuss here originates from transmissive components along the beam path, see Sec. 5.1.3. The equations derived there add up to the

Summary box 5.1 | Lever arm effect

The TM rotates around the beam's point of reflection. This induces a rotation of reflected beam axis by twice the rotation angle of the TM. The beam, therefore, accumulates additional path length.

Analytical equations for the geometric lever arm effect assuming a beam with normal incidence ($\beta = 0$) and a non-tilted PD:



$$\text{OPD}_{\text{lever}}^{2\text{D}} = 2d_{\text{lever}} \varphi^2$$

$$\text{OPD}_{\text{lever}}^{3\text{D}} = 2d_{\text{lever}} (\varphi^2 + \eta^2)$$

Figure 5.1: Sketch of the geometric lever arm coupling. The test mass (yellow quadrangle) rotates by an angle φ . Therefore, the reflected beam (red) rotates by twice that angle. The dashed line shows the reflected beam path in the non-tilted case. Due to the rotation, beam axis accumulates the additional path length from point P_0 to point P_{PD} .

test mass as well as the S/C induced coupling. In all cases, I provide equations that explain the expected optical path length differences (OPDs) between a nominal and the tilted or laterally shifted scenario.

5.1.1 The test mass induced tilt-to-length coupling

In LISA as well as in LPF, the laser beams reflect at freely floating test masses. The big advantage of freely floating test masses in comparison to mounted mirrors lies in their stability: While the S/C accelerate due to micro-propulsions by the thrusters, solar force noise, small meteoroid impacts and other, electronic, sources [47], the test masses are much quieter. However, the jitter of the S/C relative to the test masses can also be interpreted as a test mass jitter that alters the reflected beam path. This subsection covers the two coupling effects induced by test mass jitter, the lever arm and the piston effect.

The Lever Arm Effect

The lever arm effect is a pure angular jitter coupling effect. A rotation of a test mass leads to a rotation of the beam behind its reflection point. By the law of reflection, the beam's propagation axis gets tilted by twice the rotation angle of the reflective surface. Thus the beam would propagate a different length until it hits the detector. If the test mass rotates around the beam's point of reflection, we refer to this effect as the lever arm effect. The described scenario is depicted in Fig. 5.1. There, the reflected beam axis (red) reaches the length d_{lever} of the nominal reflected beam axis (dashed, black) already in the point P_0 and propagates further

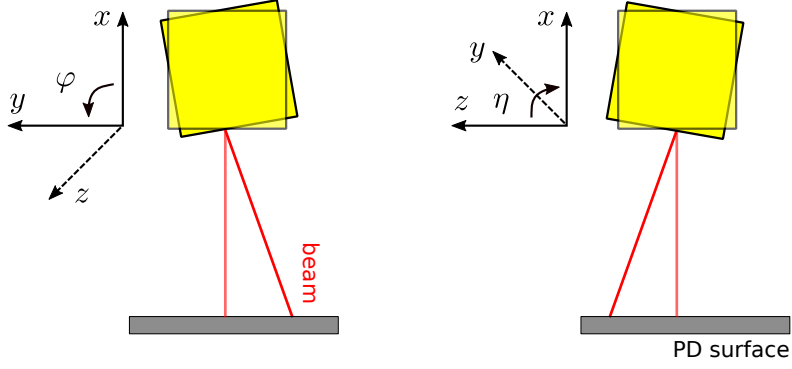


Figure 5.2: Pitch and yaw angle in a global coordinate system. Left: A positive rotation of the beam – directly or indirectly via a reflection at a rotated surface – in yaw generates a negative beam walk parallel to the y -axis. Right: A positive rotation in pitch gives a positive beam walk parallel to the z -axis.

until it impinges at the photodiode in the point P_{PD} . Hence the OPD computes as

$$\text{OPD}_{\text{lever}} = |\vec{p}_{\text{PD}} - \vec{p}_0| \quad (5.1)$$

$$= d_{\text{lever}} [\sec(2\varphi) - 1], \quad (5.2)$$

where \vec{p}_i is the position vector of a point P_i . In Eq. (5.2), I assumed for simplicity that the nominal beam hits the detector orthogonally. In practice, the beam direction and the surface normal of the detector are likely not parallel due to unavoidable imperfections in the setup. Let φ_{PD} describe the tilt of the detector surface normal with respect to the nominal beam axis. The OPD would then change to

$$\text{OPD}_{\text{lever}}^{2\text{D}} = d_{\text{lever}} [\sec(2\varphi - \varphi_{\text{PD}}) \cos(\varphi_{\text{PD}}) - 1]. \quad (5.3)$$

While these equations hold for any angle φ , $\varphi_{\text{PD}} \in (-\frac{\pi}{2}, \frac{\pi}{2})$, the tilts of the mirror and the imperfections in the setup defining the photodiode rotation are small in laser interferometers. This allows us to Taylor expand the Eqs. (5.2) and (5.3) giving

$$\text{OPD}_{\text{lever}}^{2\text{D}}(\varphi_{\text{PD}} = 0) \approx 2 d_{\text{lever}} \varphi^2, \quad (5.4)$$

$$\text{OPD}_{\text{lever}}^{2\text{D}}(\varphi_{\text{PD}}) \approx 2 d_{\text{lever}} [\varphi^2 - \varphi \varphi_{\text{PD}}]. \quad (5.5)$$

By Eq. (5.4), we see that the geometric lever arm effect is a quadratic effect when neglecting the detector rotation. I will show in Sec. 5.3 that the photodiode angle φ_{PD} cancels out when taking also non-geometric effects into account.

All equations for the lever arm effect so far show that it does not depend on the direction of the incoming beam. I characterise the beam alignment before the reflection by an angle β , which describes the rotation of the beam with respect to a beam of normal incidence. Although the beam in Fig. 5.1 deviates from a normal incidence, the OPD is only affected by the rotation angle of the test mass φ . However, the angle of the incoming beam becomes relevant as soon as three-dimensional setups are assumed. While the equations held so far for rotations in one plane, we have in space interferometry test masses jittering in all degrees of freedom. I, therefore, introduce here also the corresponding three-dimensional lever arm equations.

Let the x -axis be the sensitive axis. Then the rotations of the test mass affecting the OPL are the yaw angle φ and the pitch angle η , as shown in Fig. 5.2. The angular alignment of the incoming beam with respect to the sensitive axis is given by the propagation angle β_y in the xy -plane and β_z in the xz -plane. If the detector is tilted with respect to the nominal beam, I further describe

2D and	3D symbols	Description
d_{lever}	d_{lever}	distance between centre of rotation (CoR) and point of detection (PoD)
d_{long}	d_{long}	longitudinal, i.e. direction of sensitive axis, distance between CoR and point of interest, e.g. point of reflection (PoR) or PoD
d_{lat}	d_{lat} d_{vert}	lateral, i.e. orthogonal to sensitive axis, distance(s) between CoR and point of interest
t_{tc}	t_{tc}	thickness of transmissive component
n_{tc}	n_{tc}	refractive index of transmissive component
β	β_y β_z	(propagation) angle(s) between sensitive axis and nominal beam path
φ	φ η	rotation angle(s) of TM
φ_{PD}	φ_{PD} η_{PD}	rotation of the detector with respect to nominal beam direction
φ_{tc}	φ_{tc} η_{tc}	rotation of transmissive component with respect to the nominal beam direction

Table 5.1: Overview over the parameters used to describe the geometric TTL. Denoted are the two- and three-dimensional symbols, respectively.

its angular alignment via the angles as φ_{PD} (rotation in xy -plane) and η_{PD} (rotation in xz -plane). Furthermore, d_{lever} defines the geometric length the nominal beam propagates through the three-dimensional space from the point of reflection at the test mass to the photodiode. A summary of the definition of the parameters in the two- and three-dimensional cases is given in Tab. 5.1. With this we get

$$\text{OPD}_{\text{lever}}^{3\text{D}}(\varphi_{\text{PD}}, \eta_{\text{PD}} = 0) \approx d_{\text{lever}} \frac{2 \cos^2(\beta_z) \varphi^2 + 2 \cos^2(\beta_y) \eta^2 + \sin(2\beta_y) \sin(2\beta_z) \varphi \eta}{\cos^2(\beta_y) + \cos^2(\beta_z) \sin^2(\beta_y)}, \quad (5.6)$$

$$\text{OPD}_{\text{lever}}^{3\text{D}}(\varphi_{\text{PD}}, \eta_{\text{PD}}) \approx d_{\text{lever}} \frac{2 \cos^2(\beta_z)(\varphi^2 - \varphi \varphi_{\text{PD}}) + 2 \cos^2(\beta_y)(\eta^2 - \eta \eta_{\text{PD}}) + \sin(2\beta_y) \sin(2\beta_z) \varphi \eta}{\cos^2(\beta_y) + \cos^2(\beta_z) \sin^2(\beta_y)}. \quad (5.7)$$

It can easily be shown that these equations reduce to the two-dimensional formulas I have introduced above if we set the parameters in the orthogonal plane to zero. The equations also simplify if we assume a beam with normal incidence, i.e. $\beta_y = \beta_z = 0$,

$$\text{OPD}_{\text{lever}}^{3\text{D}}(\varphi_{\text{PD}}, \eta_{\text{PD}} = 0) \approx 2d_{\text{lever}} (\varphi^2 + \eta^2), \quad (5.8)$$

$$\text{OPD}_{\text{lever}}^{3\text{D}}(\varphi_{\text{PD}}, \eta_{\text{PD}}) \approx 2d_{\text{lever}} [(\varphi^2 - \varphi \varphi_{\text{PD}}) + (\eta^2 - \eta \eta_{\text{PD}})]. \quad (5.9)$$

Thus, the three-dimensional lever arm effect is for beams of normal incidence and small rotation angles the sum of the lever arm effects in the orthogonal planes.

The Piston Effect

In the case of the lever arm effect, we assumed the centre of rotation of the mirror to lie in the point of reflection. This is not always the case. In space interferometry, the centre of rotation rather lies in the centre of mass (CoM) of the test mass or the S/C. A rotation of the mirror around this centre will move the reflective surface in and out the beam path like a piston, see Fig. 5.3. Hence we refer to the additional path length changes due to this surface displacement as piston effect. The piston effect also describes the beam path changes due to lateral jitter of the reflective component, see Fig. 5.4.

In both cases, the piston effect is given by the sum of the distances between the point of reflection $P_{\text{refl},0}$ at a non-tilted test mass, the point of reflection P_{refl} at the tilted test mass, and

Summary box 5.2 | Angular piston effect

When the centre of rotation does not equal the point of reflection, the TM surface moves in and out the beam path. This effect generates an additional path length change, which is indicated in the right figure by the beam path above the line parallel to the PD surface.

Analytical equations for the angular piston effect assuming a beam with normal incidence ($\beta = 0$) and a non-tilted photodiode:

$$\text{OPD}_{\text{piston,ang}}^{2\text{D}} = -2d_{\text{lat}} \varphi + d_{\text{long}} \varphi^2$$

$$\text{OPD}_{\text{piston,ang}}^{3\text{D}} = -2d_{\text{lat}} \varphi + 2d_{\text{vert}} \eta + d_{\text{long}} (\varphi^2 + \eta^2)$$

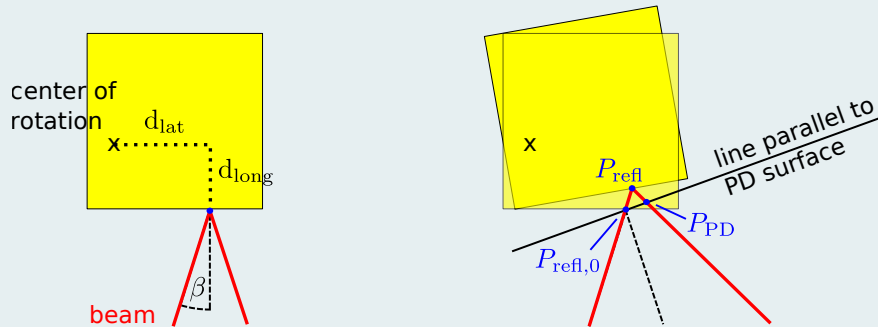


Figure 5.3: The beam accumulates the beam path from the initial reflection point $P_{\text{refl},0}$ to the new reflection point P_{refl} to the line parallel and further to the line parallel to the photodiode (PD) surface that intersects $P_{\text{refl},0}$. The longitudinal and lateral distances between the centre of rotation and the point of reflection are given by d_{long} and d_{lat} . Both are negative in this figure. The same applies to the angle of incidence β .

Summary box 5.3 | Lateral piston effect

Lateral jitter of a tilted test mass shifts its reflective surface into or out of the beam path. This effect changes the beam's path length, which is indicated in the right figure by the beam path above the line parallel to the photodiode surface. The geometric path length does not change if the test mass is not tilted.

Analytical equations for the lateral piston effect assuming a beam with normal incidence ($\beta = 0$) and a non-tilted detector:

$$\text{OPD}_{\text{piston,lat}}^{2\text{D}} = 2y\varphi_0$$

$$\text{OPD}_{\text{piston,lat}}^{3\text{D}} = 2y\varphi_0 - 2z\eta_0$$

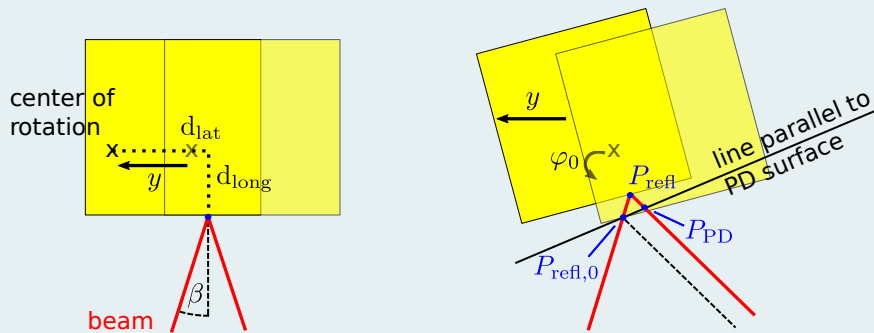


Figure 5.4: Like in the case of the angular piston effect, the beam accumulates the beam path from the initial reflection point $P_{\text{refl},0}$ to the new reflection point P_{refl} and further to the line parallel to the photodiode surface that intersects $P_{\text{refl},0}$. The test mass in the right figure is nominally rotated by an angle φ_0 . The test mass shift y is positive in this figure.

the intersection point P_{PD} of the axis of the reflected beam with a line parallel to the detector surface that crosses the reflection point which would be reached by the beam first ($P_{\text{refl},0}$ in Fig. 5.3), i.e.

$$|\text{OPD}_{\text{piston}}| = |\vec{p}_{\text{refl}} - \vec{p}_{\text{refl},0}| + |\vec{p}_{\text{PD}} - \vec{p}_{\text{refl}}|. \quad (5.10)$$

The path length of the beam after point P_{PD} equals the path length of the reflected beam due to the lever arm effect. The length change of $\text{OPD}_{\text{piston}}$ is positive if the mirror surface moves out of the beam path and negative if it moves into the path.

I derive $\text{OPD}_{\text{piston}}$ first analytically for **angular** test mass jitter. Therefore, I denote the incident beam angle at the test mass with β and the longitudinal and lateral distances between the point of reflection and the centre of rotation with d_{long} and d_{lat} . Thereby, d_{long} describes the distance between these points along the sensitive axis of the interferometer, which is defined from the bottom to the top in Fig. 5.3. I define the direction of this axis for each reflection separately. It corresponds to the direction of the incoming beam. In this scheme, d_{long} is negative. Analogously, d_{lat} is denoted as the distance along the orthogonal axis, here parallel to the non-tilted test mass surface. The direction of the axis always equals the direction of the longitudinal axis rotated by 90 degrees in the mathematical positive sense (counterclockwise). Hence d_{lat} is also negative in Fig. 5.3. Since β is the angle between the sensitive axis and the actual beam axis, it is also negative here. With this we can derive the angular piston effect as follows,

$$\text{OPD}_{\text{piston,ang}}^{2\text{D}} = 2 \sec(2\varphi) \cos(\beta + \varphi) \{d_{\text{long}} [1 - \cos(\varphi)] - d_{\text{lat}} \sin(\varphi)\}. \quad (5.11)$$

Assuming again that the photodiode were tilted with respect to the setup, I extend this equation to

$$\text{OPD}_{\text{piston,ang}}^{2\text{D}} = 2 \sec(2\varphi - \varphi_{\text{PD}}) \cos(\beta + \varphi - \varphi_{\text{PD}}) \{d_{\text{long}} [1 - \cos(\varphi)] - d_{\text{lat}} \sin(\varphi)\}. \quad (5.12)$$

For small tilt angles, we can Taylor expand the equations of the piston effect and get

$$\text{OPD}_{\text{piston,ang}}^{2\text{D}}(\varphi_{\text{PD}} = 0) \approx -2d_{\text{lat}} \cos(\beta) \varphi + [2d_{\text{lat}} \sin(\beta) + d_{\text{long}} \cos(\beta)] \varphi^2, \quad (5.13)$$

$$\text{OPD}_{\text{piston,ang}}^{2\text{D}}(\varphi_{\text{PD}}) \approx -2d_{\text{lat}} [\cos(\beta) + \varphi_{\text{PD}} \sin(\beta)] \varphi + [2d_{\text{lat}} \sin(\beta) + d_{\text{long}} \cos(\beta)] \varphi^2. \quad (5.14)$$

These equations are further simplified if we assume a beam of normal incidence, i.e. $\beta = 0$:

$$\text{OPD}_{\text{piston,ang}}^{2\text{D}} = -2d_{\text{lat}} \varphi + d_{\text{long}} \varphi^2. \quad (5.15)$$

From this, I conclude that the lateral (d_{lat}) piston term generates linear TTL while the longitudinal (d_{long}) piston term contributes a second-order coupling.

To derive the three-dimensional equation for the angular piston effect, I employ the parameters already described in the lever arm section. Additionally, I define d_{vert} as the distance between the point of reflection and the centre of rotation in the new degree of freedom. Thus, I find the

three-dimensional angular piston effect to be

$$\begin{aligned} \text{OPD}_{\text{piston,ang}}^{3\text{D}}(\varphi_{\text{PD}}, \eta_{\text{PD}} = 0) \\ \approx d_{\text{long}} \frac{\cos(\beta_y) \cos(\beta_z) (\varphi^2 + \eta^2)}{\sqrt{\cos^2(\beta_y) + \cos^2(\beta_z) \sin^2(\beta_y)}} \\ + 2(-d_{\text{lat}}\varphi + d_{\text{vert}}\eta) \frac{\cos(\beta_y) \cos(\beta_z) - \sin(\beta_y) \cos(\beta_z) \varphi - \sin(\beta_z) \cos(\beta_y) \eta}{\sqrt{\cos^2(\beta_y) + \cos^2(\beta_z) \sin^2(\beta_y)}}, \end{aligned} \quad (5.16)$$

$$\begin{aligned} \text{OPD}_{\text{piston,ang}}^{3\text{D}}(\varphi_{\text{PD}}, \eta_{\text{PD}}) \\ \approx d_{\text{long}} \frac{\cos(\beta_y) \cos(\beta_z) (\varphi^2 + \eta^2)}{\sqrt{\cos^2(\beta_y) + \cos^2(\beta_z) \sin^2(\beta_y)}} \\ + 2(-d_{\text{lat}}\varphi + d_{\text{vert}}\eta) \frac{\cos(\beta_y) \cos(\beta_z) - \sin(\beta_y) \cos(\beta_z) (\varphi - \varphi_{\text{PD}}) - \sin(\beta_z) \cos(\beta_y) (\eta - \eta_{\text{PD}})}{\sqrt{\cos^2(\beta_y) + \cos^2(\beta_z) \sin^2(\beta_y)}}. \end{aligned} \quad (5.17)$$

I simplify these equations further by assuming beams with normal incidence at the detector and find

$$\text{OPD}_{\text{piston,ang}}^{3\text{D}} \approx d_{\text{long}} (\varphi^2 + \eta^2) + 2(-d_{\text{lat}}\varphi + d_{\text{vert}}\eta), \quad (5.18)$$

showing that under this assumption, the three-dimensional angular piston effect is also the sum of the two-dimensional piston effects in two orthogonal planes. Here, the longitudinal offset generates a second-order TTL effect while the lateral displacements contribute linearly to the total geometric TTL coupling.

The piston effect originating from **lateral** test mass jitter is closely related to the angular jitter case. As visible in Fig. 5.4, the path of the beam only changes if the test mass is nominally tilted. In this case, the test mass shift changes the lateral distance between the point of reflection and the component's centre of rotation. Therefore, we find the lateral jitter equation by first replacing the angles φ and η with the static misalignment angles φ_0 and η_0 , and, second, substituting $d_{\text{lat}} \rightarrow -y$ and $d_{\text{vert}} \rightarrow -z$, where y and z describe the lateral test mass jitter. Neglecting all remaining constant and higher-order terms yields

$$\text{OPD}_{\text{piston,lat}}^{2\text{D}} = 2y \sec(2\varphi_0 - \varphi_{\text{PD}}) \cos(\beta + \varphi_0 - \varphi_{\text{PD}}) \sin(\varphi_0) \quad (5.19)$$

$$\approx 2y \varphi_0 \cos(\beta) \quad (5.20)$$

in the two-dimensional and

$$\text{OPD}_{\text{piston,lat}}^{3\text{D}} \approx 2(y \varphi_0 - z \eta_0) \frac{\cos(\beta_y) \cos(\beta_z)}{\sqrt{\cos^2(\beta_y) + \cos^2(\beta_z) \sin^2(\beta_y)}} \quad (5.21)$$

in the three-dimensional case. The series expansions show that lateral jitter induces linear geometric TTL coupling in the two- as well as in the three-dimensional case.

Assuming for further simplification a beam of normal incidence at the test mass and no detector tilt, we find

$$\text{OPD}_{\text{piston,lat}}^{2\text{D}} \approx 2y \varphi_0, \quad (5.22)$$

$$\text{OPD}_{\text{piston,lat}}^{3\text{D}} \approx 2y \varphi_0 - 2z \eta_0. \quad (5.23)$$

I conclude that for angular as well as for lateral test mass jitter, the three-dimension equation corresponds to the sum of the two-dimensional equations in the respective planes for a beam of normal incidence and no detector tilt. The geometric piston coupling terms for lateral jitter coupling are all linear.

Summary box 5.4 | Angular receiver jitter

A rotation of the local setup with respect to the received beam axis (or vice versa) generates TTL coupling. If the centre of rotation does not equal the point of detection, the detector surface moves in or out of the beam.

Analytical equations describing the OPD due to angular receiver jitter:

$$\text{OPD}_{\text{SC,ang}}^{2\text{D}} = -d_{\text{lat}} \varphi_{\text{SC}} - d_{\text{long}} \frac{\varphi_{\text{SC}}^2}{2}$$

$$\text{OPD}_{\text{SC,ang}}^{3\text{D}} = -d_{\text{lat}} \varphi_{\text{SC}} + d_{\text{vert}} \eta_{\text{SC}} - d_{\text{long}} \frac{\varphi_{\text{SC}}^2 + \eta_{\text{SC}}^2}{2}$$

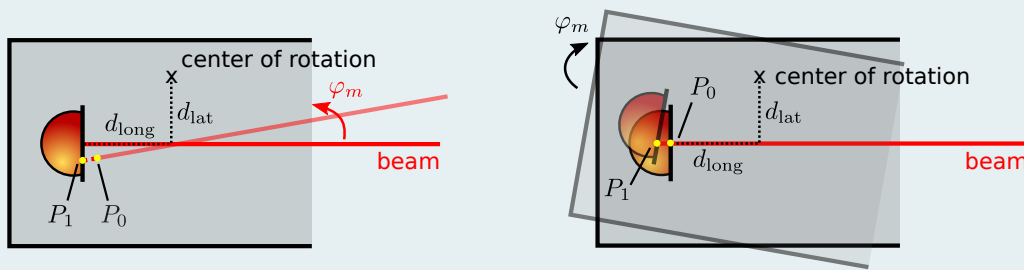


Figure 5.5: The beam accumulates the path length from point P_0 to point P_1 . The path length difference depends on the offset of the beam's point of detection with respect to the centre of rotation. The longitudinal offset is denoted with d_{long} and the lateral one is denoted with d_{lat} . Both are negative in this figure. The two scenarios of a rotating beam (left) and a rotating setup (right) are equivalent. The rotation angle of the S/C is, therefore, given by $\varphi_{\text{SC}} = -\varphi_m$.

5.1.2 Receiving system jitter

The two TTL effects described above occur in LPF, where the beams originate from the optical bench which is attached to the S/C and the measurement beam is reflected from two freely floating test masses. LPF simulated one long-arm interferometer in LISA but scaled down to a few decimetres. Therefore, the first test mass simulates the distant S/C. This reduced setup yields several differences between LPF and LISA, which also affect the TTL coupling. Neglecting for now the beam properties and the influence of the telescope in LISA, the setups in both missions differ in another relevant aspect: In the case of LPF, the TTL couples into the signal due to the beam reflection at the jittering test masses, while, in the case of LISA, we find additional TTL coupling due to a non-local beam received by a jittering local S/C. The orientation of the axis of the received beam with respect to the receiver is governed by the jitter of the far S/C and, additionally, the local S/C jitter. Considering differential angles and shifts, we can summarise both effects either as a tilt of the receiving system with respect to the beam axis or vice versa.

For the analysis presented in this work, I consider a jittering receiver, giving a beam with normal incidence. While the DWS signal would provide the differential angle of the received beam φ_m , the S/C would be rotated in the opposite direction as measured (Fig. 5.5). So I will account for this sign change, i.e. $\varphi_{\text{SC}} = -\varphi_m$.

Analogously, I describe lateral jitter via the jitter y_{SC} of the local S/C along its internal coordi-

Summary box 5.5 | Lateral receiver jitter

Lateral jitter does not generate any geometric TTL coupling for a receiver shifted along its internal lateral axis. It only changes the beam's point of incidence at the detector:

$$\text{OPD}_{\text{SC,lat}} = 0$$

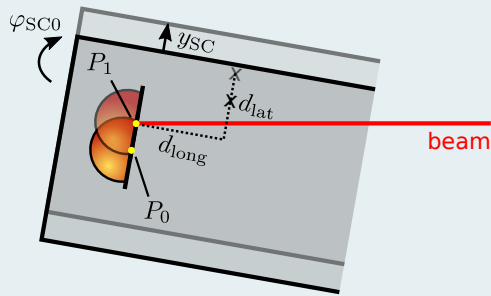


Figure 5.6: The beam accumulates no additional path length due to the receiver shift, even though it changes the lateral offset d_{lat} between the point of reflection and the centre of rotation. However, the beam's point of detection gets shifted from point P_0 (here at the centre of the detector surface) to point P_1 (here at the upper edge of the shifted detector).

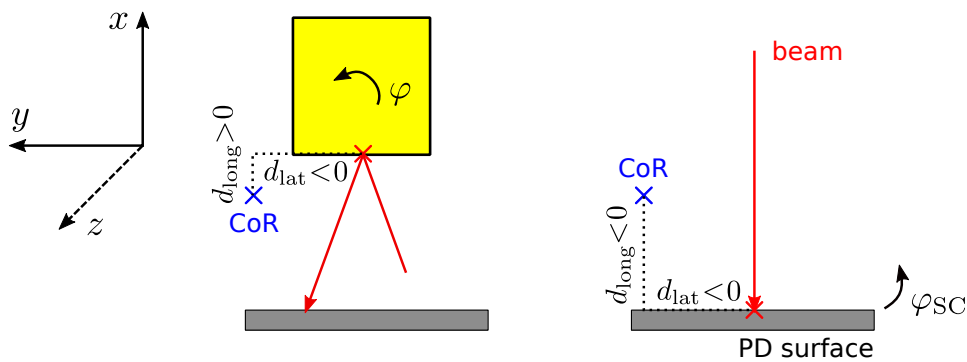


Figure 5.7: Comparison of the definitions of the longitudinal (d_{long}) and lateral (d_{lat}) offsets in case of the piston effect (left) and rotation of the setup (right).

nate system, see Fig. 5.6. This choice makes sense in constellations like LISA since the lateral GRS readout of the electrode housings around the test masses implicitly also provides the jitter of the respective optical benches.

I assume **angular** S/C jitter first. Given that the beam axis' incidence point on the detector surface does not match with the centre of rotation, as illustrated in Fig. 5.5, the photodiode would move in and out of the beam, resulting in TTL coupling. I denote the longitudinal and lateral offsets between the point of detection and the centre of rotation (CoR) as d_{long} and d_{lat} . The offset d_{long} is set to be positive if the centre of rotation lies (seen from the beam) behind the nominal detector surface. The lateral offset d_{lat} is positive if it is 'seen' by the beam at its left-hand side, see Fig. 5.7. Let the receiving S/C be rotated by an angle φ_{SC} with respect to the beam's propagation axis. Then the OPD is computed from

$$\text{OPD}_{\text{SC,ang}}^{2\text{D}} = \sec(\varphi_{\text{SC}}) \{-d_{\text{long}} [1 - \cos(\varphi_{\text{SC}})] - d_{\text{lat}} \sin(\varphi_{\text{SC}})\}. \quad (5.24)$$

Evaluating this equation for small angles φ_{SC} , we find

$$\text{OPD}_{\text{SC,ang}}^{2\text{D}} = -d_{\text{long}} \varphi_{\text{SC}}^2/2 - d_{\text{lat}} \varphi_{\text{SC}}. \quad (5.25)$$

By comparing this formula with Eq. (5.15), we find the angular jitter of the receiver to be equivalent to the angular piston effect for a beam with normal incidence despite a factor of two and a sign flip of the longitudinal term. This can easily be understood when comparing the mechanisms leading to both equations. The piston effect, as well as the effect here, describe how the movement of a component into or out of the beam path affects its OPL. In the case of the piston effect, the beam is additionally reflected, which approximately doubles the path length difference.

Mind that I have not defined a detector tilt angle for the investigated case of a jittering receiver. Since the detector surface defines the coordinate system, any constant detector tilts are interpreted as beam tilts. However, we can extend the equations above by this detector alignment angle by simply substituting $\varphi_{\text{SC}} \rightarrow \varphi_{\text{SC}} + \varphi_{\text{PD}}$.

As before, we can extend this two-dimensional equation for a three-dimensional setup. Therefore, I consider the additional offset d_{vert} of the centre of rotation as well as a rotation η_{SC} in the orthogonal plane. We find for small tilt angles

$$\text{OPD}_{\text{SC,ang}}^{3\text{D}} = -d_{\text{lat}} \varphi_{\text{SC}} + d_{\text{vert}} \eta_{\text{SC}} - d_{\text{long}} \frac{\varphi_{\text{SC}}^2 + \eta_{\text{SC}}^2}{2}. \quad (5.26)$$

Like the piston effect, the rotation of the system features a linear TTL coupling for lateral offsets and second-order coupling for longitudinal offsets.

I define **lateral** jitter of the local S/C as shifts along its internal lateral axis, see Fig. 5.6. If this axis corresponds to the detector surface, i.e. the detector is not tilted, the latter neither moves in nor out of the beam path. Correspondingly, lateral jitter does not cause any geometric TTL coupling:

$$\text{OPD}_{\text{SC,lat}} = 0. \quad (5.27)$$

However, we would find residual coupling terms for a rotated detector surface. For this case, I assume a detector tilt φ_{PD} with respect to the S/C coordinate system, and therefore the lateral jitter axis, as well as an angular S/C misalignment by $\varphi_{\text{SC}0}$. Then we find

$$\text{OPD}_{\text{SC}}^{2\text{D}} = -y_{\text{SC}} \frac{\sin(\varphi_{\text{PD}})}{\cos(\varphi_{\text{SC}0} + \varphi_{\text{PD}})} \quad (5.28)$$

$$\approx -y_{\text{SC}} \varphi_{\text{PD}} \quad (5.29)$$

Summary box 5.6 | Transmissive components

When a beam enters a component, e.g. a window or a beamsplitter, with a different refractive index n_{tc} , it changes its beam path. Furthermore, the beam accumulates stronger or weaker phase changes within this component depending on the difference between the refractive indices of the media in- and outside the component.

Analytical TTL equations for the beam propagation through a plane-parallel component assuming a beam with normal incidence ($\beta = 0$) and non-tilted photodiode:

$$\text{OPD}_{tc}^{2D} = \frac{1}{2} t_{tc} [1/n_{tc} - 1] \varphi_m^2$$

$$\text{OPD}_{tc}^{3D} = \frac{1}{2} t_{tc} [1/n_{tc} - 1] (\varphi_m^2 + \eta_m^2)$$

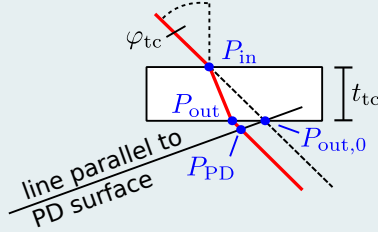


Figure 5.8: The beam changes its path inside a component with a different refractive index than the outer medium. Instead of the path from point P_{in} to point $P_{out,0}$, it propagates inside the component, scaled by the refractive index n_{tc} , from P_{in} to P_{out} and outside further to P_{PD} . The beam propagates behind point P_{PD} has the same path length until reaching the detector as behind point $P_{out,0}$.

yielding linear geometric TTL coupling. This coupling only depends on the detector tilt and, in particular, not on the S/C alignment. I will show in Sec. 5.3 that the detector tilt dependent terms will cancel in the total LPS, i.e. when additionally taking into account the non-geometric TTL contributions.

5.1.3 Plane-Parallel Transmissive Components

Before and after the measurement beam was reflected at the test masses onboard LPF, it passed the windows between the optical bench and the electrode housing. Due to the windows' refractive index, the beam accumulated a longer OPL inside this window, and, further, its beam path was changed within this component. Beyond LPF, this effect commonly occurs in many laser interferometer setups using transmissive components such as windows or beamsplitters. Therefore, I will derive here the corresponding analytical equations given N transmissive components along the beam path after its reflection at a jittering test mass or after entering the optical bench of a receiving S/C, respectively.

I assume all these components to be plane-parallel, i.e. no lenses, and to be rotated against the nominal beam path by an angle $\varphi_{tc,i}$, $i \in \{1, \dots, N\}$. The thickness of the components is given by $t_{tc,i}$ and their refractive index is set to be $n_{tc,i}$ respectively. For the computation of the full path length change due to transmissive components along the beam path, I compare the path the beam would have propagated through an equally sized component with the same refractive index as the surrounding medium, e.g. $n_{tc,i} = 1$ in vacuum, with the actual path of the refracting beam. As shown in Fig. 5.8, the unchanged beam path would be $\vec{p}_{out,0} - \vec{p}_{in}$. Instead the beam propagates from P_{in} to P_{out} within the component. The propagation direction depends on the

incident beam angle which changes according to Snell's law

$$n_{tc} \sin(\varphi'_{\text{inside } tc'}) = \sin(\varphi'_{\text{outside } tc'}) \quad (5.30)$$

$$\iff \varphi'_{\text{inside } tc'} = \arcsin(1/n_{tc} \sin(\varphi'_{\text{outside } tc'})) . \quad (5.31)$$

Since the light slows down in a denser medium, I further multiply the path length inside the component with the refractive index n_{tc} . From this length, I subtract the path length the beam would propagate at the absence of a transmissive component, i.e. $|\vec{p}_{\text{out},0} - \vec{p}_{\text{in}}|$. To account for the alignment of the detector surface relative to the component surface, I finally correct the OPL by the distance (could also be negative) the beam propagates until it crosses the line parallel to the detector surface that intersects the 'emission' point $P_{\text{out},0}$ of the beam not affected by a transmissive component. In Fig. 5.8 this length is given by $|\vec{p}_{\text{PD}} - \vec{p}_{\text{out}}|$. Consequently, we get for N components along the beam path and a beam jitter angle φ_m an OPL of

$$\begin{aligned} \text{OPL}_{tc} &= \sum_{i=1}^N n_{tc,i} |\vec{p}_{\text{out},i} - \vec{p}_{\text{in},i}| - |\vec{p}_{\text{out},0,i} - \vec{p}_{\text{in},i}| + |\vec{p}_{\text{PD},i} - \vec{p}_{\text{out},i}| \quad (5.32) \\ &= \sum_{i=1}^N t_{tc,i} \left\{ \frac{n_{tc,i}^2}{\sqrt{n_{tc,i}^2 - \sin^2(\varphi_m - \varphi_{tc,i})}} - \frac{1}{\cos(\varphi_m - \varphi_{tc,i})} \right. \\ &\quad \left. + \frac{\sin(\varphi_{tc,i} - \varphi_{\text{PD}})}{\cos(\varphi_m - \varphi_{\text{PD}})} \left[\frac{\sin(\varphi_m - \varphi_{tc,i})}{\sqrt{n_{tc,i}^2 - \sin^2(\varphi_m - \varphi_{tc,i})}} - \tan(\varphi_m - \varphi_{tc,i}) \right] \right\}, \quad (5.33) \end{aligned}$$

and for small beam tilts and detector misalignments

$$\text{OPD}_{tc}^{2D} \approx \sum_{i=1}^N \frac{1}{2} t_{tc,i} \left[\frac{n_{tc,i}^2 \cos^2(\varphi_{tc,i})}{(n_{tc,i}^2 - \sin^2(\varphi_{tc,i}))^{3/2}} - \frac{\sin^2(\varphi_{tc,i})}{\sqrt{n_{tc,i}^2 - \sin^2(\varphi_{tc,i})}} - \cos(\varphi_{tc,i}) \right] (\varphi_m^2 - 2\varphi_m \varphi_{\text{PD}}) . \quad (5.34)$$

Not taking into account the detector tilt φ_{PD} , the transmissive components add second-order TTL coupling to the overall signal. We can simplify these equations further, assuming beams with initially normal incidence and non-tilted transmissive components. We then find

$$\text{OPD}_{tc}^{2D}(\varphi_{\text{PD}}) \approx \sum_{i=1}^N \frac{1}{2} t_{tc,i} [1/n_{tc,i} - 1] (\varphi_m^2 - 2\varphi_m \varphi_{\text{PD}}) , \quad (5.35)$$

$$\text{OPD}_{tc}^{2D}(\varphi_{\text{PD}} = 0) \approx \sum_{i=1}^N \frac{1}{2} t_{tc,i} [1/n_{tc,i} - 1] \varphi_m^2 , \quad (5.36)$$

showing again a second-order behaviour scaling linearly with the thicknesses of the components. The absolute path length change within one component increases for increasing refractive indices.

Extending the formulas for three-dimensional environments, Snell's law as given by Eq. (5.31) needs to be extended as well. Therefore, I express the three-dimensional direction the beam propagates within a component (\vec{b}_{inside}) via the beam direction outside this component (\vec{b}_{outside}). Further, I denote the normal vector of the surface of the plane-parallel transmissive component by $\vec{n}\hat{v}_{tc}$. Like before, the refractive index is given by n_{tc} . Then the three-dimensional replacement on Snell's law is [48]

$$\vec{b}_{\text{inside}} = \frac{1}{n_{tc}} \vec{b}_{\text{outside}} - \left(\sqrt{1 - \frac{1}{n_{tc}^2} \left[1 - (\vec{b}_{\text{outside}} \cdot \vec{n}\hat{v}_{tc})^2 \right]} + \frac{\vec{b}_{\text{outside}} \cdot \vec{n}\hat{v}_{tc}}{n_{tc}} \right) \vec{n}\hat{v}_{tc} \quad (5.37)$$

I show for the simplified case depicted in Fig. 5.8 that this equation reduces to the two-dimensional law. I substitute $\vec{b}_{\text{outside}} \rightarrow (-\cos(\varphi_{\text{tc}}), -\sin(\varphi_{\text{tc}}))$ and $\vec{n}_{\text{tc}} \rightarrow (1, 0)$ as long as considering a non-rotated component in this example. Thus we get

$$\begin{aligned}
\vec{b}_{\text{inside}} &= \frac{1}{n_{\text{tc}}} \begin{pmatrix} -\cos(\varphi_{\text{tc}}) \\ -\sin(\varphi_{\text{tc}}) \end{pmatrix} - \left\{ \sqrt{1 - \frac{1}{n_{\text{tc}}^2} \left[1 - \left(\begin{pmatrix} -\cos(\varphi_{\text{tc}}) \\ -\sin(\varphi_{\text{tc}}) \end{pmatrix} \cdot \begin{pmatrix} 1 \\ 0 \end{pmatrix} \right)^2 \right]} \right. \\
&\quad \left. + \frac{1}{n_{\text{tc}}} \begin{pmatrix} -\cos(\varphi_{\text{tc}}) \\ -\sin(\varphi_{\text{tc}}) \end{pmatrix} \cdot \begin{pmatrix} 1 \\ 0 \end{pmatrix} \right\} \begin{pmatrix} 1 \\ 0 \end{pmatrix} \\
&= -\frac{1}{n_{\text{tc}}} \begin{pmatrix} \cos(\varphi_{\text{tc}}) \\ \sin(\varphi_{\text{tc}}) \end{pmatrix} - \left\{ \sqrt{1 - \frac{1}{n_{\text{tc}}^2} [1 - \cos^2(\varphi_{\text{tc}})]} - \frac{1}{n_{\text{tc}}} \cos(\varphi_{\text{tc}}) \right\} \begin{pmatrix} 1 \\ 0 \end{pmatrix} \quad (5.38) \\
&= \begin{pmatrix} -\sqrt{1 - \sin^2(\varphi_{\text{tc}})/n_{\text{tc}}^2} \\ -\sin(\varphi_{\text{tc}})/n_{\text{tc}} \end{pmatrix} \\
&= \begin{pmatrix} -\cos\{\arcsin[\sin(\varphi_{\text{tc}})/n_{\text{tc}}]\} \\ -\sin(\varphi_{\text{tc}})/n_{\text{tc}} \end{pmatrix},
\end{aligned}$$

which is the direction of the beam inside the component according to Snell's law.

This transformation rule for the beam direction indicates that the three-dimensional equations will be significantly more complicated than in the case of the lever arm or the piston effect. Moreover, they become exceptionally long, making it impossible to extract physical relations from them. However, I provide the dedicated equations for two simplified but common scenarios. In both cases, I choose the detector to be well aligned.

At first, I assume a beam of normal incidence and a non-tilted component, e.g., a window. Then we find the three-dimensional effect,

$$\text{OPD}_{\text{tc}}^{3\text{D}} = \frac{1}{2} t_{\text{tc}} [1/n_{\text{tc}} - 1] (\varphi_m^2 + \eta_m^2), \quad (5.39)$$

to be the sum of the two second-order coupling effects in both orthogonal planes.

In the second example, I again consider a beam with normal incidence, but tilt the component by 45° in yaw. This alignment refers to a perfectly aligned 50-50-beamsplitter. We get

$$\text{OPD}_{\text{tc}}^{3\text{D}} = \frac{1}{2^{3/2}} t_{\text{tc}} \left\{ \left[-1 + \frac{1}{(-1 + 2n_{\text{tc}}^2)^{3/2}} \right] \varphi_m^2 + \left[-1 + \frac{1}{\sqrt{-1 + 2n_{\text{tc}}^2}} \right] \eta_m^2 \right\}, \quad (5.40)$$

showing also a second-order behaviour.

Despite seeing a pure second-order coupling in these two examples, this is not always true, but it will dominate the linear contribution in most setups.

5.1.4 Total geometric coupling in respective setups

In laser interferometers, we commonly find a combination of the coupling effects introduced above. Considering either a test mass or a receiver jitter, we derive the full OPD in both cases as the sum of the acting effects, i.e.

$$\text{OPD}_{\text{TM}} = \text{OPD}_{\text{lever}} + \text{OPD}_{\text{piston}} + \text{OPD}_{\text{tc}}, \quad (5.41)$$

$$\text{OPD}_{\text{RS}} = \text{OPD}_{\text{SC}} + \text{OPD}_{\text{tc}}, \quad (5.42)$$

where the index ‘TM’ labels the test mass and ‘RS’ the receiving system.

The equations derived in the Sec. 5.1.3 all apply for components placed along the beam path after a reflection at a test mass and after entering the optical bench of a local jittering S/C, respectively. Therefore, I substitute the beam angle in the first case by $\varphi_m = 2\varphi$ and in the second by $\varphi_m = -\varphi_{SC}$.

Note also that the equations presented so far all assumed that the beam propagates in vacuum, i.e. $n_{vac} = 1$. In space missions, as well as in the large ground-based gravitational wave detectors, we have an almost perfect vacuum. However, in smaller laboratory setups, the optical bench might be placed in air or any other medium, i.e. $n > 1$. This increases the path length changes OPD_{lever} and OPD_{piston} . In the equation presented in this section, we would account for these changes by multiplying the equations with the refractive index of the outer medium n . The same applies for path length changes due to transmissive components. However, we also have to adapt Snell’s law given by Eq. (5.31) to find the propagation direction inside the components.

$$n_{tc} \sin(\varphi_{\text{inside } tc'}) = n \sin(\varphi_{\text{outside } tc'}) \quad (5.43)$$

$$\Leftrightarrow \varphi_{\text{inside } tc'} = \arcsin(n/n_{tc} \sin(\varphi_{\text{outside } tc'})) . \quad (5.44)$$

Hence, we would further substitute $n_{tc} \rightarrow n_{tc}/n$ in Eqs. (5.32)-(5.40) to find the corresponding equations for path length changes due to transmissive components placed in an arbitrary medium.

5.2 Non-geometric Tilt-To-Length Coupling

The geometric path length changes describe the length changes of the beam axis. In laser interferometric setups, the path length readout does not depend on the axis length alone but also on the properties of the beams’ wavefronts, the detector geometry and small errors of both. The longitudinal path length signal (LPS) delivered by the detector combines this information. Hence it is the sum of the geometric path length changes introduced in Sec. 5.1 and further non-geometric signal contributions [P2, 34],

$$LPS = OPD + LPS_{ng} . \quad (5.45)$$

Since TTL reduction systems (Sec. 6.2) change the geometric and non-geometric signals in different ways, it can be beneficial to derive both separately. This section focuses on the derivation of the non-geometric path length signal LPS_{ng} for two Gaussian beams that propagate at most a few meters such that a common photodiode could fully capture their wavefront.

In Sec. 3, I have defined Gaussian beams by the amplitude (3.20) and phase (3.21). The information about the OPD is there contained in the $k x_b$ term of the phase. Since x_b characterises the beam’s distance from waist at the detector, i.e. the propagation distance of its axis from the waist to the detector surface, it changes analogously to the axis length changes. So mathematically, we can distinguish between the geometric and non-geometric contribution to the LPS by neglecting the tilt-dependency of the x_b -parameter. I assume it to be constant (i.e. not angle-dependent) and substitute it for the computation of LPS_{ng} with its nominal value. Within this section, I will, therefore, use the notation x_b for the nominal distances from waist.

For simplification, I will also assume the waist size $w(x_b)$ and the radius of curvature $R(x_b)$ to be constant (i.e. not angle dependent). This does not meet the physical description of the beam properties but is valid since their changes are negligible for small tilt angles in the considered setups, see Sec. B.3.

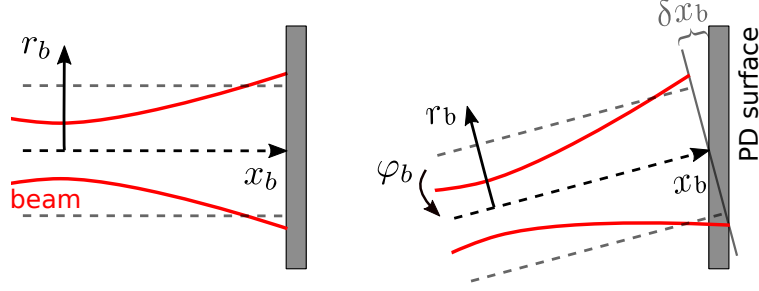


Figure 5.9: Left: For a non-tilted beam and detector, the radial beam coordinates and the detector surface are parallel to each other. Right: For a tilted beam, the beam coordinate axes and the detector plane are not aligned. The coordinate transformation of the beam parameters into photodiode parameters would add an alignment and radial position-dependent distance δx_b to the beam's propagations axis coordinate.

To derive the non-geometric LPS, the beam coordinates must be transferred into the photodiode's coordinate system. This would apply to the radial beam coordinate r_b as well as for its distance from waist x_b . The distance from waist changes via $x_b \rightarrow x_b + \delta x_b$, $b \in \{m, r\}$, where δx_b describe the longitudinal distances of the non-centre segments of the tilted Gaussian beam to the detector, see Fig. 5.9. They depend on the radial coordinates of the beams.

Since I assume only small angular tilts of the beams and the detector, these δx_b would be small close to the beam's centre of incidence at the detector. Therefore, their effect on the waist size and the radius of curvature is close to this point also small. In the derivation presented in this work, I will therefore not substitute the term δx_b into the waist $w(x_b)$ and radius of curvature $R(x_b)$. This choice will enable the evaluation of the overlap integral in the complex amplitude (see Eq. (3.22)) [34].

For the derivation of the non-geometric signal, I now replace the complex amplitude Q (Eq. (3.22)), considering these assumptions, i.e.

$$Q = \int_{\text{PD}} dS \ 2 E_{0m} E_{0r} \frac{w_{0m} w_{0r}}{w(x_m) w(x_r)} \exp \left[\frac{-r_m^2}{w(x_m)^2} + \frac{-r_r^2}{w(x_r)^2} \right] \cdot \exp \left\{ -i k \left[\frac{r_m^2}{2R(x_m)} - \frac{r_r^2}{2R(x_r)} \right] + i (\zeta(x_m) - \zeta(x_r)) - i k [(x_m - x_r) + (\delta x_m - \delta x_r)] \right\}. \quad (5.46)$$

I further insert Eq. (5.46) into Eq. (3.19) to derive the non-geometric phase changes.

The non-geometric LPS depends, on the one hand, on the geometry of the detector and, on the other hand, on the properties of the beams, namely their waist size and the distance from waist at the detector. In the following derivations, I will distinguish between these two factors in order to filter out their contributions to the signal. At first, I will study the dependency of the signal on the beam properties alone (Sec. 5.2.1). This will be done by assuming a large SEPD. At second, I will then consider other possible shapes of the detectors (Sec. 5.2.2). I will, in particular, investigate the LPS measured by QPDs since these detectors were used in LPF and will be used in LISA.

Throughout this section, the incoming angles at the detector are assumed to be small, as they have been in LPF. Thus we can always Taylor expand the equations in these angles. I will provide in this section the terms up to the second order.

5.2.1 Wavefront Dependent TTL Coupling

In order to distinguish between wavefront and detector geometry effects in the measured phase signal, I assume the detector here to be a sufficiently large SEPD. In this case, the full beam gets detected, i.e. we have no beam clipping. While we can deal mathematically with infinitely large detector surfaces, their size is naturally limited in laboratory setups. However, we achieve approximately the same performance assuming a detector surface that is at least three times as big as the beam diameter [34].

Interference of beams with the same point of detection

In the most simple case, we investigate two beams impinging at the centre of the photodiode. Thereby, both beams nominally hit the detector surface at normal incidence and the measurement beam rotates around its point of detection. Such a scenario could be achieved by ideal imaging systems as they are planned for LISA and used in GRACE-FO, see Sec. 6.2.

Furthermore, if the beams have equal beam parameters, i.e. the same waist size w_0 and the same nominal distance from waist x_b at the detector, the complex amplitude function (5.46) reduces to

$$Q = \int_{\text{PD}} dS \ 2E_0^2 \frac{w_0^2}{w^2(x_b)} \exp \left[\frac{-r_m^2 - r_r^2}{w^2(x_b)} \right] \exp \left[-i k \left(\frac{r_m^2 - r_r^2}{2R(x_b)} \right) - i k (\delta x_m - \delta x_r) \right]. \quad (5.47)$$

When the rotation of the measurement beam changes its orientation, it does no longer hit the detector orthogonally. Consequently, the beam coordinate system is not parallel to the detector coordinate system. To account for the coordinate transformation, I substitute

$$r_r = \sqrt{y^2 + z^2} \quad \delta x_r = 0 \quad (5.48)$$

$$r_m = \sqrt{\cos^2(\varphi_m) y^2 + z^2} \quad \delta x_m = -\sin(\varphi_m) y \quad (5.49)$$

to describe the beam parameters when hitting the detector surface [34]. Inserting Eqs. (5.48) and (5.49) into Eq. (5.47) yields

$$Q = \frac{2\pi E_0^2 w_0^2}{\sqrt{2(1 + \cos^2(\varphi_m)) - \frac{ikw^2(x_b)}{R(x_b)} \sin^2(\varphi_m)}} \exp \left[-\frac{k^2 w^2(x_b) \sin^2(\varphi_m)}{4(1 + \cos^2(\varphi_m)) - \frac{2ikw^2(x_b)}{R(x_b)} \sin^2(\varphi_m)} \right]. \quad (5.50)$$

I derive the phase from this complex amplitude following the formalism (3.19). The phase then converts for equal beam parameters into a length signal via Eq. (3.11). We get

$$\text{LPS}_{\text{ng}}^{\text{SEPD},2\text{D}} \approx -\frac{x_b}{4k x_R} \varphi_m^2. \quad (5.51)$$

This number becomes negligibly small in common laboratory setups since k is large and φ_m is small, i.e.

$$\text{LPS}_{\text{ng}}^{\text{SEPD},2\text{D}} \approx 0. \quad (5.52)$$

This result has also been found in numerical simulations [44]. The small residual term in Eq. (5.51) possibly originates from the simplifying assumption that the spot sizes, radii of curvature and Gouy phases are constant along the detector surface.

Summary box 5.7 | Beam parameter TTL coupling

The interference signal depends on the properties of the interfering wavefronts. Their alignment and shape, therefore, affects the LPS. Given two beams with different beam parameters $x_{m,r}$ and $x_{Rm,r}$, that are nominally aligned to each other and feature a normal incidence at the detector, we find

$$\text{LPS}_{\text{ng}}^{2\text{D}} \approx \frac{-x_m(x_{Rr}^2 + x_r^2) + x_r(x_{Rm}^2 + x_m^2)}{2[(x_{Rm} + x_{Rr})^2 + (x_m - x_r)^2]} \varphi_m^2.$$

The complexity of this equation increases when offsets between the beam's centroids of incidence, tilts of the reference beam or three-dimensional setups are accounted for. Without these additional effects, we find second-order TTL coupling.

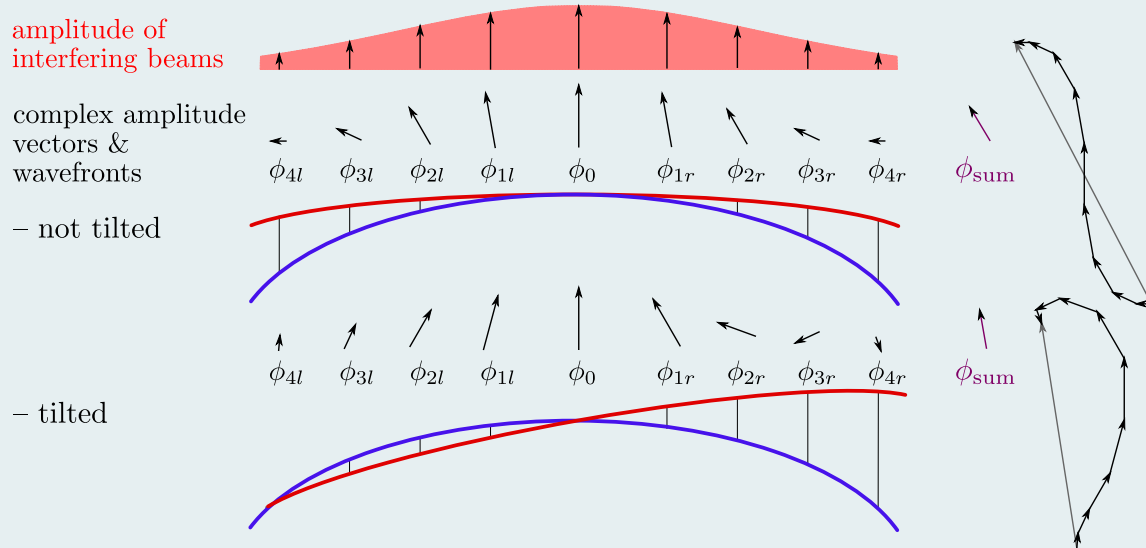


Figure 5.10: Illustration of the composition of the phase signal measured by a SEP for non-tilted and tilted wavefronts. The upper wavefront sketch describes the interference of two non-tilted beams with different beam parameters. The lower sketch assumes the same beams with the measurement beam (red wavefront) being tilted with respect to the reference beam (blue wavefront). Each point at the detector can be assigned with a local phase difference. These are described by the angle of the vector representation of the local complex amplitude above the wavefronts. A phasor pointing upwards refers to a phase difference of zero. Larger phase differences between both beams correspond to larger tilts of the complex amplitude vectors. All vectors are scaled by the magnitude of the local amplitude shown at the top of this figure. Summing up all complex amplitude vectors yields the full measured phase ϕ_{sum} .

Summary box 5.8 | Static beam offsets

A static offset between the two beams impinging at the detector breaks the symmetry between their wavefronts, i.e. there exists no shared symmetry point for both wavefronts. This induces linear non-geometric TTL coupling for equal as well as for unequal beam parameters.

$$\text{LPS}_{\text{ng}}^{2\text{D}}(x_m = x_r, x_{Rm} = x_{Rr}) \approx \frac{y_{im} - y_{ir}}{2} \varphi_m$$

$$\text{LPS}_{\text{ng}}^{3\text{D}}(x_m = x_r, x_{Rm} = x_{Rr}) \approx \frac{y_{im} - y_{ir}}{2} \varphi_m - \frac{z_{im} - z_{ir}}{2} \eta_m$$

$$\text{LPS}_{\text{ng}}^{2\text{D}} \approx \frac{(y_{im} - y_{ir}) [(x_{Rm} + x_{Rr}) x_{Rm} + (x_m - x_r) x_m]}{(x_{Rm} + x_{Rr})^2 + (x_m - x_r)^2} \varphi_m + \text{LPS}_{\text{ng}}^{2\text{D}}(y_{im} = y_{ir})$$

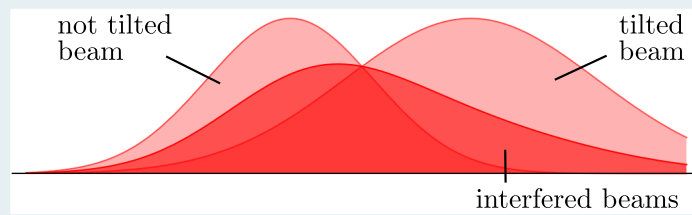


Figure 5.11: Amplitude profiles of two Gaussian beams. The left symmetric amplitude belongs to a beam impinging orthogonally on the detector. The beam corresponding to the amplitude profile at the right-hand side is tilted with respect to the detector. On the one hand, this stretches the profile and, on the other hand, shifts the beam centroid, i.e. the maximum of the amplitude along the detector surface. In that case, the amplitude profile of the interfered beams (centre) is asymmetric.

We find non-zero TTL coupling when we relax the conditions on the beam parameters and instead consider non-identical beams, see Fig. 5.10. This is, in practice, a very common phenomenon since perfectly identical beam parameters are experimentally very hard to produce. I, therefore, substitute Eqs. (5.48) and (5.49) into the complex amplitude function (5.46) and find for the LPS

$$\text{LPS}_{\text{ng}} \approx \frac{-(x_m x_{Rr} + x_r x_{Rm})}{2k [(x_{Rm} + x_{Rr})^2 + (x_m - x_r)^2]} \varphi_m^2 + \frac{-x_m(x_{Rr}^2 + x_r^2) + x_r(x_{Rm}^2 + x_m^2)}{2 [(x_{Rm} + x_{Rr})^2 + (x_m - x_r)^2]} \varphi_m^2 \quad (5.53)$$

$$\approx \frac{-x_m(x_{Rr}^2 + x_r^2) + x_r(x_{Rm}^2 + x_m^2)}{2 [(x_{Rm} + x_{Rr})^2 + (x_m - x_r)^2]} \varphi_m^2. \quad (5.54)$$

The first term in Eq. (5.53) is small analogously to the case of equal beam parameters. Hence non-identical beam parameters add second-order TTL coupling to the full LPS. This non-geometric coupling is smaller, the smaller the differences between the distances from waist $x_{m,r}$ and Rayleigh ranges $x_{Rm,r}$ are. In the limit case of equal beam parameters, we would find again zero non-geometric TTL coupling, like computed above (Eq. (5.52)).

Interference of beams with different points of incidence

In the cases described in the previous paragraphs, I assumed both beams to impinge on the same point regardless of their angle of incidence. This can be achieved by dedicated imaging systems as planned for LISA [39, 43]. The LPF optical bench was built without any lenses. Any

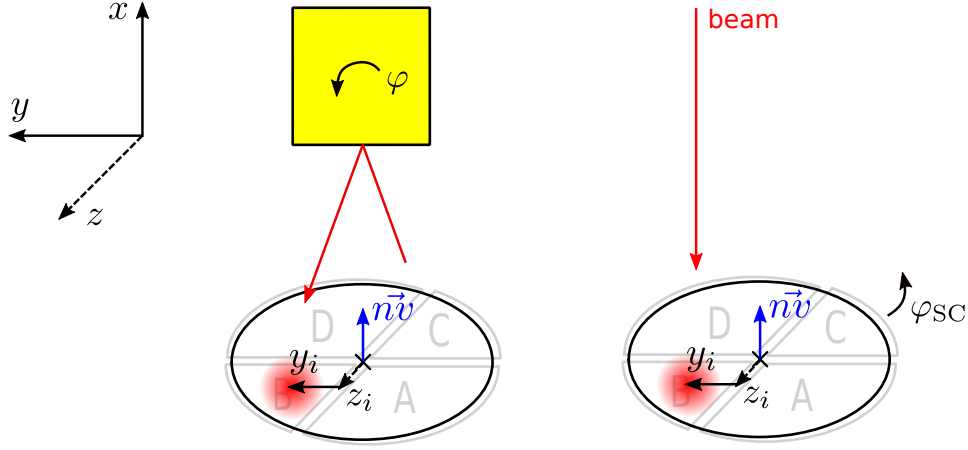


Figure 5.12: Definition of the offsets of the beams centres of incidence at the detector surfaces. The left figure shows the offset after a reflection at a component, and the right figure refers to a rotating system. If the beam rotates in a positive yaw direction – directly or indirectly via a reflection at a rotated component – the beam walks in negative y -direction along the detector surface.

beam rotation originates from the jitter of the reflective test masses relative to the optical bench. Thus, it not only altered the beam orientation but also moved it along the detector surface. I refer to this as beam walk.

An offset between both beam's points of detection induces TTL coupling since it alters the amplitude profile at the detector, which gets shifted and becomes asymmetric, see Fig. 5.11. I introduce beam offsets by substituting

$$r_r = \sqrt{(y - y_{ir})^2 + (z - z_{ir})^2} \quad \delta x_r = 0, \quad (5.55)$$

$$r_m = \sqrt{\cos^2(\varphi_m) (y - y_{im})^2 + (z - z_{im})^2} \quad \delta x_m = -\sin(\varphi_m) (y - y_{im}), \quad (5.56)$$

where $y_{im,r}$ denote the horizontal and $z_{im,r}$ the vertical offset between the beams' points of incidence and the centre of the detector surface. The offsets are defined in the detector's coordinate system, see Fig. 5.12.

Let us assume first that we have no offsets in vertical direction, i.e. $z_{im,r} = 0$. For equal beam parameters I insert Eqs. (5.55) and (5.56) into Eq. (5.47) and derive from it the non-geometric LPS

$$\text{LPS}_{\text{ng}} \approx \frac{y_{im} - y_{ir}}{2} \varphi_m + \left(-\frac{x_b}{4k x_R} + \frac{(y_{im} - y_{ir})^2 x_b}{8 x_R} \right) \varphi_m^2 \quad (5.57)$$

$$\approx \frac{y_{im} - y_{ir}}{2} \varphi_m. \quad (5.58)$$

We can neglect the last term in Eq. (5.57) since the offset difference $y_{im} - y_{ir}$ must be small, i.e. it is limited by the detector size and the necessary large overlap of both wavefronts to achieve a sufficient contrast, see Sec. 3.2.2. If the offsets between both beams are **static**, i.e. constant for any tilts φ_m , we find linear non-geometric TTL coupling.

However, the offset dependent coupling is more complicated if unequal beam parameters are

assumed. We find the corresponding LPS by inserting Eqs. (5.55) and (5.56) into Eq. (5.46), i.e.

$$\begin{aligned}
\text{LPS}_{\text{ng}}^{\text{SEPD,2D}} &\approx \frac{(y_{im} - y_{ir})^2 (x_m - x_r)}{2 [(x_{Rm} + x_{Rr})^2 + (x_m - x_r)^2]} + \frac{(y_{im} - y_{ir}) [(x_{Rm} + x_{Rr}) x_{Rm} + (x_m - x_r) x_m]}{(x_{Rm} + x_{Rr})^2 + (x_m - x_r)^2} \varphi_m \\
&- \frac{x_m x_{Rr} + x_r x_{Rm}}{2k [(x_{Rm} + x_{Rr})^2 + (x_m - x_r)^2]} \varphi_m^2 + \frac{-x_m (x_{Rr}^2 + x_r^2) + x_r (x_{Rm}^2 + x_m^2)}{2 [(x_{Rm} + x_{Rr})^2 + (x_m - x_r)^2]} \varphi_m^2 \\
&+ \frac{(y_{im} - y_{ir})^2 (x_{Rm} + x_{Rr}) (x_m x_{Rr} + x_r x_{Rm})}{[(x_{Rm} + x_{Rr})^2 + (x_m - x_r)^2]^2} \varphi_m^2 - \frac{(y_{im} - y_{ir})^2 x_m}{2 [(x_{Rm} + x_{Rr})^2 + (x_m - x_r)^2]} \varphi_m^2 \\
&\approx \frac{(y_{im} - y_{ir})^2 (x_m - x_r)}{2 [(x_{Rm} + x_{Rr})^2 + (x_m - x_r)^2]} + \frac{(y_{im} - y_{ir}) [(x_{Rm} + x_{Rr}) x_{Rm} + (x_m - x_r) x_m]}{(x_{Rm} + x_{Rr})^2 + (x_m - x_r)^2} \varphi_m \\
&+ \frac{-x_m (x_{Rr}^2 + x_r^2) + x_r (x_{Rm}^2 + x_m^2)}{2 [(x_{Rm} + x_{Rr})^2 + (x_m - x_r)^2]} \varphi_m^2.
\end{aligned} \tag{5.59}$$

$$\tag{5.60}$$

Eq. (5.59) reduces to Eq. (5.60) for the same reasons as discussed before within this subsection. So I neglect, on the one hand, all terms divided by the wavenumber k and, on the other hand, the last two terms where the squared offsets $y_{im} - y_{ir}$ are multiplied with a squared angle φ_m . If the beam offset y_{im} is static, Eq. (5.60) reduces further to

$$\begin{aligned}
\text{LPS}_{\text{ng}}^{\text{SEPD,2D}} &\approx \frac{(y_{im} - y_{ir}) [(x_{Rm} + x_{Rr}) x_{Rm} + (x_m - x_r) x_m]}{(x_{Rm} + x_{Rr})^2 + (x_m - x_r)^2} \varphi_m \\
&+ \frac{-x_m (x_{Rr}^2 + x_r^2) + x_r (x_{Rm}^2 + x_m^2)}{2 [(x_{Rm} + x_{Rr})^2 + (x_m - x_r)^2]} \varphi_m^2.
\end{aligned} \tag{5.61}$$

Thus, we find linear as well as quadratic offset-dependent TTL coupling in the case of unequal beam parameters.

Next, I investigate the TTL coupling due to additional **dynamic** beam walk induced by the geometric effects described in Sec. 5.1. The **angular** jitter of a test mass or receiving S/C makes the measurement beam's incidence point walk along the detector surface. The beam walk corresponding to the lever arm effect ($y_{i\text{lever}}$), the piston effect ($y_{i\text{piston}}$), angular S/C jitter ($y_{i\text{SC}}$) and the beam transmission through transmissive components ($y_{i\text{tc}}$) is given by

$$y_{i\text{lever}} \approx -2d_{\text{lever}} \varphi, \tag{5.62}$$

$$y_{i\text{piston,ang}} \approx -2d_{\text{lat}} \sin(\beta) \varphi + [2d_{\text{lat}} \cos(\beta) + d_{\text{long}} \sin(\beta)] \varphi^2, \tag{5.63}$$

$$y_{i\text{SC,ang}} \approx -d_{\text{long}} \varphi_{\text{SC}} - \frac{1}{2} d_{\text{lat}} \varphi_{\text{SC}}^2, \tag{5.64}$$

$$\begin{aligned}
y_{i\text{tc}} &\approx \sum_i t_{\text{tc},i} \left[-\frac{n_{\text{tc},i}^2 \cos^2(\varphi_{\text{tc},i})}{(n_{\text{tc},i}^2 - \sin^2(\varphi_{\text{tc},i}))^{3/2}} + \frac{\sin^2(\varphi_{\text{tc},i})}{\sqrt{n_{\text{tc},i}^2 - \sin^2(\varphi_{\text{tc},i})}} + \cos(\varphi_{\text{tc},i}) \right] \varphi_m \\
&- \sum_i \frac{3}{4} \frac{n_{\text{tc},i}^2 \cos(\varphi_{\text{tc},i}) \sin(\varphi_{\text{tc},i})}{(n_{\text{tc},i}^2 - \sin^2(\varphi_{\text{tc},i}))^{5/2}} (n_{\text{tc},i}^2 - 1) \varphi_m^2.
\end{aligned} \tag{5.65}$$

Mind that the similarity between the piston effect and the receiver jitter discussed in Sec. 5.1 does not hold here. In the case of receiver jitter, the simultaneously rotating detector itself defines the offsets we are interested in.

The equations (5.63) and (5.65) simplify further if we assume a beam with normal incidence, i.e. $\beta = 0$, no detector tilt, i.e. $\varphi_{\text{PD}} = 0$, and plane-parallel components that are oriented

Summary box 5.9 | Angular jitter induced beam walk on the detector

All geometric TTL effects do not only alter the beam axis length but also shift the beam's point of detection along the detector surface. This dynamic beam walk is a second-order TTL coupling contribution if both beams are nominally aligned, i.e. $y_{im0} = y_{ir}$.

$$\text{LPS}_{\text{ng}}^{2\text{D}}(x_m = x_r, x_{Rm} = x_{Rr}) \approx \frac{y'_{im}(\varphi_m = 0)}{2} \varphi_m^2$$

$$\text{LPS}_{\text{ng}}^{3\text{D}}(x_m = x_r, x_{Rm} = x_{Rr}) \approx \frac{y'_{im}(\varphi_m = 0, \eta_m = 0)}{2} \varphi_m^2 - \frac{z'_{im}(\varphi_m = 0, \eta_m = 0)}{2} \eta_m^2$$

$$\begin{aligned} \text{LPS}_{\text{ng}}^{2\text{D}} &\approx \frac{(y'_{im}(\varphi_m = 0))^2(x_m - x_r) + 2y'_{im}(\varphi_m = 0)[(x_{Rm} + x_{Rr})x_{Rm} + (x_m - x_r)x_m]}{2[(x_{Rm} + x_{Rr})^2 + (x_m - x_r)^2]} \varphi_m^2 \\ &+ \text{LPS}_{\text{ng}}^{2\text{D}}(y'_{im} = 0, y''_{im} = 0) \end{aligned}$$

If static offsets and a dynamic beam walk is given, we find further first- and second-order TTL terms for unequal beam parameters.

$$\begin{aligned} \text{LPS}_{\text{ng}}^{2\text{D}} &\approx \frac{(y'_{im}(\varphi_m = 0))^2(x_m - x_r) + 2y'_{im}(\varphi_m = 0)[(x_{Rm} + x_{Rr})x_{Rm} + (x_m - x_r)x_m]}{2[(x_{Rm} + x_{Rr})^2 + (x_m - x_r)^2]} \varphi_m^2 \\ &- \frac{y'_{im}(\varphi_m = 0)(y_{im0} - y_{ir})(x_m - x_r)}{(x_{Rm} + x_{Rr})^2 + (x_m - x_r)^2} \varphi_m - \frac{y''_{im}(\varphi_m = 0)(y_{im0} - y_{ir})(x_m - x_r)}{2[(x_{Rm} + x_{Rr})^2 + (x_m - x_r)^2]} \varphi_m^2 \\ &+ \text{LPS}_{\text{ng}}^{2\text{D}}(y'_{im} = 0, y''_{im} = 0) \end{aligned}$$

Within these equations, it is $y'_{im} = \partial y_{im} / \partial \varphi_m$ and $y''_{im} = \partial^2 y_{im} / \partial \varphi_m^2$.

orthogonally to the nominal beam direction, i.e. $\varphi_{tc,i} = 0$. We find

$$y_{ipiston,ang} \approx 2d_{lat} \varphi^2, \quad (5.66)$$

$$y_{itc} \approx - \sum_i t_{tc,i} \left[\frac{1}{n_{tc,i}} - 1 \right] \varphi_m. \quad (5.67)$$

The total beam offset is the sum of a static nominal offset y_{im0} and the beam walk present in the considered setup,

$$y_{iTM} = y_{im0} + y_{ilever} + y_{ipiston} + y_{itc}. \quad (5.68)$$

$$y_{iRS} = y_{im0} + y_{iSC} + y_{itc}. \quad (5.69)$$

For the computation of the non-geometric LPS I substitute the measurements beam's point of incidence y_{im} by the beam walks (5.68) and (5.69) respectively in the LPS, i.e. in Eq. (5.58) in the case of equal beam parameters, and in the Eq. (5.60) otherwise. Furthermore, I replace the orientation angle of the measurement beam φ_m by 2φ in the case of a jittering test mass and by $-\varphi_{SC}$ in the case of a jittering S/C. This replacement accounts for the beam angle in the equations for the non-geometric TTL coupling (Eqs. (5.58) and (5.60)) as well as for the transmissive component's beam walk (Eqs. (5.65) and (5.67)).

Let us, for simplicity, assume equal beam parameters first. Then, we find in the case of an angularly jittering test mass

$$\begin{aligned} \text{LPS}_{ng,TM,ang}^{\text{SEPD},2D} &\approx (y_{im0} - y_{ir}) \varphi - 2 [d_{lever} + d_{lat} \sin(\beta)] \varphi^2 \\ &+ \sum_i 2t_{tc,i} \left[-\frac{n_{tc,i}^2 \cos^2(\varphi_{tc,i})}{(n_{tc,i}^2 - \sin^2(\varphi_{tc,i}))^{3/2}} + \frac{\sin^2(\varphi_{tc,i})}{\sqrt{n_{tc,i}^2 - \sin^2(\varphi_{tc,i})}} + \cos(\varphi_{tc,i}) \right] \varphi^2 \end{aligned} \quad (5.70)$$

and in the case of a jittering S/C

$$\begin{aligned} \text{LPS}_{ng,RS,ang}^{\text{SEPD},2D} &\approx -\frac{y_{im0} - y_{ir}}{2} \varphi_{SC} + \frac{d_{long}}{2} \varphi_{SC}^2 \\ &+ \sum_i \frac{1}{2} t_{tc,i} \left[-\frac{n_{tc,i}^2 \cos^2(\varphi_{tc,i})}{(n_{tc,i}^2 - \sin^2(\varphi_{tc,i}))^{3/2}} + \frac{\sin^2(\varphi_{tc,i})}{\sqrt{n_{tc,i}^2 - \sin^2(\varphi_{tc,i})}} + \cos(\varphi_{tc,i}) \right] \varphi_{SC}^2. \end{aligned} \quad (5.71)$$

We see in both equations that only the linear beam walk terms couple into the non-geometric LPS and induce additional second-order TTL coupling. All second-order beam walk terms yield third- or higher-order TTL coupling and are therefore neglected here.

I now extend the analysis to beams with non-identical beam parameters. In this case, we find

for setups with a jittering test mass

$$\begin{aligned}
& \text{LPS}_{\text{ng,TM,ang}}^{\text{SEPD,2D}} \\
& \approx \frac{2(y_{im0} - y_{ir}) [(x_{Rm} + x_{Rr}) x_{Rm} + (x_m - x_r) x_m]}{(x_{Rm} + x_{Rr})^2 + (x_m - x_r)^2} \varphi \\
& + \left\{ -d_{\text{lever}} - d_{\text{lat}} \sin(\beta) + \sum_i t_{\text{tc},i} \left[-\frac{n_{\text{tc},i}^2 \cos^2(\varphi_{\text{tc},i})}{(n_{\text{tc},i}^2 - \sin^2(\varphi_{\text{tc},i}))^{3/2}} + \frac{\sin^2(\varphi_{\text{tc},i})}{\sqrt{n_{\text{tc},i}^2 - \sin^2(\varphi_{\text{tc},i})}} + \cos(\varphi_{\text{tc},i}) \right] \right\} \\
& \cdot \left[\frac{2(y_{im0} - y_{ir})(x_m - x_r)}{(x_{Rm} + x_{Rr})^2 + (x_m - x_r)^2} \varphi + \frac{4[(x_{Rm} + x_{Rr}) x_{Rm} + (x_m - x_r) x_m]}{(x_{Rm} + x_{Rr})^2 + (x_m - x_r)^2} \varphi^2 \right] \\
& + \left\{ -d_{\text{lever}} - d_{\text{lat}} \sin(\beta) + \sum_i t_{\text{tc},i} \left[-\frac{n_{\text{tc},i}^2 \cos^2(\varphi_{\text{tc},i})}{(n_{\text{tc},i}^2 - \sin^2(\varphi_{\text{tc},i}))^{3/2}} + \frac{\sin^2(\varphi_{\text{tc},i})}{\sqrt{n_{\text{tc},i}^2 - \sin^2(\varphi_{\text{tc},i})}} + \cos(\varphi_{\text{tc},i}) \right] \right\}^2 \\
& \cdot \frac{2(x_m - x_r)}{(x_{Rm} + x_{Rr})^2 + (x_m - x_r)^2} \varphi^2 \\
& + \left\{ 2d_{\text{lat}} \cos(\beta) + d_{\text{long}} \sin(\beta) - \sum_i 3 \frac{n_{\text{tc},i}^2 \cos(\varphi_{\text{tc},i}) \sin(\varphi_{\text{tc},i})}{(n_{\text{tc},i}^2 - \sin^2(\varphi_{\text{tc},i}))^{5/2}} (n_{\text{tc},i}^2 - 1) \right\} \\
& \cdot \frac{(y_{im0} - y_{ir})(x_m - x_r)}{(x_{Rm} + x_{Rr})^2 + (x_m - x_r)^2} \varphi^2 \\
& + \frac{2[-x_m(x_{Rr}^2 + x_r^2) + x_r(x_{Rm}^2 + x_m^2)]}{[(x_{Rm} + x_{Rr})^2 + (x_m - x_r)^2]} \varphi^2
\end{aligned} \tag{5.72}$$

and for setups with a jittering receiver

$$\begin{aligned}
& \text{LPS}_{\text{ng,RS,ang}}^{\text{SEPD,2D}} \\
& \approx -\frac{(y_{im0} - y_{ir}) [(x_{Rm} + x_{Rr}) x_{Rm} + (x_m - x_r) x_m]}{(x_{Rm} + x_{Rr})^2 + (x_m - x_r)^2} \varphi_{\text{SC}} \\
& + \left\{ d_{\text{long}} + \sum_i t_{\text{tc},i} \left[-\frac{n_{\text{tc},i}^2 \cos^2(\varphi_{\text{tc},i})}{(n_{\text{tc},i}^2 - \sin^2(\varphi_{\text{tc},i}))^{3/2}} + \frac{\sin^2(\varphi_{\text{tc},i})}{\sqrt{n_{\text{tc},i}^2 - \sin^2(\varphi_{\text{tc},i})}} + \cos(\varphi_{\text{tc},i}) \right] \right\} \\
& \cdot \left[-\frac{(y_{im0} - y_{ir})(x_m - x_r)}{(x_{Rm} + x_{Rr})^2 + (x_m - x_r)^2} \varphi_{\text{SC}} + \frac{(x_{Rm} + x_{Rr}) x_{Rm} + (x_m - x_r) x_m}{(x_{Rm} + x_{Rr})^2 + (x_m - x_r)^2} \varphi_{\text{SC}}^2 \right] \\
& + \left\{ d_{\text{long}} + \sum_i t_{\text{tc},i} \left[-\frac{n_{\text{tc},i}^2 \cos^2(\varphi_{\text{tc},i})}{(n_{\text{tc},i}^2 - \sin^2(\varphi_{\text{tc},i}))^{3/2}} + \frac{\sin^2(\varphi_{\text{tc},i})}{\sqrt{n_{\text{tc},i}^2 - \sin^2(\varphi_{\text{tc},i})}} + \cos(\varphi_{\text{tc},i}) \right] \right\}^2 \\
& \cdot \frac{(x_m - x_r)}{2[(x_{Rm} + x_{Rr})^2 + (x_m - x_r)^2]} \varphi_{\text{SC}}^2 \\
& - \left\{ \frac{1}{2} d_{\text{lat}} + \sum_i \frac{3}{4} \frac{n_{\text{tc},i}^2 \cos(\varphi_{\text{tc},i}) \sin(\varphi_{\text{tc},i})}{(n_{\text{tc},i}^2 - \sin^2(\varphi_{\text{tc},i}))^{5/2}} (n_{\text{tc},i}^2 - 1) \right\} \frac{(y_{im0} - y_{ir})(x_m - x_r)}{(x_{Rm} + x_{Rr})^2 + (x_m - x_r)^2} \varphi_{\text{SC}}^2 \\
& + \frac{-x_m(x_{Rr}^2 + x_r^2) + x_r(x_{Rm}^2 + x_m^2)}{2[(x_{Rm} + x_{Rr})^2 + (x_m - x_r)^2]} \varphi_{\text{SC}}^2.
\end{aligned} \tag{5.73}$$

Contrary to the equal beam parameter case, we find not only additional second-order but also new linear coupling terms.

In summary, I conclude that in the case of equal beam parameters, the static beam offset generates linear and the dynamic beam walk second-order TTL coupling. If the beams have

Summary box 5.10 | Lateral jitter induced beam walk on the detector

We only find higher-order beam walk in the case of a laterally jittering test mass. Thus, the non-geometric lateral jitter coupling becomes negligible:

$$\text{LPS}_{\text{ng,TM,lat}} \approx 0.$$

Contrary, the beam walk due to the receiver jitter is significant.

$$\text{LPS}_{\text{ng,RS,lat}}^{2\text{D}}(x_m = x_r, x_{Rm} = x_{Rr}) \approx \frac{1}{2} y_{\text{SC}} \varphi_{\text{SC}0}$$

$$\text{LPS}_{\text{ng,RS,lat}}^{3\text{D}}(x_m = x_r, x_{Rm} = x_{Rr}) \approx +\frac{1}{2} y_{\text{SC}} \varphi_{\text{SC}0} - \frac{1}{2} z_{\text{SC}} \eta_{\text{SC}0}$$

$$\text{LPS}_{\text{ng,RS,lat}}^{2\text{D}} \approx \frac{y_{\text{SC}}^2 (x_m - x_r)}{2 [(x_{Rm} + x_{Rr})^2 + (x_m - x_r)^2]} + \frac{y_{\text{SC}} [(x_{Rm} + x_{Rr}) x_{Rm} + (x_m - x_r) x_m]}{(x_{Rm} + x_{Rr})^2 + (x_m - x_r)^2} \varphi_{\text{SC}0}$$

Note that this lateral jitter coupling is independent of the S/C's centre of rotation. It only depends on the beam parameters and alignment at the detector.

unequal waist sizes or distances from waist when impinging at the detector, static offsets and dynamic beam walks will generate both first- and second-order TTL contributions. We further see that the piston effect does not couple into the non-geometric LPS if the measurement beam impinges at normal incidence at the test mass ($\beta = 0$) and, in the case of unequal distances from waist at the detector ($x_m \neq x_r$), the nominal points of detection are aligned to each other ($y_{im0} = y_{ir}$).

Next, I examine the beam walk induced by **lateral** jitter. We have learned in Sec. 5.1 that the lateral jitter is encoded in the equations for the piston effect in the case of a jittering test mass. Like in the geometric case, we find the beam walk for a jittering component simply by substituting $d_{\text{lat}} \rightarrow -y$ and $\varphi \rightarrow \varphi_0$ in Eq. (5.63) yielding

$$y_{\text{ipiston,lat}} \approx 2y \sin(\beta) \varphi_0 - 2y \cos(\beta) \varphi_0^2. \quad (5.74)$$

Considering a small test mass rotation φ_0 and also a small lateral jitter amplitude, this beam walk contains only higher than first-order terms. Thus, it does not add any non-geometric coupling terms of linear or quadratic order:

$$\text{LPS}_{\text{ng,TM,lat}}^{\text{SEPD,2D}} \approx 0. \quad (5.75)$$

In the case of a laterally jittering receiver, we have seen in Fig. 5.6 that this jitter induces no geometric path length difference, but a beam walk corresponding to the shift, i.e.

$$y_{i\text{SC,lat}} = -y_{\text{SC}} \quad (5.76)$$

Therefore, we find for an angularly misaligned receiver

$$\text{LPS}_{\text{ng,RS,lat}}^{\text{SEPD,2D}} \approx \frac{1}{2} y_{\text{SC}} \varphi_{\text{SC}0} \quad (5.77)$$

for equal beam parameters and

$$\text{LPS}_{\text{ng,RS,lat}}^{\text{SEPD,2D}} \approx \frac{[(x_{Rm} + x_{Rr}) x_{Rm} + (x_m - x_r) x_m] \varphi_{\text{SC}0}}{(x_{Rm} + x_{Rr})^2 + (x_m - x_r)^2} y_{\text{SC}} + \frac{(x_m - x_r)}{2 [(x_{Rm} + x_{Rr})^2 + (x_m - x_r)^2]} y_{\text{SC}}^2 \quad (5.78)$$

Summary box 5.11 | Tilts of the reference beam

If the reference beam does not impinge nominally on the detector, this creates linear TTL coupling if additionally a dynamic beam walk or unequal beam parameters are present.

$$\text{LPS}_{\text{ng}}^{2\text{D}}(x_m = x_r, x_{Rm} = x_{Rr}) \approx \frac{y'_{im}(\varphi_m = 0)}{2} \varphi_m \varphi_r + \text{LPS}_{\text{ng}}^{2\text{D}}(\varphi_r = 0; x_m = x_r, x_{Rm} = x_{Rr})$$

$$\begin{aligned} \text{LPS}_{\text{ng}}^{3\text{D}}(x_m = x_r, x_{Rm} = x_{Rr}) \approx & \frac{y'_{im}(\varphi_m = 0, \eta_m = 0)}{2} \varphi_m \varphi_r - \frac{z'_{im}(\varphi_m = 0, \eta_m = 0)}{2} \eta_m \eta_r \\ & + \text{LPS}_{\text{ng}}^{3\text{D}}(\varphi_r = 0; x_m = x_r, x_{Rm} = x_{Rr}) \end{aligned}$$

$$\begin{aligned} \text{LPS}_{\text{ng}}^{2\text{D}} \approx & \frac{y'_{im}(\varphi_m = 0) [(x_{Rm} + x_{Rr}) x_{Rr} - (x_m - x_r) x_r]}{(x_{Rm} + x_{Rr})^2 + (x_m - x_r)^2} \varphi_m \varphi_r \\ & - \frac{-x_m(x_{Rr}^2 + x_r^2) + x_r(x_{Rm}^2 + x_m^2)}{(x_{Rm} + x_{Rr})^2 + (x_m - x_r)^2} \varphi_m \varphi_r + \text{LPS}_{\text{ng}}^{2\text{D}}(\varphi_r = 0) \end{aligned}$$

otherwise. Correspondingly, lateral receiver jitter couples for equal beam parameters linearly into the non-geometric LPS, while we have additionally quadratic coupling in the case of unequal parameters.

Interference with a rotated reference beam

So far, I have only assumed the measurement beam to be rotated. However, the reference beam can also impinge tilted at the detector. This angular misalignment will result in a non-zero DWS readout if the measurement beam hits the photodiode with a normal incidence. However, in the DWS signal, the absolute alignment of the two beams remains unknown. For instance, the DWS angle would be zero if both beams impinge tilted but at the same angle at the detector ($\varphi_m = \varphi_r$). Here, I derive the corresponding non-geometric LPSs.

In the case of a tilted reference beam, the radial distance and longitudinal incidence dependency is then replaced by

$$r_{m,r} = \sqrt{\cos(\varphi_{m,r})^2 (y - y_{im,r})^2 + (z - z_{im,r})^2}, \quad (5.79)$$

$$\delta x_{m,r} = -\sin(\varphi_{m,r}) (y - y_{im,r}). \quad (5.80)$$

Substituting this replacement into the complex amplitude function (5.46), we find additional linear φ_r -dependent coupling terms in the equations presented in this section. While the LPS in cases with no and static beam offsets on the detector for equal beam parameters, compare Eqs. (5.52) and (5.58), does not change, this is different in the other investigated cases.

Without beam walk we find for unequal parameters

$$\text{LPS}_{\text{ng}}^{\text{SEPD},2\text{D}} \approx \frac{-x_m(x_{Rr}^2 + x_r^2) + x_r(x_{Rm}^2 + x_m^2)}{2[(x_{Rm} + x_{Rr})^2 + (x_m - x_r)^2]} (\varphi_m^2 - 2\varphi_m \varphi_r). \quad (5.81)$$

In this case, the non-geometric LPS would cancel if both beams are aligned equally ($\varphi_m = \varphi_r$). In the presented investigations, I assume the reference beam alignment to be static while the measurement beam would jitter. Thus, such equality cannot be achieved permanently. However, assuming a measurement beam that is nominally tilted like the reference beam ($\varphi_{m0} = \varphi_r$), the

reference beam tilt would cancel in this equation, yielding a second-order coupling from the jitter of the measurement beam about its nominal tilt angle.

Considering the interference of two beams with unequal beam parameters and a static offset (Eq. (5.61)), we find a linear TTL coupling term additional to the coupling in Eq. (5.81), but no further φ_r -dependent terms. However, this is different for dynamic beam walks. There, the tilt angle of the reference beam couples into the signal for equal as well as for unequal beam parameters.

We find for **angularly** jittering components respectively

$$\begin{aligned} \text{LPS}_{\text{ng}}^{\text{SEPD},2\text{D}}(x_m = x_r, x_{Rm} = x_{Rr}) &\approx \frac{y_{im0} - y_{ir}}{2} \varphi_m + \frac{y'_{im}(\varphi_m = 0)}{2} (\varphi_m^2 + \varphi_m \varphi_r), & (5.82) \\ \text{LPS}_{\text{ng}}^{\text{SEPD},2\text{D}} &\approx \frac{y'_{im}(\varphi_m = 0) (y_{im0} - y_{ir}) (x_m - x_r) \varphi_m}{(x_{Rm} + x_{Rr})^2 + (x_m - x_r)^2} \\ &+ \frac{[(y'_{im}(\varphi_m = 0))^2 + 2y''_{im}(\varphi_m = 0)(y_{im0} - y_{ir})] (x_m - x_r) \varphi_m^2}{2[(x_{Rm} + x_{Rr})^2 + (x_m - x_r)^2]} \\ &+ \frac{(y_{im0} - y_{ir}) [(x_{Rm} + x_{Rr}) x_{Rm} + (x_m - x_r) x_m] \varphi_m}{(x_{Rm} + x_{Rr})^2 + (x_m - x_r)^2} \\ &+ \frac{y'_{im}(\varphi_m = 0) [(x_{Rm} + x_{Rr})(x_{Rm} \varphi_m + x_{Rr} \varphi_r) + (x_m - x_r)(x_m \varphi_m - x_r \varphi_r)] \varphi_m}{(x_{Rm} + x_{Rr})^2 + (x_m - x_r)^2} \\ &+ \frac{-x_m(x_{Rr}^2 + x_r^2) + x_r(x_{Rm}^2 + x_m^2)}{2[(x_{Rm} + x_{Rr})^2 + (x_m - x_r)^2]} (\varphi_m^2 - 2\varphi_m \varphi_r), & (5.83) \end{aligned}$$

where $y'_{im}(\varphi_m = 0)$ is the linear and $2y''_{im}(\varphi_m = 0)$ the quadratic coefficient of either of the beam walks (5.69) or (5.68). For instance, we find in the case of equal beam parameters, a reflection at a test mass for a nominally normal incidence angle (i.e. $\beta = 0$) and transmissive components that are aligned orthogonal to the nominal beam direction (i.e. $\varphi_{\text{tc},i} = 0$),

$$\text{LPS}_{\text{ng,TM,ang}}^{\text{SEPD},2\text{D}} \approx (y_{im0} - y_{ir}) \varphi - \left[d_{\text{lever}} + \sum_i t_{\text{tc},i} \left(\frac{1}{n_{\text{tc},i}} - 1 \right) \right] (2\varphi^2 + \varphi \varphi_r). \quad (5.84)$$

As can be seen in Eq. (5.82), in the second last line of Eq. (5.83) and exemplary also in Eq. (5.84), the TTL coupling due to the reference beam tilt does not always cancel for an equally aligned measurement beam. There, we do not (only) find the differential angle of both beams coupling into the LPS but the sum of both angles.

The reference beam alignment does also couple with **lateral** jitter. We learned previously in this section that lateral receiver jitter induces significant beam walk. Computing the corresponding non-geometric TTL coupling, we find for equal and unequal beam parameters

$$\begin{aligned} \text{LPS}_{\text{ng,RS,lat}}^{2\text{D}}(x_m = x_r, x_{Rm} = x_{Rr}) &\approx \frac{1}{2} y_{\text{SC}} (\varphi_{\text{SC0}} - \varphi_r), & (5.85) \\ \text{LPS}_{\text{ng,RS,lat}}^{2\text{D}} &\approx \frac{y_{\text{SC}}^2 (x_m - x_r)}{2[(x_{Rm} + x_{Rr})^2 + (x_m - x_r)^2]} + \frac{y_{\text{SC}} [(x_{Rm} + x_{Rr}) x_{Rm} + (x_m - x_r) x_m]}{(x_{Rm} + x_{Rr})^2 + (x_m - x_r)^2} \varphi_{\text{SC0}} \\ &- \frac{y_{\text{SC}} [(x_{Rm} + x_{Rr}) x_{Rr} - (x_m - x_r) x_r]}{(x_{Rm} + x_{Rr})^2 + (x_m - x_r)^2} \varphi_r. & (5.86) \end{aligned}$$

In summary, we find additional linear TTL coupling due to angular misalignment of the reference beam. This coupling will not always cancel if the measurement beam is equally aligned, i.e. for a nullified differential angle. Given two beams with equal beam parameters and no or only static beam offsets on the detector, no effect of the reference beam alignment is measurable.

Three-dimensional setups

Like the OPD equations in Sec. 5.1, I extend the non-geometric LPS for three-dimensional setups. Here, the yaw angles $\varphi_{m,r}$ and the pitch angles $\eta_{m,r}$ define the alignment of the beams when impinging at the detector. These angles accord to the actual angles in the respective plane, i.e. describe the beam propagation direction independent of the order of the rotations the beam experiences. The beam coordinates are then described by

$$r_{m,r} = \sqrt{\cos(\varphi_{m,r})^2(y - y_{im,r})^2 + \cos(\eta_{m,r})^2(z - z_{im,r})^2}, \quad (5.87)$$

$$\delta x_{m,r} = -\sin(\varphi_{m,r})(y - y_{im,r}) + \sin(\eta_{m,r})(z - z_{im,r}). \quad (5.88)$$

These are inserted into the complex amplitude function (5.46) in order to derive the three-dimensional non-geometric LPS. However, the more complexity we add, the lengthier become the equations.

Considering **angular** jitter coupling and the simple case of equal beam parameters, we find

$$\begin{aligned} \text{LPS}_{\text{ng}}^{\text{SEPD},3\text{D}} &\approx \frac{1}{2}(y_{im0} - y_{ir})\varphi_m + \frac{1}{2}y'_{im}(\varphi_m, \eta_m = 0)(\varphi_m^2 + \varphi_m\varphi_r) \\ &\quad - \frac{1}{2}(z_{im0} - z_{ir})\eta_m - \frac{1}{2}z'_{im}(\varphi_m, \eta_m = 0)(\eta_m^2 + \eta_m\eta_r) \\ &\quad + \left[(y_{im0} - y_{ir})^2 \frac{x_b}{8x_R^2} - \frac{x_b}{4kx_R} \right] \varphi_m^2 + \left[(z_{im0} - z_{ir})^2 \frac{x_b}{8x_R^2} - \frac{x_b}{4kx_R} \right] \eta_m^2 \\ &\quad - \frac{x_b}{x_R^2 + x_b^2} y_{im0} z_{im0} \varphi_m \eta_m \end{aligned} \quad (5.89)$$

$$\begin{aligned} &\approx \frac{1}{2}(y_{im0} - y_{ir})\varphi_m + \frac{1}{2}y'_{im}(\varphi_m, \eta_m = 0)(\varphi_m^2 + \varphi_m\varphi_r) \\ &\quad - \frac{1}{2}(z_{im0} - z_{ir})\eta_m - \frac{1}{2}z'_{im}(\varphi_m, \eta_m = 0)(\eta_m^2 + \eta_m\eta_r). \end{aligned} \quad (5.90)$$

Additionally to the simplifications discussed previously in this work, we neglect the term with mixed degrees of freedom in Eq. (5.89). This term is small since it is a product of second-order displacements, which are smaller than 1 mm at commonly sized detectors, and second-order angular coupling. The beam walk on the detector surface (y_{im}, z_{im}) potentially depends here on both rotations angles, φ_m and η_m .

Let us, for simplicity, further assume a measurement beam with normal incidence at the detector and no transmissive components. Then, the linearised tilt-dependent beam walk becomes

$$y_{i\text{TM}} \approx y_{im0} - 2d_{\text{lever}}\varphi, \quad z_{i\text{TM}} \approx z_{im0} + 2d_{\text{lever}}\eta. \quad (5.91)$$

$$y_{i\text{RS}} \approx y_{im0} - d_{\text{long}}\varphi_{\text{SC}}, \quad z_{i\text{RS}} \approx z_{im0} + d_{\text{long}}\eta_{\text{SC}}, \quad (5.92)$$

We see that the lever arm beam walk in the case of a test mass rotation as well as the longitudinal pivot offset in the case of a S/C rotation have different signs for both rotation axes. This is a consequence of the definition of the yaw and pitch angles, compare Fig. 5.2. If we, for instance, substitute the beam walk for the test mass rotation case (Eq. (5.91)) into Eq. (5.90) and replace $\varphi_m \rightarrow 2\varphi$, $\eta_m \rightarrow 2\eta$ to correspond for the orientation of the reflected beam, we find

$$\text{LPS}_{\text{ng,TM,ang}}^{\text{SEPD},3\text{D}} \approx (y_{im0} - y_{ir})\varphi - (z_{im0} - z_{ir})\eta - d_{\text{lever}} \left[(2\varphi^2 + \varphi\varphi_r) + (2\eta^2 + \eta\eta_r) \right]. \quad (5.93)$$

Hence, non-geometric lever arm coupling features the same sign in both angular degrees of freedom. The same holds for the non-geometric longitudinal coupling in the case of S/C jitter, i.e.

$$\text{LPS}_{\text{ng,RS,ang}}^{\text{SEPD},3\text{D}} \approx -\frac{1}{2}(y_{im0} - y_{ir})\varphi_{\text{SC}} + \frac{1}{2}(z_{im0} - z_{ir})\eta_{\text{SC}} - \frac{1}{2}d_{\text{long}} \left[(\varphi_{\text{SC}}^2 - \varphi_{\text{SC}}\varphi_r) + (\eta_{\text{SC}}^2 - \eta_{\text{SC}}\eta_r) \right]. \quad (5.94)$$

Furthermore, I investigate the three-dimensional equations for **lateral** jitter coupling. In the case of test mass jitter, the non-geometric coupling remains zero as in the two-dimensional case,

$$\text{LPS}_{\text{ng,TM,lat}}^{\text{SEPD,3D}} = 0. \quad (5.95)$$

For a lateral jittering receiver we find the beam walk

$$y_{i\text{RS}} = y_{im0} - y_{\text{SC}}, \quad z_{i\text{RS}} = z_{im0} - z_{\text{SC}} \quad (5.96)$$

yielding for equal beam parameters

$$\text{LPS}_{\text{ng,RS,lat}}^{\text{SEPD,3D}} = \frac{1}{2} y_{\text{SC}} \varphi_{\text{SC}0} - \frac{1}{2} z_{\text{SC}} \eta_{\text{SC}0}. \quad (5.97)$$

Thus, the S/C jitter along its internal lateral and vertical axis induces linear non-geometric TTL coupling of different signs in both dimensions.

Altogether, for equal beam parameters and the assumptions made above, the three-dimensional non-geometric coupling equals the sum of the two-dimensional equations in both degrees of freedom. Since the three-dimensional equations for unequal parameters become very lengthy, I will not show them here. However, the in-plane coupling terms remain dominant also for unequal parameters.

Wavefront errors

So far, I did not consider the beams to be disturbed by clipping or initial errors. Hence their wavefronts are assumed to be perfectly fundamental Gaussian when impinging at the detector. In fact, this will not be the case in most laboratory setups. Also, in LISA, wavefront errors are assumed to significantly couple into the LPS [40]. To account for such changes, the beams can be described using Hermite- or Laguerre-Gaussian modes. Sasso et al. [40] describe the propagation of wavefront errors using Zernike modal amplitudes.

Wavefront errors can induce arbitrary TTL effects, which are in this generality impossible to describe with the methods presented here. Therefore, I will not deal with wavefront errors in this work. Instead, I assume the wavefront to be almost perfect fundamental Gaussian wavefronts and neglect any residual imperfections.

5.2.2 Detector Geometry Dependent TTL Coupling

The detector geometry can affect the signal readout in many ways. The size of the detector surface as well as other insensitive areas change the detected signal and, therefore, also the contribution of the TTL coupling. I will investigate here the non-geometric TTL coupling due to the detector alignment and particularly QPDs. Such diodes were used in LPF and will also be used in LISA to compute the DWS and DPS signal, which are used to estimate the beam alignments. Moreover, the independent measurements at the four QPD segments allow for different phase signal processing methods, i.e. different LPS definitions, yielding different coupling terms. Although I focus on QPDs, the following analysis can partially also be applied to arbitrarily shaped diodes.

Detector tilt coupling

In Sec. 5.1 I have already investigated how a tilt of the detector surface with respect to the nominal beam direction changes the OPD. This tilt also affects the non-geometric signal for any kind of detector since it changes the amplitude distributions on the detector's surface. For my analysis, I adapt the definition of the radial distances $r_{m,r}$ in the complex amplitude in Eq. (5.46), which includes the information about tilts of the incoming beams with respect to the detector surface. A rotation of the detector will hence add to the definition of the incoming angles, i.e. $\varphi_m \rightarrow \varphi_m - \varphi_{\text{PD}}$ and $\varphi_r \rightarrow \varphi_r - \varphi_{\text{PD}}$. We get

$$r_{m,r} = \sqrt{\cos(\varphi_{m,r} - \varphi_{\text{PD}})^2 (y - y_{im,r})^2 + (z - z_{im,r})^2}, \quad (5.98)$$

$$\delta x_{m,r} = -\sin(\varphi_{m,r} - \varphi_{\text{PD}}) (y - y_{im,r}). \quad (5.99)$$

For **angularly** jittering components, I insert Eqs. (5.98) and (5.99) into Eq. (5.46) assuming a large SEPD. Then we find that the detector tilt adds non-negligible TTL coupling when the measurement beam walks dynamically over the detector surface. Here, we get for equal and unequal beam parameters respectively

$$\text{LPS}_{\text{ng}}^{\text{SEPD},2\text{D}} \approx \text{LPS}_{\text{ng}}^{\text{SEPD},2\text{D}}(\varphi_{\text{PD}} = 0) - y'_{im}(\varphi_m = 0) \varphi_m \varphi_{\text{PD}}. \quad (5.100)$$

The Eq. (5.100) shows that detector tilt dependent coupling is a linear effect. Also, it is the same for equal and unequal beam parameters.

Mind that the beam offsets $y_{im,r}$ (and $z_{im,r}$ in three-dimensional cases) are defined as the distances between the centres of incidence at the tilted detector surface and the centre of this surface. In Sec. 5.2.1, I have described the dynamic beam walk without assuming a detector tilt. However, the changes of the presented beam walk equations due to this tilt are small for all considered TTL effects (compare Sec. 5.1). Therefore, these changes would only add negligible TTL coupling.

Next, I investigate the non-geometric detector tilt coupling for **lateral** jitter of either a test mass or a receiving system. In the case of a laterally jittering test mass, I have already shown in Sec. 5.2.1 that this jitter does not yield significant non-geometric TTL coupling. This does not change when considering detector tilts, i.e.

$$\text{LPS}_{\text{ng,TM,lat}}^{\text{SEPD},2\text{D}} \approx 0. \quad (5.101)$$

However, we find detector tilt coupling for a laterally jittering receiving system, yielding

$$\text{LPS}_{\text{ng,RS,lat}}^{\text{SEPD},2\text{D}} \approx \text{LPS}_{\text{ng,RS,lat}}^{\text{SEPD},2\text{D}}(\varphi_{\text{PD}}) + y_{\text{SC}} \varphi_{\text{PD}}. \quad (5.102)$$

Thus, the alignment of the detector couples linearly into the non-geometric signal for a laterally jittering receiving system.

Signal computation for arbitrary rectangular photodiode surfaces

While I have assumed so far only infinitely large SEPDs, I will now investigate the TTL coupling for arbitrary, but rectangular, photodiode surfaces. Thus, the detector is allowed to consist of one or more sensitive areas. Though, these areas must be rectangular to meet the conditions of the following integration. In comparison to infinitely large SEPDs, the boundaries of the sensitive areas will alter the measured TTL coupling. However, I will show here that the LPS

equals the sum of the phase for an infinitely large SEPD and an additional detector-shape-dependent term. The latter is small if most of the interfered beam power is detected, e.g. in the case of a large QPD with thin slits.

To prove this claim, I revisit the complex amplitude function (5.46). In there, I transform the beam coordinates into the detector coordinate system via Eq. (5.87) and (5.88) giving

$$\begin{aligned}
Q = & \int_{\text{PD}} dS \, 2 E_{0m} E_{0r} \frac{w_{0m} w_{0r}}{w(x_m) w(x_r)} \\
& \cdot \exp \left\{ - \frac{\cos^2(\varphi_m) (y - y_{im})^2 + \cos^2(\eta_m) (z - z_{im})^2}{w(x_m)^2} - \frac{\cos^2(\varphi_r) (y - y_{ir})^2 + \cos^2(\eta_r) (z - z_{ir})^2}{w(x_r)^2} \right\} \\
& \cdot \exp \left\{ - i k \left[\frac{\cos^2(\varphi_m) (y - y_{im})^2 + \cos^2(\eta_m) (z - z_{im})^2}{2R(x_m)} - \frac{\cos^2(\varphi_r) (y - y_{ir})^2 + \cos^2(\eta_r) (z - z_{ir})^2}{2R(x_r)} \right] \right\} \\
& \cdot \exp \left\{ i [\zeta(x_m) - \zeta(x_r)] - i k (x_m - x_r) - i k [(\sin(\varphi_m) - \sin(\varphi_r)) y + (\sin(\eta_m) - \sin(\eta_r)) z] \right\}
\end{aligned} \tag{5.103}$$

$$\equiv \int_{\text{PD}} dS \exp [- (c_{yy} y^2 + c_y y + c_{zz} z^2 + c_z z + c_0)], \tag{5.104}$$

where

$$c_{yy} = \cos^2(\varphi_m) \left[\frac{1}{w(x_m)^2} + \frac{i k}{2R(x_m)} \right] + \cos^2(\varphi_r) \left[\frac{1}{w(x_r)^2} - \frac{i k}{2R(x_r)} \right] \tag{5.105}$$

$$\begin{aligned}
c_y = & -2 \cos(\varphi_m) y_{im} \left[\frac{1}{w(x_m)^2} + \frac{i k}{2R(x_m)} \right] - 2 \cos(\varphi_r) y_{ir} \left[\frac{1}{w(x_r)^2} - \frac{i k}{2R(x_r)} \right] \\
& - i k [\sin(\varphi_m) - \sin(\varphi_r)]
\end{aligned} \tag{5.106}$$

$$c_{zz} = \cos^2(\eta_m) \left[\frac{1}{w(x_m)^2} + \frac{i k}{2R(x_m)} \right] + \cos^2(\eta_r) \left[\frac{1}{w(x_r)^2} - \frac{i k}{2R(x_r)} \right] \tag{5.107}$$

$$\begin{aligned}
c_z = & -2 \cos(\eta_m) z_{im} \left[\frac{1}{w(x_m)^2} + \frac{i k}{2R(x_m)} \right] - 2 \cos(\eta_r) z_{ir} \left[\frac{1}{w(x_r)^2} - \frac{i k}{2R(x_r)} \right] \\
& + i k [\sin(\eta_m) - \sin(\eta_r)]
\end{aligned} \tag{5.108}$$

$$\begin{aligned}
c_0 = & y_{im}^2 \cos^2(\varphi_m) \left[\frac{1}{w(x_m)^2} + \frac{i k}{2R(x_m)} \right] + y_{ir}^2 \cos^2(\varphi_r) \left[\frac{1}{w(x_r)^2} - \frac{i k}{2R(x_r)} \right] \\
& + z_{im}^2 \cos^2(\eta_m) \left[\frac{1}{w(x_m)^2} + \frac{i k}{2R(x_m)} \right] + z_{ir}^2 \cos^2(\eta_r) \left[\frac{1}{w(x_r)^2} - \frac{i k}{2R(x_r)} \right] \\
& + \ln \left[2 E_{0m} E_{0r} \frac{w_{0m} w_{0r}}{w(x_m) w(x_r)} \right] - i [\zeta(x_m) - \zeta(x_r)] + i k (x_m - x_r) \\
& + i k [y_{im} \sin(\varphi_m) - y_{ir} \sin(\varphi_r) - z_{im} \sin(\eta_m) + z_{ir} \sin(\eta_r)].
\end{aligned} \tag{5.109}$$

Since I restricted the analysis to detector surfaces of rectangular shape, Eq. (5.104) does not include a cross term of the two degrees of freedom of the detector surface, i.e. $c_{yz} = 0$. The integration of Eq. (5.104) thus yields

$$\begin{aligned}
& \int_{\text{PD}} dS \exp [- (c_{yy} y^2 + c_y y + c_{zz} z^2 + c_z z + c_0)] \\
= & \frac{\pi}{4 \sqrt{c_{yy}} \sqrt{c_{zz}}} \exp \left[\frac{1}{4} \left(\frac{c_y^2}{c_{yy}} + \frac{c_z^2}{c_{zz}} - 4c_0 \right) \right] \operatorname{erf} \left[\frac{2c_{yy} y - c_y}{2\sqrt{c_{yy}}} \right] \operatorname{erf} \left[\frac{2c_{zz} z - c_z}{2\sqrt{c_{zz}}} \right] \Big|_{\text{PD}}.
\end{aligned} \tag{5.110}$$

Thereby I denote with $F(y, z)|_{\text{PD}}$ the integrated function evaluated over the surface of the photodiode PD, i.e. $F(y, z)|_{\text{PD}} = \int_{\text{PD}} dS f(y, z)$. Since I chose rectangular surfaces, i.e. $\text{PD} = \{(y, z) | y_1 < y < y_2, z_1 < z < z_2\}$, I integrate over y and z and the integration boundaries equal

the boundaries of the diode surface given in this coordinate frame. If the photodiode consists of several sensitive segments, I apply this derivation to each of these segments and sum them up. The argument of the overlap integral (5.110), finally, yields the phase signal

$$\phi = \arg \left(\frac{\pi}{4\sqrt{c_{yy}}\sqrt{c_{zz}}} \exp \left[\frac{1}{4} \left(\frac{c_y^2}{c_{yy}} + \frac{c_z^2}{c_{zz}} - 4c_0 \right) \right] \operatorname{erf} \left[\frac{2c_{yy}y - c_y}{2\sqrt{c_{yy}}} \right] \operatorname{erf} \left[\frac{2c_{zz}z - c_z}{2\sqrt{c_{zz}}} \right] \Big|_{\text{PD}} \right). \quad (5.111)$$

Note that this evaluation of the phase corresponds to the LISA Pathfinder phase definition. I will discuss other phase definitions below.

I have claimed above that the computed phase equals the sum of the phase of an infinitely large SEPD and a detector-shape-dependent term. To prove this statement, I derive the integral (5.110) for SEPDs first:

$$\int_{\text{SEPD}} dS \exp \left[- (c_{yy}y^2 + c_yx + c_{zz}z^2 + c_zz + c_0) \right] = \frac{\pi}{\sqrt{c_{yy}}\sqrt{c_{zz}}} \exp \left[\frac{1}{4} \left(\frac{c_y^2}{c_{yy}} + \frac{c_z^2}{c_{zz}} - 4c_0 \right) \right]. \quad (5.112)$$

Thus the phase for an SEPD equals

$$\phi_{\text{SEPD}} = \arg \left(\frac{\pi}{\sqrt{c_{yy}}\sqrt{c_{zz}}} \exp \left[\frac{1}{4} \left(\frac{c_y^2}{c_{yy}} + \frac{c_z^2}{c_{zz}} - 4c_0 \right) \right] \right). \quad (5.113)$$

Applying the identity rules for the argument function, I can rewrite the products inside the argument function in Eq. (5.111) as the sum of argument functions. While this identity in general only holds modulo π , it can be applied for detectors capturing most of the incoming beam power without this modulator. In this case, the absolute value of the argument functions of the error functions would be much smaller than π . Therefore, it is

$$\begin{aligned} \phi &= \arg \left(\frac{\pi}{\sqrt{c_{yy}}\sqrt{c_{zz}}} \exp \left[\frac{1}{4} \left(\frac{c_y^2}{c_{yy}} + \frac{c_z^2}{c_{zz}} - 4c_0 \right) \right] \right) \\ &+ \arg \left(\frac{1}{2} \operatorname{erf} \left[\frac{2c_{yy}y - c_y}{2\sqrt{c_{yy}}} \right] \Big|_{\text{PD}} \right) + \arg \left(\frac{1}{2} \operatorname{erf} \left[\frac{2c_{zz}z - c_z}{2\sqrt{c_{zz}}} \right] \Big|_{\text{PD}} \right) \end{aligned} \quad (5.114)$$

$$= \phi_{\text{SEPD}} + \arg \left(\frac{1}{2} \operatorname{erf} \left[\frac{2c_{yy}x - c_y}{2\sqrt{c_{yy}}} \right] \Big|_{\text{PD}} \right) + \arg \left(\frac{1}{2} \operatorname{erf} \left[\frac{2c_{zz}y - c_z}{2\sqrt{c_{zz}}} \right] \Big|_{\text{PD}} \right). \quad (5.115)$$

Hence, the phase signal for arbitrary rectangular detector surfaces indeed corresponds to a sum of the signal computed by an SEPD and additional detector-shape-dependent terms. This proves the claim.

Analyses have shown that the arguments of the error functions are small if the diodes are large and capture most of the incoming beam power. In particular, they become zero if we consider infinitely large SEPDs. In this case, the phase signal (5.115) reduces to the LPS measured by an SEPD.

Signal computation for quadrant photodiodes

An example of detector shapes are large QPDs. Such photodiodes have been used in LPF and will be installed in LISA. Precisely speaking, the QPDs in these missions will be circular while I

Summary box 5.12 | Detector geometry TTL coupling

Detectors of rectangular shape and limited size or with insensitive regions alter the measured phase. Thereby the phase signal (LPF signal definition) equals the sum of the LPS measured by an infinitely large single element diode and the contributions of the insensitive regions:

$$\phi = \phi_{\text{SEPD}} + \arg \left(\frac{1}{2} \operatorname{erf} \left[\frac{2c_{yy} y - c_y}{2\sqrt{c_{yy}}} \right] \Big|_{\text{PD}} \right) + \arg \left(\frac{1}{2} \operatorname{erf} \left[\frac{2c_{zz} z - c_z}{2\sqrt{c_{zz}}} \right] \Big|_{\text{PD}} \right)$$

In the particular case of quadrant photodiodes and beams with the same parameters and the same point of detection, the non-geometric phase signal contribution is given by:

$$\text{LPS}_{\text{ng}}^{\text{QPD},2\text{D}} = \text{LPS}_{\text{ng}}^{\text{SEPD},2\text{D}} - \frac{1}{1 - \operatorname{erf} \left(\frac{D}{2} \sqrt{\frac{k x_R}{x_R^2 + x_b^2}} \right)} \left[\frac{D x_b}{4\sqrt{\pi} \sqrt{k x_R (x_R^2 + x_b^2)}} \exp \left(-\frac{D^2}{4} \frac{k x_R}{x_R^2 + x_b^2} \right) \right] \varphi_m^2$$

assume here for the simplified computation an outer rectangular shape. However, the difference between the signals computed by a detector of either shape is assumed to be small if most of the beam power is captured by the detector, i.e. little light will reach the outer sensitive regions of the diode.

Therefore, large QPDs are assumed to capture the full incoming light besides the light impinging at an insensitive cross slit through the detectors center, see Fig. 3.2. The signal (5.115) becomes

$$\begin{aligned} \phi_{\text{QPD}} &= \phi_{\text{SEPD}} + \arg \left(\frac{1}{2} \operatorname{erf} \left[\frac{2c_{yy} y - c_y}{2\sqrt{c_{yy}}} \right] \Big|_{-\infty}^{-D_y/2} + \frac{1}{2} \operatorname{erf} \left[\frac{2c_{yy} y - c_y}{2\sqrt{c_{yy}}} \right] \Big|_{D_y/2}^{\infty} \right) \\ &\quad + \arg \left(\frac{1}{2} \operatorname{erf} \left[\frac{2c_{zz} z - c_z}{2\sqrt{c_{zz}}} \right] \Big|_{-\infty}^{-D_z/2} + \frac{1}{2} \operatorname{erf} \left[\frac{2c_{zz} z - c_z}{2\sqrt{c_{zz}}} \right] \Big|_{D_z/2}^{\infty} \right) \end{aligned} \quad (5.116)$$

$$\begin{aligned} &= \phi_{\text{SEPD}} + \arg \left(-\frac{1}{2} \operatorname{erf} \left[\frac{2c_{yy} y + c_y}{2\sqrt{c_{yy}}} \right] \Big|_{D_y/2}^{\infty} + \frac{1}{2} \operatorname{erf} \left[\frac{2c_{yy} y - c_y}{2\sqrt{c_{yy}}} \right] \Big|_{D_y/2}^{\infty} \right) \\ &\quad + \arg \left(-\frac{1}{2} \operatorname{erf} \left[\frac{2c_{zz} z + c_z}{2\sqrt{c_{zz}}} \right] \Big|_{D_z/2}^{\infty} + \frac{1}{2} \operatorname{erf} \left[\frac{2c_{zz} z - c_z}{2\sqrt{c_{zz}}} \right] \Big|_{D_z/2}^{\infty} \right), \end{aligned} \quad (5.117)$$

where $D_{y,z}$ are the slit widths of the horizontal and vertical slit respectively. For small slit widths, offsets and beam tilt angle, the arguments of the error functions are also small. In this case, the corresponding phase would deviate only slightly from ϕ_{SEPD} . However, there are many cases where these contributions are not negligible.

When inserting the given representations of the c_i 's, i.e. Eqs. (5.105)-(5.109), into Eq. (5.117) to evaluate the phase signal, the equations becomes very lengthy. In the most simplified case of two identical beams, where the measurement beam rotates around their common center of incidence, and equal slit width $D = D_y = D_z$, we get

$$\text{LPS}_{\text{ng}}^{2\text{D}} \approx -\frac{1}{1 - \operatorname{erf} \left(\frac{D}{2} \sqrt{\frac{k x_R}{x_R^2 + x_b^2}} \right)} \left[\frac{D x_b}{4\sqrt{\pi} \sqrt{k x_R (x_R^2 + x_b^2)}} \exp \left(-\frac{D^2}{4} \frac{k x_R}{x_R^2 + x_b^2} \right) \right] \varphi_m^2. \quad (5.118)$$

Hence, the non-geometric signal contribution for a quadrant diode is a second-order effect. We have seen in simulations that quadratic series expansions of the LPS model the simulated signal of an SEPD well but are sometimes insufficient to describe the signal measured by a QPD. In

these cases, the equations have to be extended to the fourth-order. This will be further discussed in Sec. 7.2.2.

Alternative phase signal definitions for quadrant photodiodes

For the signals derived for QPDs in this section, I evaluate the argument of the sum of the complex amplitudes of all sensitive segments, i.e.

$$\text{LPS} = \frac{1}{k} \phi = -\frac{1}{k} \arg(Q_A + Q_B + Q_C + Q_D). \quad (5.119)$$

The complex amplitudes Q_j , $j \in \{A, B, C, D\}$ are defined analogously to Eq. (3.16) for each quadrant of the detector by

$$Q_j = \bar{P}_j c_j \exp(-i \phi_j). \quad (5.120)$$

This signal definition has been used during the LPF mission, for which reason it is also called the LISA Pathfinder signal. However, it is also possible to define different signals for QPDs [36].

Another prominent example is the arithmetic mean phase (AP) signal. It computes the phases for each segment and then takes the arithmetic mean of their sum, i.e.

$$\text{LPS}^{\text{AP}} = \frac{\phi_A + \phi_B + \phi_C + \phi_D}{4k} = -\frac{\arg(Q_A) + \arg(Q_B) + \arg(Q_C) + \arg(Q_D)}{4k}. \quad (5.121)$$

The AP signal has proven in several simulations that it is less affected by TTL coupling [37, TN2]. However, it is designed for beams impinging approximately at the diode's centre. If the beams' points of detection are, e.g., shifted horizontally to the left, the detected power at the left half of the detector will be larger than the power detected at the right-hand side. In the most extreme case, the beam would be fully captured by the left half of the diode while no light impinges at the right-hand side. Still, the phases computed for both sides will be weighted equally, not representing the shifted power distribution.

The non-geometric TTL coupling in the LPF signal is stronger than the respective coupling in the AP signal [37, TN2]. However, the LPF signal is for small slit width similar to the signal derived by an SEPD. Therefore, several coupling effects cancel in the full signal, as I will show in Sec. 5.3. Also, the LPF signal equals the signal for SEPDs if the slit width becomes zero. This is not true for the AP signal definition.

Sensing errors and detector imperfections

I discussed in Sec. 5.2.1 that small wavefront errors change the phase signal. The same applies to imperfections of the detector geometry and other parameters affecting the sensitivity of small fractions of the diode's surface, e.g., scratches or residual dust particles. These irregularities can induce arbitrary LPS changes. Therefore, I will not discuss these errors within this work.

5.3 Cancellations in the Full Longitudinal Path Length Signal

At the detector, the geometric and non-geometric TTL coupling add up to the total signal. While I have investigated in Sec. 5.1 and Sec. 5.2 both effects separately, we find that some of them cancel each other in the combined LPS. Within this section, I will particularly study the geometric effects added with the non-geometric phase signal induced by the corresponding beam walk, as well as the impact of detector tilts on the signal.

Angular jitter: Cancellation of the signal for identical beams and dynamic beam walk

Given two Gaussian beams with equal beam parameters that are nominally not tilted, i.e. $\varphi_{m,r} = 0$, and impinge on the same point at the detector, i.e. $y_{im0} - y_{ir} = 0$, we find the geometric and the non-geometric signal contribution to cancel each other in several situations. Here, I investigate the cancellations for angularly jittering test masses and receivers, respectively. Let us first assume the measurement beam to jitter angularly around a point along its propagation axis. This is equivalent to a rotation of the receiver around a longitudinal offset as well as to the lever arm effect caused by a reflection. To derive the associated non-geometric LPS, I insert the beam walks (5.62) and (5.64), setting $d_{\text{lat}} = 0$, respectively into Eq. (5.58). Hence we get

$$\text{LPS}_{\text{ng,lever}}^{\text{SEPD},2\text{D}} \approx 2d_{\text{lever}} \varphi^2, \quad (5.122)$$

$$\text{LPS}_{\text{ng,SC,long}}^{\text{SEPD},2\text{D}} \approx \frac{1}{2}d_{\text{long}} \varphi_{\text{SC}}^2. \quad (5.123)$$

The full LPS is the sum of the OPD and non-geometric contribution. We find the OPDs for the lever arm effect (5.4) and the S/C rotation (5.25) for $d_{\text{lat}} = 0$ to be inverse to the beam walk induced coupling. Hence, in the computation of the full LPS, both cancel out and yielding zero TTL coupling:

$$\text{LPS}_{\text{lever}}^{\text{SEPD},2\text{D}} = \text{OPD}_{\text{lever}}^{2\text{D}} + \text{LPS}_{\text{ng,lever}}^{\text{SEPD},2\text{D}} \approx 0, \quad (5.124)$$

$$\text{LPS}_{\text{SC,long}}^{\text{SEPD},2\text{D}} = \text{OPD}_{\text{SC,long}}^{2\text{D}} + \text{LPS}_{\text{ng,SC,long}}^{\text{SEPD},2\text{D}} \approx 0. \quad (5.125)$$

Hence, given equal beam parameters, longitudinal offsets of the centre of rotation from the point of reflection or point of detection do not affect the total LPS. In Sec. B.2, I aim to give an additional, intuitive proof of this cancellation.

Further analysis shows that we get the same result for transmissive components along the beam path. Inserting the respective beam walk (5.65) into Eq. (5.58), we get

$$\text{LPS}_{\text{ng,tc}}^{\text{SEPD},2\text{D}} \approx \sum_i \frac{1}{2}t_{\text{tc},i} \left[-\frac{n_{\text{tc},i}^2 \cos^2(\varphi_{\text{tc},i})}{(n_{\text{tc},i}^2 - \sin^2(\varphi_{\text{tc},i}))^{3/2}} + \frac{\sin^2(\varphi_{\text{tc},i})}{\sqrt{n_{\text{tc},i}^2 - \sin^2(\varphi_{\text{tc},i})}} + \cos(\varphi_{\text{tc},i}) \right] \varphi_m^2. \quad (5.126)$$

The beam walk dependent term is, again, inverse to the corresponding OPD (5.34), i.e.

$$\text{LPS}_{\text{tc}}^{\text{SEPD},2\text{D}} \approx 0. \quad (5.127)$$

I conclude that in the case of beams with equal parameters, transmissive components along the beam path add no further TTL coupling to the signal.

However, these findings do not hold for every kind of TTL coupling. In particular, the angular piston effect cancels only partially. When deriving the non-geometric LPS contribution by inserting Eq. (5.63) into Eq. (5.58), we get

$$\text{LPS}_{\text{ng,piston,ang}}^{\text{SEPD},2\text{D}} \approx -2d_{\text{lat}} \sin(\beta) \varphi^2, \quad (5.128)$$

which is a second-order TTL coupling. The geometric piston coupling (Eq. (5.13)) on the other hand, does also include linear coupling terms. When adding up the geometric and non-geometric contributions, we find

$$\text{LPS}_{\text{piston,ang}}^{\text{SEPD},2\text{D}} \approx -2d_{\text{lat}} \cos(\beta) \varphi + d_{\text{long}} \cos(\beta) \varphi^2. \quad (5.129)$$

Summary box 5.13 | Detector tilt TTL coupling

Detector tilts affect the geometric (propagation distance to the detector surface) and the non-geometric (angle of incidence of both interfering beams) TTL coupling. For large SEPDs, both effects cancel since the detector tilt affects the measurement and reference beam equivalently:

$$\text{LPS}^{\text{SEPD}}(\varphi_{\text{PD}}) - \text{LPS}^{\text{SEPD}}(\varphi_{\text{PD}} = 0) = 0.$$

Thus we have non-negligible TTL coupling left if the point of reflection and the centre of rotation do not coincide. The same applies to angular jitter of the receiving setup around a point that deviates laterally from the beam's nominal point of detection, i.e.

$$\text{LPS}_{\text{SC,lat,ang}}^{\text{SEPD,2D}} \approx -d_{\text{lat}} \varphi_{\text{SC}}. \quad (5.130)$$

Lateral jitter: Cancellation of the signal for identical beams and dynamic beam walk

The investigations in Secs. 5.1 and 5.2 have shown that lateral test mass jitter yields linear geometric TTL coupling but no non-geometric counterpart. Contrary, a lateral jittering receiver measures no geometric TTL coupling but linear and – in the case of unequal beam parameters – quadratic non-geometric TTL coupling. Thus, the geometric and the non-geometric coupling terms cannot cancel each other in both cases. Correspondingly, the lateral test mass jitter is fully described by the geometric length changes of the beam path, and the measured coupling from lateral receiver jitter entirely originates from the jitter induced beam walk on the detector.

Cancellation of the detector tilt

We have seen in Sec. 5.1 and Sec. 5.2.2 that the geometric as well as the non-geometric TTL coupling feature coupling terms depending of the detector tilt φ_{PD} . The following paragraphs will demonstrate that these detector tilt dependent terms cancel out in the full LPS.

Let us first consider an **angularly** jittering receiving system. In an ideal receiver, the detector surface is aligned to the system's coordinate frame. However, a misalignment of the detector is often unavoidable in the construction phase. The full OPD for a jittering receiver is given by Eq. (5.42). I adapt $\text{OPD}_{\text{SC,ang}}^{\text{2D}}$ (Eq. (5.25)) by substituting $\varphi_{\text{SC}} \rightarrow \varphi_{\text{SC}} + \varphi_{\text{PD}}$. Thereby, we account for the detector tilt. Neglecting all constants, this equation yields the TTL coupling induced by the offset of the centre of receiver rotation only. Considering then only the detector tilt dependent terms, we find

$$\begin{aligned} & \text{OPD}_{\text{RS,ang}}^{\text{2D}}(\varphi_{\text{PD}}) - \text{OPD}_{\text{RS,ang}}^{\text{2D}}(\varphi_{\text{PD}} = 0) \\ & \approx -d_{\text{long}} \varphi_{\text{SC}} \varphi_{\text{PD}} - \sum_i t_{\text{tc},i} \left[\frac{n_{\text{tc},i}^2 \cos^2(\varphi_{\text{tc},i})}{(n_{\text{tc},i}^2 - \sin^2(\varphi_{\text{tc},i}))^{3/2}} - \frac{\sin^2(\varphi_{\text{tc},i})}{\sqrt{n_{\text{tc},i}^2 - \sin^2(\varphi_{\text{tc},i})}} - \cos(\varphi_{\text{tc},i}) \right] \varphi_{\text{SC}} \varphi_{\text{PD}}. \end{aligned} \quad (5.131)$$

The associated non-geometric coupling is computed by inserting the offset $y_{i\text{RST}}$ (5.69) into

Eq. (5.100). This gives

$$\begin{aligned} & \text{LPS}_{\text{ng,RS,ang}}^{\text{SEPD,2D}}(\varphi_{\text{PD}}) - \text{LPS}_{\text{ng,RS,ang}}^{\text{SEPD,2D}}(\varphi_{\text{PD}} = 0) \\ & \approx d_{\text{long}} \varphi_{\text{SC}} \varphi_{\text{PD}} + \sum_i t_{\text{tc},i} \left[\frac{n_{\text{tc},i}^2 \cos^2(\varphi_{\text{tc},i})}{(n_{\text{tc},i}^2 - \sin^2(\varphi_{\text{tc},i}))^{3/2}} - \frac{\sin^2(\varphi_{\text{tc},i})}{\sqrt{n_{\text{tc},i}^2 - \sin^2(\varphi_{\text{tc},i})}} - \cos(\varphi_{\text{tc},i}) \right] \varphi_{\text{SC}} \varphi_{\text{PD}}. \end{aligned} \quad (5.132)$$

In order to derive the full LPS, I add up Eq. (5.131) and Eq. (5.132), i.e.

$$\begin{aligned} & \text{LPS}_{\text{RS,ang}}^{\text{SEPD,2D}}(\varphi_{\text{PD}}) - \text{LPS}_{\text{RS,ang}}^{\text{SEPD,2D}}(\varphi_{\text{PD}} = 0) \\ & = [\text{OPD}_{\text{RS,ang}}^{2\text{D}}(\varphi_{\text{PD}}) - \text{OPD}_{\text{RS,ang}}^{2\text{D}}(\varphi_{\text{PD}} = 0)] + [\text{LPS}_{\text{ng,RS,ang}}^{\text{SEPD,2D}}(\varphi_{\text{PD}}) - \text{LPS}_{\text{ng,RS,ang}}^{\text{SEPD,2D}}(\varphi_{\text{PD}} = 0)] \end{aligned} \quad (5.133)$$

$$\approx 0 \quad (5.134)$$

Hence the detector tilt indeed cancels for angularly jittering receivers.

Analogously, I show that the φ_{PD} -dependent terms cancel for angular test mass jitter. The OPD for test mass rotations is given by Eq. (5.41). Thus the respective detector tilt dependent terms are

$$\begin{aligned} & \text{OPD}_{\text{TM,ang}}^{2\text{D}}(\varphi_{\text{PD}}) - \text{OPD}_{\text{TM,ang}}^{2\text{D}}(\varphi_{\text{PD}} = 0) \\ & \approx -2d_{\text{lever}} \varphi \varphi_{\text{PD}} - 2d_{\text{lat}} \sin(\beta) \varphi \varphi_{\text{PD}} \\ & - \sum_{i=1}^N 2t_{\text{tc},i} \left[\frac{n_{\text{tc},i}^2 \cos^2(\varphi_{\text{tc},i})}{(n_{\text{tc},i}^2 - \sin^2(\varphi_{\text{tc},i}))^{3/2}} - \frac{\sin^2(\varphi_{\text{tc},i})}{\sqrt{n_{\text{tc},i}^2 - \sin^2(\varphi_{\text{tc},i})}} - \cos(\varphi_{\text{tc},i}) \right] \varphi \varphi_{\text{PD}}. \end{aligned} \quad (5.135)$$

For the corresponding non-geometric coupling, I insert the offset $y_{i\text{TM}}$ (Eq. (5.68)) into Eq. (5.100) and substitute $\varphi_m \rightarrow 2\varphi$. This gives

$$\begin{aligned} & \text{LPS}_{\text{ng,TM,ang}}^{\text{SEPD,2D}}(\varphi_{\text{PD}}) - \text{LPS}_{\text{ng,TM,ang}}^{\text{SEPD,2D}}(\varphi_{\text{PD}} = 0) \\ & \approx [2d_{\text{lever}} + 2d_{\text{lat}} \sin(\beta)] \varphi \varphi_{\text{PD}} \\ & + \sum_i 2t_{\text{tc},i} \left[\frac{n_{\text{tc},i}^2 \cos^2(\varphi_{\text{tc},i})}{(n_{\text{tc},i}^2 - \sin^2(\varphi_{\text{tc},i}))^{3/2}} - \frac{\sin^2(\varphi_{\text{tc},i})}{\sqrt{n_{\text{tc},i}^2 - \sin^2(\varphi_{\text{tc},i})}} - \cos(\varphi_{\text{tc},i}) \right] \varphi \varphi_{\text{PD}}. \end{aligned} \quad (5.136)$$

In order to filter out how the full LPS depends on the detector tilt, I add up Eq. (5.135) and Eq. (5.136) giving

$$\begin{aligned} & \text{LPS}_{\text{TM,ang}}^{\text{SEPD,2D}}(\varphi_{\text{PD}}) - \text{LPS}_{\text{TM,ang}}^{\text{SEPD,2D}}(\varphi_{\text{PD}} = 0) \\ & = [\text{OPD}_{\text{TM,ang}}^{2\text{D}}(\varphi_{\text{PD}}) - \text{OPD}_{\text{TM,ang}}^{2\text{D}}(\varphi_{\text{PD}} = 0)] + [\text{LPS}_{\text{ng,TM,ang}}^{\text{SEPD,2D}}(\varphi_{\text{PD}}) - \text{LPS}_{\text{ng,TM,ang}}^{\text{SEPD,2D}}(\varphi_{\text{PD}} = 0)] \end{aligned} \quad (5.137)$$

$$\approx 0. \quad (5.138)$$

Hence, we see that the detector tilt φ_{PD} cancels out in the full LPS for angular jitter of either of the considered setups.

Next, I investigate the detector tilts for **laterally** jittering systems. For non-tilted detectors, the lateral jitter coupling for receiving systems is fully described by its non-geometric TTL contribution. However, in the case of a tilted detector, the geometric TTL coupling of a laterally

jittering receiver is given by Eq. (5.29). Adding this equation to its non-geometric counterpart Eq. (5.102), we find as before

$$\text{LPS}_{\text{RS}}^{\text{SEPD},2\text{D}}(\varphi_{\text{PD}}) - \text{LPS}_{\text{RS}}^{\text{SEPD},2\text{D}}(\varphi_{\text{PD}} = 0) \approx 0. \quad (5.139)$$

Having a laterally jittering test mass, we have found in Sec. 5.2 that this jitter induces no non-geometric TTL coupling. To confirm my claim that the detector tilt cancels in the full signal, I have to show that also the geometric counterpart includes no linear or quadratic detector tilt dependent terms. Indeed, the corresponding Eq. (5.20) shows no detector tilt dependency. So we have, in particular,

$$\text{LPS}_{\text{TM}}^{\text{SEPD},2\text{D}}(\varphi_{\text{PD}}) - \text{LPS}_{\text{TM}}^{\text{SEPD},2\text{D}}(\varphi_{\text{PD}} = 0) \approx 0. \quad (5.140)$$

In summary, the detector tilt angle φ_{PD} also cancels for lateral jitter coupling in the full signal when considering a large SEPD. Thus it can be neglected if the full measured signal consists of both the OPD and the non-geometric LPS. If either of these contributors changes, the detector tilts can add significant TTL coupling. The cancellation can, e.g., be disturbed by QPDs with wide slit widths. However, the changes are negligible in the case of the LPF setup, which will be discussed in Sec. 7.2.1.

5.4 Summary of the Tilt-To-Length Coupling Effects

In the above sections, I presented several TTL coupling effects and discussed whether they add mainly first-, second- or higher-order coupling terms. We have further seen that, in the case of equal beam parameters and large SEPDs, several of these effects cancel in the complete signal. For unequal beam parameters or QPDs most of these cancellations do not hold any longer. However, the residual TTL would be small for minor parameter discrepancies and QPDs with small slit width when using the LPF signal definition. Therefore, I summarise the principal behaviour of the single coupling mechanisms and further, non-geometric, coupling effects for angular jitter in Tab. 5.2 and for lateral jitter in Tab. 5.3 assuming equal beam parameters and SEPDs.

system	mechanism	summary box	characterisation of the signal		
			geometric	non-geometric	complete
TM	lever arm effect	5.1, 5.9	quadratic	quadratic	0
TM	piston effect [lateral]	5.2, 5.9	linear	0	linear
TM	piston effect [longitudinal]	5.2, 5.9	quadratic	0	quadratic
RS	lateral CoR	5.4, 5.9	linear	0	linear
RS	longitudinal CoR	5.4, 5.9	quadratic	quadratic	0
both	transmissive components	5.6, 5.9	quadratic	quadratic	0
both	static beam offsets	5.8	0	linear	linear
both	reference beam tilt	5.11	0	linear	linear
both	detector tilt	5.13	linear	linear	0
both	insensitive detector slit (QPD)	5.12	0	quadratic	quadratic
both	arbitrary detector geometry	5.12	0	arbitrary	arbitrary

Table 5.2: Summary of the characteristics of the geometric, non-geometric and complete TTL coupling effects for **angular jitter** assuming equal beam parameters, large SEPDS and beams that impinge at normal incidence at the test mass and detector, respectively (if not otherwise stated). In addition, as done throughout this section, I use the LPF signal definition for the computation of the QPD signal. I characterise the effects as ‘linear’, ‘quadratic’ or ‘arbitrary’ regarding to their series expressions for small angles. Effects that are not existent or only couple at higher-orders, will be labelled with a ‘0’.

system	mechanism	summary box	characterisation of the signal		
			geometric	non-geometric	complete
TM	piston effect	5.3, 5.10	linear	0	lateral
RS	receiver jitter	5.5, 5.10	0	linear	linear
both	static beam offsets	5.8	0	0	0
both	reference beam tilt	5.11	0	linear	linear
both	detector tilt	5.13	linear	linear	0

Table 5.3: Summary of the characteristics of the geometric, non-geometric and complete TTL coupling effects for **lateral jitter** assuming equal beam parameters, large SEPDS and beams that impinge at normal incidence at the test mass and detector, respectively (if not otherwise stated). I characterise the effects as ‘linear’, ‘quadratic’ or ‘arbitrary’ regarding to their series expressions for small angles. Effects that are not existent or only couple at higher-orders, will be labelled with a ‘0’.

Chapter 6

Tilt-To-Length Suppression Strategies

In the analytical derivations in Sec. 5, I have characterised various TTL mechanisms. From this analysis, one can deduce design or realignment recommendations to suppress or counteract TTL coupling in an optical setup. Furthermore, I contextualise the suppression strategies which have been experimentally verified previously, e.g., imaging systems, and my work. Of particular interest for this thesis are the suppression strategies used in the space-based interferometers LISA and LPF.

The suppression strategies introduced in this chapter partly rely on my analytical work above and partly refer to the work published by others, as I will state at appropriate places in the text.

6.1 Suppression by Design, Alignment or Subtraction

In this section, I will present TTL suppression strategies that are or can be used in space-based laser interferometers. I will distinguish between strategies concerning the design of the interferometer and suppression schemes that can be applied during a mission as realignments or subtractions of a dedicated model.

6.1.1 Suppression by design

The suppression of TTL coupling by design is advantageous since it reduces the need for further suppression schemes a priori.

I have shown in Sec. 5.3 that multiple TTL coupling mechanisms cancel if both interfering beams feature exactly the same beam parameters, i.e. the same waist size and the same distance from waist at the detector, and are detected by a large SEPD. Hence, a modification of the beams such that they fulfil this requirement would reduce TTL coupling. However, in heterodyne interferometers like in LPF and LISA, this is not feasible.

Moreover, the alignment of the beams is crucial for TTL mitigation since static beam offsets as well as tilts of the reference beam couple linearly into the measurement (Sec. 5.2.1). Thus, the beams are ideally aligned so that they nominally impinge at the same point and with a normal incidence at the detector.

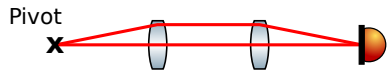


Figure 6.1: Schematic of the TTL suppression via imaging systems. Properly aligned systems image the pivot onto the detector surface, thereby mitigating any geometric TTL coupling.

A system design with the centre of mass at the point of reflection (test mass setup) or detection (receiver setup) would make the system jitter about that point. In the case of a jittering test mass, this design would eliminate the angular piston effect (Sec. 5.1.1). However, in many interferometers, such an alignment is hard to achieve. So, a freely falling test mass' centre of mass, i.e. its natural centre of rotation, likely does not equal the point of reflection. If instead, the S/C jitters relative to the test mass, the offset between the S/C's centre of rotation and the point of reflection can be minimised, provided that the S/C carries only one test mass. Considering a rotating receiver, only transmissive components and pure non-geometric TTL effects would still couple into the signal (Secs. 5.1.2 and 5.1.3). The residual coupling would then be dominated by static offsets of the beams at the detector and the inequality of the beam properties (parameters and angular alignment).

A mitigation scheme that has not been discussed here, but has been proven successful in an experiment, is the imaging system [39, 43]. Imaging systems are lens systems that, on the one hand, change the beams' spot sizes at the detector and, on the other hand, image the centre of rotation onto the detector. Properly aligned imaging systems can therefore suppress the full geometric angular TTL coupling and the beam walk contribution to the non-geometric signal. The residual TTL coupling is comparable to the case discussed in the previous paragraph. It would, again, be dominated by the difference between the beam parameters and their angle of incidence at the detector. Static offsets of the beam's points of incidence also generate TTL coupling. However, this offset decreases if the system compresses the beam. A schematic of a possible imaging system is depicted in Fig. 6.1 showing the correction of a beam tilt for a perfectly aligned system. Note that similar results can be achieved using not lenses but curved mirrors.

6.1.2 Suppression by alignment

In many cases, the interferometer design alone cannot entirely suppress the TTL coupling, or the setup properties change during the mission time, e.g. due to temperature changes. Then, realignments of certain optical components can mitigate or counteract the measured TTL coupling.

So, a shift of a test mass, which jitters angularly around its centre of mass, can reduce the lateral offset between the point of reflection and the centre of rotation. This realignment suppresses the linear lateral contribution of the piston effect (Sec. 5.1.1). Note that this realignment strategy only provides a successful suppression strategy if the point of rotation is fixed to the test mass. Considering a S/C that jitters relative to the test mass, such a test mass shift would not affect the offset between the point of reflection and the centre of rotation.

Similarly, angular corrections of the test mass can eliminate the coupling of lateral jitter: Given a non-tilted reflective component, its lateral jitter would neither shift it into nor away from the beam path and, therefore, does not add any TTL coupling (see Sec. 5.1.1). This alignment scheme applies to lateral test mass jitter as well as lateral S/C jitter relative to the test mass.

In the case of a jittering receiver, neither shifts nor tilts affect the geometric TTL coupling,

but a lateral realignment can decrease the static offset between both interfering beams, which contribute linear coupling to the interferometric measurement (Sec. 5.2.1).

In general, the lateral beam realignment of the measurement or the reference beam will alter the offset of their points of detection. The resulting linear non-geometric TTL coupling can, therefore, counteract other linear coupling mechanisms (Sec. 5.2.1).

A further method to suppress TTL coupling is discussed in [39, 43]: When combining the readouts of the four QPD segments via the AP signal definition, a lateral shift of the detector adds linear, and a longitudinal shift adds quadratic TTL coupling. These terms can then counteract the existent coupling of various origins. Note that this suppression scheme can only be used with the AP signal. When the signal is defined via the LPF signal computation and the QPD is a large diode with thin slits, a lateral shift would have little effect on the full coupling. Longitudinal detector shifts for this signal definition are discussed in App. B.1.2.

6.1.3 Subtraction of tilt-to-length coupling

In post-processing, residual TTL coupling can be fitted using the DWS readouts for a prediction of the angular system alignment and, if available, a readout for the lateral test mass position. Given these coupling parameters, a linear or higher-order fit model can be subtracted from the signal in order to remove the TTL noise. Such a suppression scheme depends on the precision of the angular and position readout but has been proven successful during the LPF mission [11]. However, reducing the coupling by design or alignment will improve the TTL mitigation since less noise of the fitting quantities would be added to the measurement via subtraction. This will be demonstrated in the next section by the LPF results.

6.2 Suppression Strategies in Space Interferometers

TTL coupling is a major noise source in space interferometers [11, 39, 40, 41, 42]. Different design choices and alignment mechanisms were, are, and will be applied for its suppression. Within this section, I aim to give an overview of the strategies known today and compare them with the prediction by my analytical TTL description. The main focus of this work lies on the LPF mission which ended in 2017 and provided valuable data for the analysis of TTL coupling in space interferometers [11]. In LISA, TTL coupling would, without suppression, be one of the major noises. Therefore, several suppression schemes are currently planned to be implemented in LISA, for example, imaging systems [39, 43].

6.2.1 Tilt-to-length suppression in LISA Pathfinder

In LPF, the misalignment between the test masses and the optical bench inside the S/C induced a cross-talk of S/C jitter, that coupled into the x12-readout (compare Eq. (2.8)). This cross-coupling noise exceeded the white noise model between 20 mHz and 200 mHz and was there visible as a ‘bump’ [11]. Despite the cross-coupling noise being only visible since the interferometer noise was well below the required level, two attempts were made to remove this cross-talk in order to consolidate the original noise model [45].

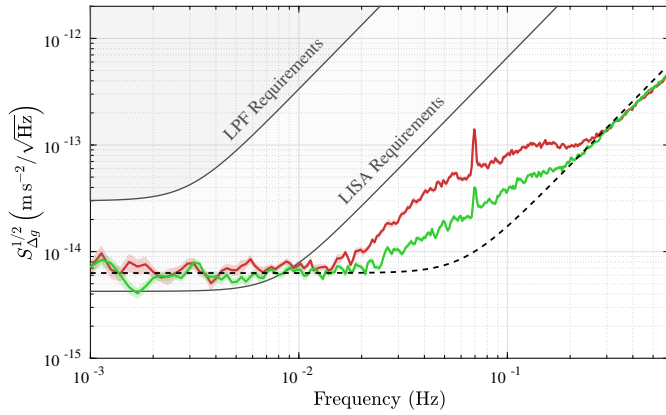


Figure 6.2: The LPF performance before (red) and after (green) the test mass realignments during the engineering days in March 2016. The performance improved approximately by a factor of 2 but was still the dominating noise between 20 and 200 mHz. The dashed line shows the performance model.

Alignment of the test masses

TTL noise in LPF originated from the jitter of the S/C relative to the test masses. As discussed in the previous section, lateral jitter can in this case be reduced by an angular realignment of the test masses. However, a lateral shift of the test masses would have no significant effect on the overall TTL coupling for angular S/C jitter: This shift would not change the distance between the point of reflection and the centre of S/C rotation as intended.

During the engineering days in March 2016, the lateral and angular alignments of the test masses were adjusted. This adjustment relied on a simplified geometric piston model, which assumed test mass jitter. The realignment reduced the TTL coupling in the measurement band by a factor of 2 in the ASD, see Fig. 6.2 [45]. A list of these realignments and further discussion are provided in Sec. 9.1.

Subtraction of linear fit model

After the realignment, the TTL coupling was still limiting the sensitivity, see Fig. 6.2. Thus, the residual coupling was removed in post-processing via subtraction. Therefore, a linear model of the measured S/C rotational and translational acceleration was fitted and then subtracted from the Δg measurement [45]. This model was

$$\Delta g_{\text{xtalk}} = C_{\varphi} \ddot{\bar{\varphi}} + C_{\eta} \ddot{\bar{\eta}} + C_y \ddot{\bar{y}} + C_z \ddot{\bar{z}} + C_{y,s} \bar{y} + C_{z,s} \bar{z} + C_{o_1} \ddot{o}_1, \quad (6.1)$$

where \bar{j} , $j \in \{\varphi, \eta, y, z\}$, denote the mean rotations or displacements of the test masses. These mean values describe the negative S/C motion. The accelerations orthogonal to the sensitive x -axis couple into the x12-readout as well as the translational stiffnesses along the y - (\bar{y}) and the z -axis (\bar{z}). Additionally, residual x -motion of the S/C with respect to the test masses can leak into the signal and is also included in the fit. The linear coupling coefficients C_j depend on the geometric properties of the LPF setup as well as the beam properties and the geometry of the four interferometers, in particular the x12-interferometer. This fit model subtracted the residual TTL well from the Δg measurement.

However, the fit coefficients themselves provided no physical interpretation of the underlying cross-coupling effect and, therefore, no information on how the corresponding TTL noise could be suppressed. Also, some coefficients were highly correlated. As a consequence, different fit models performed comparably well. Since the fit coefficients varied over time, frequent recalculations were necessary [45].

These disadvantages can be overcome with a TTL model, which depends on the particular test

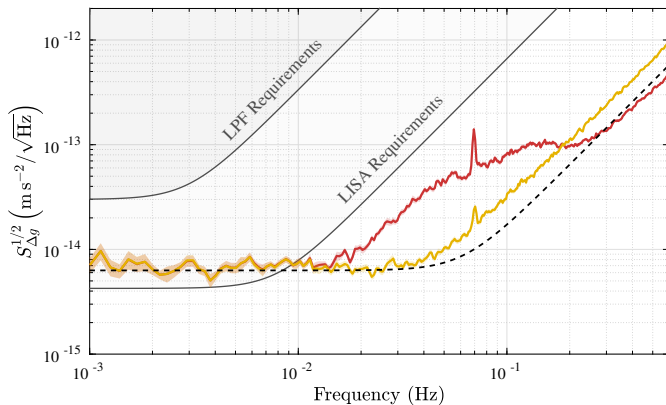


Figure 6.3: The LPF performance before (red) and after (yellow) subtraction of a linear TTL model fitted to the red curve during the engineering days in March 2016, i.e. before the realignment of the test masses. The subtraction subtracted the TTL noise well at lower frequencies. However, it added additional noise above 200 mHz.

mass alignments. Such a model can be derived by interpreting the analytical TTL equations (Sec. 5) for the LPF setup. I will present the result in Sec. 7.2.

A model as the derived analytical TTL model can describe the cross-talk for long mission durations relying on a constant set of setup and beam parameters – given no significant setup alterations due to temperature or other external changes. Thus it allows the direct subtraction of TTL noise for every data set without adaption. Furthermore, this model explains how the coupling depends on the test mass alignments, which can subsequently be realigned for a reduced cross-coupling.

Combination of both suppression strategies

Both reduction strategies presented here, the suppression via realignment and the subtraction via the fit model, were necessary to remove the cross-talk from the measurement sufficiently (Fig. 2.4). As we see in Fig. 6.2, the performed realignment did not remove the full bump. I will analyse this further in Sec. 9.1. Then again, the analysis of the data of the engineering days shows that a fit model without prior realignment led to additional noise at higher frequencies (Fig. 6.3). This noise originates from sensing noise in the GRS readout and is naturally unwanted. Consequently, both suppression schemes either have to be combined, or the test mass realignment model has to be improved for a full cancellation of the TTL noise.

6.2.2 Tilt-to-length suppression in LISA

TTL coupling is one of the most significant contributors to the LISA measurement noise budget. There, it mainly originates from the S/C jitter, and the coupling coefficients are expected to be larger than they were for LPF. Therefore, TTL noise needs to be reduced in LISA already by design. The residual coupling will be mitigated by further compensation techniques, which I will introduce below.

Tilt-to-length noise origins

For the full LISA science signal, the readouts of the long-arm and the two test mass interferometers in the S/C at the ends of the respective arm will be combined. The TTL noise coupling in these measurements can be divided into three groups of coupling origins [49]. First, coupling noise enters the test mass interferometer [39]. This noise is most comparable to the noise we find in LPF. Furthermore, the noise in the long-arm interferometer splits into two coupling types:

The noise originating from the transmitting S/C [40] and the noise originating from the receiving S/C [41, 43]. I will introduce these TTL noises here separately.

I start by explaining the contributions originating from the transmitted beam. This beam's wavefront is disturbed due to imperfections in the alignment of the optical components within the sending S/C. The resulting wavefront errors, such as spherical aberrations, defocus, astigmatism, coma and trefoil, induce significant non-geometric TTL coupling when combined with the pointing jitter of the transmitter [40]. These noises are not covered by the analytical equations presented in Sec. 5.

The local S/C then adds further TTL noise to the long-arm measurement. When the far beam reaches the receiving S/C it will be widened to several kilometres. The fraction of this beam that enters the local S/C through the telescope's outer pupil of 300 mm diameter (see Fig. 2.2) will almost be flat regardless of the orientation of the S/C it originates from: Due to the large distance between both S/C, the wavefronts are almost circular, with the midpoint of this circle lying in the transmitter S/C. Except for the wavefront errors, the wavefront segment received by the local S/C will, in a good approximation, have the same properties for any rotation of the transmitter. However, the angular jitter of the local S/C will first rotate the telescope scheme in and out of the beam path, and, second, induce a tilt of the received wavefront with respect to the outer pupil of the receiving telescope. This angle will be magnified by a factor of 135 when the telescope suppresses the beam from its 300 mm to 2.24 mm diameter [41, 43]. In addition, the alignment of the local optical components can change the alignment and wavefront of the received beam. I describe the TTL coupling for a receiving system in Sec. 5.1.2, however, not considering a telescope or imaging systems. The presented equations do not hold for the non-geometric coupling effects since only the local reference beam is Gaussian.

The inter-satellite measurement yields the main TTL noise. Further noise adds to the full science signal via the test mass interferometer readout [39]. As stated above, this noise is most comparable to the LPF case: The lateral and angular jitter of the S/C with respect to the test mass yields further TTL terms. Hereby, like for the received beam, the offset between the centre of rotation and the point of reflection lets the S/C - or the test mass respectively - move into or out of the beam path (piston coupling). Since two Gaussian beams interfere at the test mass interferometer, the equations presented in Sec. 5 can be used to characterise this noise.

LISA design

Contrary to LPF, it is planned to suppress the TTL coupling in LISA already by design. An example of such design suppression strategies is the implementation of imaging systems in front of the test mass and long-arm photodiodes [39, 43]. These imaging systems can be used, on the one hand, to minimise the geometric angular TTL coupling and, on the other hand, to compress the beam's spot size at the detector. The compression of the beam will reduce any lateral misalignments of the beams (i.e. not the lateral jitter of a test mass) but magnify the angle of incidence. As shown by Eq. (5.54), this angular increase will also magnify the non-geometric TTL coupling. Thus, a residual TTL coupling of angular jitter due to the non-geometric TTL contributions and imperfections of the imaging system would remain [39, 43].

In general, TTL will be mitigated in LISA by a reduction of the overall misalignments in the optical system. So, also the piston effect will be reduced: Recalling that each LISA S/C hosts two test masses (Fig. 2.2), the offset between the point of reflection and the centre of S/C rotation will be large for at least one test mass. Thus, the angular jitter of the respective S/C will always create significant piston coupling. A similar effect would be observed in the long-arm interferometer since the S/C would rotate into or out of the received beam. Due to the

respective alignment choices, these two effects would mostly cancel in the sum of the test mass and the long-arm readout [TN2, TN3].

More details on the currently considered design strategies can be found in [TN3].

Alignment compensations

While the LISA design is planned to reduce the TTL coupling significantly, the full mitigation will be technologically impossible. Therefore, the residual TTL coupling will be minimised via realignment before launch [49].

A planned suppression scheme is the beam alignment mechanism, i.e. a set of optical plates which correct the alignment of the beam [49]. Such a realignment, e.g., changes the point of incidence at the detector. As I have shown in Sec. 5.2.1, the resulting changed distance between the points of incidence of the measurement and the reference beam would change the non-geometric TTL coupling. Mind that the beam offset due to the realignment of the plates will be scaled down on the detector by the employed imaging systems in between both. Also, the measured non-geometric coupling would not exactly correspond to the equations presented in Sec. 5.2.1 since the received beam is rather a flat-top and not a Gaussian beam.

The residual coupling and the coupling changes due to the launch, transfer or any long-term distortions of the optical system are currently assumed to be one order of magnitude larger than in LPF, however, significantly smaller than before the performed realignments [49, TN3].

During the mission, the wavefront errors of the transmitted beam couple with the pointing jitter. These errors are expected to increase with increasing distance from the beam's optical axis. Therefore, the beam pointing is continuously corrected [40].

Subtraction

Finally, the residual TTL coupling in-flight will be fitted and subtracted from the signal in post-processing using the DWS readout of the long-arm interferometer [49]. The suppression strategies presented above are not expected to be alternatives to the subtraction but reduce the TTL coupling to an amount that can successfully be removed from the measurement by this subtraction scheme. Since LISA will consist of three S/C each carrying two optical benches and test masses, the used model will be more complex than the LPF TTL model (Eq. (6.1)). The efficiency of this subtraction relies on how well the TTL contribution can be distinguished from the gravitational wave signals and further noises after the processing of the readout through the TDI scheme. It has proven successful in simulation [49].

6.2.3 Tilt-to-length suppression in other space-based laser interferometers

In the currently operating geodesy mission GRACE-FO, which consists of two S/C that are exchanging laser beams, TTL was predicted to be one of the main noise sources [23]. TTL is suppressed in GRACE-FO by design. I will shortly present the applied suppression scheme in App. A.2.

The space-based gravitational wave observatories planned for the future, e.g. TianQin, Taiji and DECIGO, will likely face the same TTL noise sources as LISA does. Therefore, studies not limited to LISA are ongoing [50, 51, 52]. However, an analysis of designs or alignment strategies

for the TTL reduction within one of these missions has, to the author's knowledge, not been published yet.

Part III

Tilt-To-Length Coupling Analysis for LISA Pathfinder

Chapter 7

Tilt-To-Length Coupling Models for LISA Pathfinder

TTL cross-coupling models describe how accelerations but also misalignments in orthogonal degrees of freedom couple into the interferometric Δg measurements. I introduce here two such models. On the one hand, I review the fit model which has been used during the LPF mission to subtract TTL coupling, see Sec. 6.2.1. On the other hand, I make use of the analytical TTL descriptions derived in Sec. 5 to build a comprehensive physical model. Both models are compared and applied to the mission data in the following sections.

The details of the TTL coupling fit have been extracted from scripts kindly provided by the LTP Calibration Team. They have been partially published in [17, 45]. The analytical TTL model fully relies on my analytical equations presented in Sec. 5. It is the first analytical model explaining the TTL coupling changes due to the test mass realignments for the suppression as well as in experiment (further details in Secs. 8 and 9).

7.1 The Tilt-To-Length Coupling Fit Model

The first model I apply in the following investigations is the one that has been used for TTL suppression during the LPF mission, compare Sec. 6.2.1. I apply this fit using the LISA technology package data analysis (LTPDA) toolbox in MATLAB. It uses a linear fit to estimate how the cross-accelerations (i.e. the angular and lateral accelerations) of the S/C, test mass position dependent stiffnesses and S/C accelerations along the sensitive x -axis couple into the

Summary box 7.1 | TTL noise in LPF: The fit model

The TTL noise in Δg was fitted by the linear model

$$\Delta g_{\text{xtalk}}^{\text{fit}} = C_{\varphi} \ddot{\varphi} + C_{\eta} \ddot{\eta} + C_y \ddot{y} + C_z \ddot{z} + C_{y,s} \bar{y} + C_{z,s} \bar{z} + C_{o_1} \ddot{o}_1$$

and subtracted from the measurement. The mean accelerations and offsets describe in a good approximation the corresponding degree of S/C jitter, just with an inverse sign. The coupling coefficients depend, among other things, on the test mass alignments, but their physical origin cannot be deduced from the fit result.

Δg measurements [17, 20]. I recall it here:

$$\Delta g_{\text{xtalk}} = C_\varphi \ddot{\bar{\varphi}} + C_\eta \ddot{\bar{\eta}} + C_y \ddot{\bar{y}} + C_z \ddot{\bar{z}} + C_{y,s} \bar{y} + C_{z,s} \bar{z} + C_{o_1} \ddot{o}_1. \quad (7.1)$$

The fit model only considers linear cross-coupling since higher-order coupling terms are considered to be too small. The first four input parameters describe the accelerations in the degrees of freedom orthogonal to the measurement axis (x -axis). These are given as second-order derivatives of the mean test mass rotations or displacements, i.e. \bar{j} for $j \in \{\varphi, \eta, y, z\}$. These accelerations describe, in a good approximation, the S/C jitter, just with an inverse sign. Further, the mean lateral displacement readouts of the test masses \bar{y} and \bar{z} couple into Δg via stiffnesses. Last, the jitter of the S/C along the sensitive axis does not alter the distance between the test masses but the path length of the measurement beam due to small asymmetries in the setup. These asymmetries are, for instance, the small deviations of the incoming angles at both test masses and the alteration of the beam walk on the detector due to these optical bench shifts. The coefficients C_j are the parameters to be estimated. As discussed in Sec. 6.2.1, they do not provide a physical interpretation of the TTL coupling even though they would, in theory, depend on the setup and test mass alignments. However, the fit model successfully subtracted the noise attributed to TTL coupling throughout the LPF mission.

After the test mass realignments in March 2016 (Sec. 9.1) the TTL noise contributions of the accelerations in φ and the stiffnesses terms were found to be small. Therefore, the fit model (7.1) was reduced to

$$\Delta g_{\text{xtalk}} = C_\eta \ddot{\bar{\eta}} + C_y \ddot{\bar{y}} + C_z \ddot{\bar{z}} + C_{o_1} \ddot{o}_1 \quad (7.2)$$

in later times of the mission. If not otherwise stated, I will assume the TTL model (7.1) in the following since it pictures the complete set of considerable TTL coupling terms.

When applying the fit model to the data, I use the DFACS readouts. The angular readouts of the test masses are first processed by the DMU. The DFACS angular data equal the DMU readouts with a subtracted constant offset. The corresponding data is then used to control the test mass alignment. However, the DFACS and the DMU used different clocks onboard LPF. Hence, we see tiny time shifts between both data sets. Since the GRS data, i.e. the y - and z -readouts and hence also their accelerations, have the same time stamps as the angular DFACS data, I use the respective angular readouts in the following data analysis.

This choice yields a limitation in the study of some time segments: For most timespans, 10 Hz data are only available for one of these angular data sets. For the other set of readout data, only 1 Hz data are provided. While in most noise runs (i.e. scientific measurements without any ongoing experiments), 10 Hz DFACS data are given, this is different in the long cross-talk experiment (LXE) which I will analyse in Sec. 8. In the analysis of this experiment, I can, therefore, only rely on the 1 Hz data.

Given the respective data, I use the LTPDA function ‘lscov’ to apply a least-square fit in the frequency domain. This algorithm decreases the difference between the fit model and the Δg data until the tolerance criterion of 10^{-10} is satisfied (i.e. when the previous and the current relative residuals differ by less than this number). Even though the TTL noise was coupling into the Δg readout up to 200 mHz, the fit is only applied only up to the 70 mHz. At this frequency, noise originating from the thrusters couples into the readout [53] (e.g. visible in Figs. 2.4), which would affect the cross-coupling result. The lower frequency limit in the fit is set to 2 mHz, i.e. 2 mHz below the original fit domain to cover the differential frequencies in the LXE (Sec. 8). Further, the fit procedure uses the 4-term Blackman-Harris window (BH92).

7.2 The Analytical Tilt-To-Length Coupling Model

After introducing the fit model used in LPF, I build here a comparable analytical model, which provides a physical interpretation of the coupling coefficients. Therefore, I make use of the different TTL coupling effects analytically described in Sec. 5. In that section, I only considered one reflective test mass, while there are two in LPF. A TTL effect induced by the first test mass will always also generate beam walk on the second test mass, which results in a different lateral distance between the beam's point of reflection and the centre of rotation and, therefore, a changing piston effect.

In order to construct an analytically based TTL coupling model comparable to the fit approach in Sec. 7.1, I first adapt the analytical LPF descriptions for the LPF setup (Sec. 7.2.1). This analytical result will be verified in Sec. 7.2.2 by optical simulations performed with the software IfoCAD [33, 54, 55]. Although the comparison of both shows minor inaccuracies (several magnitudes below the modelled coupling), primarily due to the series expansion in the analytical derivation, we have to handle these results with care. The model can only be as precise as our knowledge of the system and the parameters we insert. Thus, the reliability of the final analytical model is limited by our knowledge of the setup and beam parameters. I will estimate the respective error bars in Sec. 7.2.3. Finally, in Sec. 7.2.4, I transform the derived LPF LPS into a model describing the relative test mass acceleration and extract the coupling coefficients for the cross-accelerations.

7.2.1 The Tilt-To-Length Formula for LISA Pathfinder

LPF measured the distance changes between its two test masses via the x12 interferometer, see Fig. 7.1. In the following analysis, I will focus on the measurements by the detector PD12A. After the first test mass reflection, the measurement beam impinging at this diode experienced no beamsplitter transmission. However, it experienced an uneven number of beamsplitter reflections until impinging at PD12A. Each reflection mirrors the beam alignment. Therefore, the internal coordinate system of PD12A was also mirrored horizontally. The signs of the lateral beam walk on the detector also account for this sign convention.

The measurement beam underwent length changes in this setup due to both test masses' lever arm and piston effects. Furthermore, it transmitted once through the window between the optical bench and the first test mass after its first test mass reflection and twice through the window between the optical bench and the second test mass. Thus, all coupling effects induced by the jitter of the first test mass as well as the refractions through the windows between both test masses generated a beam walk on the second test mass, affecting the lateral piston coupling at this test mass, see Fig. 7.2. The reflections at the static beamsplitters and mirrors can be neglected in our analysis since it exists a coordinate transformation that transfers the beam path to a path without these reflections [P3]. However, these reflections modified the incoming angle at the second test mass and the detector. All these effects add up to the full analytical description of TTL coupling due to test mass jitter in LPF.

Further, I account for the satellite behaviour. Since the test masses were relatively stable on short time scales, we assume their misalignments to be static. On the other hand, the S/C and hence the optical bench experienced a time-dependent and comparable large angular ($\varphi_{\text{ob}}, \eta_{\text{ob}}$) and lateral ($y_{\text{ob}}, z_{\text{ob}}$) jitter. This angular jitter is equivalent to test mass rotations around the centre of mass of the satellite, i.e. approximately the centre of the optical bench, by the negative optical bench rotation angle. Also, the lateral jitter of the satellite corresponded to antiparallel shifts of the test masses.

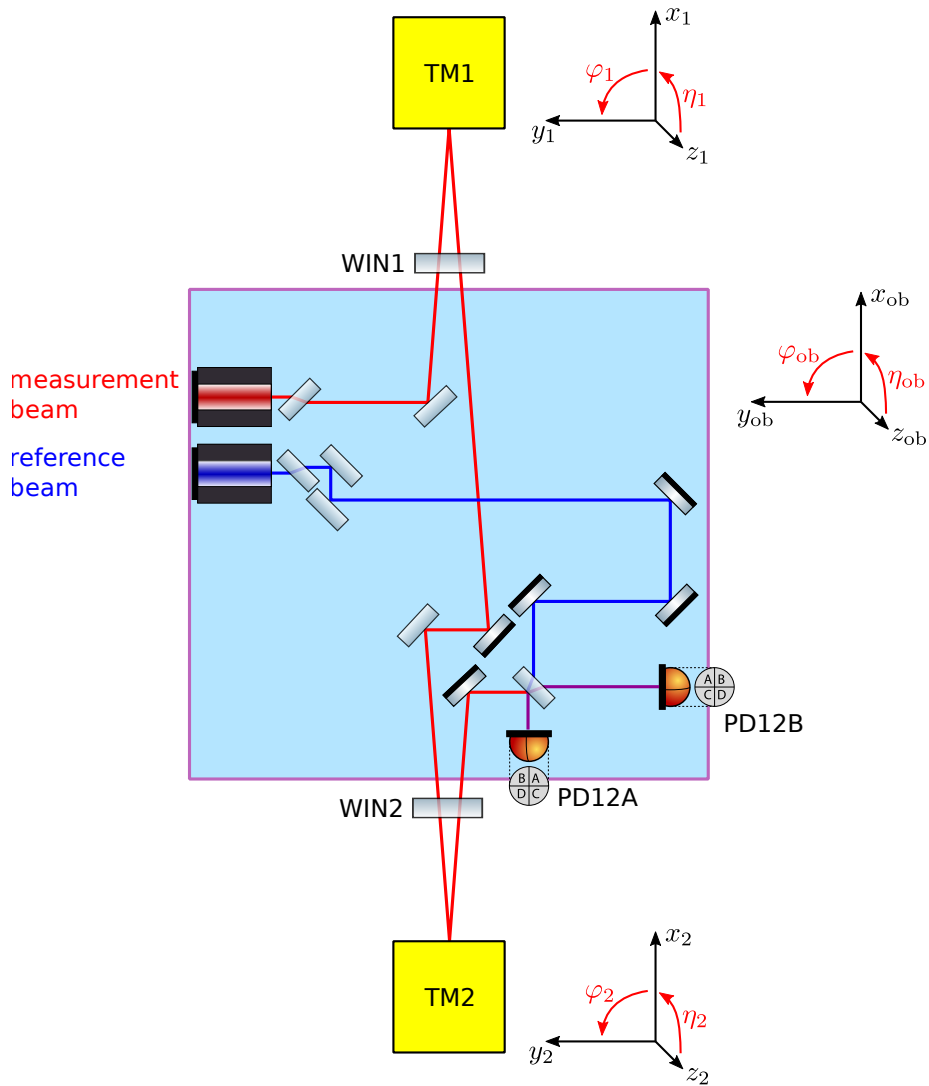


Figure 7.1: LPF setup reduced to the measurement of the differential distance between both test masses, i.e. the measurement of the x_{12} -interferometer. TM1 and TM2 denote the two test masses. They are separated from the optical bench (blue box in the centre). The measurement beam (red) passes the windows WIN1 and WIN2 before and after being reflected at the test masses. The horizontal coordinate system of the detector PD12A is mirrored to account for the uneven number of reflections of the interfering beams.

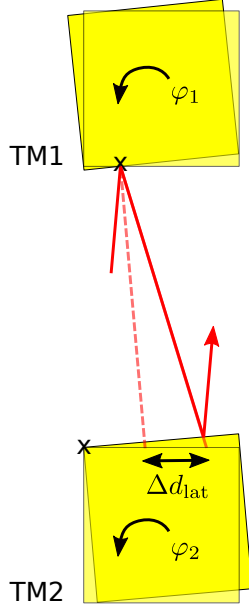


Figure 7.2: The rotation of the first test mass (TM1) induces a beam walk on the second one (TM2). Consequently, the lateral offset between the centre of rotation (black cross) and the point of reflection at TM2 changes and affects the piston coupling. The (yaw) rotation angle of the test masses are denoted φ_1 for TM1 and φ_2 for TM2.

I derived the exact equations describing the OPD and beam walk on the detector in LPF computationally via the algorithms presented in Appendix C. Moreover, I derived the non-geometric LPS via the formalism introduced in Sec. 3.2 and further discussed in Sec. 5.2 assuming quadrant photodiodes, unequal beam parameters and the computed beam walk. The characteristics of the beams and components, which were inserted into the equations, are summarised in Tab. C.1.

Since the complete analytical formula becomes very lengthy and, therefore, hardly usable for an understanding of the TTL mechanisms in LPF, I present here only the equations for inserted setup parameters (see Tab. C.1). For now, I keep the nominal rotations of the test masses as variables as they might change during the mission. To characterise the contribution of the single TTL effects to the full encountered coupling, I first present the formulas for these single effects. The single effects do not exactly add up to the total signal since this sum neglects the cross effects in the non-geometric signal contribution, compare, e.g., Eq. (5.72). However, these cross-terms are small such that also the deviation of the sum of the single effects and the complete signal is small. For further simplifications, I do not show here the coupling terms too small to significantly contribute to the overall coupling, i.e. sub-picometre terms.

The full geometric and non-geometric lever arm effects, including the rotations from both test masses and the respective beam walk on the second test mass, become

$$\begin{aligned}
 \text{OPD}_{\text{lever}}^{\text{LPF}} &\approx 117.715 \cdot 10^{-6} \frac{\text{m}}{\text{rad}} \varphi_{\text{ob}} + 14.215 \cdot 10^{-6} \frac{\text{m}}{\text{rad}} \eta_{\text{ob}} \\
 &+ 1.42592 \frac{\text{m}}{\text{rad}^2} \varphi_2 \varphi_{\text{ob}} + 1.41712 \frac{\text{m}}{\text{rad}^2} \eta_2 \eta_{\text{ob}} \\
 &- 0.71296 \frac{\text{m}}{\text{rad}^2} \varphi_{\text{ob}}^2 - 0.70856 \frac{\text{m}}{\text{rad}^2} \eta_{\text{ob}}^2, \\
 \text{LPS}_{\text{ng,lever}}^{\text{LPF}} &\approx -72.548 \cdot 10^{-6} \frac{\text{m}}{\text{rad}} \varphi_{\text{ob}} + 4.570 \cdot 10^{-6} \frac{\text{m}}{\text{rad}} \eta_{\text{ob}} \\
 &+ 0.74685 \frac{\text{m}}{\text{rad}^2} \varphi_1 \varphi_{\text{ob}} - 0.71476 \frac{\text{m}}{\text{rad}^2} \varphi_2 \varphi_{\text{ob}} + 0.74584 \frac{\text{m}}{\text{rad}^2} \eta_1 \eta_{\text{ob}} - 0.71532 \frac{\text{m}}{\text{rad}^2} \eta_2 \eta_{\text{ob}} \\
 &- 0.016042 \frac{\text{m}}{\text{rad}^2} \varphi_{\text{ob}}^2 - 0.015260 \frac{\text{m}}{\text{rad}^2} \eta_{\text{ob}}^2.
 \end{aligned} \tag{7.3}$$

$$\tag{7.4}$$

Adding both up, we find the complete lever arm effect

$$\begin{aligned}
\text{LPS}_{\text{lever}}^{\text{LPF}} &= \text{OPD}_{\text{lever}}^{\text{LPF}} + \text{LPS}_{\text{ng,lever}}^{\text{LPF}} \\
&\approx 45.167 \cdot 10^{-6} \frac{\text{m}}{\text{rad}} \varphi_{\text{ob}} + 18.785 \cdot 10^{-6} \frac{\text{m}}{\text{rad}} \eta_{\text{ob}} \\
&\quad + 0.74685 \frac{\text{m}}{\text{rad}^2} \varphi_1 \varphi_{\text{ob}} + 0.71115 \frac{\text{m}}{\text{rad}^2} \varphi_2 \varphi_{\text{ob}} + 0.74583 \frac{\text{m}}{\text{rad}^2} \eta_1 \eta_{\text{ob}} + 0.70180 \frac{\text{m}}{\text{rad}^2} \eta_2 \eta_{\text{ob}} \\
&\quad - 0.72900 \frac{\text{m}}{\text{rad}^2} \varphi_{\text{ob}}^2 - 0.72382 \frac{\text{m}}{\text{rad}^2} \eta_{\text{ob}}^2.
\end{aligned} \tag{7.5}$$

The nominal angular misalignments of the test masses, i.e. φ_1 , φ_2 , η_1 , and η_2 , can have values up to 10^{-4} rad. Therefore, the test mass independent linear S/C jitter and test mass alignment dependent terms are of the same magnitude and contribute in equal measure to the full coupling. Also, we see that the geometric and non-geometric linear coupling, particularly the coupling, which depends on the nominal test mass misalignments, are of the same magnitude.

This is different for the piston effect:

$$\begin{aligned}
\text{OPD}_{\text{piston}}^{\text{LPF}} &\approx 18.892 \cdot 10^{-6} \frac{\text{m}}{\text{rad}} \varphi_{\text{ob}} - 14.032 \cdot 10^{-6} \frac{\text{m}}{\text{rad}} \eta_{\text{ob}} \\
&\quad - 0.32898 \frac{\text{m}}{\text{rad}^2} \varphi_1 \varphi_{\text{ob}} - 0.32887 \frac{\text{m}}{\text{rad}^2} \varphi_2 \varphi_{\text{ob}} - 0.32898 \frac{\text{m}}{\text{rad}^2} (\eta_1 + \eta_2) \eta_{\text{ob}} \\
&\quad + 1.99381 [(-\varphi_1 + \varphi_2) y_{\text{ob}} + (\eta_1 - \eta_2) z_{\text{ob}}] \\
&\quad + 0.32892 \frac{\text{m}}{\text{rad}^2} \varphi_{\text{ob}}^2 + 0.32898 \frac{\text{m}}{\text{rad}^2} \eta_{\text{ob}}^2,
\end{aligned} \tag{7.6}$$

$$\text{LPS}_{\text{ng,piston}}^{\text{LPF}} \approx 0.006 \cdot 10^{-6} \frac{\text{m}}{\text{rad}} \varphi_{\text{ob}} + 16 \cdot 10^{-6} [(-\varphi_1 + \varphi_2) y_{\text{ob}} + (\eta_1 - \eta_2) z_{\text{ob}}] \tag{7.7}$$

$$\begin{aligned}
\text{LPS}_{\text{piston}}^{\text{LPF}} &= \text{OPD}_{\text{piston}}^{\text{LPF}} + \text{LPS}_{\text{ng,piston}}^{\text{LPF}} \\
&\approx 18.898 \cdot 10^{-6} \frac{\text{m}}{\text{rad}} \varphi_{\text{ob}} - 14.032 \cdot 10^{-6} \frac{\text{m}}{\text{rad}} \eta_{\text{ob}} \\
&\quad - 0.32898 \frac{\text{m}}{\text{rad}^2} \varphi_1 \varphi_{\text{ob}} - 0.32887 \frac{\text{m}}{\text{rad}^2} \varphi_2 \varphi_{\text{ob}} - 0.32898 \frac{\text{m}}{\text{rad}^2} (\eta_1 + \eta_2) \eta_{\text{ob}} \\
&\quad + 1.99382 [(-\varphi_1 + \varphi_2) y_{\text{ob}} + (\eta_1 - \eta_2) z_{\text{ob}}] \\
&\quad + 0.32892 \frac{\text{m}}{\text{rad}^2} \varphi_{\text{ob}}^2 + 0.32898 \frac{\text{m}}{\text{rad}^2} \eta_{\text{ob}}^2.
\end{aligned} \tag{7.8}$$

Here, we find that the non-geometric piston effect adds almost no TTL coupling to the overall signal. The non-geometric coupling in Eq. (7.7) is several magnitudes smaller than the geometric TTL noise (7.6). Moreover, the geometric piston effect alone describes the lateral jitter coupling, i.e. the coupling induced by the y_{ob} and z_{ob} jitter of the S/C. Also, the geometric piston effect is a strong linear angular coupling effect.

The path length signal changes due to the transmissive components are smaller than those of the lever arm and the piston effect. However, they still add considerable noise.

$$\begin{aligned}
\text{OPD}_{\text{tc}}^{\text{LPF}} &\approx -1.526 \cdot 10^{-6} \frac{\text{m}}{\text{rad}} \varphi_{\text{ob}} + 0.183 \cdot 10^{-6} \frac{\text{m}}{\text{rad}} \eta_{\text{ob}} \\
&\quad - 0.01849 \frac{\text{m}}{\text{rad}^2} \varphi_2 \varphi_{\text{ob}} - 0.01826 \frac{\text{m}}{\text{rad}^2} \eta_2 \eta_{\text{ob}} \\
&\quad + 0.00924 \frac{\text{m}}{\text{rad}^2} \varphi_{\text{ob}}^2 + 0.00913 \frac{\text{m}}{\text{rad}^2} \eta_{\text{ob}}^2,
\end{aligned} \tag{7.9}$$

$$\begin{aligned}
\text{LPS}_{\text{ng,tc}}^{\text{LPF}} &\approx 1.178 \cdot 10^{-6} \frac{\text{m}}{\text{rad}} \varphi_{\text{ob}} - 0.059 \cdot 10^{-6} \frac{\text{m}}{\text{rad}} \eta_{\text{ob}} \\
&\quad + 0.00939 \frac{\text{m}}{\text{rad}^2} (-\varphi_1 + \varphi_2) \varphi_{\text{ob}} - 0.00905 \frac{\text{m}}{\text{rad}^2} \eta_1 \eta_{\text{ob}} + 0.00906 \frac{\text{m}}{\text{rad}^2} \eta_2 \eta_{\text{ob}},
\end{aligned} \tag{7.10}$$

$$\begin{aligned}
\text{LPS}_{\text{tc}}^{\text{LPF}} &= \text{OPD}_{\text{tc}}^{\text{LPF}} + \text{LPS}_{\text{ng,tc}}^{\text{LPF}} \\
&\approx -0.348 \cdot 10^{-6} \frac{\text{m}}{\text{rad}} \varphi_{\text{ob}} + 0.124 \cdot 10^{-6} \frac{\text{m}}{\text{rad}} \eta_{\text{ob}} \\
&\quad - 0.00939 \frac{\text{m}}{\text{rad}^2} \varphi_1 \varphi_{\text{ob}} - 0.00910 \frac{\text{m}}{\text{rad}^2} \varphi_2 \varphi_{\text{ob}} - 0.00905 \frac{\text{m}}{\text{rad}^2} \eta_1 \eta_{\text{ob}} - 0.00920 \frac{\text{m}}{\text{rad}^2} \eta_2 \eta_{\text{ob}} \\
&\quad + 0.00924 \frac{\text{m}}{\text{rad}^2} \varphi_{\text{ob}}^2 + 0.00913 \frac{\text{m}}{\text{rad}^2} \eta_{\text{ob}}^2.
\end{aligned} \tag{7.11}$$

While we have seen in Sec. 5.1.3 that the transmissive components add mostly quadratic TTL coupling, this is different here. In the case of the LPF setup, we further have to consider the beam walk on the second test mass due to the transmissions between the two test masses. Due to the different refraction index of the component, the beam changes its orientation within the component and therefore is shifted with respect to the original beam behind the component. This offset is tilt-dependent since the beam's refraction angle depends on its propagation direction before the refraction. The corresponding beam walk on the second test mass changes the lateral distance between the point of reflection and the centre of rotation at the second test mass. This changed lateral distances between these two points induces linear (compare Sec. 5.1.1) TTL coupling terms in the Eqs. (7.9)-(7.11).

I also investigate the expected non-geometric coupling induced by the nominal offset between the points of incidence of the measurement and the reference beam. This is the only TTL coupling effect not included in the three coupling mechanisms discussed. We find

$$\text{LPS}_{\text{ng,other}}^{\text{LPF}} \approx 0. \tag{7.12}$$

Remarkably, there are no TTL contributions that do not originate from either of the three effects above. This can be explained by the fact that the S/C tilt angle cancels in the beam direction after the beam reflection at both test masses. Therefore, the angles of incidence of the interfering beams at the detector do not change by angular S/C jitter.

Hence the complete TTL coupling in LPF originates from the lever arm, the piston and the effect of transmissive components. It adds up to

$$\begin{aligned}
\text{OPD}^{\text{LPF}} &\approx 135.081 \cdot 10^{-6} \frac{\text{m}}{\text{rad}} \varphi_{\text{ob}} \\
&\quad - 0.32898 \frac{\text{m}}{\text{rad}^2} \varphi_1 \varphi_{\text{ob}} + 1.07857 \frac{\text{m}}{\text{rad}^2} \varphi_2 \varphi_{\text{ob}} - 0.32898 \frac{\text{m}}{\text{rad}^2} \eta_1 \eta_{\text{ob}} + 1.06988 \frac{\text{m}}{\text{rad}^2} \eta_2 \eta_{\text{ob}} \\
&\quad + 1.99381 [(-\varphi_1 + \varphi_2) y_{\text{ob}} + (\eta_1 - \eta_2) z_{\text{ob}}] \\
&\quad - 0.37479 \frac{\text{m}}{\text{rad}^2} \varphi_{\text{ob}}^2 - 0.37045 \frac{\text{m}}{\text{rad}^2} \eta_{\text{ob}}^2,
\end{aligned} \tag{7.13}$$

$$\begin{aligned}
\text{LPS}_{\text{ng}}^{\text{LPF}} &\approx -71.667 \cdot 10^{-6} \frac{\text{m}}{\text{rad}} \varphi_{\text{ob}} + 5.073 \cdot 10^{-6} \frac{\text{m}}{\text{rad}} \eta_{\text{ob}} \\
&\quad + 0.73670 \frac{\text{m}}{\text{rad}^2} \varphi_1 \varphi_{\text{ob}} - 0.70544 \frac{\text{m}}{\text{rad}^2} \varphi_2 \varphi_{\text{ob}} + 0.73578 \frac{\text{m}}{\text{rad}^2} \eta_1 \eta_{\text{ob}} - 0.70606 \frac{\text{m}}{\text{rad}^2} \eta_2 \eta_{\text{ob}} \\
&\quad + 16 \cdot 10^{-6} [(-\varphi_1 + \varphi_2) y_{\text{ob}} + (\eta_1 - \eta_2) z_{\text{ob}}] \\
&\quad - 0.01563 \frac{\text{m}}{\text{rad}^2} \varphi_{\text{ob}}^2 - 0.01486 \frac{\text{m}}{\text{rad}^2} \eta_{\text{ob}}^2,
\end{aligned} \tag{7.14}$$

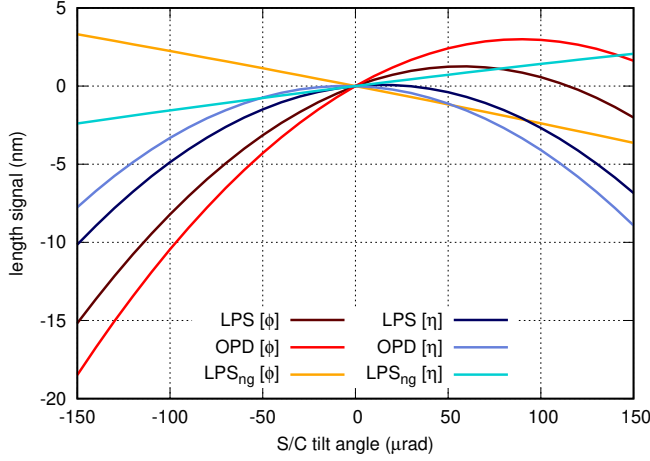


Figure 7.3: The analytically derived LPS for LPF and its geometric and non-geometric contributors for yaw and pitch jitter.

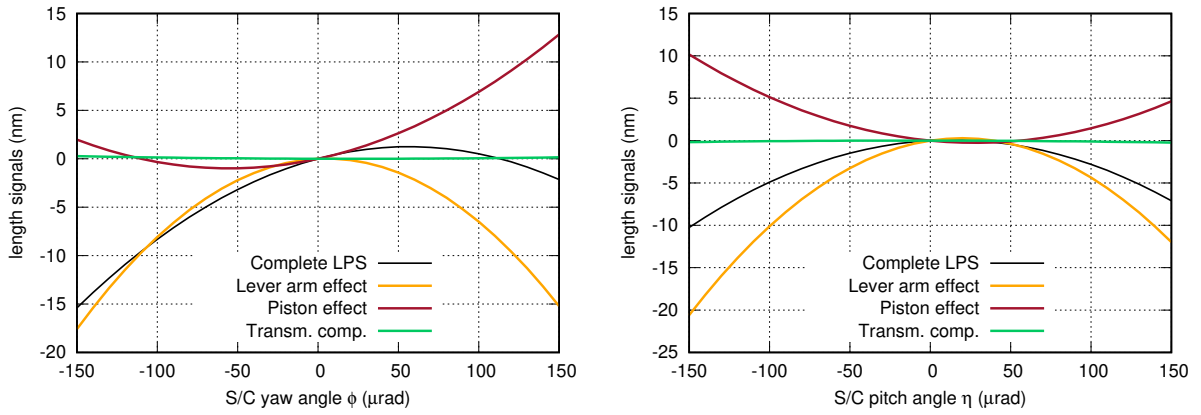


Figure 7.4: The full LPS for LPF and its contributors: the lever arm effect, the piston effect and the transmissive components. The full signal has been computed with IfoCAD. The other curves show the analytically derived contributions (equations shown in this section). Both computations include the nominal test mass alignments from Tab. C.1. The left figure shows the result for S/C jitter in yaw and the right figure for pitch jitter.

$$\begin{aligned}
\text{LPS}^{\text{LPF}} \approx & -63.415 \cdot 10^{-6} \frac{\text{m}}{\text{rad}} \varphi_{\text{ob}} + 5.073 \cdot 10^{-6} \frac{\text{m}}{\text{rad}} \eta_{\text{ob}} \\
& + 0.40772 \frac{\text{m}}{\text{rad}^2} \varphi_1 \varphi_{\text{ob}} + 0.37313 \frac{\text{m}}{\text{rad}^2} \varphi_2 \varphi_{\text{ob}} + 0.40680 \frac{\text{m}}{\text{rad}^2} \eta_1 \eta_{\text{ob}} + 0.36382 \frac{\text{m}}{\text{rad}^2} \eta_2 \eta_{\text{ob}} \\
& 1.99382 [(-\varphi_1 + \varphi_2) y_{\text{ob}} + (\eta_1 - \eta_2) z_{\text{ob}}] \\
& - 0.39042 \frac{\text{m}}{\text{rad}^2} \varphi_{\text{ob}}^2 - 0.38531 \frac{\text{m}}{\text{rad}^2} \eta_{\text{ob}}^2.
\end{aligned} \tag{7.15}$$

Typically, the test masses' angular misalignments could take any value up to the magnitude of approximately 10^{-4} rad. Therefore, the linear angular jitter terms are of the same magnitude as the terms describing the coupling of the angular test mass alignments into the readout. We further see that the geometric second-order S/C jitter coupling is more than a factor 20 larger than the associated non-geometric effect. The latter originates mainly from the lever arm effect. A comparison of the geometric, the non-geometric and the complete signal is shown in Fig. 7.3 for yaw and pitch jitter. In general, the signal dependency on the yaw angle is stronger due to the beam alignment in the xy -plane.

The lateral jitter couples strongly into the phase signal. However, it is only present in the geometric signal contribution.

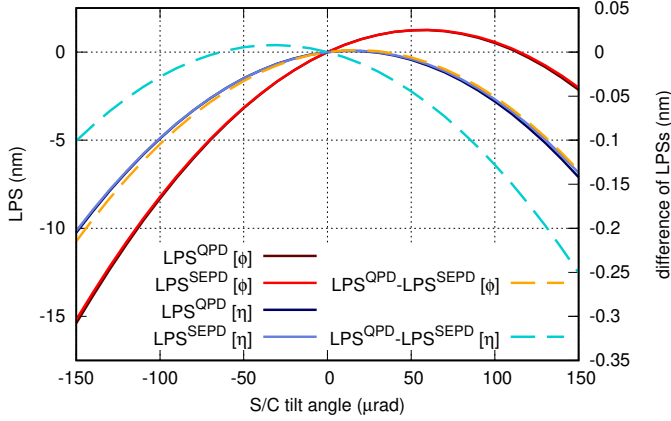


Figure 7.5: The analytically derived LPS for LPF given an SEPD or QPD for pitch and yaw jitter. The solid lines show the full signals with scaling given by the left y -axis. The dashed lines show the differences between the signals with scaling given by the right y -axis.

When we compare the three effects and their contribution to the full TTL coupling, we find the lever arm and piston effect to be dominant, see Fig. 7.4. Meanwhile, the contribution of the windows is comparatively small. The comparison between the couplings for S/C jitter in φ and η shows the most prominent differences for the piston effect. This is due to its dependency on the angle of incidence at the test masses, which is different in the xy - and the xz -plane.

In Sec. 5.2.2 we have claimed that the difference between the signal computed by an SEPD and a QPD with thin slits is small. Assuming a single element diode, the LPF signal would become

$$\begin{aligned}
 \text{LPS}^{\text{LPF,SEPD}} &\approx 60.787 \cdot 10^{-6} \frac{\text{m}}{\text{rad}} \varphi_{\text{ob}} + 5.332 \cdot 10^{-6} \frac{\text{m}}{\text{rad}} \eta_{\text{ob}} \\
 &+ 0.42877 \frac{\text{m}}{\text{rad}^2} \varphi_1 \varphi_{\text{ob}} + 0.33512 \frac{\text{m}}{\text{rad}^2} \varphi_2 \varphi_{\text{ob}} \\
 &+ 0.42637 \frac{\text{m}}{\text{rad}^2} \eta_1 \eta_{\text{ob}} + 0.32875 \frac{\text{m}}{\text{rad}^2} \eta_2 \eta_{\text{ob}} \\
 &+ 1.99382 [(-\varphi_1 + \varphi_2) y_{\text{ob}} + (\eta_1 - \eta_2) z_{\text{ob}}] \\
 &- 0.38194 \frac{\text{m}}{\text{rad}^2} \varphi_{\text{ob}}^2 - 0.37756 \frac{\text{m}}{\text{rad}^2} \eta_{\text{ob}}^2.
 \end{aligned} \tag{7.16}$$

Comparing Eq. (7.16) with Eq. (7.15) shows indeed only small differences. This is graphically confirmed by Fig. 7.5. In this figure, the solid curves show the computed signals for yaw and pitch rotations each. The dashed curves show their deviation, whose scaling is given by the right y -axis. The deviation is a factor 50 smaller than the original signal. However, it is still of the magnitude 10^{-10} m. Therefore, it depends on the amplitude of the jitter if it becomes a considerable noise contributor. In the case of the S/C jitter measured in LPF, this difference would be negligible.

7.2.2 Verification of the Model with IfoCAD

To verify the analytical description of TTL effects, I compare it with numerical simulations. Therefore, I used the C++ library IfoCAD [33, 54, 55]. IfoCAD is a program that, e.g., is used to simulate various kinds of interferometric setups and computes the signals as they would be measured in an experiment. The LPF setup has been implemented in IfoCAD by Gudrun Wanner. This implementation includes all optical components of the LPF optical bench, the windows of the vacuum chambers surrounding the test masses, as well as the test masses themselves. The latter are nominally rotated by the angles φ_{0i} , η_{0i} , $i \in \{1, 2\}$, provided in Tab. C.1. These angles correspond to the nominal alignments of the test masses during the mission (Sec. 9.1). In IfoCAD, the test mass rotations were firstly applied in yaw and secondly in pitch.

I compare the analytically derived TTL coupling with the simulation results obtained from

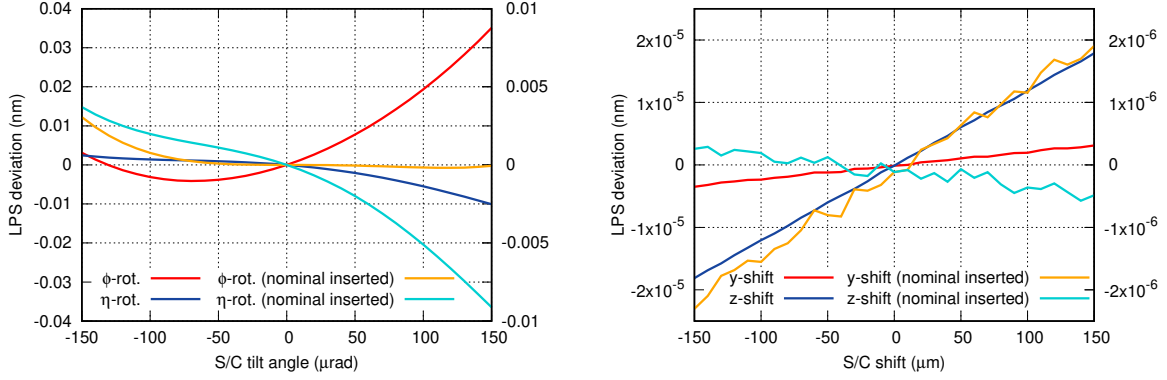


Figure 7.6: Deviation between the computed IfoCAD LPSs and the analytical result with and without primarily inserted nominal angular test mass alignments (see Tab. C.1). The red and dark blue curves show the deviation between the model Eq. (7.15) and the signal computed by IfoCAD. Their scaling corresponds to the left y -axis. The oranges and light blue curves show the deviation between the model Eq. (7.17), i.e. with primarily inserted test mass angles, and the IfoCAD signal. The scaling corresponds to the right y -axis. Left figure: angular S/C jitter. Right figure: lateral S/C jitter.

IfoCAD for various misalignment cases. Since the analytical model Eq. (7.15) is limited by several simplifications and, in particular, the series expansion up to second-order, I compute additionally its second-order correspondence with a priori inserted nominal test mass alignments. Precisely, when applying the algorithms explained in Appendix C, I insert first all parameters, including the test mass alignments. Then, I derive the series expansion of the model only with respect to the S/C jitter. This gives

$$\begin{aligned} \text{LPS}^{\text{LPF}} \approx & -136.876 \cdot 10^{-6} y_{\text{ob}} + 25.150 \cdot 10^{-6} z_{\text{ob}} + 44.149 \cdot 10^{-6} \frac{\text{m}}{\text{rad}} \varphi_{\text{ob}} + 10.479 \cdot 10^{-6} \frac{\text{m}}{\text{rad}} \eta_{\text{ob}} \\ & - 0.38964 \frac{\text{m}}{\text{rad}^2} \varphi_{\text{ob}}^2 - 0.38536 \frac{\text{m}}{\text{rad}^2} \eta_{\text{ob}}^2. \end{aligned} \quad (7.17)$$

The result Eq. (7.17) does not precisely equal the result we would find when inserting the nominal test mass alignments into Eq. (7.15). The deviations of both models from the signal computed with IfoCAD is shown in Fig. 7.6. Both models show only small differences to the numerical result. In particular, for lateral S/C jitter, the deviations are close to the machine accuracy. Not including the nominal alignments into the series expansion improves the analytical result by almost a factor of 10 for yaw and lateral jitter. For pitch rotations, the result slightly improved.

The deviation between the analytical and the numerical results for angular jitter mostly relies on the simplified assumptions for our computation. For instance, I assumed in the analytical derivation of the non-geometric effects in Sec. 5.2 that the waist size, radius of curvature and Gouy phase are constant along the detector surface. A comparison of the deviations between our analytical and the numerical model for the geometric and non-geometric contributors each (Fig. 7.7) shows that the latter is indeed two orders of magnitude larger than the deviations in the geometric comparison. Thus the assumptions for the non-geometric model explain the small remaining inaccuracies of our complete model, compare Fig. 7.6 for primarily inserted beam alignment parameters and Fig. 7.7 for the non-geometric model. The deviations in the case of the OPD are close to machine accuracy. Here, the residual depends on the definition of the three-dimensional orientations of the beams after several reflections and refractions.

In summary, the analytical model describes the occurring TTL effects very accurately. Hence, I will use it in Sec. 8 in the data analysis for the LPF mission.

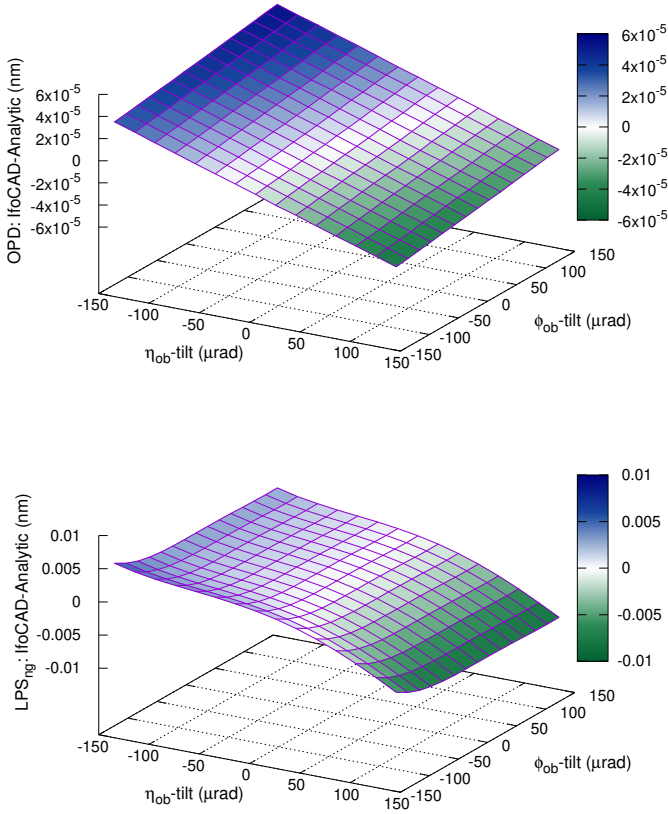


Figure 7.7: Deviation between the analytical TTL computations and the numerical results provided by IfoCAD for the LPF setup and optical bench rotations in yaw and pitch. The upper figure shows this deviation for the OPD. In the analytical computation, I used the exact model (for the computation, see Sec. C.1). The lower figure shows the deviation for the non-geometric LPS. The analytical signal is a second-order series expansion with a priori inserted nominal alignment parameters (Eq. (7.17)).

7.2.3 Stability of Coefficients

I proved in the previous section that the analytical model matches well with numerical simulations. Thus, this model is expected to describe the TTL coupling observed during mission operation well. However, it depends on the accuracy of the measurements of the setup and beam parameters (compare Tab. C.1). Here I will list the respective errors in the analytical coupling model.

In general, I assume the following parameters to be subject to measurement inaccuracies or in-flight changes of the optical system:

- (a) The lever arm lengths:

The lever arm lengths are affected by distortions of the optical bench itself but also by longitudinal displacements of the test masses. The corresponding length changes couple with the angular alignments of the test masses as well as the S/C jitter. E.g., the coefficients describing the dependency of the angular coupling coefficients on the test mass alignments would change by 2% for a 1% length change of the lever arm between both test masses. Thus, this coupling depends on the knowledge of the actual positions of the test masses. The additional longitudinal test mass displacement in-flight would be much smaller, making their effect on the coupling coefficients negligible.

- (b) The longitudinal distances between the points of reflection and the centre of S/C rotation: These distances can differ for the same reasons as in the case of the lever arm lengths. Additionally, we assumed the centre of S/C rotation to lie at the centre of the optical bench. However, the actual centre of mass can deviate from this point and dynamically

change during the mission due to fuel consumption. These errors couple into the analytical model at the same magnitude as the lever arm length changes.

- (c) The lateral distances between the points of reflection and the centres of rotation:
I only consider beam tilts to change the lateral offsets of the points of reflection at the test masses and, therefore, the piston effect. Such tilts are expected to be corrected by rotations of the test masses which makes the analysis of this coupling more complicated. However, if the beam walk would be the same at both test masses, its effect on the full TTL coupling would mostly cancel. I will further investigate this effect in Sec. 10.4.3. On the other hand, the lateral position of the S/C's centre of mass can deviate from its definition within this work. These changes would again equally affect the piston effect at both test masses, mostly cancelling it.
- (d) Window properties:
We have seen in this section that the windows in between the optical bench and the test masses are the smallest TTL contributors compared to the lever arm and the piston effect. Therefore, small changes of their thickness, alignment or refractive index would be negligible in the full TTL coupling.
- (e) The angular beam alignment:
Changes in the beam alignment would change the lateral position of the reflections points at the test masses (see (c)) but would also be (partially) corrected by test mass rotations. In general, these changes couple linearly with the S/C angular jitter, i.e. they have a small effect on the test mass alignment dependent coupling. Beam alignments will be further analysed in Sec. 10.4.
- (f) Static offsets of the beams' centres of detection:
As shown by Eq. (7.12), the static beam offsets at the detector do not affect the full TTL coupling, so neither will changes of this offset.
- (g) The beam parameters:
Measurement errors of the beam parameters couple into the TTL noise via its non-geometric contributions. The measurement accuracy of the waist size and the distance from waist is limited. According to [56], the measurement of the beam's waist was very accurate ($w_{0m} = 542 \pm 4 \mu\text{m}$, $w_{0r} = 500 \pm 8 \mu\text{m}$) yielding a maximal error of the Rayleigh range of 3.4%. The measurement of the distance between the waist and the beam source ($z_m = 142 \pm 19 \text{mm}$, $z_r = 500 \pm 8 \text{mm}$) correspond to a measurement error of 13%. However, this relative error decreases for longer beam paths yielding an error of 3.6% for the distance from waist at the diode PD12A.
- (h) Arbitrary wavefront or detector errors:
Arbitrary imperfections of the beams' wavefronts and the detector surface alter the measured LPS. These effects are not included in the analytical model but can cause a small deviation between the analytically predicted coupling and the photodiode readout.

For the following analysis of the analytical TTL coupling coefficients, I originally assumed a measurement error of the beam parameters of 10%. This error estimate relied on internal discussions. As the small measurement errors in the case of the LPF setup [56] show, this assumption was more conservative than necessary, i.e. three times as large as the measured errors. On the other hand, I neglected the uncertainties of the setup parameters, particularly the lever arm length and the location of the centre of S/C rotation. Also, I did not consider wavefront errors in this analysis. A qualitative error estimation for the complete set of input parameters is currently a work in progress.

Coefficient	$x_{Rm} (\pm 10\%)$	$x_{Rr} (\pm 10\%)$	$x_m (\pm 10\%)$	$x_r (\pm 10\%)$
φ_{ob}	-3.6%/+3.3%	-2.8%/+3.1%	-1.3%/+1.4%	-1.7%/+1.6%
$\varphi_{01} \varphi_{ob}$	-4.8%/+4.3%	-4.7%/+5.1%	-0.3%/+0.4%	-0.6%/+0.3%
$\varphi_{02} \varphi_{ob}$	-5.7%/+5.1%	-4.7%/+5.1%	-1.7%/+1.9%	-2.3%/+2.0%
φ_{ob}^2	-12.7%/+15.3%	-4.1%/+4.7%	-32.1%/+31.2%	-37.8%/+37.4%
η_{ob}	-9.3%/+8.4%	-10.5%/+11.4%	-11.1%/+11.8%	-14.0%/+13.4%
$\eta_{01} \eta_{ob}$	-4.8%/+4.3%	-4.6%/+5.1%	-0.3%/+0.4%	-0.6%/+0.4%
$\eta_{02} \eta_{ob}$	-5.6%/+5.1%	-4.6%/+5.1%	-1.7%/+1.9%	-2.3%/+2.0%
η_{ob}^2	-12.8%/+15.4%	-4.3%/+4.9%	-33.5%/+32.6%	-39.1%/+38.7%

Table 7.1: Stability of the coefficients of the analytically derived non-geometric path length signal LPS_{ng} (Eq. (7.14)) depending on the single beam parameter uncertainties.

Coefficient	$x_{Rm} (\pm 10\%)$	$x_{Rr} (\pm 10\%)$	$x_m (\pm 10\%)$	$x_r (\pm 10\%)$
φ_{ob}	-0.4%/+0.3%	$\pm 0.3\%$	-0.1%/+0.2%	$\pm 0.2\%$
$\varphi_{01} \varphi_{ob}$	-8.6%/+7.9%	-8.4%/+9.2%	-0.5%/+0.8%	-1.1%/+0.6%
$\varphi_{02} \varphi_{ob}$	-9.6%/+10.7%	-9.7%/+8.9%	-3.5%/+3.1%	-3.8%/+4.3%
φ_{ob}^2	-0.5%/+0.6%	$\pm 0.2\%$	-1.3%/+1.2%	$\pm 1.5\%$
η_{ob}	-2.4%/+2.2%	-4.2%/+3.9%	-4.4%/+4.1%	-5.0%/+5.2%
$\eta_{01} \eta_{ob}$	-8.6%/+7.9%	-8.4%/+9.2%	-0.5%/+0.8%	-1.2%/+0.6%
$\eta_{02} \eta_{ob}$	-9.8%/+10.9%	-9.8%/+9.0%	-3.6%/+3.2%	-3.9%/+4.5%
η_{ob}^2	-0.5%/+0.6%	$\pm 0.2\%$	$\pm 1.3\%$	$\pm 1.5\%$

Table 7.2: Stability of the coefficients of the analytically derived full LPS (Eq. (7.15)) depending on the single beam parameter uncertainties.

Coefficient	absolute error [m/rad ²]	relative error of LPS _{ng}	relative error of LPS
φ_{ob}	$-6.660 \cdot 10^{-6} / + 6.792 \cdot 10^{-6}$	-9.5%/+9.3%	$\pm 1.0\%$
$\varphi_{01} \varphi_{\text{ob}}$	$-0.07559 / + 0.07475$	-10.3%/+10.1%	-18.5%/+18.3%
$\varphi_{02} \varphi_{\text{ob}}$	$-0.09886 / + 0.10063$	-14.3%/+14.0%	-26.5%/+27.0%
φ_{ob}^2	$-0.01645 / + 0.01206$	-77.1%/+105.2%	$-3.1\%/4.2\%$
η_{ob}	$-0.955 \cdot 10^{-6} / + 0.939 \cdot 10^{-6}$	-18.8%/+18.5%	$-5.0\%/+4.9\%$
$\eta_{01} \eta_{\text{ob}}$	$-0.07517 / + 0.07431$	-10.2%/+10.1%	-18.5%/+18.3%
$\eta_{02} \eta_{\text{ob}}$	$-0.09804 / + 0.0998$	-14.1%/+13.9%	-26.9%/+27.4%
η_{ob}^2	$-0.01621 / + 0.01187$	-79.9%/+109.1%	$-3.1\%/+4.2\%$

Table 7.3: Error estimate of the coefficients of the analytically derived non-geometric (Eq. (7.14)) and the complete LPS (Eq. (7.15)) for beam parameter uncertainties of 10%.

The deviations in the non-geometric model for a beam parameter uncertainty of 10% are summarised in Tab. 7.1. For the assumed uncertainties, strong deviations occur in the coefficient of the linear η_{ob} -term. These are approximately equally large for deviations of each of the four beam parameters, ranging from 8% to 14%. Also, in the second-order φ_{ob}^2 - and η_{ob}^2 -terms strongly depend on the measurement accuracy of the beam parameters. In particular, for inaccuracies of the measured distances from waist, the non-geometric coefficients vary up to almost 40%. On the other hand, uncertainties of the Rayleigh ranges affect the reliability of the calculated coefficients differently. While the coefficient uncertainty for measurement uncertainties of the reference beam's Rayleigh range lies below 5%, it is about three times as large if the measurement beam's uncertainty varies by the same amount.

The OPDs do not depend on beam parameters and, therefore, are not affected by their uncertainties. When adding the geometric to the non-geometric signal contributors, we find that the stability of the coefficients of the complete model increases (i.e. the uncertainty decreases) if the respective geometric and non-geometric coefficients have the same sign and decreases (i.e. the uncertainty increases) otherwise. The results are summarised in Tab. 7.2. The terms that featured a high instability in the case of the non-geometric model are much more stable in this consideration. On the other hand, the geometric and non-geometric coefficients of the $\varphi_{0i}\varphi_{\text{ob}}$ - and $\eta_{0i}\eta_{\text{ob}}$ -terms, $i \in \{1, 2\}$, partially cancel each other in all considerations leading to a higher instability. In particular, uncertainties of the beam's Rayleigh ranges lead to an uncertainty of these coefficients by almost 10%. In conclusion, we find that the errors of the linear coupling terms depend on the measurement accuracy of the Rayleigh ranges. However, the second-order coupling terms change very little if the actual beam parameters differ from their measured values.

While analysing in Tab. 7.1 and 7.2 the uncertainty of the coefficients for deviations of single beam parameters, the errors increase when all four beam parameters simultaneously differ from their measured value. Summarised in Tab. 7.3, the relative error of the full signal is then up to three times as large as when theoretically allowing only one parameter to differ from its measurement. In the case of the non-geometric signal, the relative error is even worse. For the assumed uncertainties of the beam parameters, the quadratic coefficient can vary by about 100%.

I will use the errors summarised in Tab. 7.3 when comparing the analytical findings with the coefficients fitted to the LPF data in Sec. 8.

Summary box 7.2 | TTL noise in LPF: The analytical model

The linear analytical TTL model, describing how cross-accelerations affect the Δg measurements, is

$$\begin{aligned} \Delta g_{\text{xacc}}^{\text{ana}} \approx & -\ddot{\varphi}_{\text{ob}} \left[\text{const.} \left[\frac{\text{m}}{\text{rad}} \right] + 0.20449_{-0.03791}^{+0.03749} \frac{\text{m}}{\text{rad}} \varphi_1 + 0.18714_{-0.04958}^{+0.05047} \frac{\text{m}}{\text{rad}} \varphi_2 \right] \\ & -\ddot{\eta}_{\text{ob}} \left[\text{const.} \left[\frac{\text{m}}{\text{rad}} \right] + 0.20403_{-0.03770}^{+0.03727} \frac{\text{m}}{\text{rad}^2} \eta_1 + 0.18247_{-0.04917}^{+0.05007} \frac{\text{m}}{\text{rad}} \eta_2 \right] \\ & -\ddot{y}_{\text{ob}} \left[\text{const.} + 1.00000_{-0}^{+0} \frac{1}{\text{rad}^2} (-\varphi_1 + \varphi_2) \right] \\ & -\ddot{z}_{\text{ob}} \left[\text{const.} + 1.00000_{-0}^{+0} \frac{1}{\text{rad}} (\eta_1 - \eta_2) \right]. \end{aligned}$$

The constant terms in the coupling coefficients depend on the setup parameters but also on nominal misalignments of the test masses, whose measurement accuracy is limited by the available measurement architecture designed to measure differential angles. Thus they are fitted in the experiment.

7.2.4 TTL Noise in Δg

So far, I have derived in this section the LPS changes (Eq. (7.15)) and analysed the stability of the coupling coefficients. In order to determine the TTL noise in the Δg readout from the analytical LPS, I adapt it in two steps: I interpret the LPS for test mass displacements and differentiate the equations twice to find the corresponding acceleration.

First, I calibrate the analytically derived LPS to the LPF readouts. While the x12-interferometer onboard LPF was designed to measure the distance changes of the two test masses, the LPS provides the beams' full path length signal changes. Yet, the beam was reflected at the test masses, giving approximately two times the desired length change. Furthermore, the distance changes in LPF were defined via

$$\Delta x = x_2 - x_1, \quad (7.18)$$

which would have decreased for an increase of the test mass distances (compare Fig. 7.1). Therefore, I switch the signs in the analytical equation. Additionally accounting for the incidence angle at the second test mass, I divide Eq. (7.15) by $2 \cos(\beta_{y2})$, i.e.

$$\text{LPS}_x^{\text{LPF}} \approx -\frac{\text{LPS}^{\text{LPF}}}{2 \cos(\beta_{y2})}. \quad (7.19)$$

In the second step, in order to determine the TTL noise in the Δg readout, I take the double time-derivative of Eq. (7.19). Since we assumed the test mass alignments to be stable in short time segments, they can be treated as constants. However, the S/C jitters significantly, making its angular and lateral alignment parameters time-dependent. Neglecting second- and higher-

order terms but considering the possible errors of the analytical coupling coefficients, we find

$$\begin{aligned}
\Delta g_{\text{xacc}}^{\text{ana}} \approx & -\ddot{\varphi}_{\text{ob}} \left[+ 31.805_{-3.340}^{+3.406} \frac{\mu\text{m}}{\text{rad}} + 0.20449_{-0.03791}^{+0.03749} \frac{\text{m}}{\text{rad}^2} \varphi_1 + 0.18714_{-0.04958}^{+0.05047} \frac{\text{m}}{\text{rad}^2} \varphi_2 \right] \\
& - \ddot{\eta}_{\text{ob}} \left[+ 2.544_{-0.479}^{+0.471} \frac{\mu\text{m}}{\text{rad}} + 0.20403_{-0.03770}^{+0.03727} \frac{\text{m}}{\text{rad}^2} \eta_1 + 0.18247_{-0.04917}^{+0.05007} \frac{\text{m}}{\text{rad}^2} \eta_2 \right] \\
& - \ddot{y}_{\text{ob}} \left[+ 1.00000_{-0}^{+0} \frac{1}{\text{rad}} (-\varphi_1 + \varphi_2) \right] \\
& - \ddot{z}_{\text{ob}} \left[+ 1.00000_{-0}^{+0} \frac{1}{\text{rad}} (\eta_1 - \eta_2) \right].
\end{aligned} \tag{7.20}$$

While the DWS measurements determine angular changes very accurately, the exact alignment of the test masses with respect to the optical bench stays unknown. Relaxations and stresses of the system, e.g., due to temperature fluctuations, can change the propagations direction of the beam. This cannot be distinguished from test mass rotations by the DWS alone. Here, the GRS readout provides a second independent measurement. However, this signal can also be biased. Thus, we expect the measured test mass angles to deviate from their actual alignment. Consequently, the coefficients scaling the cross-accelerations in Eq. (7.20) gain an additional constant term, depending on these unknown alignments. Likewise, the given constant terms in the coefficients of the angular accelerations might differ and, therefore, have to be handled with care. A more conservative model would therefore be

$$\begin{aligned}
\Delta g_{\text{xacc}}^{\text{ana}} \approx & -\ddot{\varphi}_{\text{ob}} \left[\Xi_{\varphi} \left[\frac{\text{m}}{\text{rad}} \right] + 0.20449_{-0.03791}^{+0.03749} \frac{\text{m}}{\text{rad}^2} \varphi_1 + 0.18714_{-0.04958}^{+0.05047} \frac{\text{m}}{\text{rad}^2} \varphi_2 \right] \\
& - \ddot{\eta}_{\text{ob}} \left[\Xi_{\eta} \left[\frac{\text{m}}{\text{rad}} \right] + 0.20403_{-0.03770}^{+0.03727} \frac{\text{m}}{\text{rad}^2} \eta_1 + 0.18247_{-0.04917}^{+0.05007} \frac{\text{m}}{\text{rad}^2} \eta_2 \right] \\
& - \ddot{y}_{\text{ob}} \left[\Xi_y + 1.00000_{-0}^{+0} \frac{1}{\text{rad}} (-\varphi_1 + \varphi_2) \right]
\end{aligned} \tag{7.21}$$

$$\begin{aligned}
& - \ddot{z}_{\text{ob}} \left[\Xi_z + 1.00000_{-0}^{+0} \frac{1}{\text{rad}} (\eta_1 - \eta_2) \right] \\
\equiv & - (C_{\varphi}^{\text{ana}} \ddot{\varphi}_{\text{ob}} + C_{\eta}^{\text{ana}} \ddot{\eta}_{\text{ob}} + C_y^{\text{ana}} \ddot{y}_{\text{ob}} + C_z^{\text{ana}} \ddot{z}_{\text{ob}}),
\end{aligned} \tag{7.22}$$

where Ξ_i , $i = \varphi, \eta, y, z$, are constants. The constants Ξ_y and Ξ_z are unitless, and the constants of the angular coefficients Ξ_{φ} and Ξ_{η} are in units of length per radian. For the LPF mission, these constants can be fitted and counteracted by a dedicated realignment of the test masses to suppress the TTL coupling.

In the following data analysis sections, I will make use of the model Eq. (7.21). I apply it to the data from a cross-talk experiment and the engineering days in the early mission phase. Further, I will investigate the long-term behaviour of these coefficients and show that they are indeed affected by component relaxations and temperature changes.

7.2.5 Comment on the difference between my and the old models

The first TTL models for LPF relied mainly on a simplified piston model for test mass rotations and gained more complexity during the mission [57]. However, these models did not sufficiently describe the TTL noise in LPF (see Sec. 6.2.1). The model presented in this work now accounts for all TTL mechanisms introduced in Sec. 5.

Besides the complexity, we find two significant differences between my models and the model available during the LPF mission. First, my analytical model does not assume test mass but

S/C jitter, which was more dominant in LPF. Second, lateral shifts of the test masses were found not to change the distance between the S/C centre of rotation and the point of reflection at the test masses. This finding implies that the angular acceleration coefficients do not include piston terms that depend on the lateral test mass displacements.

The second perception was found during the collaboration with Larissa Tevlin in the course of her ‘Praxisprojekt’ and Bachelor’s thesis [58, 59]. It led to a breakthrough in the LPF data analysis presented in the following chapter.

Chapter 8

Analysis of the Long Cross-Talk Experiment

The long cross-talk experiment (LXE) was one of two TTL experiments performed during the LPF mission extension phase. It was designed to investigate TTL coupling from all degrees of freedom [P10].

In the following, I will first introduce the two cross-talk experiments performed during the LPF mission (Sec. 8.1). In Sec. 8.2 and Sec. 8.3, I will analyse the performance of the fit model Eq. (7.1) and the analytical model Eq. (7.21) derived in the previous chapter for the time of the LXE. Both models and their performances will be compared in Sec. 8.4. In the subsequent section 8.5, I will analyse the performance of several adaptations of the fit model and compare the results with the analytical ones. I will also describe how to use the fit model results to compute a TTL model depending on the test mass positions, as the analytical model does (Sec. 8.6). Moreover, I will extend our analysis to second-order models in Sec. 8.7. In Sec. 8.8, I will investigate how the different coupling terms contribute to the overall TTL coupling. Lastly, I will study the visibility of the TTL coupling during the LXE in the o_1 -readout (Sec. 8.9).

The analysis of the LXE data was supported by the work of Larissa Tevlin in the course of a ‘Praxisprojekt’ and her Bachelor’s thesis [58, 59]. Some of the results presented in this chapter differ slightly from her work due to the usage of different angular data (DMU vs. DFACS data, see Sec. 7.1). Additionally, my error analysis in Sec. 8.2.3 relies on a different noise run.

8.1 The Cross-Talk Experiments in LISA Pathfinder

Two cross-talk experiments were performed during the extension phase of the LPF mission [P10]. Both experiments were designed to measure TTL coupling. Firstly, the short cross-talk experiment was set up. It started on the 21st January 2017, 0:30 AM coordinated universal time (UTC), and lasted for five hours. During this time, six types of sinusoidal injections (i.e. periodically changing forces along y or z) were applied to the test masses inducing a S/C movement. The first three injections took place in the xy -plane.

1. At first, sinusoidal injections of equal frequencies and amplitudes were applied on the test masses, i.e. they were shifted parallel to each other along y . We refer to these injections as ‘in-phase’ injections. They provoked a lateral jitter of the S/C.

injection type	amplitude	frequency	duration	ramp duration	wait time
$y_1 = y_2$	0.5 μm	17 mHz	30 min	8 min	5 min
$y_1 = -y_2$	0.5 μm	12 mHz	30 min	8 min	5 min
y_1, y_2	0.3 μm	10 mHz, 17 mHz	50 min	5 min	10 min
$z_1 = z_2$	0.5 μm	5 mHz	50 min	8 min	5 min
$z_1 = -z_2$	0.5 μm	8 mHz	30 min	8 min	5 min
z_1, z_2	0.3 μm	5 mHz, 8 mHz	70 min	5 min	-

Table 8.1: Sequence of performed injections during the short cross-talk experiment (21st January 2017). The injections lasted between 30 and 70 minutes and were ramped in and out for 8 minutes. In between the injections, several minutes of waiting time were administered. Table credit: [P10]

2. In the next step, the injections were applied at the same amplitude and frequency but with different signs, i.e. the test masses moved inversely to each other. We refer to these as ‘out-of-phase’ injections. The S/C responded with angular jitter with an amplitude of 2.5 μrad .
3. At third, injections with equal amplitudes but at different frequencies were applied to both test masses. In response, the S/C shook pseudo-chaotically in y and φ .

The injection types four to six followed the same scheme in the xz -plane. Therefore, these three injections were applied along the z -axis. In addition, different injection frequencies were chosen. A summary of this experiment is given in Table 8.1.

During the short cross-talk experiment, the injections were only performed for one test mass alignment. However, we have seen in the previous chapter that the TTL coupling depends significantly on the test mass alignments. Thus, the short cross-talk experiment served as a testbed for the LXE performed two weeks later.

The LXE lasted from the 4th February 2017, 9PM UTC, until the 6th February 2017, 11PM UTC. It consisted of twelve sub-experiments. For each sub-experiment, the test masses were intentionally displaced, i.e. brought to different ‘set-points’. At these set-points, injections were applied as in the short cross-talk experiment. It was decided to perform only the set of y -injections if the set-point only included displacements relative to the initial position in y or φ , i.e. the first, fourth, sixth and seventh experiment, and vice versa for z -injections if the set-point only included displacements in z and η , i.e. the second, third, fifth and eighth experiment. A summary of all sub-experiments is given in Table 8.2. Since we are primarily interested in S/C and not test mass jitter, I will, for simplicity, omit here and in the following the index ‘0’ indicating static offsets.

#	Start time (month.day hour:minutes)	End time (month.day hour:minutes)	Set-point (Relative to initial)
1	02.04 22:02	02.05 00:08	y_1 : -30 μm
2	02.05 00:36	02.05 03:34	z_2 : 10 μm
3	02.05 04:00	02.05 07:00	z_1 : 21.6 μm
4	02.05 07:27	02.05 09:34	y_2 : -22 μm
5	02.05 10:00	02.05 13:00	η_1 : 12.1 μrad
6	02.05 13:25	02.05 15:25	φ_2 : 20 μrad
7	02.05 16:00	02.05 18:11	φ_1 : 30 μrad
8	02.05 18:35	02.05 21:34	η_2 : -20.3 μrad
9	02.05 22:05	02.06 03:27	y_1 : -10 μm , z_1 : 5 μm
10	02.06 04:32	02.06 09:35	y_1 : -20 μm , y_2 : -10 μm , z_1 : 15 μm , z_2 : 5 μm
11	02.06 10:03	02.06 15:34	y_1 : -25 μm , y_2 : -15 μm , z_1 : 20 μm , z_2 : 15 μm , φ_1 : 10 μrad , η_1 : 5 μrad
12	02.06 16:00	02.06 21:35	y_1 : -35 μm , y_2 : -25 μm , z_1 : 25 μm , z_2 : 25 μm , φ_1 : 20 μrad , η_1 : 10 μrad , φ_2 : 10 μrad , η_2 : -5 μrad

Table 8.2: Timeline of the sub-experiments within the LXE, which were performed between the 4th and 6th of February 2017. Times are given in UTC. The shown set-points were commanded relative to their initial position (discussed in Sec. 9, see Tab. 9.2). Table credit: [P10]

8.2 Modelling Tilt-To-Length Noise with the Fit Approach

The data from the LXE provide a testbed for TTL models. I will use these data in the following to analyse the performance of the fit (Eq. (7.1)) and the analytical model (Eq. (7.21)). The respective model performs well if it subtracts the measured accelerations at the injection frequencies. Both models will then be compared and discussed in Sec. 8.4. At first, I will have a close look at the fit model. It has been successfully used for the TTL noise subtraction in noise runs during the LPF mission.

8.2.1 Performance of the fit model

The performance of the fit model Eq. (7.1) is measured by the residuals after its subtraction from the Δg noise. During the LXE, the TTL noise was dominant at the injection frequencies (see Tab. 8.1). However, TTL noise is also present at higher frequencies, i.e. it is expected to couple into the Δg measurements at frequencies up to 200 mHz. The fit also considers and aims to subtract the noise at these frequencies downgrading its performance at the injection frequencies. The fit function considers the frequencies in the range from 2 mHz to 70 mHz (see Sec. 7.1). Thus, the fit model still considers noise that does not originate from the S/C injections themselves if the test masses are not perfectly aligned in the respective injection plane.

Applying the fit model to the LXE data, we find that it subtracts significant parts of the TTL noise indicated by the peaks at the injection frequencies, see exemplary Fig. 8.1 and [59]. The performance of the fit model for all twelve sub-experiments is shown in Fig. D.1.

While the noise at the frequencies of the y -injections, i.e. 10, 12 and 17 mHz, gets fully subtracted in most cases, we find a larger residual at the frequencies of the z -injections, i.e. at 5 and 8 mHz. The subtraction of the fit model from the measured Δg reduces the noise by almost one magnitude at 5 mHz and at least by 60% at 8 mHz. The worse performance for z -injections likely results from the fact that the test masses are aligned better in the xy -plane than in the xz -plane. Therefore, the fit model compensates for the cross-accelerations \ddot{z} and $\ddot{\eta}$ at higher

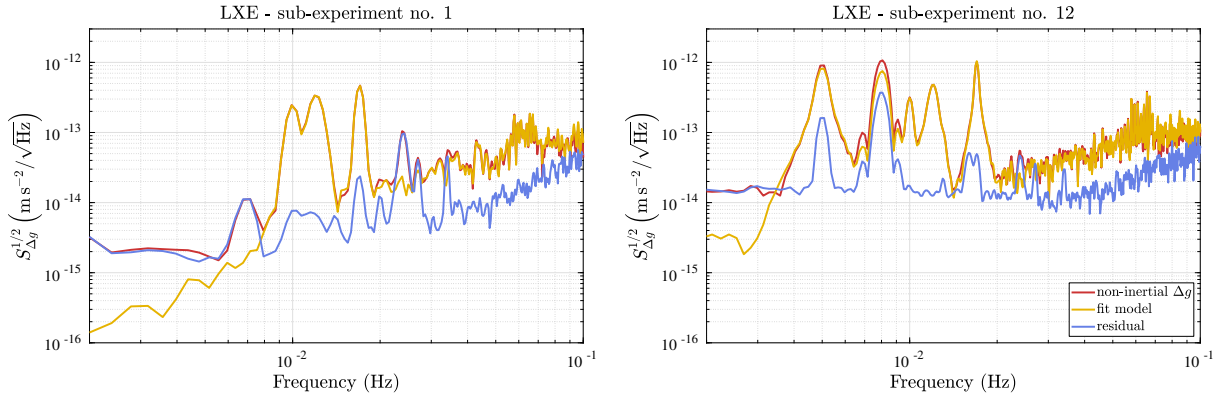


Figure 8.1: Performance of the fit model during the first (left) and the last (right) sub-experiment of the LXE. The red curve shows the ASD of the measured Δg with the inertial forces already subtracted. The yellow curve shows the respective density of the linear model fitted to the data. The blue curve shows the residual remaining after the subtraction of the fit from the measurement. The fit model subtracts the noise at the injection frequencies, i.e. 10, 12 and 17 mHz in the first sub-experiment and additionally 5 and 8 mHz in the last sub-experiment, well. The peaks at 16 mHz (only in the right figure), 24, 27 and 34 mHz correspond to multiples of the injection frequencies and are not covered by the used linear model. The same applies to the peak at the differential frequency 7 mHz (left figure).

frequencies reducing the performance at the lower injection frequencies. I will analyse the noise contributors further in Sec. 8.8.

Furthermore, we see in Fig. 8.1 that the fit does not subtract the noise at multiples or differences of the injection frequencies. These are not covered by a linear TTL model but can be modelled with a higher-order model, see Sec. 8.7. Altogether, the fit model performs well at subtracting the noise at the injection frequencies and also subtracts significant parts of the noise at higher frequencies.

8.2.2 Correlations in the fit model

When I introduced the fit model first in Sec. 6.2.1, I recalled that the model fitted for the noise subtraction in the noise runs is not the only qualified model. Quite the contrary, there are

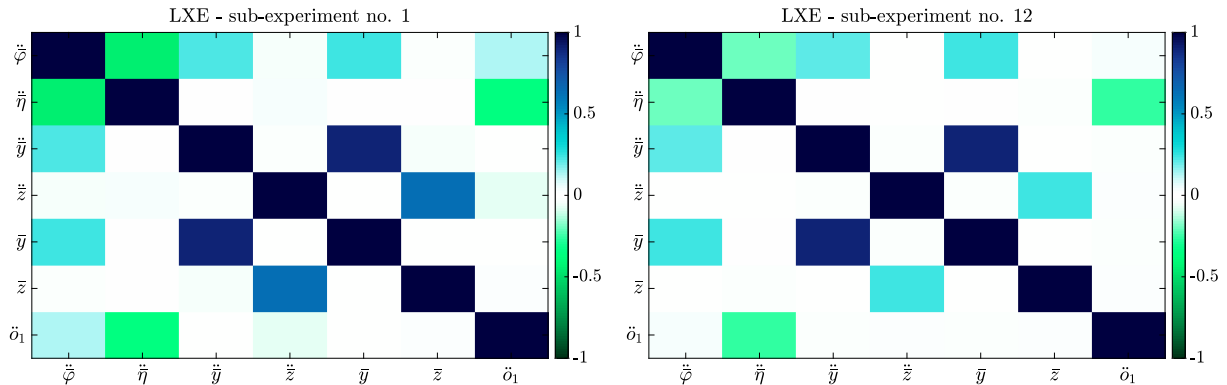


Figure 8.2: Correlations in the fit model during the first (left) and last (right) sub-experiment of the LXE. The darker the color, the stronger is correlation between the cross-coupling contributors. Naturally, the correlation along the diagonal is always 1.

sets of adequate models that subtract the TTL noise comparably well [45]. The origin of this ambiguity lies in the correlation of the quantities in the fit model. We also find correlations between the cross-coupling contributors during the LXE despite the performed injections, see exemplary Fig. 8.2 or Fig. D.2 and [59] for the full set of sub-experiments.

The cross-coupling terms \ddot{y} and \bar{y} , and accordingly \ddot{z} and \bar{z} , are highly correlated. The sinusoidal injections applied to the S/C leads to sinusoidal fluctuations of the displacement and the acceleration parameter, both differing only in amplitude and sign. Moreover, we find in all sub-experiments a considerable correlation between $\ddot{\varphi}$ and $\ddot{\eta}$. This correlation originates from a small leakage of the test mass or S/C motion from one plane into the other one. It is stronger if only y -injections are applied to the S/C and the strongest in the sub-experiments 6 and 7, where one of the test masses was rotated in yaw to its respective set-point. The in-plane correlation between $\ddot{\varphi}$ and \ddot{y} or \bar{y} is strongest in sub-experiments with set-points including displacements along the y -axis. A possible explanation for this phenomenon is the imperfection of the performed injections. However, we do not find the same correlations in the xz -plane. Instead, the correlation between $\ddot{\eta}$ and \ddot{o}_1 is higher than the correlation between $\ddot{\varphi}$ and \ddot{o}_1 in most experiments. This relation is not fully understood yet. Still, several observations could explain these correlations: We found that the torques applied to both test masses were not exactly the same. The residual difference was thereby more significant in the xy -plane [59]. Also, the different noise levels of the cross-accelerations at higher frequencies can be held responsible for the different correlations in both planes. I will further discuss this in Sec. 8.8.

Due to the found correlations, we have to handle the exact values of the fitted coefficients with care. While the complete model subtracts the TTL noise well, there are comparably well-performing models with deviating coefficients. Thus the coefficients of the found model may not necessarily correspond to an underlying physical model.

8.2.3 Error bars of the fitted coefficients

The fit of the TTL noise during the sub-experiments of the LXE yielded the coupling coefficients shown in Fig. 8.3. These are plotted with their standard error determined by the fit algorithm. This error depends on the variance of the respective fit coefficient over the considered frequency range. Thus, it increases for noisier data but can also be affected by the uncertainty of the coefficients due to correlations. In general, we see in Fig. 8.3 that the errors of the coefficients are larger for sub-experiments having only injections in the orthogonal plane. This is most significant in the case of the stiffness coefficients.

However, we find the cross-acceleration coefficients to change in experiments, in which we would expect them to stay constant based on our analytical model Eq. (7.21), i.e. in sub-experiments with lateral set-points or set-points in the orthogonal plane. The shown error bars do not cover these changes. Therefore, we chose a different method to determine the uncertainty of the fit coefficients: The variation of the fit coefficients during noise runs.

For the times of the noise runs, the coefficients are expected to stay constant. Furthermore, such noise measurements were taken throughout the entire mission time. We analysed the stability of the coupling coefficients within one noise run, which was split up into several time segments allowing the application of the fit method on each of these segments.

The variation of the fit coefficients during a noise run depicts the expected uncertainty of the fitted coefficients during the LXE best if the changes within the setup are smallest and the test mass alignments are comparable. Thus, a natural choice would either be the noise run on the 2nd of February 2017 (days of the year (DOYs) 032 and 033), which took place only one and a half

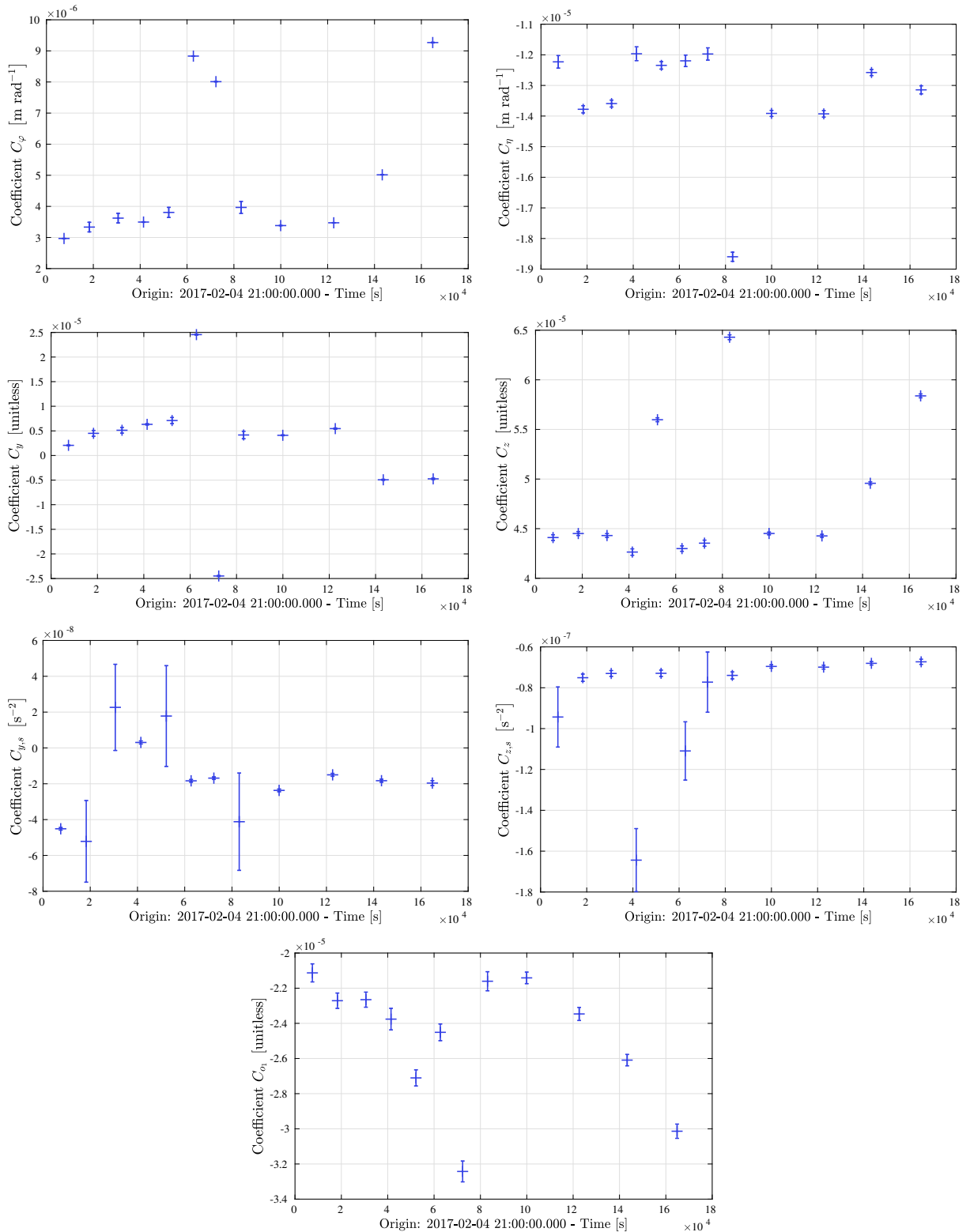


Figure 8.3: Fitted coupling coefficients for all sub-experiments of the LXE. The coefficients' error bars show the certainty of the respective coefficients derived by the fit algorithm (method introduced in Sec. 7.1).

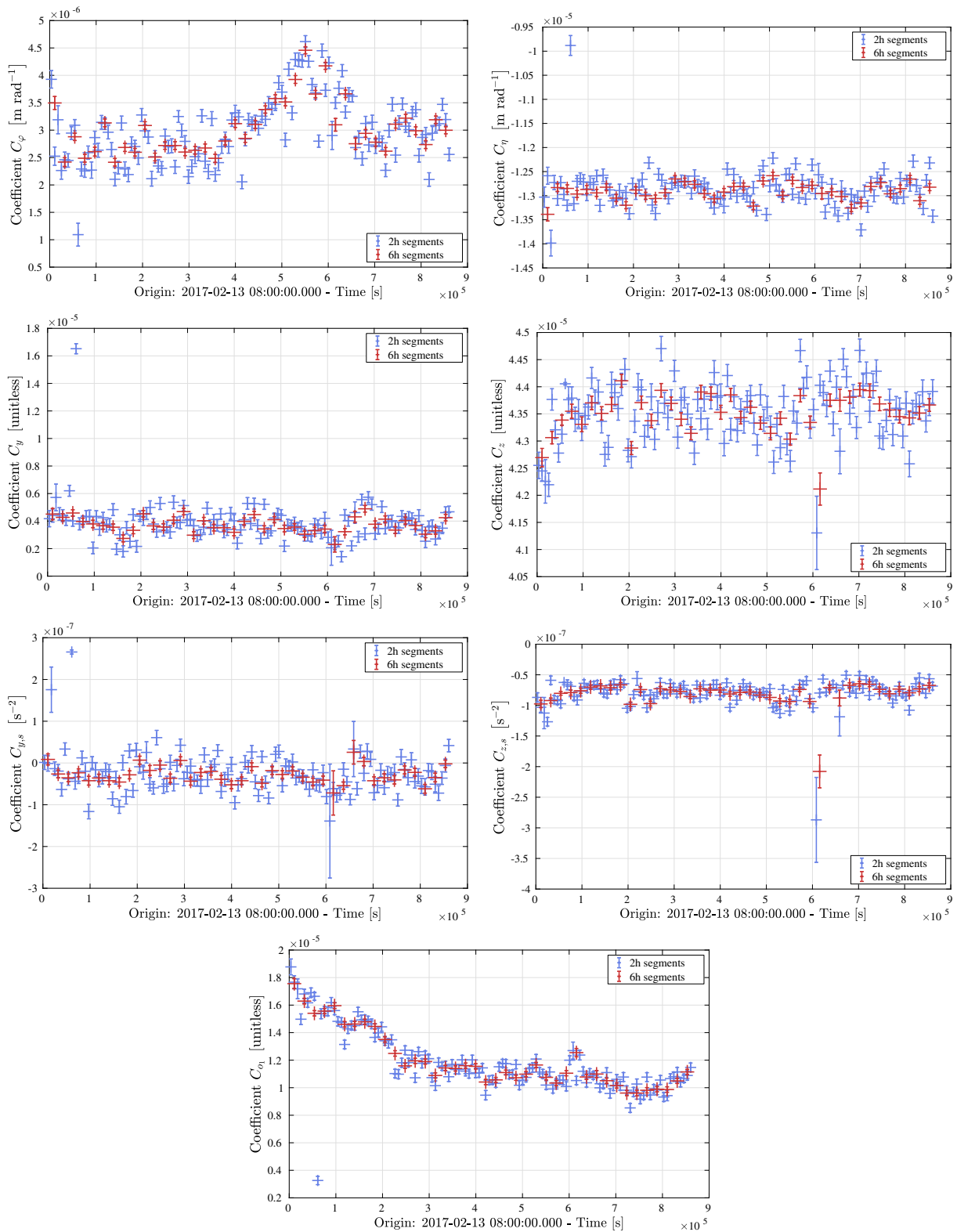


Figure 8.4: Fitted coupling coefficients for the noise run mid-February 2017. The noise run was split up into time segments of different lengths: 2 hours (blue) and 6 hours (red). The coefficients' error bars show the standard errors provided by the fit. We see that most coefficients are distributed within a certain range about a mean value. Only C_{O1} drifts.

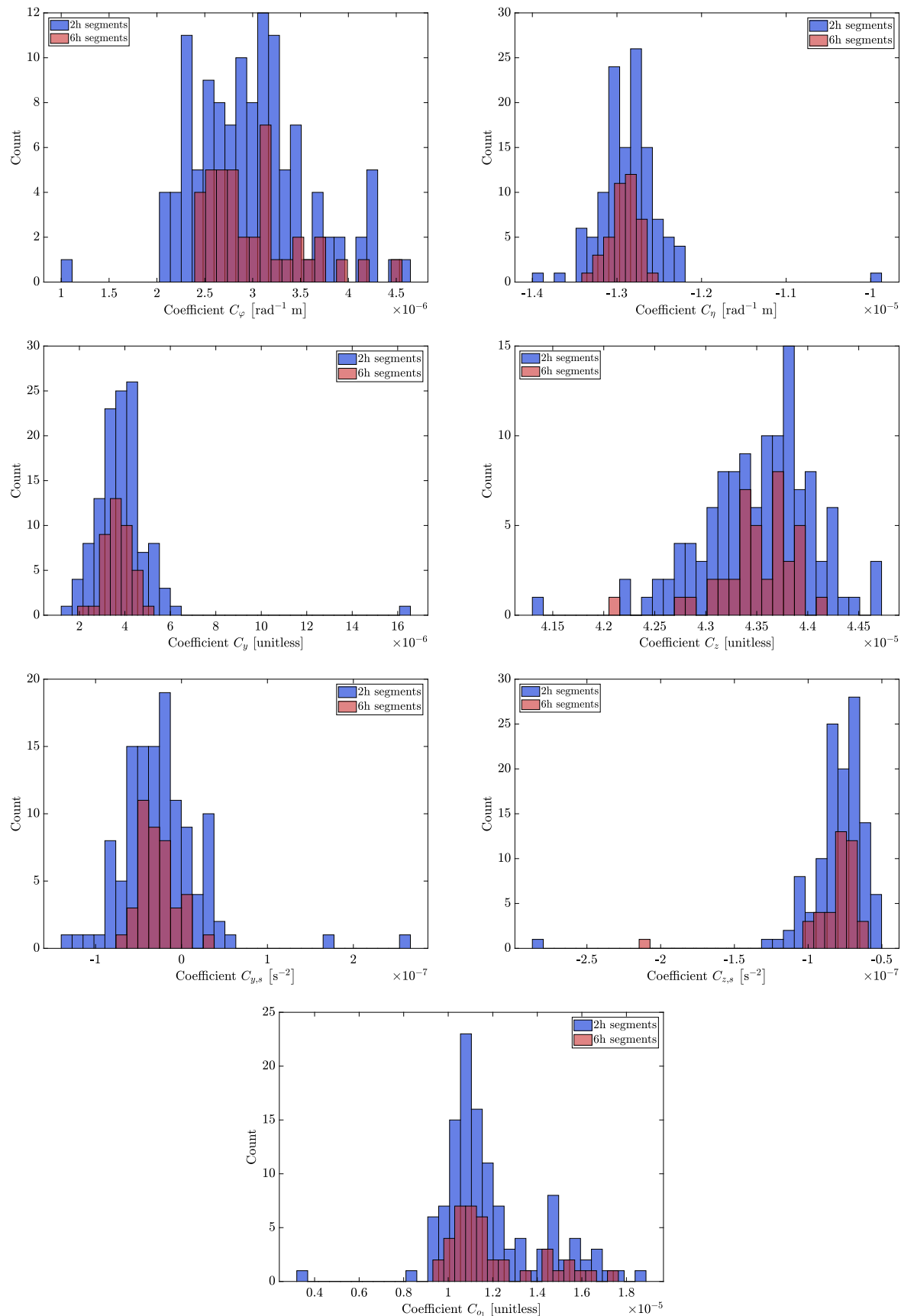


Figure 8.5: Histograms of the fitted coupling coefficients of the noise run mid-February 2017. The noise run was split up into time segments of different lengths: 2 hours (blue) and 6 hours (red). Most coefficients are roughly Gaussian distributed.

coefficient	mean value	absolute error	relative error	standard deviation
C_φ	$2.98 \mu\text{m rad}^{-1}$	$\pm 1.76 \mu\text{m rad}^{-1}$	59 %	$0.60 \mu\text{m rad}^{-1}$
C_η	$-12.86 \mu\text{m rad}^{-1}$	$\pm 2.05 \mu\text{m rad}^{-1}$	16 %	$0.40 \mu\text{m rad}^{-1}$
C_y	3.89	± 7.55	194 %	1.47
C_z	43.52	± 1.70	4 %	0.55
$C_{y,s}$	-0.02s^{-2}	$\pm 0.20 \text{s}^{-2}$	824 %	0.05s^{-2}
$C_{z,s}$	-0.08s^{-2}	$\pm 0.12 \text{s}^{-2}$	148 %	0.02s^{-2}
C_{o_1}	11.90	± 7.76	65 %	2.28

Table 8.3: The estimated errors of the fit coefficients based on the variability of the coefficients during the noise run mid-February 2017.

days before the LXE, or the long noise run starting mid-February 2017 (starting at DOY044), which was the first noise run after the cross-talk investigation. Since the preceding noise run lasted only 13 hours and 20 minutes, and, therefore, only a fraction of the time attributed to the LXE, my error estimates rely on the subsequent long noise run. A comparable analysis for the short noise run before the LXE can be found in [59].

The mid-February noise run took place from the 13th of February 2017, 8 AM UTC, until the 3rd of March, 10 PM UTC. For the error analysis, I use the data of the first ten days of the noise run, i.e. until the 23rd of February. Thus I analyse the fit coefficient behaviour over a timespan of 240 hours, which is five times as long as the LXE. The sub-experiments of the LXE lasted between two and five and a half hours. The 2-hour segments correspond to (most) of the sub-experiments where a single alignment parameter changed, while the sub-experiments with several changed alignment parameters ran for approximately 5 hours. Therefore, I divided the noise run into segments of 2 and 6 hours and computed the fit coefficients for these segments. These segments of comparable length to the LXE sub-experiments are expected to provide close results in terms of the stability of the fit.

The result of the fit is summarised in Fig. 8.4 and Fig. 8.5. We find that the fitted coupling coefficients are distributed around a mean value. Only the C_{o_1} coefficient drifts slightly. The deviations and numerical errors become smaller for longer time segments. However, the single coefficients do not coincide within their error bars throughout the noise run. This observation corresponds to our assumption that the numerical errors do not explain the uncertainties of the coefficients.

In the following sections, I will use the variability of the 2-hour segments to define appropriate uncertainties of the fit coefficients. The result is shown in Tab. 8.3. I will use the standard deviation in the following analysis to describe the errors of the fitted coefficients during the LXE. There, we are primarily interested in the uncertainties of the cross-accelerations coefficients, i.e. C_φ , C_η , C_y and C_z , since they can directly be compared with the analytically derived coefficients (see Sec. 8.3).

8.3 Modelling Tilt-To-Length Noise with the Analytical Model

The analytically derived TTL model (Eq. (7.21)) describes how the alignment of the test masses changes the coefficients of the cross-accelerations and, therefore, the cross-coupling in the Δg measurement. I discuss here how we have to modify the analytical model to make it comparable to the fit approach investigated in the previous section and analyse the performance of the resulting model.

8.3.1 Modifications of the analytical model

In the presentation of the analytical model Eq. (7.21) I did not define the constant offsets of the coupling coefficients Ξ_i since they rely on parameters that cannot be certainly determined. First, the setup itself might change due to the stresses and relaxations of the material. Second, the uncertainty of the beam parameters also affects the constant coefficients offsets. However, the corresponding error is comparably small, see Tab. 7.3. Third, the exact alignment of the test masses is unknown. Although LPF had a very accurate differential angular readout, the absolute angles of the test masses also relied on the setup (DWS readout) and the orientation of the electrode housing with respect to these masses (GRS readout). However, the test mass alignment has a significant effect on the Ξ_i 's.

Therefore, the offsets of the coupling coefficients will be determined from the fitted coupling coefficients. Precisely, I will compute the mean of the fitted coefficients taking into account only the sub-experiments whose set-points are not expected to affect the corresponding coefficients. These are the coefficients of the sub-experiments having only lateral set-points, i.e. sub-experiments 1-4, 9 and 10, or set-points only in the orthogonal plane, i.e. sub-experiments 5 and 8 for the coefficients C_φ and C_y , and sub-experiments 6 and 7 for the coefficients C_η and C_z .

Having determined the constant offsets of the cross-acceleration coefficients, we have an analytical model describing how the accelerations in the degrees of freedom orthogonal to the sensitive measurement axis couple into the Δg measurement. However, this analytical model does not include the stiffnesses and residual longitudinal S/C accelerations, whereas the fit model Eq. (7.1) does. Thus, I will fit these terms to the residual we find after subtracting the cross-accelerations from Δg . By this we find the complete analytical TTL model

$$\Delta g_{\text{xtalk}}^{\text{ana}} = \Delta g_{\text{xacc}}^{\text{ana}} + C_{y,s} \bar{y} + C_{z,s} \bar{z} + C_{o_1} \ddot{o}_1, \quad (8.1)$$

where the coefficients $C_{y,s}$, $C_{z,s}$ and C_{o_1} are computed via a fit similar to the one presented in Sec. 8.2, just reduced to these terms [59]. The stiffness terms have proven to play a minor role in the subtraction of TTL noise. However, I aim to provide here a model comparable to the fit approach Eq. (7.1), such that we can directly compare the performance of both models.

8.3.2 Performance of the analytical model

Like for the fit model, I investigate how well the analytical model subtracts the TTL noise at the injection – but also at higher – frequencies. The result is shown in Fig. 8.6 representatively for the first and the last sub-experiment and in Fig. D.3 and [59] for the complete set of sub-experiments. We find that the analytical model maps the injected noise to a reasonable degree. Also, at higher frequencies, the noise was significantly reduced. Further, the fit of the stiffness contribution together with the residual longitudinal S/C motion removed parts of the residual noise given by the difference between the measured Δg and the analytical model.

In general, the analytical model subtracts the noise at the injection frequencies in y -direction, i.e. 10, 12 and 17 mHz, better than at the frequencies of the z -injections, i.e. 5 and 8 mHz. Furthermore, like the fit model, the linear analytical model does not subtract the noise at multiples of and the differential injections frequencies. These could be covered by a higher-order model (Sec. 8.7). In some sub-experiments, the cross-coupling calculated with the analytical model underestimates the TTL noise, e.g., visible at the z -injections frequencies 5 and 8 mHz in the last experiment in Fig. 8.6. The uncertainties of the coefficients summarised in Tab. 7.2 could potentially hold responsible for these differences.

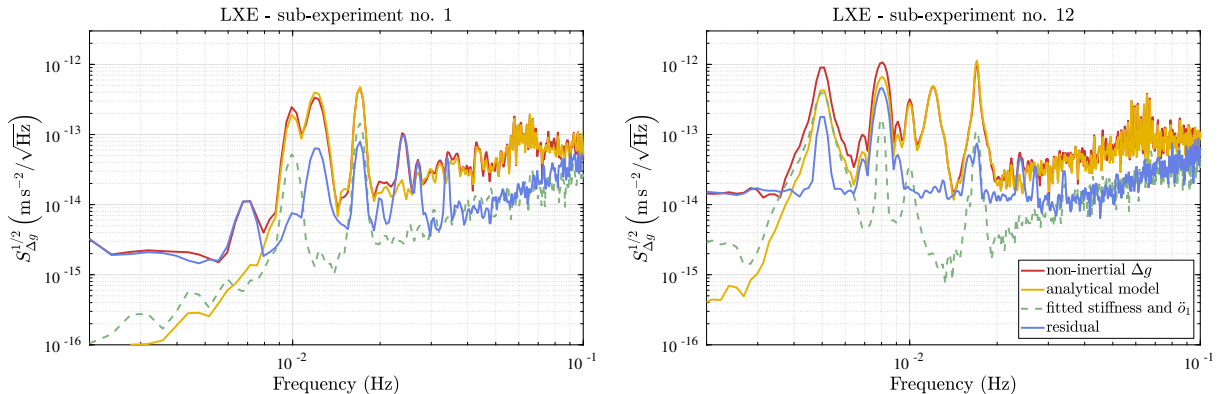


Figure 8.6: Performance of the analytical model during the first (left) and the last (right) sub-experiment of the LXE. The red curve shows the ASD of the measured Δg with the inertial forces already subtracted. The yellow curve shows the respective ASD of the linear analytical model (Eq. (7.21)). The dashed green line pictures the ASD of the stiffness terms and the cross-coupling of residual longitudinal S/C motion fitted to the difference between the measured Δg and the analytical model. The blue curve shows the residual remaining after the subtraction of the analytical model and the fitted terms from the measurement. The analytical model subtracts big parts of the noise in the injection frequencies, i.e. 10, 12 and 17 mHz in the first sub-experiment and additionally 5 and 8 mHz in the last sub-experiment. The peaks at 16 (only in right figure), 24, 27 and 34 mHz correspond to multiples of the injection frequencies and are not covered by the used linear model. The same applies to the peak at the differential frequency 7 mHz.

In summary, the performance analysis shows that the analytical model (7.21) based on the TTL coupling effects introduced in Sec. 5, models well how the TTL noise coupled into the Δg measurements. Since the analytical model also explains how the TTL coupling changed with the test mass alignments, it would have provided a powerful tool not only for the subtraction of the TTL noise but also for the estimation of a proper test mass realignment for TTL suppression.

8.4 Comparison of Both Models

In the previous Secs. 8.2 and 8.3, I have analysed the performances of the fit model Eq. (7.1) and the analytical model Eq. (8.1). Here, I will compare these performances in general and the estimated coupling coefficients in particular.

8.4.1 Comparison of the performances

In the two previous subsections, I have discussed that both models subtract significant noise at the injection frequencies. Comparing the performances of both models shown in Figs. 8.1 and 8.6, we find that the fit model performs slightly better than the analytical approach. In several sub-experiments with y -injections, e.g., the first sub-experiment, the fit model subtracts more noise at the frequencies 12 and 17 mHz. These are the injection frequencies related to angular S/C jitter in yaw. Also, the fit model subtracts the noise in sub-experiments 5 and 6, which correspond to set-points in yaw, better than the analytical model. In general, both models perform better when subtracting the noise induced by the y -injections than the noise at the z -injection frequencies. While I assume the quality of the subtraction in the analytical case to rely mostly on the measurement accuracy of the beam parameters, the fit coefficients also

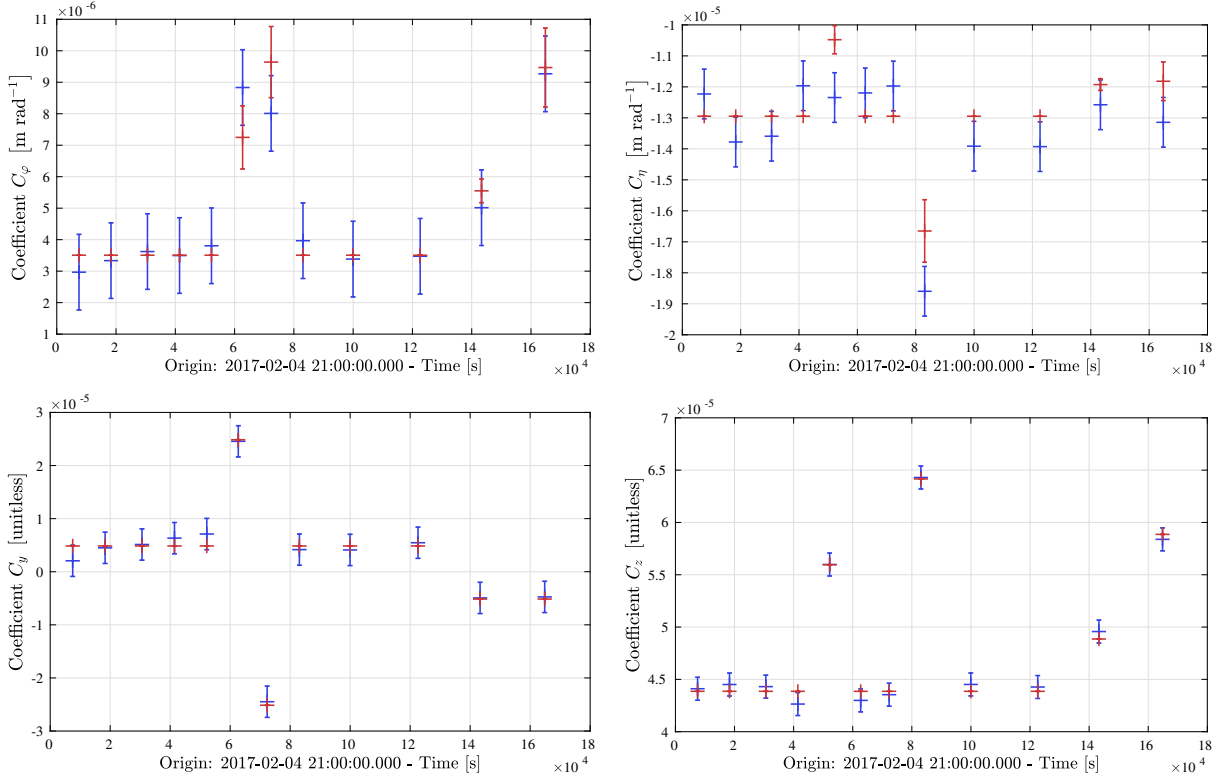


Figure 8.7: Comparison of the fitted (blue) and analytical (red) cross-acceleration coupling coefficients for all sub-experiments of the LXE. The offsets of the analytical coefficients correspond to the mean of the fitted coefficients of experiments which are assumed not to be affected by the chosen set-point. The analytical coefficients that change in correspondence to a set-point are plotted with their absolute errors (compare Eq. (7.21) and Tab. 7.3). Thus, the analytical lateral coefficients do not show any errors. However, they would lie within the errors bars of the fit if their variability does not exceed our estimation (Sec. 8.2.3). The error bars of the fitted coefficients are set to twice the standard deviation (compare Tab. 8.3), thus corresponding to a confidence interval of 95%. The lateral coupling coefficients match well. Also, the coefficients C_φ match each other within the given error bars. We find the largest deviations for the coefficients C_η .

aim to cover the noise at higher frequencies, thus degrading the performance at the injection frequencies. Any deficiencies of the fit model can also leak into the analytical model, which uses the fit result for the estimation of the constant offsets of its coupling coefficients, compare Sec. 8.3. Both models significantly reduce the noise at higher frequencies.

8.4.2 Comparison of the coupling coefficients

Having seen that both models, the analytical and the fit model, subtract significant parts of the injected TTL noise, I will compare here the derived coupling coefficients themselves. Since the analytical model performs slightly worse than the fit model at some injection frequencies, this comparison can show if the analytical coefficients tend to be under- or overestimated by the included possibly inaccurate beam parameters. On the other hand, a deviation between the coefficients of both models can also rely on the correlations between the single cross-accelerations, stiffness terms and the residual longitudinal S/C acceleration. Thus, this comparison gives us further insights into the correlations affecting the fit.

The computed coefficients are shown in Fig. 8.7. I compare the cross-acceleration coefficients here since the analytical model only covers these four coefficients. For the comparison, I adapted the error bars of both models. The errors of the fit coefficients are derived based on the variability of the respective coefficients within the noise run in mid-February 2017, see Tab. 8.3. I plot in Fig. 8.7 the coefficients' double standard deviations. These error bars correspond to a confidence interval of 95%, i.e. 95% of the respective coefficients are assumed to lie within this range. On the other hand, the constant offsets of the analytical coefficients equal the mean of the fitted coefficients considering only sub-experiments in which we do not expect the coefficients to change. Thus, this mean of the analytical coefficients should be covered by the error bars of the fit coefficients. Any deviations from this offset are accompanied with the absolute errors given in Eq. (7.21) and additionally summarised in Tab. 7.3. As discussed in Sec. 7.2.3, these errors originate from the uncertainty of the included beam parameters.

Fig 8.7 shows that the lateral cross-acceleration coefficients computed with both models match each other well. The fitted coefficients deviate only slightly for sub-experiments in which they are assumed to be stable. Moreover, the deviations of the coefficients in experiments that include angular set-points are in a good approximation the same for the fit and the analytical model. This consistency of the results for lateral cross-accelerations indicates that the correlation between the lateral stiffness terms and the lateral cross-accelerations does not significantly affect the fit result.

For the angular cross-accelerations, we find a slightly poorer agreement in Fig. 8.7. However, the coefficients C_φ of the fit and the analytical model correspond to each other within the given error bars. Note that the analytically derived coefficients in the two experiments involving a yaw rotation of the first, but not the second test mass, i.e. the 7th and 11th sub-experiment, lie above the fit result. Contrary, the analytically derived coefficient for the experiment involving a yaw rotation of the second, but not the first test mass, i.e. the 6th sub-experiment, lies below the fitted coefficient. In the last sub-experiment, both test masses undergo a yaw offset. In this case, the analytical and the fitted coefficient C_φ match well. This finding suggests that the performance of the analytical model could be improved by decreasing the factor of the alignment parameter φ_1 for C_φ in Eq. (7.21), while increasing the factor of φ_2 . These changes should relate to a suitable adaption of the measured beam parameters. However, the LXE provides not enough data for a reliable recommendation. The differences between the analytical and the fitted coefficient in Fig. 8.7 can also be coincidental or originate from a biased fit.

We find the strongest deviations between the analytical and the fit coefficients in the case of C_η . The fitted coefficients within experiments, in which they are not expected to deviate, are less stable than the C_φ coefficients. They lie above their mean in the four experiments with only y -injections and below the analytical estimate otherwise. Moreover, the fitted coefficients for the 5th and 8th sub-experiment deviate from the analytical ones. In the case of the 12th sub-experiment, their error bars barely overlap each other.

Two observations can potentially explain this effect. First, a fraction of the S/C motion in yaw also couples into the orthogonal plane, accelerating the S/C motion in pitch [58]. However, this observation does not explain the differences of the offsets for the first four experiments involving only lateral set-points and are, therefore, expected to be stable. For a quantitative analysis, I will circumvent these correlations by removing pairs of coefficients from the fit in Sec. 8.5 and investigate their effect on the fit result. Second, the systematic differences of the C_η coefficients can also be a result of TTL noise at higher frequencies. In experiments not including z -injections, the C_η coefficient would account for this noise alone, while it accounts for the noise at the injection frequencies as well as the higher frequency noise. I will further investigate these noise contributors in Sec. 8.8.

In summary, both models' lateral acceleration coefficients match very well and better than the respective angular coefficients. The strongest deviations exist for the C_η coefficient. However, in this case, we also find a similar principle behaviour of the coefficients derived by either of these models. Thus, the analytical and the fitted model describe the effects of the test mass set-points similarly, but in some cases with a different amplitude.

8.5 Adaptions of the Fit Model

I assume the differences between the angular coefficients in Fig. 8.7 to result either from the uncertainties in the measurement of the beam parameters coupling into the analytical coefficients or from noise in the data and correlations within the fit model. Within this section, I adapt the fit model in different ways to further characterise the difference between these coefficients. Similar adaptions have been previously discussed by Larissa Tevlin within her Bachelor's thesis [59]. I focus on the related changes for the angular acceleration coefficients, which showed more significant deviations than the lateral acceleration coefficients. However, I will also show the result for the lateral acceleration coefficients in all cases, ensuring an agreement of the latter.

Within this section, I will compare the fit coefficients of the original fit model Eq. (7.1) with the coefficients we find for a model excluding the lateral stiffness terms and a model excluding the residual longitudinal S/C motion. These terms were not part of the analytically derived cross-acceleration model. The removal will show if and how the correlations between the acceleration coefficients and the stiffnesses or the longitudinal S/C accelerations respectively affect the overall fit result. Furthermore, I will analyse the coefficients we find when adding angular stiffness terms to the fit model. This adaption is motivated by the fact that the fitted coefficients for the lateral accelerations, which have a stiffness counterpart, match the analytically derived coefficients well. A comparison between coefficients gained from these model fit variants is shown in Fig. 8.8. Last, I aim to investigate the correlations between the pitch and yaw accelerations by splitting the LXE into sub-experiments with y - and z -injections only.

In general, the investigation of the fitted coefficients in Fig. 8.8 shows no differences in the systematic behaviour in sub-experiments affecting the corresponding coefficients. Thus, none of the models yields an explanation of the deviations found for the C_η coefficients. I will introduce the fit model adaption separately in the following, focusing on the performances each.

The first investigated adaption of the fit model is the removal of the stiffness terms from the fit. Instead, I included the respective mean coupling coefficients $\Xi_{y,s}$ and $\Xi_{z,s}$ and subtracted them from the measurement before performing the fit:

$$\Delta g_{\text{xtalk,acc}} = \Delta g_{\text{xtalk}} - \Xi_{y,s} \bar{y} - \Xi_{z,y} \bar{z} \quad (8.2)$$

$$= C_\varphi \ddot{\varphi} + C_\eta \ddot{\eta} + C_y \ddot{y} + C_z \ddot{z} + C_{o_1} \ddot{o}_1. \quad (8.3)$$

This adaption had little effect on the coefficients, C_φ , C_y and C_z , even though the lateral stiffness terms are highly correlated to the lateral accelerations. However, by this model, I significantly decreased all C_η coefficients, see Fig. 8.8. This variation of the fit model subtracted the noise at the injection frequencies less well than the original fit model (compare Fig. D.4), in particular at the z -injections frequencies. In view of the comparison of the fitted and the analytical coefficients, this model adaption does not resolve the deviations of the respective C_η coefficients.

In the correlation analysis in Sec. 8.2.2, I have shown that the pitch acceleration and the residual longitudinal acceleration of the S/C are stronger correlated than the yaw acceleration and the longitudinal acceleration in most experiments (also compare Fig. D.2 for a complete overview).

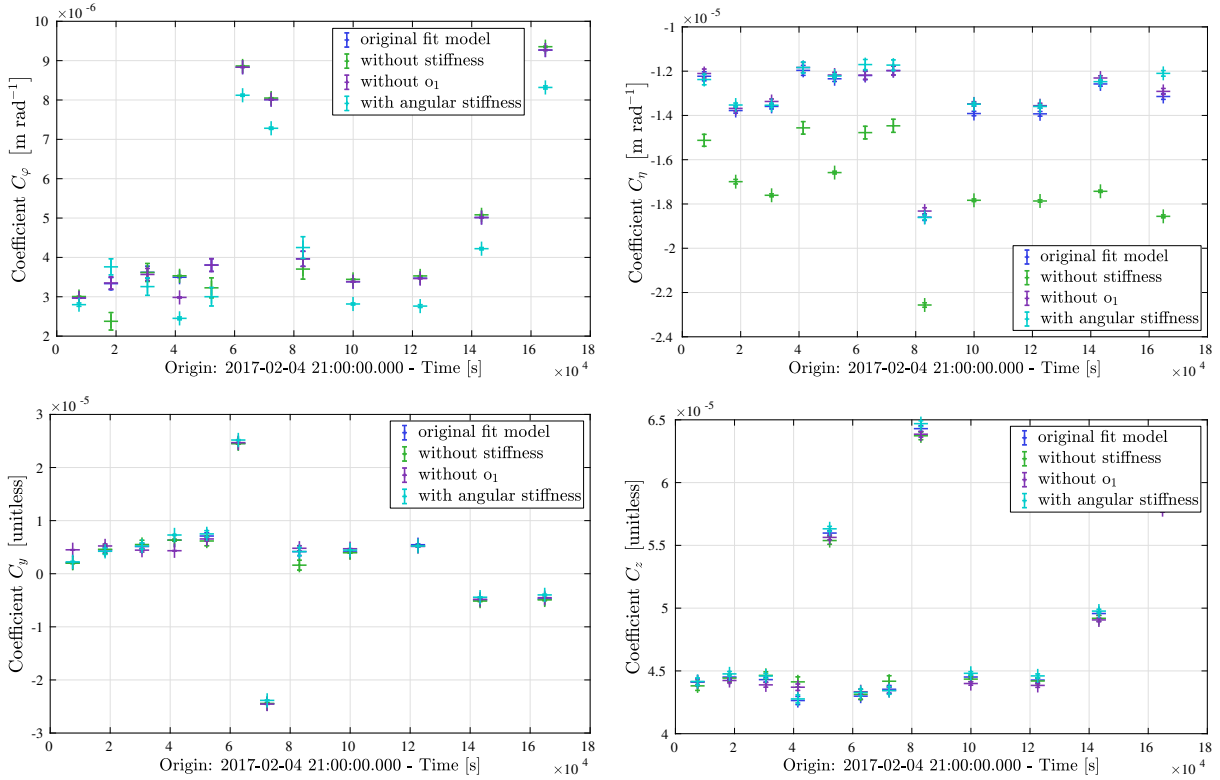


Figure 8.8: Comparison of the coupling coefficients for variants of the fit model applied to the LXE. All coefficients are shown with the error provided by the respective fit.

To analyse this correlation, I removed the longitudinal S/C acceleration from our fit without replacement:

$$\Delta g_{\text{xtalk,xtterms}} = C_\varphi \ddot{\varphi} + C_\eta \ddot{\eta} + C_y \ddot{y} + C_z \ddot{z} + C_{y,s} \bar{y} + C_{z,s} \bar{z}. \quad (8.4)$$

The cross-acceleration coefficients almost perfectly match the coupling coefficients of the original fit model. Therefore, the correlation between the pitch and the longitudinal S/C accelerations does not resolve the deviation between the analytical and the fitted coefficients. The performance of this fit model variant improved at the frequencies of the z -injections (compare Fig. D.5) while it decreased slightly at higher frequencies.

The third adaption of the original fit model contained additional angular stiffness terms, i.e.

$$\Delta g_{\text{xtalk,angstiff}} = C_\varphi \ddot{\varphi} + C_\eta \ddot{\eta} + C_y \ddot{y} + C_z \ddot{z} + C_{\varphi,s} \bar{\varphi} + C_{\eta,s} \bar{\eta} + C_{y,s} \bar{y} + C_{z,s} \bar{z} + C_{o_1} \ddot{o}_1. \quad (8.5)$$

In general, we expect that including more terms in the fit model improves the performance of the fit. The results shown in Fig. D.6 meet this expectation. In particular, this model reduced the residual noise at the z -injection frequencies. This improvement of the performance comes with minor changes of the coupling coefficients. So, the lateral and the pitch cross-acceleration coefficients stayed almost invariant under this adaption. The fitted coefficient C_φ is found to be smaller than in the fits by the other models in almost all sub-experiments. I expect this change to result from the correlation between C_φ and $C_{\varphi,s}$.

Last, I aim to break the correlation between the two angular accelerations, which has been discussed in Sec. 8.2.2. For this, I group the sub-experiments into experiments with y - and experiments with z -injections. In sub-experiments with set-points including φ or y offsets, i.e. offsets in the xy -plane, y -injections were performed. Analogously, z -injections were performed in sub-experiments with a set-point including η or z offsets, i.e. offsets in the xz -plane. The test

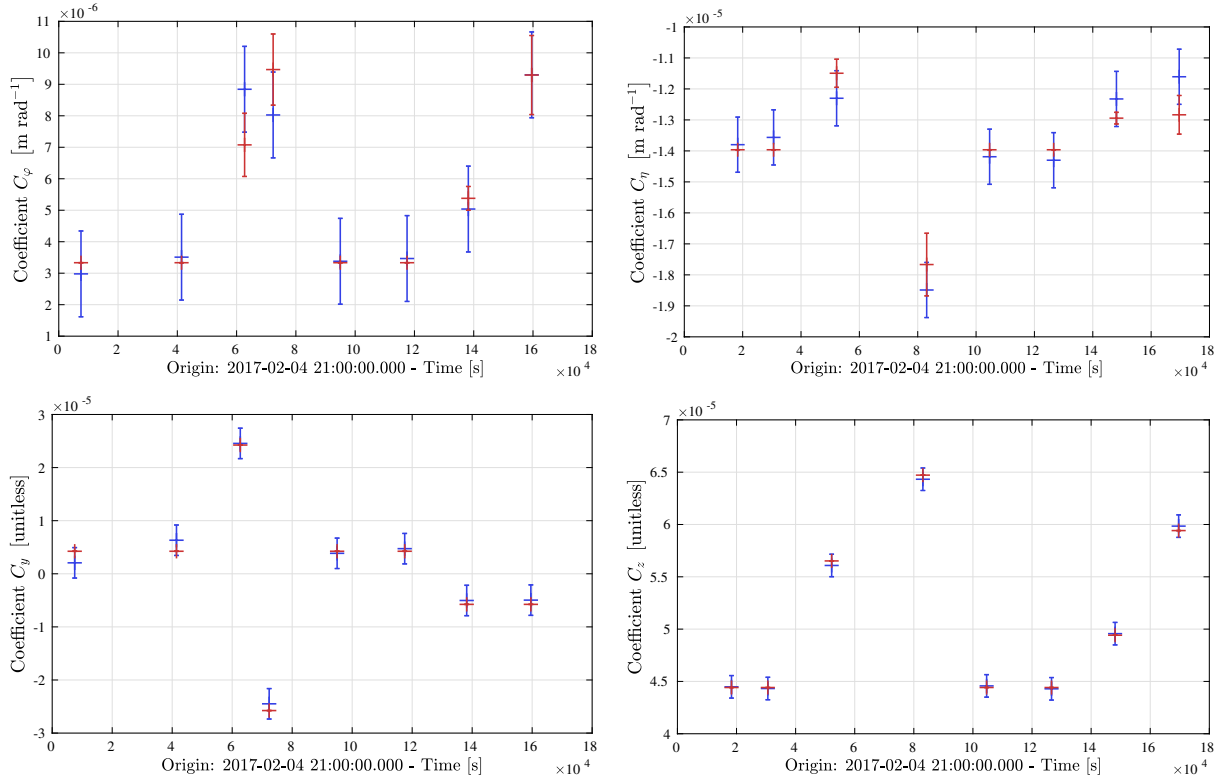


Figure 8.9: Comparison of the fitted (blue) and analytical (red) coupling coefficients for the sub-experiments of the LXE, which have been split up into time segments with y - and segments with z -injections. Only the cross-acceleration coefficients in the same plane as the performed injections have been fitted. The offset of the analytical coefficients corresponds to the mean of the fit coefficients in the four sub-experiments for which the fit has been performed and which should not be affected by the dedicated set-point in an ideal case. The error bars of the analytical coefficients in sub-experiments with angular set-points correspond to the absolute errors given in Eq. (7.21). The error bars of the fitted coefficients are twice the standard deviation of the respective coefficients and model within the noise run mid-February. In all cases, the coefficients coincide within the error bars.

masses had been aligned in both planes in the last four sub-experiments. Therefore, injections in y and afterwards in z had been applied. For my analysis, I split these four experiments between these types of injections, giving in total 16 time-segments with either y or z injections. When investigating time segments with y -injections, I subtract first the cross-acceleration coupling terms within the orthogonal plane from the Δg measurement and then fit the remaining cross-coupling terms to the difference, i.e.

$$\Delta g_{\text{xtalk},y} = \Delta g_{\text{xtalk}} - \Xi_{\eta} \ddot{\eta} - \Xi_z \ddot{z} \quad (8.6)$$

$$= C_{\varphi} \ddot{\varphi} + C_y \ddot{y} + C_{y,s} \bar{y} + C_{z,s} \bar{z} + C_{o_1} \ddot{o}_1. \quad (8.7)$$

Thereby, coefficients Ξ_{η} and Ξ_z are constants and correspond to the mean of the respective coefficients derived by the original fit model for sub-experiments where these coefficients were assumed to be stable. Analogously I define the fit model for time segments with z -injections:

$$\Delta g_{\text{xtalk},z} = \Delta g_{\text{xtalk}} - \Xi_{\varphi} \ddot{\varphi} - \Xi_y \ddot{y} \quad (8.8)$$

$$= C_{\eta} \ddot{\eta} + C_z \ddot{z} + C_{y,s} \bar{y} + C_{z,s} \bar{z} + C_{o_1} \ddot{o}_1. \quad (8.9)$$

Applying these fit models to the data, we find the coefficients shown in Fig. 8.9. The lateral cross-acceleration coefficients match as well as in the previously investigated fit models. Furthermore, the deviation between the angular cross-acceleration coefficients decreased. In the case of the pitch coefficient C_{η} , all coefficients now coincide within the given error bars. Mind that the error bars in Fig. 8.9 are slightly larger here than in the case of the original fit model, see Fig. 8.7. They have been derived with the same method as introduced in Sec. 8.2.3 considering the adapted models. Also, the performance of this adapted fit model is approximately as good as the performance of the original fit model.

The split of the models for the y - and the z -injections yields well matching analytical and fitted coefficients, see Fig. 8.9. However, the fitted coupling coefficients themselves changed very little compared to the ones shown in Fig. 8.7. The reason for the decreased deviations between both models lies in the mean offset I substitute into the analytical model and which depends on the mean of the unaffected coefficients in sub-experiments with injections in the same plane. For the C_{η} coefficient showing the most critical differences, we observed a characteristic offset of the coefficients in experiments only including y -injections. These correspondingly affected the calculated mean.

I assume this offset to originate from noise in the pitch acceleration quantity at higher frequencies and will investigate it further in Sec. 8.8. In experiments including z -injections, the fit coefficients would be less affected by this higher frequency noise since the fit also accounts for the noise at the higher frequencies. Therefore, the coefficients computed there describe the pitch acceleration coupling more accurately and yield an appropriate constant offset for the analytical coefficients.

In summary, I investigated here different variations of the fit model used during the LPF mission. The principal behaviour of the fitted coefficient was the same for all fit models. Thus, the correlations between the coupling terms cannot be held responsible for the differences we found between the analytical and the fitted C_{η} coupling coefficients. However, the coefficients match well if I split the experiments into time segments featuring only y - and others with only z -injections. Also, in this case, the improvement cannot be explained by the correlations themselves but rather with noise at higher frequencies, potentially changing this coefficient in experiments without z -injections and thereby affecting the constant offset I substitute into the analytical model.

Having now shown the correspondence of both models within their error bars and since the analytical model performs well in all 12 sub-experiments of the LXE (compare Sec. 8.4.1), I use it not only for the analysis of the LXE but also of cross-coupling effects during other time

segments of the LPF mission. These are the engineering days at the beginning of the mission and further realignments of the test masses applied in June 2016 (see Sec. 9) but also the long-term behaviour of the fit coefficients during the noise runs (see Sec. 10).

8.6 Extraction of a Tilt-To-Length Model from the Fit Results

The analysis within this chapter has shown that an analytical model exists that describes how the coupling coefficients depend on the test mass alignments. Also, we have seen that the fit and the analytical acceleration coefficients correspond to each other within their error bars (Fig. 8.7). For her ‘Praxisprojekt’ [58], Larissa Tevlin had further used the fitted coefficients of the twelve sub-experiments of the LXE to compute a model comparable to the analytical model. Since for each coefficient existed a set of twelve numbers, which depended on the four degrees of freedom for the two test masses each plus an additional constant offset, the respective system of equations was overdetermined:

$$\mathbf{M} \cdot \mathbf{p} = \mathbf{C}_j, \quad (8.10)$$

where $\mathbf{M} \in \mathbb{R}^{9 \times 12}$ contains the set-points for each sub-experiment, $\mathbf{p} \in \mathbb{R}^9$ is the vector of the coefficients we want to find, and $\mathbf{C}_j \in \mathbb{R}^{12}$, $j \in \{\varphi, \eta, y, z\}$, provides the 12 respective coupling coefficients. Larissa Tevlin successfully ran a minimiser to find the optimal coupling coefficient representations. The result showed minor differences between the fitted coefficients and the coefficients computed with the solution \mathbf{p} of the minimisation routine [58].

We conclude that it is possible to find a TTL model showing the dependency of the coupling coefficients on the test mass alignments, using only the fit results. Although this model suffers from correlations between the coefficients and noise contributions other than the injected noise, it would provide a valuable tool for the TTL noise subtraction or the TTL suppression via test mass realignments.

8.7 Application of Second-Order Models

We have seen in Figs. 8.1 and 8.6 that neither the linear fit nor the analytical model subtracts the peaks at multiples of the injection frequencies. I will show here that the double frequencies can be subtracted using a model that also considers quadratic terms. Since the applied injections were all sinusoidal, it follows from trigonometric addition theorems that quadratic models would account for these frequencies. The same would, in principle, also hold for the differential frequencies.

In order to add the quadratic terms to the analytical model, I differentiate Eq. (7.19) two times with respect to the time, as I did in Sec. 7.2.4, now including the higher-order terms. By this, we find

$$\begin{aligned} \Delta g_{\text{xacc},2\text{nd}}^{\text{ana}} &\approx \Delta g_{\text{xacc}}^{\text{ana}} \\ &- (\varphi_{\text{ob}} \ddot{\varphi}_{\text{ob}} + \dot{\varphi}_{\text{ob}}^2) \left[2 \cdot \left(-0.19581^{+0.00605}_{-0.00825} \frac{\text{m}}{\text{rad}^2} \right) \right] \\ &- (\eta_{\text{ob}} \ddot{\eta}_{\text{ob}} + \dot{\eta}_{\text{ob}}^2) \left[2 \cdot \left(-0.19325^{+0.00595}_{-0.00813} \frac{\text{m}}{\text{rad}^2} \right) \right]. \end{aligned} \quad (8.11)$$

The effect of the set-points on the analytical second-order coefficients is negligible here. The coefficients mainly depend on setup parameters, i.e. the lever arm length and the longitudinal

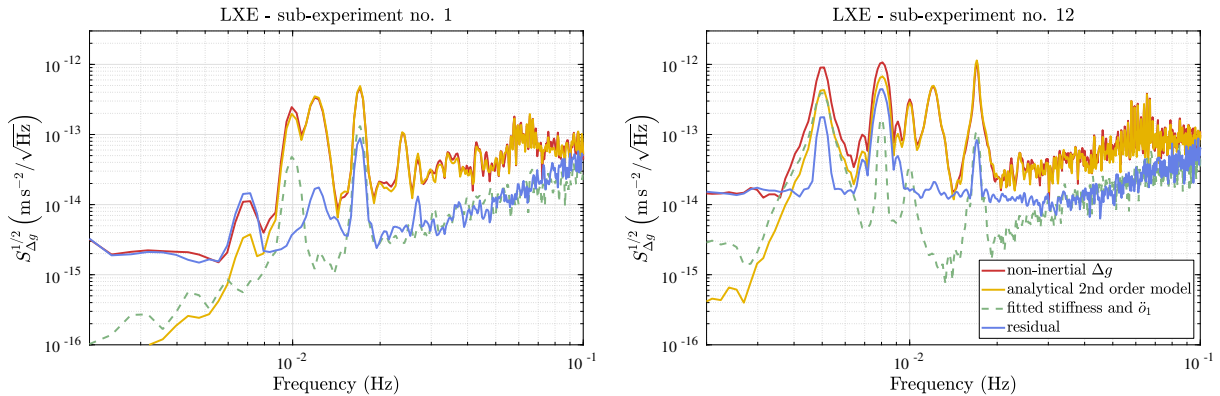


Figure 8.10: Performance of the second-order analytical model during the first (left) and the last (right) sub-experiment of the LXE. The red curve shows the ASD of the measured Δg with the inertial forces already subtracted. The yellow curve shows the respective density of the second-order analytical model. The dashed green line pictures the ASD of the stiffness terms and the residual longitudinal S/C motion fitted to the difference between the measured Δg and the analytical model. The blue curve shows the residual remaining after the subtraction of the analytical model and the fitted terms from the measurement. The analytical model subtracts significant parts of the noise in the injection frequencies, i.e. 10, 12 and 17 mHz in the first experiment and additionally 5 and 8 mHz in the last sub-experiment. Further, the second-order model subtracts the peaks at 16 mHz (only in right figure), 24, 27 and 34 mHz corresponding to multiples of the injection frequencies. The peak at the differential frequency 7 mHz (left figure) is not subtracted.

distance between the points of reflection and the centre of rotation of the optical bench. Therefore, I can make use of the analytically derived second-order coefficient when subtracting the analytical model from the data of the LXE and analysing the performance. That means, in particular, that this offset does not rely on the fit result as in the case of the constant offsets of the analytical model.

The result is exemplarily shown for the first and the last sub-experiment in Fig. 8.10. The performances for the complete set of sub-experiments are depicted in Fig. D.8. We see that in all sub-experiments, the peaks at the multiples of the injection frequencies, i.e. 16, 24, 27, and 34 mHz are well subtracted now. Thus, the second-order analytical terms provide a good description of the quadratic TTL coupling simulated by the injections.

Likewise, we can extend the linear fit model Eq. (7.1). While there are theoretically ten second-order terms yielding ten additional fit coefficients, we can reduce this number to two based on the analytical investigation. All second-order coupling coefficients except the ones scaling the quadratic ‘same plane’ angular terms denoted $C_{\varphi 2}$ and $C_{\eta 2}$ are expected to have a negligible effect on the total coupling.

This expectation is confirmed by the residuals we find after subtraction of the linear fit model, see Figs. 8.1 and D.1. There, we find residuals at the multiples of injections frequencies referring to angular S/C jitter, i.e. 13, 16, 24, 27 and 34 mHz. In contrast, no characteristic residuals at multiples of the frequencies of the in-phase injections, i.e. 10 and 20 mHz, can be seen. Thus I set up the second-order fit model

$$\begin{aligned} \Delta g_{\text{xtalk,2nd}} = & C_{\varphi} \ddot{\varphi} + C_{\eta} \ddot{\eta} + C_y \ddot{y} + C_z \ddot{z} + C_{y,s} \ddot{y} + C_{z,s} \ddot{z} + C_{o_1} \ddot{o}_1 \\ & + 2C_{\varphi 2} \left(\overline{\varphi} \ddot{\varphi} + \dot{\varphi}^2 \right) + 2C_{\eta 2} \left(\overline{\eta} \ddot{\eta} + \dot{\eta}^2 \right). \end{aligned} \quad (8.12)$$

This model subtracts the multiples of the injection frequencies well, as shown exemplarily in

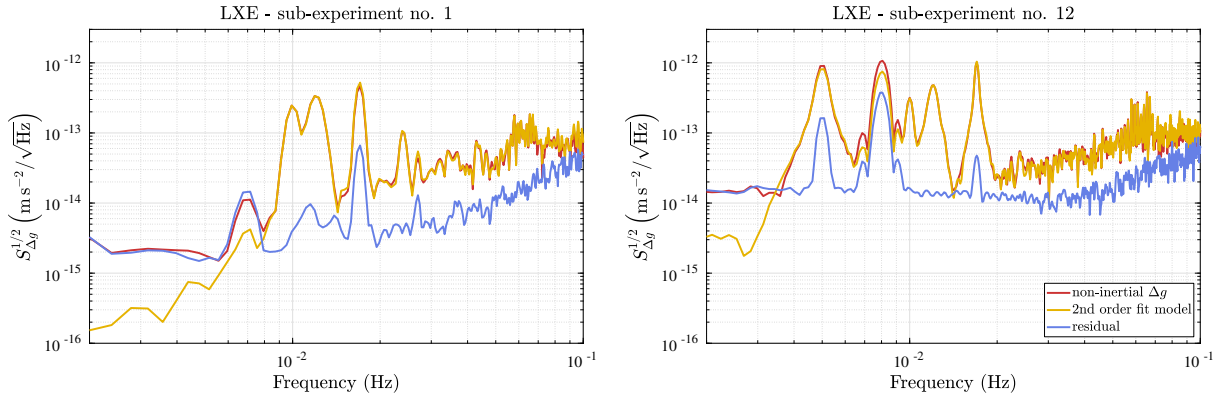


Figure 8.11: Performance of the second-order fit model during the first (left) and the last (right) sub-experiment of the LXE. The red curve shows the ASD of the measured Δg with subtracted inertial forces. The yellow curve shows the respective density of the second-order fit model. The blue curve shows the residual remaining after subtracting the fit from the measurement. The fit model removes significant parts of the noise in the injection frequencies, i.e. 10, 12 and 17 mHz in the first experiment and additionally 5 and 8 mHz in the last sub-experiment. Further, the second-order model subtracts the peaks at 16 mHz (only in the right figure), 24, 27 and 34 mHz corresponding to multiples of the injection frequencies. The peak at the differential frequency 7 mHz (left figure) is not subtracted.

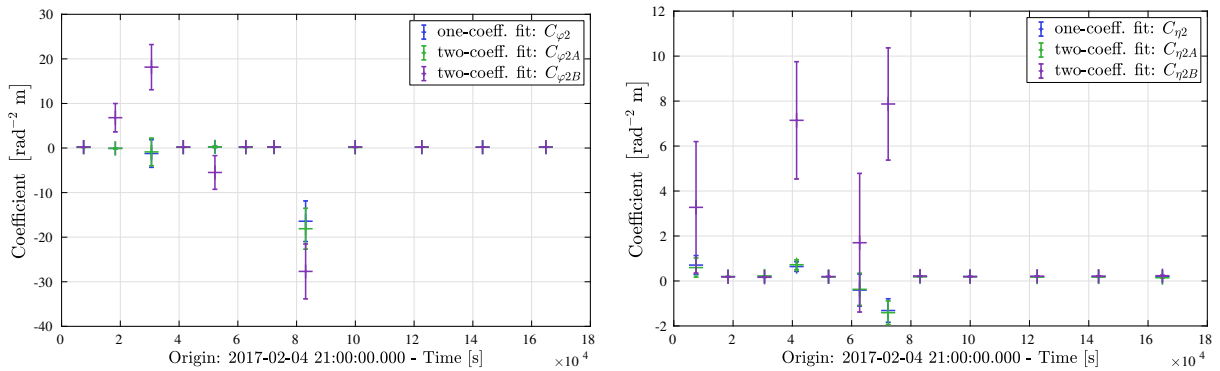


Figure 8.12: Second-order fit coefficients for the twelve sub-experiments of the LXE. Shown are the coefficients for the second-order model with one and with two coefficients for the two angular degrees of freedom each. The coefficients are approximately stable beside the outliers in experiments where no injections are performed in the respective plane. The shown error bars are the standard errors computed via the fit algorithm.

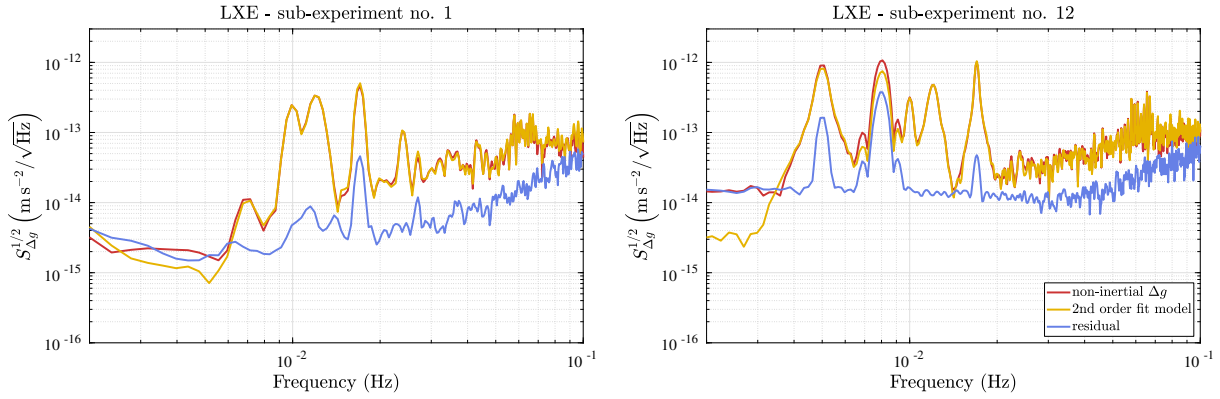


Figure 8.13: Performance of the second-order fit model with two angular coefficients each during the first (left) and the last (right) sub-experiment of the LXE. The red curve shows the ASD of the measured Δg with the inertial forces already subtracted. The yellow curve shows the respective ASD of the second-order fit model. The blue curve shows the residual remaining after the subtraction of the fit from the measurement. The fit model subtracts significant parts of the noise in the injection frequencies, i.e. 10, 12 and 17 mHz in the first experiment and additionally 5 and 8 mHz in the last sub-experiment. Further, the second-order model subtracts the peaks at 16 (only in right figure), 24, 27 and 34 mHz corresponding to multiples of the injection frequencies. The peak at the differential frequency 7 mHz (left figure) is not subtracted.

Fig. 8.11 and for the complete set of sub-experiments in Fig. D.9. Furthermore, as shown in Fig. 8.12, the fitted second-order coefficients $C_{\varphi 2}$ and $C_{\eta 2}$ deviate only slightly in the sub-experiments including injections in the respective plane. In the respective four sub-experiments with injections only in the orthogonal plane, some of these coefficients differ substantially but also have large standard errors, see Fig. 8.12. These errors correspond to the second-order input terms being very small, particularly if no injection is applied in the corresponding plane. This leads to a large variance of these coefficients and makes the result less reliable.

Neglecting the respective four coefficients with large error bars and computing the mean fit coefficient based on the eight other fitted coefficients gives

$$C_{\varphi 2} \approx 0.19382 \frac{\text{m}}{\text{rad}^2}, \quad (8.13)$$

$$C_{\eta 2} \approx 0.19328 \frac{\text{m}}{\text{rad}^2}. \quad (8.14)$$

These numbers lie within the error bounds of the analytically derived coefficients.

Investigating the performances of the second-order models, we find here and for the application of the second-order analytical model residual noise at the differential frequencies (3 and 7 mHz), which is not subtracted by the additional second-order terms. These can be removed by an adaption of the fit model. The second-order fit model improves if we fit one coefficient for each of the two second-order terms in each plane, i.e.

$$\begin{aligned} \Delta g_{\text{xtalk}, 2\text{nd}, 2} = & C_{\varphi} \ddot{\varphi} + C_{\eta} \ddot{\eta} + C_y \ddot{y} + C_z \ddot{z} + C_{y,s} \ddot{y} + C_{z,s} \ddot{z} + C_{o_1} \ddot{o}_1 \\ & + 2 C_{\varphi 2A} \overline{\varphi} \ddot{\varphi} + 2 C_{\varphi 2B} \overline{\dot{\varphi}}^2 + 2 C_{\eta 2A} \overline{\eta} \ddot{\eta} + 2 C_{\eta 2B} \overline{\dot{\eta}}^2. \end{aligned} \quad (8.15)$$

This adapted model performs as shown in Fig. 8.13 for the first and last sub-experiment and in Fig. D.10 for the complete set of sub-experiments. In particular, for the first sub-experiment, we see that the fit model Eq. (8.15) predicts the peak at 7 mHz well, i.e. at the difference of the injection frequencies 10 and 17 mHz. The same applies to the other sub-experiments, where a peak at the differential frequency is visible. The respective derived coefficients are shown in

Fig. 8.12. Like in the model with only one second-order coefficient per plane (Eq. (8.12)), the coefficients cannot be well fitted in experiments having no injection in the respective plane. In these cases, the second-order effect is too small.

Together, I have found two second-order models, both subtracting the noise at multiples of the injection frequencies well. However, only the model with two second-order coefficients for the two planes each also subtracts the noise at the differential frequencies 3 and 7 mHz. This contradicts our expectation based on the analytical model. We cannot explain this observation yet.

In summary, I have shown here for the first time that the linear fit model can be extended to a quadratic model subtracting the peaks at multiples and, if we extend it to a model with two second-order coefficients in the two planes each, also the differential frequencies. Likewise, the quadratic analytical model subtracts the peaks at the multiples of the injection frequencies. This comparison shows that the fit can be extended to higher orders if needed, not necessarily also including more fit parameters since the analytical result provides a good alternative. However, during the noise runs of the LPF mission, this was not necessary since the noise level was very low.

8.8 Noise Contributors

Within the last sections, we have seen that the fit models and the analytical approach perform better at the frequencies of the y -injections. I assumed the difference between the two planes to lie in the quality of the alignment of the test masses. To prove this assumption, I will investigate here how the cross-coupling terms contribute to the measured Δg . As shown in Fig. 8.14, the peaks at the injection frequencies originate from the cross-coupling terms in the respective plane, i.e. the peaks at 5 and 8 mHz are modelled by the $\ddot{\eta}$ -, \ddot{z} - and $\ddot{\bar{z}}$ -terms while the peaks at 10, 12 and 17 mHz are modelled by the $\ddot{\varphi}$ -, \ddot{y} - and $\ddot{\bar{y}}$ -terms. We also find that the noise at higher frequencies in all sub-experiments (Fig. D.11, see also [59]), mostly originates from the \ddot{z} -term. On average, the $\ddot{\eta}$ -term adds the second-highest noise at these frequencies.

Recalling the observations from the previous subsections, the fit model does not subtract the peaks originating from z -injections as well as the peaks originating from the injections in y . Since the fit accounts for the noise at the full frequency range considered, the high acceleration noise in \ddot{z} and $\ddot{\eta}$ is assumed to downgrade the fit performance at these frequencies. Also, this noise level can explain the systematically larger C_η coefficients in the sub-experiments only including y -injections, see Secs. 8.4 and 8.5.

These findings raise the question of the origin of the high \ddot{z} TTL coupling. Therefore, I will investigate in Sec. 9 the realignments of the test masses performed during the engineering days, which aimed to suppress the TTL coupling. Also, I will investigate the long-term behaviour of the coupling coefficients during noise runs in Sec. 10. I will show there that the TTL coupling from the accelerations in \ddot{z} indeed increased during the mission.

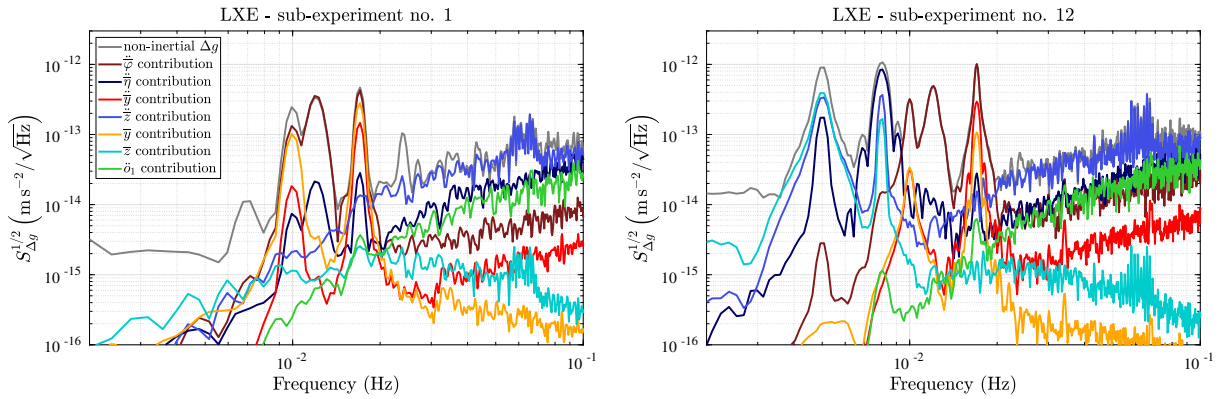


Figure 8.14: Contribution of the cross-coupling terms to the measured Δg in the first (left) and the last (right) sub-experiment of the LXE. The noise at the injection frequencies depends on the terms in the respective plane. The acceleration \ddot{z} is the most significant noise contributor at higher frequencies in all sub-experiments.

8.9 Injections in the o_1 -Readout

We have seen in the previous figures that the injections performed during the LXE are visible in the ASD of Δg as peaks at the injection frequencies. The o_1 -signal is much noisier than the Δg measurement since it also contains the longitudinal S/C jitter, which mostly cancelled in the x12-interferometer. However, some of the injections are also visible in the ASD of the o_1 -measurement, see exemplary Fig. 8.15 or Fig. D.12 for the full set of sub-experiments.

The most significant peaks are the 8 mHz peak in the case of experiments with z -injections and 17 mHz peak in the case of experiments with y -injections. Furthermore, some experiments show a small peak at 12 mHz. Recalling the injection scheme summarised in Tab. 8.1, we find that 8 and 12 mHz correspond to the angular accelerations of the S/C. The peak at 17 mHz could, on the one hand, result from the in-phase injections along y . However, the equivalent injections along z applied at 5 mHz are not visible in Fig. 8.15. On the other hand, the 17 mHz peak could originate from the accelerations of the second test mass in the pseudo-chaotic injection step. The analogue in the orthogonal plane has been applied at 8 mHz and is therefore visible in the ASD plot.

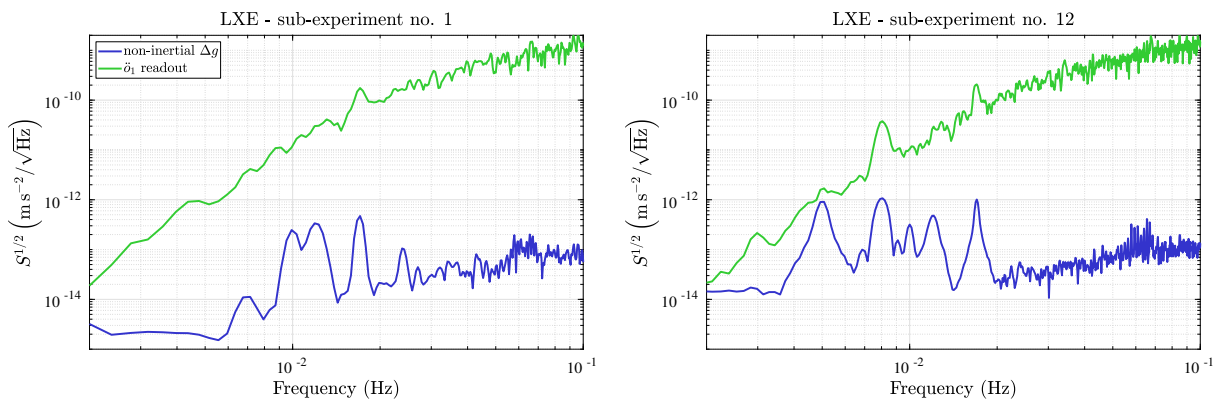


Figure 8.15: The ASD of the non-inertial Δg (blue) and the accelerations measured by the x1-interferometer \ddot{o}_1 (green) during the first and the last sub-experiment of the LXE. The injections applied to the S/C are partially also visible in the o_1 -readout.

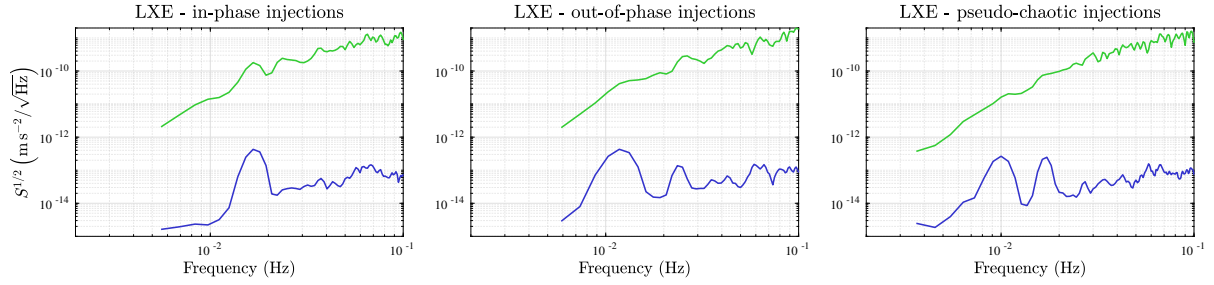


Figure 8.16: ASDs of the non-inertial Δg (blue) and the accelerations \ddot{o}_1 measured by the x1-interferometer (green) for the times of the single injections during the first sub-experiment of the LXE.

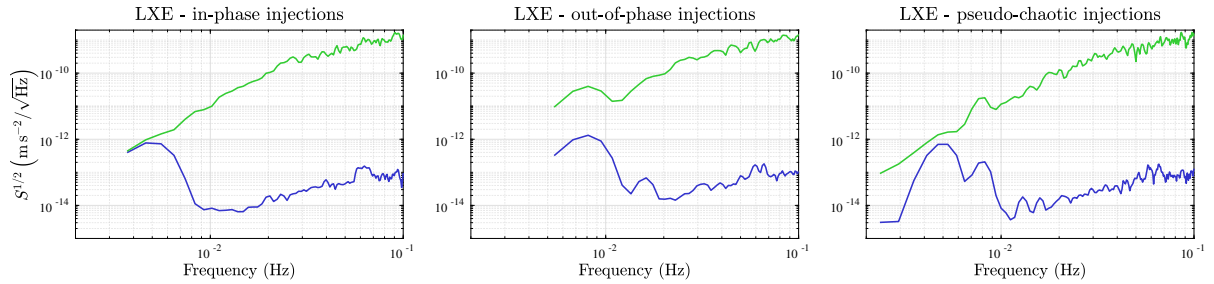


Figure 8.17: The ASDs of the non-inertial Δg (blue) and the accelerations \ddot{o}_1 measured by the x1-interferometer (green) for the times of the single injections during the second sub-experiment of the LXE.

I compare here our assumptions with the ASD plots of the o_1 -readouts for the single injections phases. Due to their short duration, the ASD computation is limited at low frequencies, partly affecting our analysis.

Fig. 8.16 shows the respective ASDs for the first sub-experiment of the LXE. Here, we find a peak at 17 mHz for the in-phase injections. Furthermore, in the case of the out-of-phase injections, the noise increase at 12 mHz is not significant. However, we encounter a peak at the double frequency, i.e. 24 mHz, which refers to the second-order coupling of the angular accelerations of the S/C. No significant peaks can be seen in the \ddot{o}_1 ASD for the third kind of injections.

For the second sub-experiment, we find in Fig. 8.17 a more significant peak at 8 mHz during the out-of-phase injections and also during the pseudo-chaotic injections. No significant peak can be seen for the in-phase injections.

In summary, we also partly see the TTL noise in the measurements of the x1-interferometer. Due to the short injection duration, a clear relation between the kind of injection and the strength of the readout cannot be deduced from the measurements. However, the visible peaks in the first and the second sub-experiment of the LXE correspond to different types of injections, which is not understood yet.

8.10 Summary of the Model Analysis

Within this section, I analysed the TTL coupling within the LXE. I applied both TTL models, the fit model and the analytical model, to the data and both are able to replicate the induced coupling.

During the mission, the fit model was usually applied to the data of the noise runs. I showed here that it is also able to subtract the large noise in the experiments. The coupling coefficients computed via the fit model provide no information about the physical source of the coupling or a strategy how to mitigate this noise. However, given a set of coupling coefficients for different known test mass positions as during the LXE, a model can be deduced that depends on the test mass alignments.

With the analytical model, I have presented for the first time a model which can coherently explain how the TTL coupling depends on the test mass alignments. An extension of this model including two additional terms also subtracts the noise at multiples of the injection frequencies. The comparison of the linear analytical with the fit model has shown a coincidence of both models coupling coefficients within their error bars. This agreement validates the derivation of a test mass position-dependent model from the fitted coupling coefficients. The investigation of the remaining difference between both models was used to analyse the limits of both models, i.e. the dependency of the analytical model on the certainty of the included parameters, and the effect of the correlation of the fit parameters and TTL noise at different frequencies on the fit result.

Chapter 9

Test Mass Realignments during the Mission

I have shown in Sec. 6.1.2 that the TTL noise in the measurements can be counteracted by realigning the test masses. Such an adaption of the test mass set-points had been performed three times during the LPF mission. At first, during the engineering days (at DOY076) in March 2016 and later at two days in June 2016 (DOY171 and DOY177) [P10, 60]. Here, I will analyse the performed realignments and compare them with the expectations based on the analytical TTL model Eq. (7.21).

The analysis within this section relies entirely on my analytical model (7.21), which I apply for the first time on the data before and after the engineering days and additional times of test mass realignments.

9.1 Engineering Days

At the beginning of the mission phase, TTL was the largest noise contributor between 20 and 200 mHz (compare Fig. 6.2). In order to find the optimal test mass orientations, several injections and rotations have been performed during the engineering days taking place from the 14th to the 17th of March 2016 [P10, 60]. These injections split between either in- or out-of-phase injections in the y - or z -direction and differed in amplitude, frequency and duration, see Tab. 9.1. For each of the injection timespans, the TTL coupling model Eq. (7.1) can be fitted, showing how the coefficients change with respect to the performed angular realignments of the test masses, see Fig. 9.1. In addition to the injection timespans, the fit has been applied to the pre- and post-engineering noise measurement showing how the final realignment of the test masses (DOY076 column in Tab. 9.2) reduced the TTL coupling noise.

I have shown in Sec. 7.2 that the acceleration cross-coupling coefficients depend on the angular alignment of the test masses. Analysing Fig. 9.1, we find that the angular realignments reduced the φ -acceleration dependent coupling well. Also, the coefficients scaling the lateral accelerations, C_y and C_z , have been significantly reduced. The coefficient C_η slightly decreased.

I will compare here the realignments, which we would perform based on the analytical model (7.21), with the actual angular corrections performed during the mission. Within the analytical model, I replace the constant summand of the cross-acceleration coupling coefficients with the value I compute with the fit model for the pre-engineering phase. Since the coupling coefficients must be

start time (month.day hour:minutes)	end time	injection type	amplitude	frequency	duration
14.03 08:00	14.03 20:00	pre-engineering noise			
15.03 07:50	15.03 09:00	$y_1 = y_2$	1 μm	10 mHz	70 min
15.03 09:03:31	15.03 09:45	$y_1 = -y_2$	0.5 μm	10 mHz	41.5 min
rotation of test masses in φ ; final set-points: φ_1 : -64 μrad , φ_2 : +19 μrad					
15.03 18:30	15.03 18:55	$y_1 = -y_2$	0.5 μm	10 mHz	25 min
15.03 19:00	15.03 19:48	$y_1 = y_2$	1 μm	10 mHz	48 min
15.03 19:50	15.03 20:21	$z_1 = z_2$	1 μm	5 mHz	31 min
15.03 20:23	15.03 20:45	$z_1 = -z_2$	0.5 μm	5 mHz	22 min
16.03 07:37	16.03 08:25	$z_1 = -z_2$	0.5 μm	5 mHz	48 min
16.03 08:25	16.03 09:04:21	$z_1 = z_2$	1 μm	5 mHz	39 min
rotation of TM1 in η_1 and return to original alignment					
16.03 10:37	16.03 11:41	$z_1 = z_2$	0.5 μm	10 mHz	64 min
16.03 11:41	16.03 12:40	$z_1 = -z_2$	0.5 μm	10 mHz	59 min
16.03 12:39	16.03 13:04	$y_1 = y_2$	0.5 μm	20 mHz	25 min
16.03 13:04	16.03 13:43	$y_1 = -y_2$	0.5 μm	20 mHz	39 min
rotation of test masses in both angular degrees of freedom					
16.03 14:28:10		redefine DFACS angles (see Tab. 9.2)			
Rotation of test masses to new DFACS zero angles					
17.03 08:00	17.03 20:00	post-engineering noise			

Table 9.1: Timeline of the injections and test mass realignments during the engineering days performed between the 14th and 17th of March 2016. Times are given in UTC. The shown set-points were commanded relative to their initial position.

description	symbol	[unit]	DOY076	DOY171	DOY177
			(16.03.2016 14:28)	(19.6.2016 8:20)	(25.6.16 8:00)
phi1	φ_1	[μrad]	-59.25	-56.32	-61.2
phi2	φ_2	[μrad]	-21.35	-33.01	-9.7
eta1	η_1	[μrad]	-3.5	-2.14	-4.9
eta2	η_2	[μrad]	3.5	10.3	-3.3

Table 9.2: Adaptions of the test mass set-points in order to optimise the cross-talk suppression. These angular alignments have been applied to the test masses relative to their alignment before the engineering days. These offsets have been commanded as calibration of the DWS signals, i.e. the DFACS offset values have been changed accordingly. Times are given in UTC. Table credit: [P10]

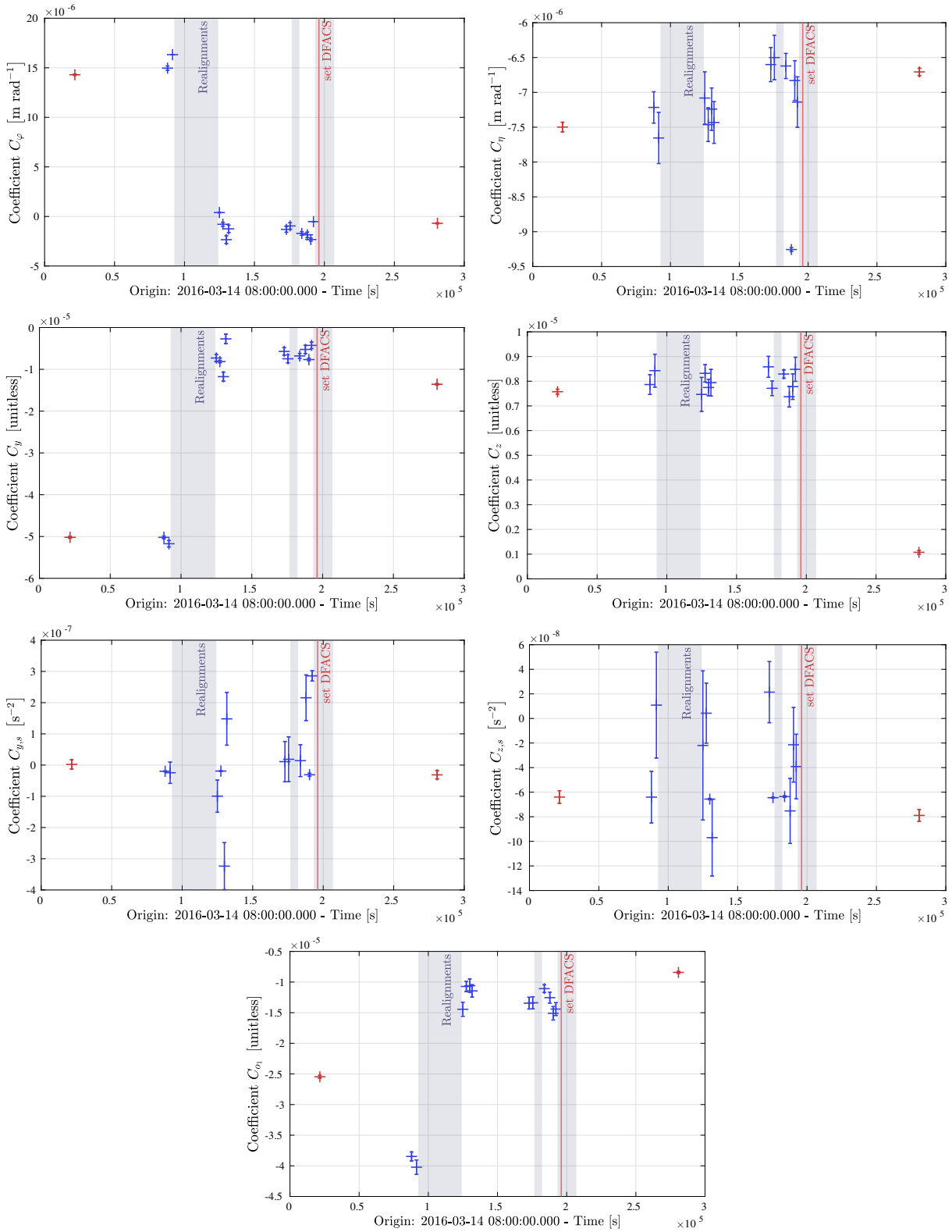


Figure 9.1: Fitted coupling coefficients during the engineering days in March 2016. Red markers: Coefficients for the pre- and post-engineering noise. Blue markers: Coupling coefficients for the injection times spans summarised in Tab. 9.1. The coefficients' error bars show the respective coefficients' uncertainty (standard errors) by the fit method. The shaded area denotes the timespans where the test masses have been rotated to different set-points. On the 16th of March at 14:28 UTC (red line), the DFACS angles were redefined.

	angular realignments:			cross-coupling coefficients:		
	mission	analytical		before (fit)	after (fit)	after (analytical)
φ_1 [μrad]	-59.25	-60.5	C_φ [$\mu\text{m}/\text{rad}$]	14.3	-0.7	-1.8
φ_2 [μrad]	-21.35	-10.3	C_η [$\mu\text{m}/\text{rad}$]	-7.5	-6.7	-7.5
η_1 [μrad]	-3.5	15.8	C_y [10^{-6}]	-50.2	-13.6	-12.2
η_2 [μrad]	3.5	23.4	C_z [10^{-6}]	7.6	1.1	0.6

Table 9.3: Comparison of set-points derived during the engineering days and the respective analytical predictions. At the left-hand side of the table are shown the angular corrections performed during the mission based on the analysis of the engineering days data and the corrections the analytical model predicts based on the coefficients fitted in the pre-engineering phase. At the right-hand side of the table are shown the acceleration coupling coefficients fitted before and after the realignments, i.e. in the pre-engineering and post-engineering phase, as well as the coefficients calculated with the analytical model with the set-points defined in the mission.

zero for zero TTL coupling, the analytical coefficient description provides the following system of equations which I solve for the optimal test mass alignment angles:

$$\begin{aligned}
0 &\stackrel{!}{=} C_{\varphi,\text{fit}} + 0.20449 \frac{\text{m}}{\text{rad}} \varphi_1 + 0.18714 \frac{\text{m}}{\text{rad}} \varphi_2, \\
0 &\stackrel{!}{=} C_{\eta,\text{fit}} + 0.20403 \frac{\text{m}}{\text{rad}} \eta_1 + 0.18247 \frac{\text{m}}{\text{rad}} \eta_2, \\
0 &\stackrel{!}{=} C_{y,\text{fit}} + 1.00000 \frac{1}{\text{rad}} (-\varphi_1 + \varphi_2), \\
0 &\stackrel{!}{=} C_{z,\text{fit}} + 1.00000 \frac{1}{\text{rad}} (\eta_1 - \eta_2).
\end{aligned} \tag{9.1}$$

There, the constant coefficients $C_{j,\text{fit}}$, $j \in \{\varphi, \eta, y, z\}$ correspond to the fitted coefficients during the pre-engineering phase (first coefficient column in Tab. 9.3). In Tab. 9.3, I compare the angular realignments set in the mission with the ones derived analytically by the system of equations (9.1). We find that the realignments in ϕ are performed in the same direction as the analytical model suggests. In particular, the computed alignments in ϕ_1 match each other very well. The difference in the φ_2 alignment potentially explains the offset of the coefficient C_y after the alignments, which is worse than the other three cross-acceleration coefficients, see Fig. 9.1. In terms of the η realignments, the analysis during the mission and the analytical approach provide very different results. While the alignment of both test masses has been changed only slightly in this degree of freedom, the analytical estimate recommends a significantly larger rotation. This analytically suggested correction would have little effect on the C_z coefficients compared to the realignment performed during the mission since it yields approximately the same differential angle ($\eta_1 - \eta_2$) in both cases. However, it would change the C_η coefficient significantly. We see in Fig. 9.1 that C_η was almost not affected by the realignment within the mission.

Next, I insert the alignment parameters set during the mission in the analytical model, thereby predicting the coupling coefficients for the time of the post-engineering phase. These can then be compared with the actual fit results for the corresponding timespan, as summarised at the right-hand side of Tab. 9.3. We find indeed comparable results. The angular acceleration coefficients deviate by about $1 \mu\text{m}/\text{rad}$ and the deviation in the C_y coefficient is of the same magnitude, while the deviation in C_z is half the size. These deviations are small compared to the large coefficient changes in C_φ , C_y and C_z .

Several reasons can cause these differences. First, we have seen in the analysis of the noise run after the LXE that the fit coefficients are not stable and can deviate within a noise run, even when considering long continuous time segments, see Figs 8.4 and Tab. 8.3. Hence the

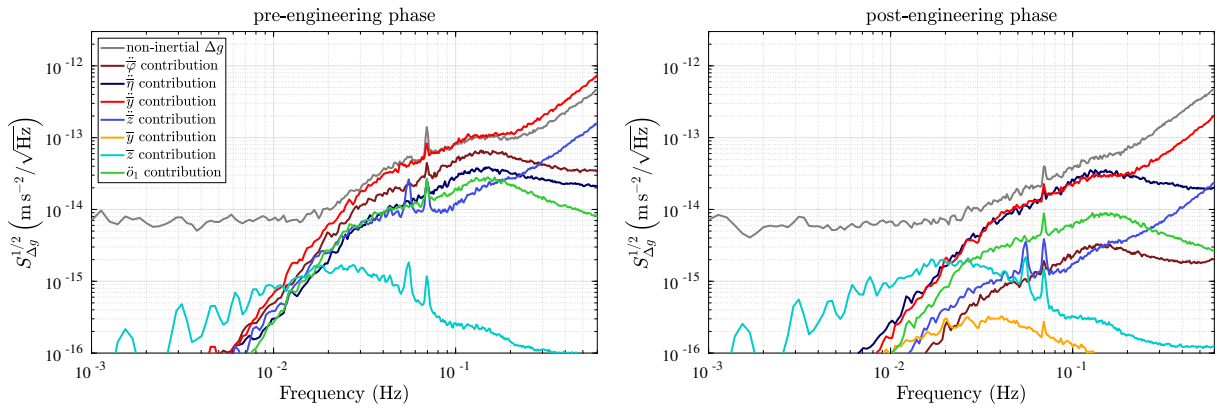


Figure 9.2: Noise contributors in the pre- and post-engineering phase of the engineering days (Tab. 9.1). Before the realignments, the noise in the fit quantities (in particular \bar{y}) added noise at higher frequencies when the fit model was subtracted from the Δg measurement.

coefficients derived for the pre- and post-engineering phase can potentially suffer from this variability. Moreover, the analytical coefficients have shown to rely on the measurement accuracy of the beam parameters and can hence deviate slightly given unavoidable measurement errors, see Tab. 7.3. Given these uncertainties, the deviation between the fit coefficients during the post-engineering phase and their analytical counterparts is reasonable.

Next, I investigate how the realignments changed which fit quantities coupled the most into the measured Δg . Fig. 9.2 demonstrates that, in the beginning, the noise in the $\bar{\varphi}$ and \bar{y} accelerations was dominant but decreased due to the test mass realignments. The noise contribution of the accelerations in φ now lies more than one order of magnitude below the noise floor. However, the S/C accelerations along y still contribute significant noise together with the accelerations in η . The comparison with the coupling coefficients in Tab. 9.3 shows that these noises also correspond to larger coupling coefficients and, therefore, match our expectation.

The Δg -noise reduction prediction by the analytical model for the realignments performed during the mission, as well as the analytically derived test mass rotations, can be modelled. Therefore, I consider the pre-engineering noise and add the noise changes computed by the analytical model with inserted respective angular changes (Eq. (7.21), setting the constants Ξ_j to zero). Since the analytical model does not cover the noise contributions due to the stiffnesses and the longitudinal S/C jitter (o_1 -readout), their contributions computed with the fit model (7.1) (compare Fig. 9.2) will be taken into account additionally.

Considering the angular realignments performed during the mission, the result is displayed in Fig. 9.3. At the left-hand side of the figure, the noise reduction expected by the analytical model is shown by the dashed purple line. However, this model does not include the stiffnesses and o_1 -noise contribution (dashed grey line). Therefore, we see that the purple line lies slightly above the green line showing the post-engineering noise. Additionally, noise from the fitting quantities (particularly the lateral parameters relying on GRS measurements) adds in above approximately 50 mHz. This noise originates only from the model subtraction and would not be present in actual noise measurements. If subtracting the stiffness and o_1 -noise contributions also from the pre-engineering noise, the analytically predicted residual noise after the realignment matches the measured noise curve besides the higher frequency noise added in due to the fit quantities, see right-hand side of Fig. 9.3.

As shown in Fig. 9.2, the o_1 noise contributions, which is significantly larger than the stiffness contributions, decreased due to the test mass realignments. From the presented modelling,

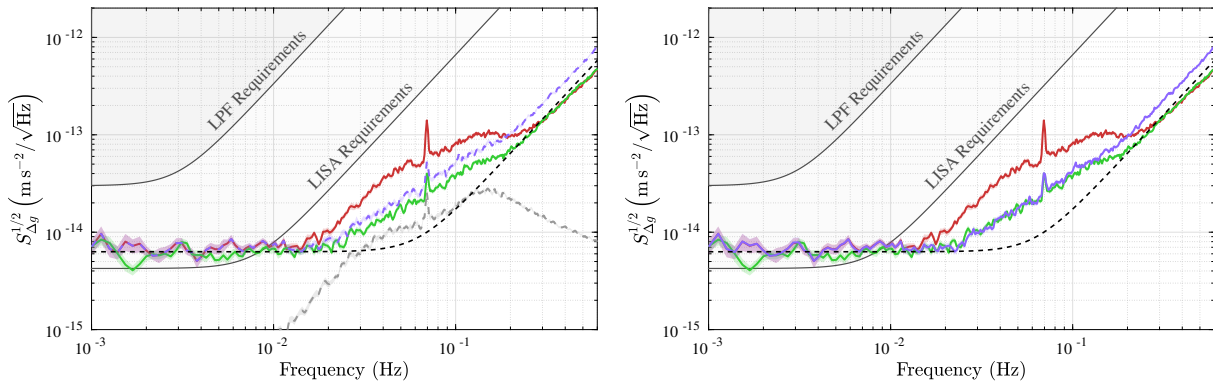


Figure 9.3: Analytical modelling of the realignment noise during the engineering days. In both figures, the red line represents the noise before and the green line the noise after the realignments. The dashed black line shows the performance model. Left figure: Analytical model for the realignments performed during the engineering days added to the pre-engineering noise (dashed purple line), and the sum of the fitted stiffness and o_1 -noise contributions (dashed grey line). Right figure: Analytical model added to the pre-engineering noise minus the fitted stiffness and o_1 -noise contributors (purple line).

we cannot certainly say if this noise either would actually decrease, therefore minimising the difference between the analytically predicted noise decrease and the measured post-engineering noise (left-hand side of Fig. 9.3), or is correlated to the other noise contributors leading to a residual difference between the predicted and measured noise change. This will be investigated further in the future. Note, therefore, that the fit model without the o_1 term also subtracted most of the TTL noise during the LXE (Sec. 8.5 and Fig. D.5).

I also apply the analytical model using the test mass realignment angles predicted analytically (Tab. 9.3). The result is shown in Fig. 9.4. Like in the previous case, where I modelled the noise after the realignments performed during the mission, the noise change according to the analytical model does not exactly match the result we would find if subtracting the TTL fit model (7.1). The residual difference between both subtractions relies on the o_1 noise contributor. If also subtracting the stiffness and o_1 noise contribution, the analytically predicted realignment yields the noise curve we would find when subtracting the TTL noise via the fit model. Thus, the analytical model (7.21) provides a valuable model also for the description of the realignments during the engineering days in March 2016.

In summary, the analytical alignment computation suggests realignment angles that could potentially have decreased the TTL coupling further. This finding has been demonstrated in Fig. 9.4. Moreover, this analytically predicted realignment relied only on the first fit during the pre-engineering days, not requiring a series of injections. However, it remains unclear how the o_1 noise contribution affects the accuracy of this modelling. In general, the analytical model shows that it can model the TTL coupling for other times than the LXE.

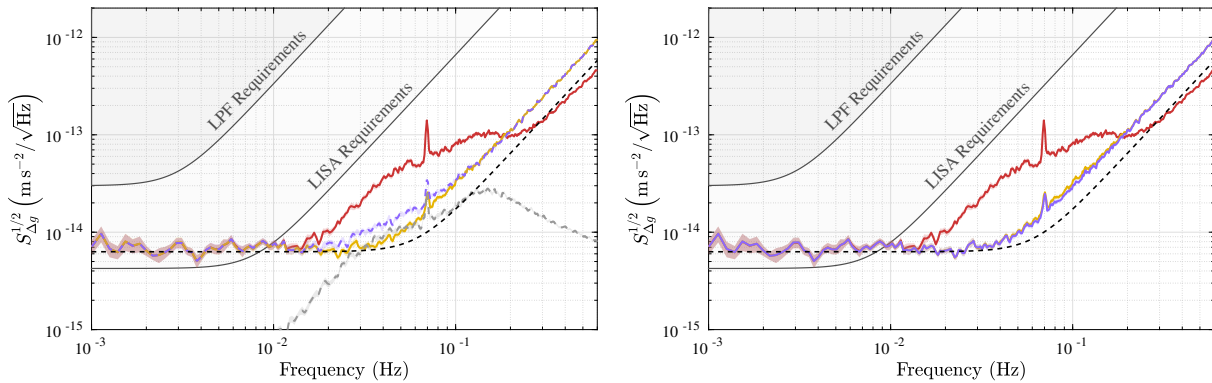


Figure 9.4: Analytical modelling of the expected realignment noise applying the analytically derived test mass rotations (Tab. 9.3) during the engineering days. In both figures, the red line represents the noise before the realignments and the yellow line the residual noise after the subtraction of the fit model. The dashed black line shows the performance model. Left figure: Analytical model for the analytically derived realignment angles added to the pre-engineering noise (dashed purple line), and the sum of the fitted stiffness and o_1 -noise contributions (dashed grey line). Right figure: Analytical model added to the pre-engineering noise minus the fitted stiffness and o_1 -noise contributors (purple line).

9.2 Further Realignment of the Test Masses

The nominal angular alignments of the test masses have only been adapted twice after the initial realignment during the engineering days. That was at the 19th (DOY171) and the 25th (DOY177) of June 2016, i.e. about three months later. The corrected alignments are shown in Tab. 9.2 and were based on the updated TTL model available at that time [60]. Comparing the final alignment angles with the ones derived analytically based on the data from the pre-engineering noise (Tab. 9.3) shows now a better agreement in both φ angles. The deviations in the η angles provided by both analyses remain.

In order to analyse how the coupling coefficients have changed due to these realignments, I investigate the noise runs before, in between and afterwards, see Tab. 9.4. In an ideal system, the coefficients prior to the realignment DOY171 should correspond to the coefficients I computed for the end of the engineering days. However, we find different coupling coefficients for the noise

noise run	cross-coupling coefficients [fitted analytical]					
	DOY168		DOY172		DOY192	
start time	15.06.2016 13:30		20.06.2016 08:00		10.07.2016 08:00	
end time	18.06.2016 08:00		24.06.2016 08:00		11.07.2016 09:55	
C_φ [$\mu\text{m}/\text{rad}$]	-0.6	-	-3.3	-2.1	2.7	1.2
C_η [$\mu\text{m}/\text{rad}$]	-5.7	-	-3.5	-4.2	-7.9	-7.2
C_y [10^{-6}]	-12.8	-	-27.1	-27.5	2.0	0.7
C_z [10^{-6}]	6.4	-	0.9	0.9	14.1	11.8

Table 9.4: Comparison of the fitted (left) and analytically predicted (right) cross-coupling coefficients during noise runs prior, in between and after the test mass realignments in June 2016 (Tab. 9.2). The noise runs are named here after the first DOY fully lying within the investigated noise run. Mind that the DOYs as defined in LPF always started at 8 AM. Times are given in UTC.

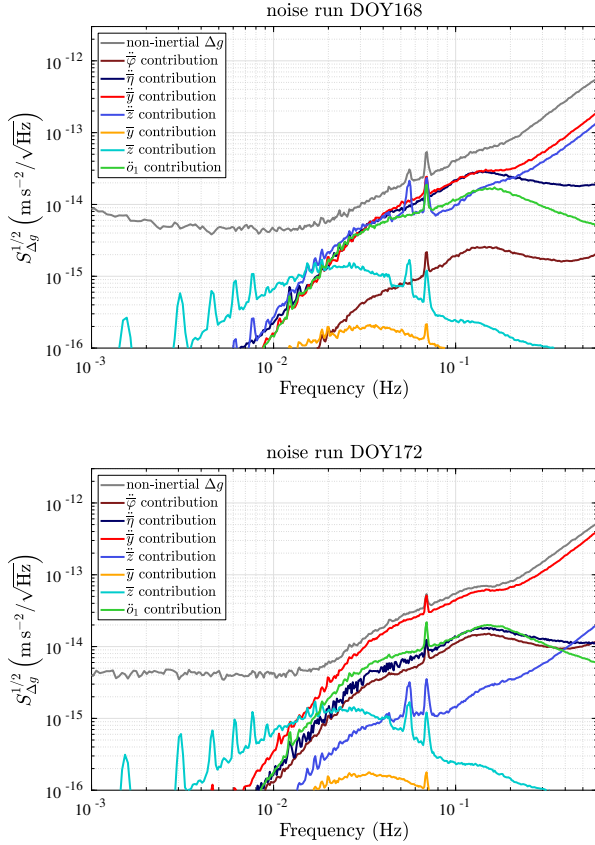


Figure 9.5: Noise contributors during the noise run prior to the test mass realignments in June 2016 (DOY168). Most contributors show a similar noise level as after the engineering days (Fig. 9.2). The noise contribution due to the \ddot{z} - and \ddot{o}_1 -accelerations increased.

Figure 9.6: Noise contributors in the noise runs between (starting at DOY172) and after (DOY192) the realignments in June 2016. The first realignment decreased the noise due to the accelerations in the xz -plane but increased the noise in the xy -plane leading in total to a more prominent TTL noise. In the ASD plot for the noise run after the second realignment, we find more significant noise coupling from the xz -plane into the measurement, but the noise in the xy -plane significantly decreased, lowering the total TTL noise.

run prior to the realignments (DOY168) than for the post-engineering phase. While C_φ , C_η and C_y have changed only slightly and these changes can therefore correspond to the variability of the fit results, we see a significant change of the C_z coefficients, which increased by almost a factor of six, compare Tabs. 9.3 and 9.4. Consequently, the level of \ddot{z} noise into the Δg measurement also increased as can be seen in Fig. 9.5.

I also fit the coupling coefficients for the noise run between both realignments and the first noise run after the realignments. Due to the first realignment, the coefficients increased in the xy -plane but decreased in the xz -plane. The second realignment had the opposite effect. This can also be seen when comparing the noise level of the cross-coupling contributors, see Fig. 9.6. While the y acceleration was most prominent after the first realignment (DOY171), the accelerations in η and z became the most significant noise contributors after the second realignment (DOY192).

The noise changes in the xz -plane are of particular interest here. This noise was significantly decreased after the first realignment. In particular, the noise contribution of the \ddot{z} acceleration became negligible. Presumably, the TTL bump in the LPF sensitivity curve could have been mitigated in the second realignment (DOY177) if the test masses would only have been rotated in φ .

For both realignments, I additionally compute the coefficient change we would expect based on the analytical model, i.e. when solving the system of equations (9.1) setting the offsets to

the fitted coefficients during the noise run DOY168. The comparison of the cross-coupling coefficients derived via the model or analytically shown in Tab. 9.4 reveals that the analytical model computes slightly smaller coefficient changes in most cases. The deviation between both values corresponds to approximately $1\mu\text{m}/\text{rad}$ in the case of the coefficients scaling the angular accelerations. It is of the same magnitude in the case of the coefficient C_y . Therefore, these deviations can originate from the variability of the fit results. Comparing the coefficients C_z shows, on the one hand, two matching coefficients in the noise run between the realignment steps and, on the other hand, a larger deviation after the last realignment. Keeping in mind that this coefficient already changed significantly with respect to its fit for the post-engineering noise, I assume this deviation to rely on rotations of the test masses in η not tracked by the DWS signal. I will further discuss this in Sec. 10.

In summary, we find coefficient changes with the analytical model comparable to the fit results except the C_z coefficient, which will be analysed in the following section. Moreover, the analysis of the fit contributors during noise runs between (DOY172) and after (DOY192) the realignments in June 2016 yields that the overall TTL noise in LPF could have been mitigated if no test mass rotations in η would have been applied.

Chapter 10

Long-Term Analysis of the TTL Coefficients

In the previous sections, the comparison of the fitted coupling coefficients and the analytical model held as a verification of the analytical model. I will now use this model to characterise the long-term stability of the TTL coupling coefficients. When comparing the coupling coefficients, which I computed for the noise run after the final test mass realignment in July 2016 (Sec. 9.2) and the noise run after the LXE mid-February (derived in Sec. 8.2), we see significant differences between some of the fitted acceleration coefficients, see Tab. 10.1. In particular, the coefficient C_z , which was already the dominating noise contribution in July 2016, tripled.

In this chapter, I will show for the entire mission duration that the fitted coupling coefficients partially drift and, in particular, significantly change when the temperature inside the satellite changes. Since no intentional realignments have been applied to the test masses after the 25th of June 2016, they cannot be held responsible for the coefficient changes. I will also discuss in which sense the coupling coefficients provide an additional measure for the stability of LPF's optical system.

I discuss here for the first time the long-term stability of the TTL coupling coefficients. Also, the behaviour of the angular readouts for to entire mission duration has, to my knowledge, not been compared elsewhere. The analysis of the spot position changes due to the cooldown relies on [P1, 61, 62].

noise run	fitted cross-coupling coefficients	
	after final DFACS redefinition	after LXE
start time	10.07.2016 08:00	13.02.2017 08:00
end time	11.07.2016 09:55	23.02.2017 08:00
C_φ [$\mu\text{m}/\text{rad}$]	2.7	3.0
C_η [$\mu\text{m}/\text{rad}$]	-7.9	-12.9
C_y [10^{-6}]	2.0	3.9
C_z [10^{-6}]	14.1	43.5

Table 10.1: Comparison of the fitted cross-coupling coefficients during noise runs after the final test mass realignment and after the LXE. Times are given in UTC.

10.1 Characterisation of the Coupling Coefficients' Stability

For my analysis, I computed the TTL coupling coefficients for 36 timespans throughout the LPF mission using the fit model (7.1). The respective timespans are summarised in Tab. D.1 and correspond to noise runs with very low actuation ('URLA' segments). The fitted acceleration coefficients are shown in Fig. 10.1.

As expected, the coefficients changed with the realignments of the test masses at the end of June 2016. Moreover, the acceleration coefficients in the xz -plane, i.e. C_η and C_z , changed due to temperature changes, particularly visible during the cooldown.

This cooldown took place during the mission extension phase, from January to May 2017. At that time, the whole satellite was cooled down to investigate the instrument performance at lower temperatures. On the 23rd of January 2017, the temperature was first decreased by about 10°C . In absolute temperatures, the electrode housings cooled down from a mean temperature of 22°C to 12°C , see Fig. 10.2. This step was repeated on the 29th of April 2017, decreasing the temperatures below the design range of the sensors. The mean temperature inside the electrode housings was estimated to be 2°C which refers to a further decrease of 10°C . In between both cooldowns, the temperatures increased by slightly more than 1°C during to the DRS operations [18].

An overview of the mean temperatures corresponding to the timespans accounted for the TTL coefficient fits is shown in Fig. 10.2. The temperature changes led to a shift of the C_η and C_z coefficients to different levels, where both remained approximately stable besides few outliers in the second phase of the cooldown (indicated with the darker blue in Fig. 10.1). The level of the coefficients after the cooldown phase approximately corresponds to the respective value before the cooldown. I refer to these abrupt coefficient changes as **jumps**.

Aside from the jumps, the C_z coefficient increased at long time scales. This **drift** was the largest between the engineering days and the test mass realignment in June 2016 but also visible after June until the beginning of the cooldown.

Note that the lateral acceleration coefficients fitted for the 35th timespan, i.e. the second last timespan, suffer from large uncertainties. Therefore, I do not consider this fit result in my analysis.

In accordance with the analytical model (7.21), the coupling coefficient changes can be explained via rotations of the test masses. However, any additional changes in the optical system potentially also affect the analytical model and likewise the coupling coefficients. I will discuss both effects in the following.

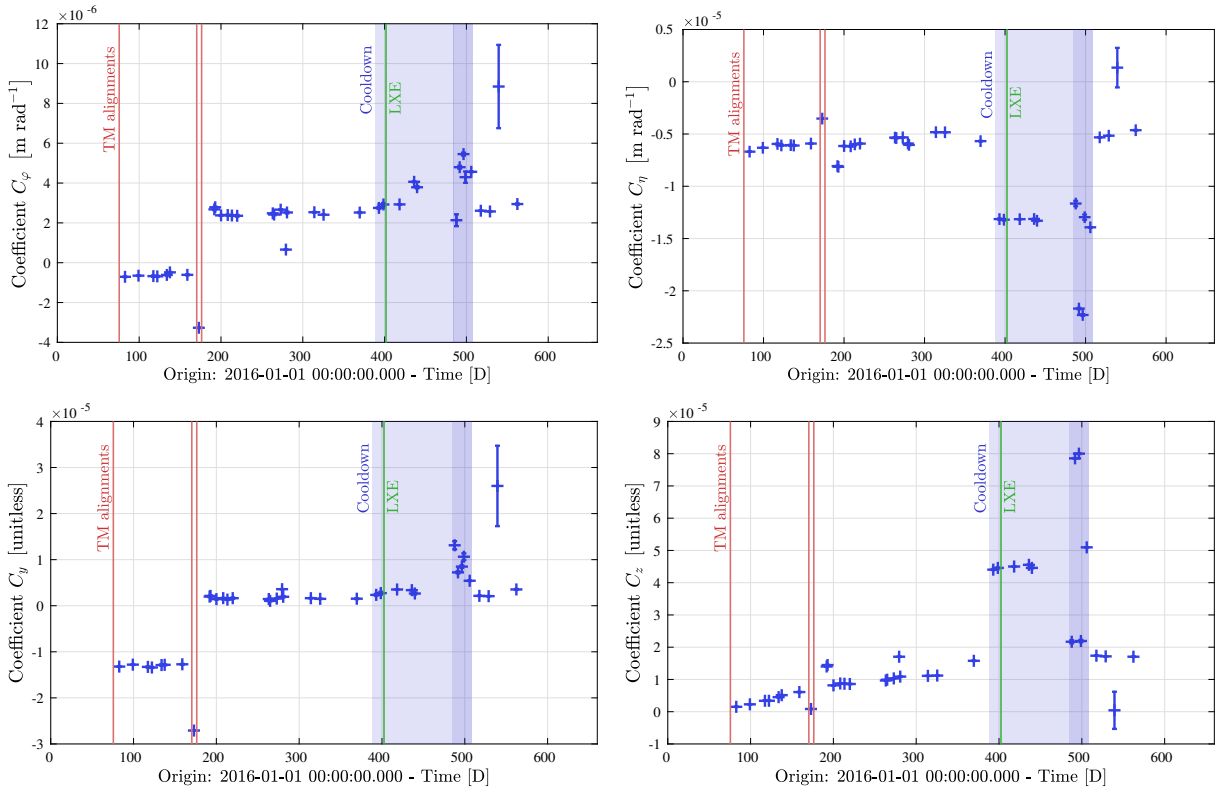


Figure 10.1: Fitted coupling coefficients during the entire mission duration. The red lines display the times where the DFACS nominal alignment had been redefined and the green lines correspond to the time of the LXE. The blue shaded area shows the timespan of the cooldown, with the darker blue indicating the timespan of the lowest temperatures. The blue crosses correspond to the coupling coefficients fitted for noise runs with very low actuations (Tab. D.1).

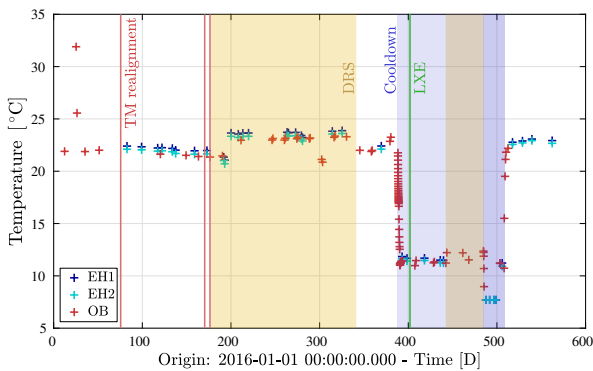


Figure 10.2: Temperature changes during the LPF mission. The blue crosses show the mean temperatures within the first (EH1) and second (EH2) electrode housing. They have been computed for the same noise runs as the TTL coefficients (Tab. D.1). The red crosses show the mean temperature at the optical bench at the times of the spot position measurements (Sec. 10.4). The temperature increased during the DRS operations (yellow shaded areas). The two times of decreased temperature during the first DRS phase corresponded to thruster anomalies. Before the cooldown, the temperature increased again when the test masses were grabbed and released. The measured temperatures during the second cooldown phase were higher than the actual temperatures since the sensor had reached its minimum possible readout value [18].

10.2 Stresses and Relaxations

The LPF optical system was subject to stresses and relaxations due to environmental changes which happened over time but could also be induced intentionally for an experiment. An example for such an investigation is the cooldown performed during the LPF extension phase [18].

In general, temperature fluctuations couple into the interferometric measurements via thermally induced forces acting on the test masses and thermal elastic distortions of the optical system [18]. In particular, the windows between the optical bench and the electrode housings are subject to expansions, changes of their refractive indices due to temperature changes, and thermally induced mechanical stresses [63].

Relaxations, stresses, as well as any other distortion of the optical system potentially also affect the beam path and alignment. These would have a direct effect on the coupling coefficients but also induce a tilt of the test masses in order to correct the differential angle of the incident beams at the detector (DFACS loop). This test mass tilt would then yield additional coupling coefficient changes. We can analyse this effect by investigating the angular readout at the x1- and x12-interferometer. If the test mass would tilt to correct an angular misalignment originating from distortions of the optical bench, we would see a stable DWS but changing GRS angular readout (Sec. 10.3).

Additionally, such distortions also correspond to a beam walk on the detector. Therefore, I will also investigate the beams' spot positions (Sec. 10.4).

10.3 Analysis of the Angular Readouts

As discussed in Sec. 10.2, various optical parameters can change due to the cooldown. Among them are the transmissive components on the optical bench and the windows to the electrode housings. The investigation of the TTL noise contributors in Sec. 7.2.1 indicated that these components have a small effect on the overall coupling compared to the contributions of the lever arm and the piston effect. Both couple into the readout via rotations of the test masses. Therefore, I further investigate the test masses' angular alignments during the cooldown.

I summarise in Fig. 10.3 the mean angular readouts associated with the timespans for which the coupling coefficients have been computed (Tab. D.1). The DWS readouts were used by the DFACS control loop for the test mass positions. They should, therefore, only change for intentional test mass realignments, i.e. after the engineering days and after the two alignments in June 2016. However, we also find offsets of the DWS angles for the 28th and the 31st timespan, i.e. for the first and the fourth data point during the second cooldown. Therefore, I will exclude the data for these timespans from our tilt analysis. Note that the two offsets of DWS angles are also visible in the GRS readout. Thus, the first four GRS measurements would approximately yield the same angle when correcting them for the DWS angle change. During the time of the 32nd noise run considered here, the S/C was already heated up again.

The GRS values are shown in yellow in Fig. 10.3. They are a measure for the angular alignment of the test masses with respect to their housings. Therefore, the drifts and jumps of the GRS measurements do not necessarily show pure test mass tilts but could also partially correspond to a rotation of the housing with respect to the optical bench. A pure rotation of the electrode housing would neither change the test mass nor the beam alignment (neglecting negligible shifts due to a rotated window). Based on the GRS readouts alone, we cannot distinguish the test mass and electrode housing tilts from each other.

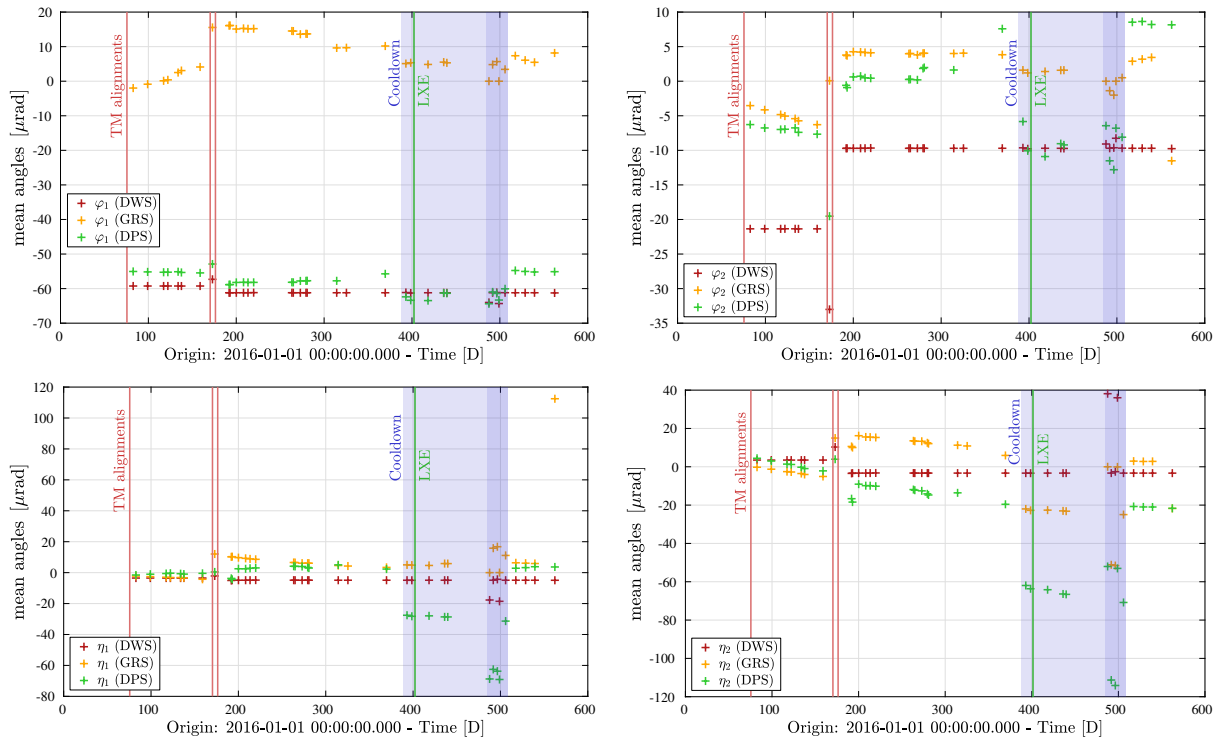


Figure 10.3: Mean angular readouts from the DWS and the GRS measurements. Additionally, I show the angular estimate via the DPS, which relates to the points of incidence of the interfering beams. The mean angles are computed for the same timespans used for the computation of the coupling coefficients during the LPF mission (Tab. D.1).

The third set of angular readouts relies on the DPS measurements: Since a tilt of a test mass generates a beam walk on the detector, the measurement of the power changes at the quadrants of the detector and can be used to compute the corresponding angle. This readout is less accurate than the other two angle measurements. Also, thermal distortions can make the beams shift at the detector (without an actual beam rotation), which would be read out as an angular change. However, the DPS readout provides a third reference for the question of whether the optical system or the electrode housing is rotated.

10.3.1 Application of the analytical model using the GRS angles: The jumps

The coefficient jumps visible in Fig. 10.1, aside from the test mass realignments, refer to the cooldown commanded in the LPF extension phase [18]. We find the most significant jumps for the C_η and the C_z coefficient. Following the analytical model (7.21), these coefficients depend on the pitch angle of the test masses:

$$\Delta C_\eta = 0.20403 \frac{\text{m}}{\text{rad}^2} \eta_1 + 0.18247 \frac{\text{m}}{\text{rad}^2} \eta_2 \quad (10.1)$$

$$\Delta C_z = 1.00000 \frac{1}{\text{rad}} (\eta_1 - \eta_2) \quad (10.2)$$

Moreover, the C_y coefficient did not change during the first but slightly increased during the second cooldown. The computations of the coefficient C_φ show no jump at the beginning of the first cooldown. However, this coefficient increased during this cooldown phase and additionally when the temperature was further decreased (second cooldown). From the analytical model we would therefore expect no yaw angle changes at the beginning of the cooldown and small

	mean GRS readouts [μrad]				mean DPS readouts [μrad]			
	φ_1	φ_2	η_1	η_2	φ_1	φ_2	η_1	η_2
before cooldown	10.2	3.8	3.4	5.9	-55.7	7.6	2.3	-19.6
first cooldown	5.2	1.4	5.3	-22.7	-62.4	-9.0	-28.2	-64.5
second cooldown	5.2	-1.7	16.3	-51.4	-61.2	-12.2	-63.1	-112.7
after cooldown	6.3	3.2	6.1	2.8	-55.0	8.4	3.4	-21.1

Table 10.2: Mean angular GRS and DPS readouts before and during the first and second cooldown. The angles during the cooldowns refer to the mean of all considered values, i.e. all angles plotted for the first cooldown in Fig. 10.3 and the second and third angles during the second cooldown.

	cross-coupling coefficients [fitted analytical]							
	before cooldown	cooldown 1		cooldown 2		after cooldown		
C_φ [$\mu\text{m}/\text{rad}$]	2.5 -	3.3	1.0	5.1	2.7	2.7	6.2	
C_η [$\mu\text{m}/\text{rad}$]	-5.7 -	-13.2	-10.6	-22.0	-16.2	-5.9	-14.2	
C_y [10^{-6}]	1.5 -	2.9	4.1	7.9	-0.3	2.6	11.7	
C_z [10^{-6}]	15.8 -	44.8	46.3	79.3	84.5	17.2	14.9	

Table 10.3: Comparison of the fitted and analytically predicted cross-coupling coefficients before, during and after the first and second cooldown. In the case of the cooldowns, I show the mean coupling coefficient of the computations within these cooldown phases. Thereby, I neglect the first, fourth and fifth shown coefficient during the second cooldown since these fits are assigned either to a changes DWS readout (Fig. 10.3) or the heating of the S/C.

changes later on:

$$\Delta C_\varphi = 0.20449 \frac{\text{m}}{\text{rad}^2} \varphi_1 + 0.18714 \frac{\text{m}}{\text{rad}^2} \varphi_2 \quad (10.3)$$

$$\Delta C_y = -1.00000 \frac{1}{\text{rad}} (\varphi_1 - \varphi_2) \quad (10.4)$$

Assuming that distortions of the optical system bend the beam, the DWS readout would change. Therefore, the DFACS control loop would command a test mass rotation to correct the measured DWS angle. However, this rotation would then be visible in the GRS readout.

I will test the assumption by inserting the GRS angular readouts (Tab. 10.2) into the analytical model (7.21) computing the coefficient changes expected for actual test mass tilts. The results are summarised in Tab. 10.3.

For now, I do not include beam shifts due to the initial beam misalignment in my analysis since we do not know the origin of the misalignment. Assuming that the measurement beam would have been tilted by the fibre injector optical subassembly (FIOS) by an angle α in pitch or yaw, the beam would impinge on the first test mass displaced by $0.18 \alpha \text{ m}/\text{rad}$. Assuming further that this tilt would be fully corrected by a rotation of this test mass, we would find the same beam displacement on the second test mass and the x12-photodiodes. The corresponding change of the piston effects at both test masses would almost cancel each other (see also Sec. 10.4.3). Likewise, the beam offset at the detector would not couple into the angular coupling coefficients via the non-geometric coupling contributions: The beam tilt due to S/C jitter cancels after the second test mass reflection and, therefore, the angle of incidence at the detector remains unchanged. Also, the beam shifts have no measurable effect on the lateral acceleration coefficients.

	mean GRS readouts [μrad]				mean DPS readouts [μrad]			
	φ_1	φ_2	η_1	η_2	φ_1	φ_2	η_1	η_2
after ED	-2.0	-3.5	-2.2	-0.2	-55.0	-6.3	-1.5	4.4
before realignment	4.1	-6.3	-4.3	-5.1	-55.5	-7.7	-0.5	-2.1
after realignment	15.1	4.3	9.7	16.2	-58.2	0.6	2.5	-9.1
before cooldown	10.2	3.8	3.4	5.9	-55.7	7.6	2.3	-19.6

Table 10.4: Mean angular GRS and DPS readouts after the engineering days (ED), before and after the test mass realignments in June 2016, and before the cooldown starting in January 2017. The angles given for a timespan after the test mass realignments refer to the 11th data point, i.e. neglecting the first two data points after these realignments.

We see in Fig. 10.3 that the GRS yaw angles decrease for both cooldowns. These changes are much smaller than in the case of the pitch angles. Likewise, the coupling coefficients C_φ and C_y change only slightly. However, the coupling coefficients predicted by the analytical model (Eq. (7.21)) for inserted GRS do not correspond to the fitted coefficients (Tab. 10.3). The deviations are larger for the lateral coefficient C_y , which depends by approximately a factor of five stronger on the angular readouts. I conclude that the angular deviation of the GRS φ -readouts cannot originate from test mass tilts (alone).

The fitted and analytical results match better in the xz -plane. The analytically predicted coefficients C_η change in accordance with the fitted results. However, the analytically computed changes are slightly smaller. Also, the analytical C_z coefficient prediction correlates to the fit. Here, the analytical result lies slightly above the fit result. However, the deviation between the analytical and the fit result is one magnitude smaller than the total deviation of the coefficient due to the temperature changes.

In summary, the assumed test mass rotations can explain big parts of the coefficient changes due to the cooldown in the xz -plane. In the xy -plane, we see no corresponding systematic of the analytically predicted and the fitted coefficient changes.

10.3.2 Application of the analytical model using the GRS angles: The drifts

Aside from the small jumps at the time of the cooldown, the C_φ , C_η and the C_y coefficients stayed constant over long time scales, see Fig. 10.1. However, the C_z coefficient drifted upwards between the engineering days and the realignments. Furthermore, this coefficient also showed an upward trend between the realignments and the cooldown, however, less significant than before.

I exclude the first two data points after the realignments from this analysis. The coefficients, as well as the GRS and DPS angles, deviate here from the following data points. I assume this divergence to refer to a thruster anomaly, which temporarily decreased the temperature within the satellite [18]. In the remaining considered data points, the drifts of C_z and the GRS and DPS readouts become more evident. Note further that all coefficients and angles between the realignments and the cooldown, except for the last one, respectively, correspond to DRS operations, during which the temperature was increased by about 2°C .

The coefficient drifts during the DRS operations are presumably not related to temperature changes of the system like the coefficient jumps since the temperature drifted only slightly within this period of the mission, see Fig. 10.2. However, we cannot fully exclude such a relation for the first drift.

	cross-coupling coefficients [fitted analytical]							
	after ED		before realign		after realign		before cooldown	
C_φ [$\mu\text{m}/\text{rad}$]	-0.7	-	-0.6	0.0	2.4	-	2.5	1.3
C_η [$\mu\text{m}/\text{rad}$]	-6.7	-	-5.9	-8.0	-6.1	-	-5.7	-9.3
C_y [10^{-6}]	-13.2	-	-12.7	-22.1	1.4	-	1.5	5.8
C_z [10^{-6}]	1.5	-	6.1	4.3	8.2	-	15.8	12.2

Table 10.5: Comparison of the fitted and analytically predicted cross-coupling coefficients after the engineering days, before and after the test mass realignments in June 2016, and before the cooldown starting in January 2017. The coefficients given for a timespan after the test mass realignments refer to the 11th data point, i.e. neglecting the first two data points after these realignments.

Investigating the GRS readouts for the timespans of the drifts in Fig. 10.3, i.e. between the engineering days and the realignments as well as between the realignments and the cooldown, we find drifts in all angular degrees of freedom. The only exception is the angle φ_2 between the realignments and the cooldown, which stayed constant. The related angular readouts are summarised in Tab. 10.4. These angular changes would result in coefficient changes that do not correspond to the fit results, see Tab. 10.5.

The opposite drifts of the GRS yaw angles would only partially cancel each other in the computation of C_φ (compare Eq. (10.3)). Furthermore, they would significantly change the C_y coefficient (Eq. (10.4)). However, this lateral coefficient remained stable. Thus, I assume that the yaw GRS angles do not show actual test mass rotations.

Again, the comparison provides more consistent results for the vertical plane. The given GRS pitch angles yield analytical coefficients that could explain more than half of the amount of the fitted C_z coefficient changes for both drifts. The coefficient C_η gets underestimated for both timespans.

10.3.3 Interpretation of the coefficient comparison using GRS angles

The comparison between the fit coefficients and the prediction of the analytical model using the GRS angles shows, in general, smaller deviations in the xz -plane than in the xy -plane.

In the xy -plane, the drifts and the jumps of the GRS yaw angles do not explain the C_φ and C_y coefficients, which are mostly stable. We find the largest divergence between the analytically predicted and fitted C_y coefficients for the noise run before the first realignment in June 2016 (see Tab. 10.5). I conclude that the GRS housings must have drifted over time and in response to the cooldown.

Also, comparing the GRS angles with the DPS yaw angles before the cooldown (Fig. 10.3) shows that the DPS angles are on average more stable. This observation seconds the housing drift.

In the xz -plane, the analytically derived coefficients can explain most of the changes of the fit coefficients due to the cooldown (Tab. 10.3). The small over- and underestimations of the C_η and C_z coefficients during the cooldown could be explained by a pitch drift of the first electrode housing. Investigating the coefficients for the times of the two drifts, we find that the analytical model explains approximately half of the changes of the C_z coefficient. Therefore, I assume rotations of the electrode housings also in this case.

The rotations of the housings have only a small effect on the TTL coupling through their windows but do not change the direction of the beams. However, test mass rotations do. Since the DFACS control loop keeps the differential angle at the photodiodes stable, I assume that beams have been tilted prior to their test mass reflections. Such a change of the beam direction could originate from stresses to the FIOSs or any other optical component along the beam path. This tilt would then be corrected by a test mass rotation. However, it would lead to an offset of the beam's point of incidence on the detector, which would be measurable in spot position measurements (Sec. 5.2).

Furthermore, the beam walk on the detector that does not originate from the test mass tilts would also add to the changes of the DPS angles. Thus, the DPS readout is affected by angular changes of both beams due to test mass tilts as well as any other tilt sources. An indicator for beam tilts by other optical components than the test masses are the beam's spot positions in all interferometers, which I will investigate in the next subsection.

10.4 Analysis of the Long-Term Spot Positions

Fig. 10.4 shows both beam's relative spot position changes at the reference interferometer throughout the mission. The spot position measurements shown in this plot are divided by the OPL of the respective beam between the FIOS and the detector surface. Due to this normalisation, the shown changes do not depend on the path length of the respective beam. Additionally, the position value of the first measurement was subtracted from all measurements in order to show only the position changes during the mission.

Since these measurements were taken by the reference interferometer, neither of the beams was affected by the test mass alignment. Nonetheless, we find small drifts of the spot positions over time and, in particular, rapid position changes related to the cooldown. The most significant beam walk was measured along the vertical (z -) axis and is larger for the measurement beam than for the reference beam. These spot position changes must have been originated from alterations of the optical system itself.

I show the absolute spot positions in all interferometers in Fig. D.13.

10.4.1 Possible sources for spot position changes

Stresses on the FIOSs potentially shift and bend the emitting beams [61, 64]. The shifts would be propagated to the photodiodes and yield the same offset in all interferometers. The beam tilts would scale with the optical path length between the FIOS and the respective photodiode. However, the differential tilt angle would be counteracted by rotating the first test mass. If both FIOSs bend equally, the differential angle would be zero in the x1- and the x12-interferometer and no test mass rotation would be performed. Correspondingly, both beams accumulate their offsets along their full path to the detector. On the contrary, if only the measurement beam tilts, this tilt would be corrected by a rotation of the first test mass. Therefore, the x1- and the x12-interferometer would only measure the shift the measurement beam accumulated at the propagation distance between the FIOS and the first test mass.

In between the FIOSs and the detectors, the beams are affected by the temperature and relaxation effects on the beamsplitters and mirrors, but also the optical bench baseplate itself. When, e.g., temperature induced stresses distort the full baseplate, the beamsplitters and mirrors bonded to it would slightly misalign with respect to the beam path. We expect the largest

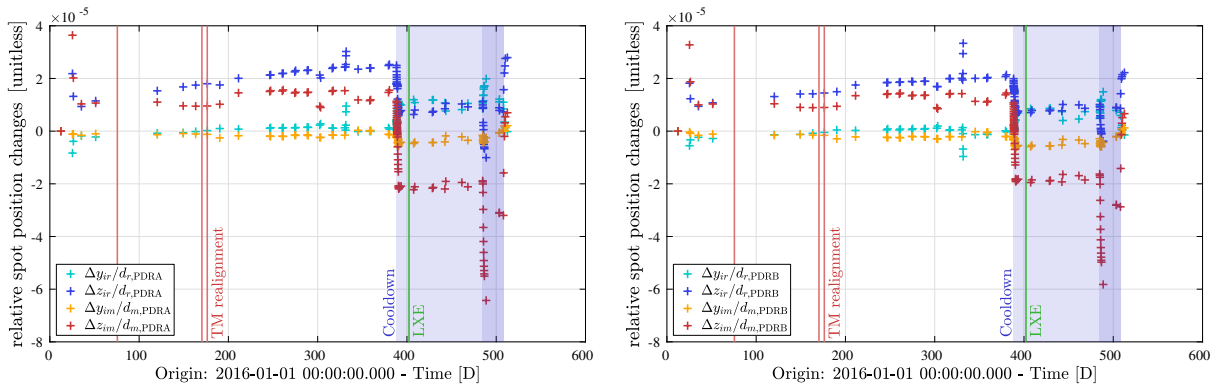


Figure 10.4: Relative spot positions changes of the reference (y_{ir} , z_{ir}) and the measurement beam (y_{im} , z_{im}) at the reference interferometer. The spot position of the respective first measurement was subtracted from all position measurements. The result was divided by the OPL of the beam from the FIOS to the photodiode. Left figure: Spot position changes at the A-diode (PDRA). Right figure: Spot position changes at the B-diode (PDRB).

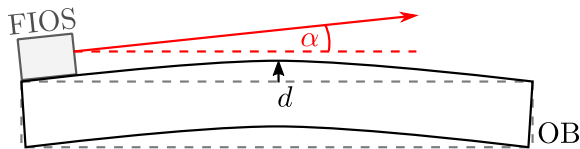


Figure 10.5: Sketch of the beam tilt due to the deformation of the optical bench. The angle α describes the uptilt of the beam for an uplift d of the centre of the baseplate.

effect to originate from a bulge of the baseplate changing the vertical alignment of the beam with respect to the optical bench, see Fig. 10.5. Such a bulge can be induced by stresses on the mounting of the optical bench [61]. Additionally, the refractive index of the beamsplitters changes with the temperature, inducing a shift of the transmitting beams. In LPF, such distortions were kept small by the material choice. The baseplate, as well as beamsplitters and mirrors, were made of Zerodure[®] which has a low coefficient of thermal expansion [65].

Finally, the photodiodes were placed in titanium cassettes mounted onto a titanium base [65]. The cassette and its base can expand or compress due to the surrounding temperature changes. Also, the detector mounts can contract or expand depending on the temperature. Both effects would lead to an additional beam walk which would be the same for the incoming reference and measurement beam.

10.4.2 Interpretation of the spot position changes

The analysis of the spot positions showed that the photodiodes drifted by less than a micrometre in any direction [61]. Likewise, the lateral and vertical offset of the beam at the FIOS would yield only minor spot position changes. The largest changes would originate from beam tilts since these multiply with the beam's propagation distance to the detector surface. I introduced here two beam tilt sources: the beam pointing variation induced by the FIOS and the beam tilt relative to the optical bench due to a curving baseplate.

In LPF, thermal stresses on the FIOSs have shown to tilt the measurement beam by up to $3 \mu\text{rad}/\text{K}$ [61]. Given the temperature decrease of 10°C during the cooldown, this would yield a tilt of $30 \mu\text{rad}$. This magnitude of angular tilt also corresponds to the spot position changes of the measurement beam in the reference and frequency interferometer (Fig. D.13). Since both FIOSs are identical in construction, we would expect the reference beam to be similarly affected.

However, the spot position changes of the reference beam yield a downtilt of approximately half the magnitude as the measurement beam. Therefore, we find a differential angle of approximately $15\ \mu\text{rad}$, which would be measured equally by the x1- and the x12-interferometer. Consequently, the differential tilt would be corrected by tilting the measurement beam via an angular rotation of the first test mass.

We can rule out that the FIOSs alone are responsible for the spot position changes in the x12-interferometer during the cooldown. The first reason is that the differential beam angle is too small to explain the coupling coefficient changes. According to our analytical model (7.21), the jump of the C_z coefficient during the cooldown demands a differential test mass angle of about $30\ \mu\text{rad}$. Since it needs a test mass tilt of half the size of the beam tilt to correct its alignment, only $7.5\ \mu\text{rad}$ can be accounted to the FIOS. In addition, the first test mass would fully compensate for the beam orientation. However, by the large η_2 readouts shown in Fig. 10.3 we would also expect a rotation of the second test mass. Note that also the beam walk on the detector due to the FIOS tilt has a negligible effect on the coupling coefficients.

The missing test mass rotations could be explained by stresses on the optical bench. In pre-launch tests, a bulge of up to $1.7\ \mu\text{m}$ has been demonstrated due to mechanical stresses of the optical bench mounts, which yielded a measurement beam walk of $37\ \mu\text{m}$ on the B-diode of the reference interferometer [61]. For such a deformation, we compute a beam tilt at the FIOS between 25 and $34\ \mu\text{rad}$ depending on how the FIOS tilts with the baseplate, i.e. which segment of the FIOS would be tangential to the assumed circularly curving baseplate. This beam tilt increases when the beam is reflected at the mirrors, which are also tilted due to the baseplate distortion. The same applies to the reference beam. However, the increase of the beam tilts depend on the number of reflections and the position of the mirrors, compare Fig. 2.5. Thus, we expect different beam orientations at the x1- and x12-interferometer leading to compensation by rotations of both test masses.

A comparison of the vertical beam walk in all interferometers – divided by the respective OPL – shows that during both cooldowns, the spot position at the A-diodes decreased further than in the B-diodes (see exemplary Fig. 10.4). Since I removed the effect of the OPL from the spot position readout in this comparison, this difference cannot originate from a beam tilt by the distorted FIOSs. As shown in Fig. 2.5, the offset from the centre of the optical bench along x is always larger for the A-diodes than for the B-diodes. Therefore, we can set up two scenarios explaining our observation: Either the baseplate arched upwards along the y -axis, i.e. it lifts along the optical axis between the test masses (like in Fig. 10.5), or it arched downwards along the x -axis, i.e. the centre between both test masses lowers. The first case would mainly affect the reference beam alignment in the x12-interferometers, while the second effect has a larger effect on the measurement beam.

Combined with the beam tilt by the FIOSs and the electrode housing rotations (Sec. 10.3), both baseplate distortions could potentially explain the vertical spot position changes and GRS readouts. To find the most likely deformation is the subject of our current analysis.

10.4.3 Note on the piston effects for deflected beams

I argued above that a tilt of the measurement beam at the FIOS would induce a beam walk on the test masses. I will discuss here the corresponding changes of the piston effect and how this couples into the TTL coefficients.

The beam walk on the first test mass depends only on the measurement beam's tilt angle. However, the beam walk on the second test mass is affected by rotations of the first test mass,

which correct the differential angle. Therefore, the beam walk on the second test mass also depends on the differential angle in the x1-interferometer.

Above, I derived from the spot position changes at the reference interferometer the corresponding beam tilts considering that they only originate from the FIOS. According to this analysis, the measurement beam was tilted by approximately $30\ \mu\text{rad}$ and the reference beam by $15\ \mu\text{rad}$ in pitch during the temperature decrease of 10°C . I subtract the differential angle from the measurement beam tilt after its reflection at the first test mass. Then, we find a vertical beam walk at the first test mass of $5.5\ \mu\text{m}$ and of $10.8\ \mu\text{m}$ at the second test mass. These beam shifts along the test masses change the C_η coefficient by up to $5.5\ \mu\text{m}/\text{rad}$, i.e. half of the coefficient change during the cooldown. These beam offsets do not couple into the C_z coefficient, which changed the most during the mission. Its changes can, therefore, only be explained with actual test mass tilts. However, this computed deviation of C_η could potentially explain the overestimation of this coefficient by the analytical model shown in Tab. 10.3.

I introduced a second explanation for the measured test mass tilts in Sec. 10.4.2, a curving optical bench. In this case, the beam walk in the detector is more difficult to estimate. In general, it can be expected that the beam walk on the first test mass is shorter since the beam would accumulate most of its tilt along its beam path. The offset at the second test mass would then depend on the propagation distance of the beam, its number and location of reflections, as well as the beam tilt correction by the first test mass. Accordingly, the beam walk on the second test mass could decrease but also increase compared to the beam walk on the first test mass. In either case, this beam walk would only affect the C_η coefficient demanding a test mass rotations to explain the C_z changes.

Like the C_η coefficient, also the C_φ coefficient is affected by beam shifts along the test masses. These changes would be smaller since also the beam tilts in yaw are assumed to be smaller based on the beam walk observed in the reference interferometer.

10.5 Summary of the Long-Term Coupling Coefficient Stability

In this chapter, I analysed the stability of the coupling coefficients over the entire mission time. I found that all coefficients but the C_z coefficient are long-term stable. However, the coefficients strongly depend on the temperature stability. Cooling the entire S/C down by 10°C , the coefficients rapidly changed. This is most obvious for the coefficients depending on changes in the xz -plane.

I concluded that these changes must originate from distortions of the optical system and, respectively, induced rotations of the test masses. The larger distortions in the xz -plane correspond to measurements of the FIOS and optical bench stability [P1, 61].

From the interpretation of the GRS angles and spot positions changes, I derived a scenario explaining the readouts as well as test mass rotations which would correspond to the coupling coefficient changes during the cooldown. I assume distortions of the FIOSs as well as a curving optical bench. Despite the changes being small in both cases, the beam tilts increase with temperature and, in the second case, increase further due to reflections.

Note that the presented explanation of the coefficient changes is only a first estimate. A more detailed analysis is needed to consolidate these findings.

Part IV

Outlook and Conclusion

Chapter 11

Take-Away Messages for LISA

We have seen in Sec. 6.2 that LISA will be much more complex than LPF. Also, the TTL mitigation techniques used in both missions partially differ. However, several of the findings presented in this work are also relevant for LISA.

11.1 Modelling Tilt-To-Length Coupling

The application of my analytical model (7.21) to the LPF data has demonstrated for the first time that modelling TTL coupling for complex space-based interferometers is possible. This model provides a physical explanation for the TTL coupling coefficient changes due to the test mass realignments.

To find this model, I accounted for a number of system parameters and test mass and beam tilts in the complete three-dimensional setup. These made the exact analytical equations long and complex. Also, the different coupling contributors are hard to distinguish on the basis of the complete measured TTL coupling noise. This complexity would even increase in the case of the LISA constellation. However, the series expansion of the LPF model for small angular tilts and the insertion of the constant setup parameters simplified it, providing a simple linear (or quadratic) TTL model. From the analysis presented in this thesis, we expect that an analogous model can be found for LISA by either modelling it or deriving the coupling coefficients from simulations or experiments (e.g., via the method introduced in Sec. 11.3).

11.2 Subtraction of Tilt-To-Length Coupling

A similarity between LPF and LISA is the subtraction of TTL coupling noise in post-processing. In both missions, a model was or will be fitted to the mission data using the DWS angular readouts. Due to the complexity of the LISA constellation, the respective model will contain more parameters than the LPF model [49].

I have demonstrated in Sec. 6.2.1 that a reduction of the TTL coupling by design or realignment is relevant for the successful subtraction of the TTL coupling. The larger the misalignments in the system, the larger are the subtraction coefficients. Since these coefficients multiply with the DWS readouts (and GRS readouts if used by the model), they simultaneously add sensing noise to the Δg measurement. Therefore, the mitigation of TTL noise in the signal will be better for

smaller initial TTL coupling.

Currently, the coupling coefficients for LISA are estimated to be of the order mm/rad [49], i.e. more than one order of magnitude larger than the coupling coefficients during the LPF mission.

The daily computation of the coupling coefficients during the LISA mission is planned to compensate for the drift of instrument alignment [49, TN4]. This strategy is advocated by our observation of the coefficient changes during the LPF mission.

11.3 Back-Up: Coefficient Calibration Scheme

The alignment yielding the best TTL suppression will be determined and applied on ground [TN4]. As the insufficient TTL subtraction in LPF before the test mass realignments (Fig. 6.3) showed, this optimization of the alignment is beneficial for a successful TTL subtraction via the fit model. Currently, no further realignments are planned after launch since the fit method would account for any TTL coupling changes in flight.

We are confident that this suppression strategy will yield the sensitivity required in LISA. Still, from our analysis of the LXE we can deduce a realignment strategy that could serve as a backup plan:

In the case that the coupling coefficients drift too strong in long-term time scales, the temperatures changes unintentionally, or the launch has a significant effect on the TTL coupling, a realignment might also be necessary for LISA. Such a realignment would then be based on a model, which interprets respective simulations and on-ground investigations. Assuming further that this realignment would not yield the expected TTL minimisation, a calibration scheme comparable to the LXE could help derive a proper model. I will introduce the principle idea of this calibration scheme here.

By changing the realignment parameters, e.g., the beam alignment [49], several times and computing the dedicated TTL coefficients, we would gain a set of such coefficients dependent on the parameter changes. Having more sets of coefficients than degrees of freedom of the considered realignment, a TTL model can be computed using a minimising scheme. The application of this method on the data of the LXE (Sec. 8.6) drives our confidence in this strategy. However, due to the complexity of LISA, more set-points would be needed than in the case of LPF. Also, due to the number of set-points, the application of the full scheme would take longer.

Mind that during the LXE injections had been applied to increase the TTL noise and, therefore, improved the fit of the coupling coefficients. However, such injections are possibly unnecessary when applying the calibration scheme. So, we have seen significant coefficient changes in the investigation of TTL coupling in the noise runs prior and after the test mass realignments in the early mission phase. These changes directly referred to the applied test mass rotations, which could be explained via my analytical model. If the realignments in LISA change the fitted TTL coupling coefficients in a comparable significant way, the daily data could be used for the derivation of the TTL model. This particularly means that the calibration scheme would not interrupt the scientific measurements except for the realignments themselves.

11.4 The Test Mass Interferometer Readout

We have seen in Sec. 8.9 that the applied injection frequencies are partially also visible in the measurements of the x1-interferometer, even though the included S/C accelerations make this readout noisier than the x12-interferometer measurements. The analogue to the x1-interferometer in LPF will be the test mass interferometer in LISA. Since two local beams interfere at this interferometer, its readout will characterise the optical system alignment without the need for the propagation of the data through TDI. Therefore, the data from this interferometer can potentially be used for a calibration of the test mass interferometer TTL coupling, provided that such calibration manoeuvres would be carried out.

However, the measurement of the test mass interferometer does also contain TTL noise originating from the system's centre of rotation (piston effect). Due to the LISA design choices, this noise will mostly cancel when the readouts of the test mass and the long-arm interferometer are combined. Therefore, a suppression of the TTL noise in the test mass interferometer alone, which cancels in the complete signal, would be counterproductive.

Moreover, any calibration should account for the fact that the noise in the test mass interferometer is, in general, assumed to be much smaller than the noise in the long-arm interferometer.

Chapter 12

Summary

A significant noise source in space-based laser interferometers is the coupling of angular and lateral motion of the S/C, or its test masses, into the interferometric phase readout. This noise is called tilt-to-length (TTL) coupling.

During the LPF mission, this coupling was the dominant noise source between 20 and 200 mHz. However, its analysis was difficult since no available model sufficiently described the physical relationship between the measured coupling and the test mass alignments. Consequently, the realignment of the test masses during the engineering days and in June 2016 did only partially subtracted the TTL noise. The residual coupling noise was then successfully subtracted via linear fit model, which, however, did not yield a physical explanation of its fit coefficients, either.

In order to understand the TTL coupling and its dependency on the test mass alignments better, a long cross-talk experiment (LXE) was performed during the LPF mission extension phase. Still, no available TTL model consistently described the induced TTL coupling.

For this reason, I started modelling TTL coupling analytically for most general setups and LPF particularly. I presented the results of my analysis in this thesis.

In the derivation of the general analytical TTL model, I distinguished between lateral and angular cross-coupling, geometric and non-geometric noise contributions, and jittering objects, which are either a reflecting mirror (e.g. a test mass) or a receiving system (e.g. a S/C). For all these cases, I explained the underlying mechanisms and provided, wherever possible, an analytical equation quantitatively describing this respective TTL coupling. Therefore, the results can be used not only for the characterisation of the coupling effects but also for the development of TTL suppression strategies. These include suppression via design, realignment and subtraction in post-processing.

The application of the found TTL equations to the LPF setup yielded the first analytical model successfully describing the TTL noise during the LPF mission. This model has been validated by the optical simulation software IfoCAD and the LPF mission data. In particular, for the LXE, the analytical model shows comparable results to the linear fit model, which was used during the LPF mission for the subtraction of TTL noise. In general, both models successfully subtract the injected TTL noise. Thereby, the analytical model also showed that the linearisation of the TTL effects at the angles describing the test mass alignments was sufficient. Second-order TTL noise could also be modelled but was negligible for the small jitter amplitude during the noise runs.

Furthermore, the LXE provided a database for additional investigations of TTL coupling models depending on the applied test mass set-points. First, the TTL fit model was changed by the addition or removal of assorted fit quantities in order to investigate the performances of these adapted models and the correlations in the original model. Each model yielded the same characteristic response to the test mass rotations and displacements. I showed further that the quality of noise subtraction of the fit at the injections frequencies mostly depended on the presence of TTL coupling noise at other frequencies. This interpretation was confirmed by an analysis of the noise contributors, which revealed that the coupling of S/C motion in the xz -plane was dominant during that time of the mission. Moreover, I reported that the data of the LXE could be used for a minimiser routine, which makes use of the fitted coupling coefficients and yields a TTL model that depends on the test mass alignment changes like the analytical model. Last, I showed that the TTL coupling noise is also visible in the readout of the x1-interferometer.

The analytical model not only consistently described the TTL coefficient changes induced in an experiment but also their response to the test mass realignment in the early mission phase. Therefore, I conclude that the analytical model provides a valuable tool for the TTL subtraction but also for the estimate of test mass realignments suppressing the TTL noise.

A long-term analysis of the fitted coupling coefficients revealed that not all coefficients are stable over a long mission duration. In particular, in the case of temperature changes, the optical system is distorted, yielding amongst other test mass rotations, thereby changing the TTL coupling. This was most significant in the xz -plane. I discussed the possible origin of the test mass rotations and presented several optical bench distortions that can potentially explain the readouts. The consolidation of these first findings is subject to our ongoing analysis.

In summary, we learned from the analysis of the TTL coupling in LPF that modelling TTL coupling for space-based laser interferometers is possible. However, the resulting models are complex and lengthy. On the other hand, such a model derived analytically or, e.g., by an interpretation of fit or experimental results for changed alignment parameters, yields the information on how to suppress TTL coupling via design or realignment. The latter is relevant for a successful subtraction of TTL coupling via a fit model.

Having understood the TTL coupling in LPF and its origins boosts our confidence that modelling and suppressing the TTL noise in LISA will also be successful. The minimisation of this noise in LISA improves its sensitivity to cosmic events revealing the mysteries of our universe.

Appendices

Appendix A

GRACE Follow-On

A.1 Mission and Instrument

For 15 years, from 2002 to 2017, the Gravity and Climate Experiment (GRACE) [66, 67] measured the Earth’s gravity field using a microwave ranging system. The measurement principle relied on the idea that heavy masses accelerate objects in free fall. GRACE consisted of two satellites orbiting Earth on a polar orbit about 450 km above its surface. The satellites followed each other at an average distance of about 220 km. Thereby, the leading S/C was accelerated first by a heavy mass, e.g., a mountain, increasing the distance between both S/C. After passing that object, it slowed down since the gravitational force of the object then acted in the other direction. The same happened to the trailing satellite with a time shift of roughly half a minute, i.e., the time this satellite needed to propagate the 220 km to the prior position of the leading S/C. This behaviour induced a dynamically varying distance between both satellites. By measuring the distance with a microwave ranging system, GRACE mapped the gravity field of the Earth and its changes over time [23, 66]. Its successor mission, the Gravity Recovery and Climate Experiment Follow-On (GRACE-FO) [23], was launched in May 2018. While based on the design of the original GRACE mission, it is additionally equipped with the laser ranging instrument (LRI) [24]. The LRI measures the distance changes via laser interferometers and is, therefore, the first laser interferometric range measurement system between two remote S/C. It performs as a technology demonstrator for future geodesy missions, but also for the gravitational wave detector LISA [23, 24].

In GRACE-FO, the optical axis between the centres of masses of both satellites is blocked by the microwave ranging system, such that the LRI is placed around it, see Fig. A.1. The LRI measures the distance changes of one round trip of the laser beams. Therefore, either of the S/C acts as master satellite and transmits a frequency stabilised beam (TX beam, wavelength $\lambda \approx 1064.5$ nm) to the transponder S/C. There, a fraction of the expanded incoming beam enters the S/C (RX beam) and interferes with the beam from a local oscillator (LO beam) at a QPD. The QPD measures the relative angle of the incoming beam via DWS (see Sec. 3.2.4). Additionally, the frequency difference between both beams can be extracted from the measurement. This difference is essential for heterodyne interferometry. The frequency difference at the quadrant diode is digitally locked to 10 MHz. To achieve that, the transponder laser must emit a beam with a frequency, that accounts for this difference as well as for the Doppler shift the RX beam accumulated, i.e.

$$\nu_{\text{transponder}} = \nu_{\text{master}} + \nu_{\text{Doppler-shift}} + 10 \text{ MHz} . \quad (\text{A.1})$$

The Doppler shift frequency $\nu_{\text{Doppler-shift}}$ contains the information about the relative S/C velocity

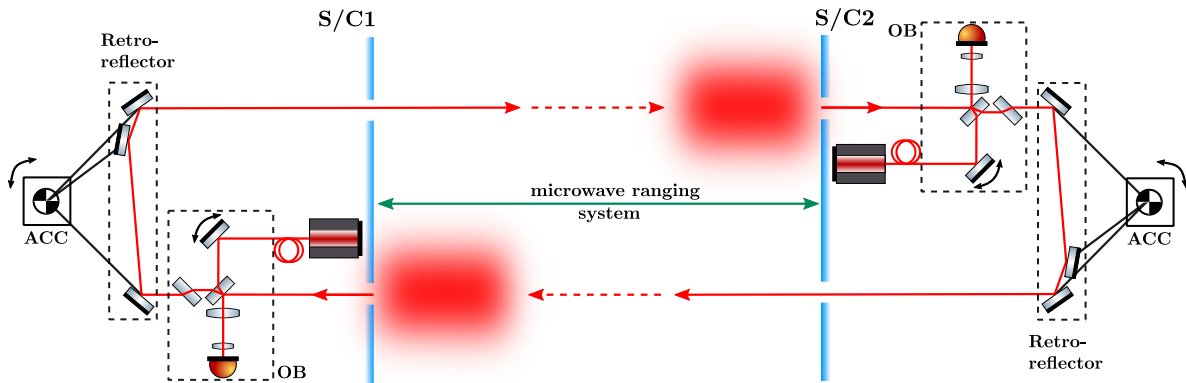


Figure A.1: Simplified optical layout of the laser ranging instrument onboard GRACE-FO (red beam path). The retroreflectors ensure that the beam is sent back anti-parallel to the path of the incoming beam. The rotatable mirrors on the optical bench (OB) are steering mirrors aligning the local beam to the incoming beam. In an optimal case, the vertex point of the retroreflector is placed in the centre of the local accelerometer (ACC), i.e. the centre of mass of the S/C. The microwave ranging system is aligned along the optical axis between both S/C (green).

and thus the distance changes. Meanwhile, the DWS signal of the quadrant diode provides the differential angle between both beams. It is used to align the LO beam to the RX beam via a fast steering mirror. In total, 10% of the LO beam interfere with the RX beam. The other 90% is reflected at the retroreflector, which ensures that this beam is sent back anti-parallel to the RX beam. This mechanism provides a sufficiently accurate pointing to the master S/C. The satellites are designed such that each can take the role of the master or transponder satellite, respectively [23, 24].

The LRI was switched on in June 2018 and worked at the first attempt. Since then, it has provided continuous data except for interruptions due to S/C operations. Its noise lies below the initial requirements. It achieves an accuracy of $10 \text{ nm}/\sqrt{\text{Hz}}$ at 40 mHz and $300 \text{ pm}/\sqrt{\text{Hz}}$ at 1 Hz [23].

The successful performance of the LRI is promising for LISA since the principle and the key parameters of the laser interferometric system applied in LISA match the LRI onboard GRACE-FO in many aspects. The measurement band of both missions is in the Millihertz (mHz) regime, heterodyne interferometry is used with a heterodyne frequency of a few Megahertz (MHz) and the received power is in the order of Nanowatts (nW). Furthermore, in LISA an offset-phase locked transponder scheme with a digital phase-locked loop phasemeter will be applied as well. In both missions, the laser frequency stability is achieved using an optical reference cavity. The locking procedures for the cavity as well as for the transponder loop are autonomously driven. The QPD measurements provide a DWS readout for angular correction. Last, the beam pointing follows a five degree of freedom (DOF) acquisition procedure. These DOFs are the pitch and yaw angles of the transmitting and the receiving S/C as well as the frequency difference between both beams [23].

A.2 Tilt-To-Length Coupling in GRACE-FO

The TTL coupling in GRACE-FO originates from S/C attitude jitter. Although it is suppressed by several alignment choices [24], it was still considered to be the limiting noise at low frequencies [23]. Here, I give an overview of the setup choices for TTL suppression.

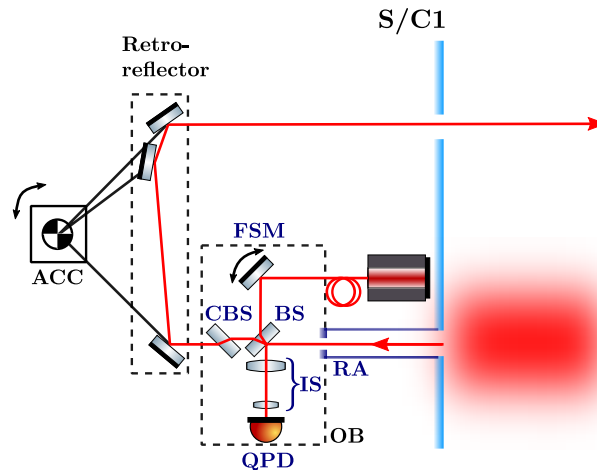


Figure A.2: Description of the setup on the optical bench (OB) of one GRACE-FO satellite. The received beam enters the optical bench via the receiving aperture (RA). There it combines with the local beam at the beamsplitter (BS). Both beams pass the imaging system (IS) and interfere at the quadrant photodiode (QPD). Thereby, the fast steering mirror (FSM) ensures zero DWS angles at the diode by aligning the local beam. Potential TTL coupling induced by the transmission through the BS, is balanced by the compensation plate or compensation beamsplitter (CBS) after the BS.

Ideally, the LRI would have been placed along the optical axis, i.e. the axis connecting the reference points of the accelerometers, since this would reduce the coupling from the S/C attitude jitter. However, this axis is occupied by the microwave ranging system. Thus, a triple mirror assembly was designed, directing the beam around the microwave system, see Fig. A.2. The assembly forms a retroreflector with its vertex point in the intersection point of the three mirror planes. The vertex of the retroreflector was placed as close as possible to the centre of mass of the S/C, i.e. its centre of rotation. Due to this choice, a number of parameters are not affected by the S/C attitude jitter. So firstly, the full round trip path length, which is two times the distance between the beam's origin and the plane normal to the beam direction intersecting the retroreflector's vertex point, remains invariant under S/C jitter. Second, the transmitted beam always propagates anti-parallel to the incident beam, ensuring a proper pointing. Further, the lateral offset of the incident and transmitted beam from an axis, which is parallel to these beams and intersects the vertex points, is the same. However, in practice, small deviations between the vertex point and the S/C's point of rotation will induce TTL coupling due to S/C jitter. Also, small misalignments of the mirrors can couple into the measurements [24].

Further TTL coupling is suppressed by design choices on the optical bench, see Fig. A.2. The beamcombiner is placed at an equal distance to the receiving aperture, where the fraction of the far beam enters the optical bench, and the fast steering mirror, that reflects the locally generated beam. The waist of the local beam is ideally situated at the steering mirror. The imaging system between the beam combiner and the QPD images the receiving aperture and the local beam waist onto the detector surface. Thus a tilt of either of the combined beams leads to a magnified tilt on the diode (i.e. eight times as large), but no beam walk. As we have seen in Sec. 5.2, suppressing the beam walk significantly reduces the non-geometric TTL coupling. Further, the imaging system matches the beam sizes onto the quadrant diode and improves the contrast of the interference signal. Since the receiving aperture and the beam waist have the same distance to the imaging system, aberrations of the latter are largely common to both beams. This reduces the coupling from beam tilts into the measurement. The residual coupling originates from different spatial profiles and misalignments of the beams [24].

The QPD behind the imaging system provides a DWS signal. The system autonomously uses this DWS signal to align the steering mirror, which rotates the local beam towards zero DWS. Hence, a maximal contrast and an optimal alignment of the beams is achieved. In particular, the alignment of the locally generated beam (i.e. the transmitted beam) to the received beam reduces the beam pointing error at the far spacecraft [24].

TTL coupling due to the transmission of the tilted beams through the beamcombiner is suppressed by placing a compensation beamsplitter of the same thickness and material but rotated by 90 degrees after the beamcombiner. Lastly, also far-field curvature errors generate TTL coupling but can hardly be avoided and have proven to be small [24].

The results of the GRACE-FO mission have shown that the setup choices successfully suppress TTL coupling making it no limiting noise source [23]. Furthermore, it is possible to model the TTL coupling terms making use of the centre-of-mass calibration manoeuvres [42].

Appendix B

Further Analytical Approaches

B.1 Longitudinal Displacement Strategies

In Sec. 5 I discussed TTL effects occurring in laser interferometers and their principal behaviour. Additionally, these effects can change when shifting the test mass or detector longitudinally. In this section, I describe the TTL coupling for longitudinal realignments and explain in which cases these can be applied to counteract other TTL effects.

B.1.1 Longitudinal Shifts of the Test Masses

In LPF the x -axis was the sensitive axis. Therefore, the longitudinal jitter of the test masses was particularly relevant since it directly affects the interferometric signal. In addition, any longitudinal offsets of the test masses affect the lever arm length and the point of reflection at the test masses. These changes would then also change the TTL coupling.

Within this section, I investigate the case where a test mass was slightly longitudinally displaced and kept stable at its new position for further measurements. Such a shift could accumulate with mission time but could also be applied intentionally to reduce or counteract other TTL coupling effects.

Analytically, this shift varies the length of the lever arm d_{lever} and the lateral offset d_{lat} of the point of reflection with respect to the centre of rotation, see Fig. B.1. In practice, the longitudinal offset d_{long} between the point of reflection and the centre of rotation could also change if the centre of rotation is not placed within the centre of mass of the test mass as I assume here, but at a different point, e.g., the centre of mass of the S/C. For a longitudinal shift Δx the new lever arm length becomes

$$d'_{\text{lever}} = d_{\text{lever}} + \Delta d_{\text{lever}} \tag{B.1}$$

$$= d_{\text{lever}} + \Delta x \frac{\cos(2\beta)}{\cos(\beta)} \tag{B.2}$$

or, assuming additionally a tilt of the detector by φ_{PD} ,

$$d'_{\text{lever}} = d_{\text{lever}} + \Delta x \frac{\cos(2\beta)}{\cos(\beta) \cos(\varphi_{\text{PD}})}. \tag{B.3}$$

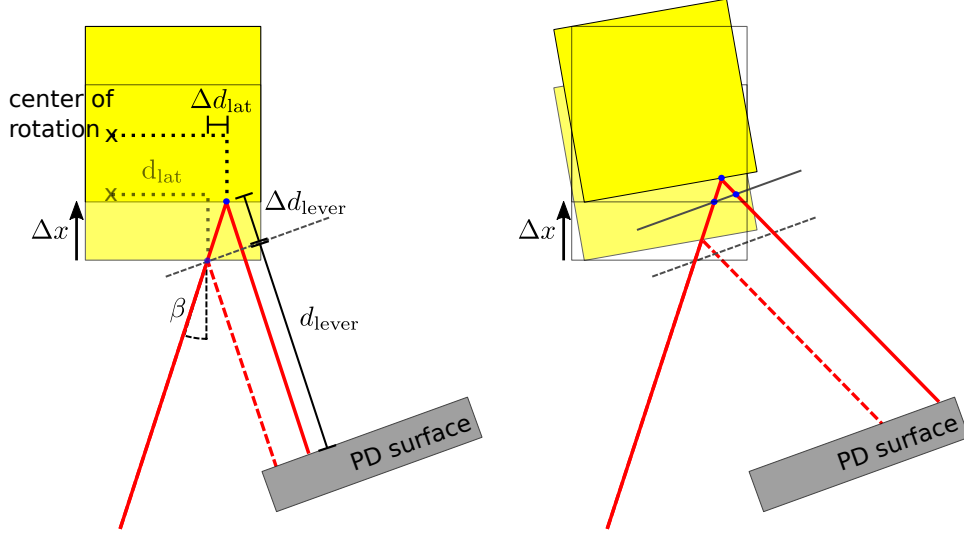


Figure B.1: A longitudinal shift of a test mass changes the distance the beam propagates nominally to the detector surface as well as (for $\beta \neq 0$, here $\beta < 0$) the point of reflection at the test mass surfaces. The latter affects the lateral difference between the point of reflection and the centre of rotation.

The lateral offset of the centre of rotation changes to

$$d'_{\text{lat}} = d_{\text{lat}} + \Delta d_{\text{lat}} \quad (\text{B.4})$$

$$= d_{\text{lat}} + \Delta x \tan(\beta). \quad (\text{B.5})$$

The offset d'_{lat} only changes, if the angle of incidence β is not zero. In this case, we can minimise the lateral piston effect by applying an offset Δx such that d'_{lat} in Eq. (B.5) becomes zero.

Inserting the replacements (B.5) and (B.2) into the OPDs derived for the lever arm (Eq. (5.2)) and the piston effect (Eq. (5.11)), we get the OPD for the changed setup.

$$\text{OPD}'_{\text{lever}} = \text{OPD}_{\text{lever}} + \Delta x \cos(2\beta) \sec(\beta) [\sec(2\varphi) - 1] \quad (\text{B.6})$$

$$\approx \text{OPD}_{\text{lever}} + 2\Delta x \cos(2\beta) \sec(\beta) \varphi^2, \quad (\text{B.7})$$

$$\text{OPD}'_{\text{piston}} = \text{OPD}_{\text{piston}} - 2\Delta x \sec(2\varphi) \cos(\beta + \varphi) \tan(\beta) \sin(\varphi) \quad (\text{B.8})$$

$$\approx \text{OPD}_{\text{piston}} - 2\Delta x \sin(\beta) \varphi + 2\Delta x \sin(\beta) \tan(\beta) \varphi^2. \quad (\text{B.9})$$

Thus the longitudinal displacement generates additional geometric second-order lever arm coupling and new first- and second-order piston coupling terms.

Next, I investigate how the longitudinal test mass shift changes the non-geometric signal contribution. Therefore, I derive the dependence of the beam walk along the detector surface on the longitudinal shifts. We find in total

$$y'_{\text{im}} = y_{\text{im}} + \Delta x \frac{2 \sin(\beta)}{\cos(\varphi_{\text{PD}})} + \Delta y_{\text{ilever}} + \Delta y_{\text{ipiston}}, \quad (\text{B.10})$$

where

$$\Delta y_{\text{ilever}} \approx -2\Delta x \cos(2\beta) \sec(\beta) \varphi, \quad (\text{B.11})$$

$$\Delta y_{\text{ipiston}} \approx -2\Delta x \sin(\beta) [\tan(\beta) \varphi - \varphi^2]. \quad (\text{B.12})$$

I insert the changed beam walk (Eq. (B.10)) into the corresponding non-geometric LPS, e.g., Eq. (5.60) for large SEPDS, yielding

$$\text{LPS}_{\text{ng}}(x'_{im}(\varphi_{\text{PD}} = 0)) \approx \text{LPS}_{\text{ng}} + 2\Delta x [\sin(\beta) \varphi - \sin(\beta) \tan(\beta) \varphi^2 - \cos(2\beta) \sec(\beta) \varphi^2]. \quad (\text{B.13})$$

Therefore, we find for setups with equal beam parameters and large single element diodes that the longitudinal shift cancels in the full LPS:

$$\text{LPS}' = \text{OPD}'_{\text{lever}} + \text{OPD}'_{\text{piston}} + \text{LPS}_{\text{ng}}(x'_{im}(\varphi_{\text{PD}} = 0)) \quad (\text{B.14})$$

$$\approx \text{OPD} + 2\Delta x [-\sin(\beta) \varphi + \sin(\beta) \tan(\beta) \varphi^2 + \cos(2\beta) \sec(\beta) \varphi^2] \quad (\text{B.15})$$

$$+ \text{LPS}_{\text{ng}} + 2\Delta x [\sin(\beta) \varphi - \sin(\beta) \tan(\beta) \varphi^2 - \cos(2\beta) \sec(\beta) \varphi^2] \quad (\text{B.16})$$

$$= \text{LPS}.$$

However, this equality breaks for the likely case of unequal beam parameters or beam clipping at the detector surface. Here, we find additional first- and second-order coupling. Given that the linear coupling is dominant, a longitudinal shift can be used to counteract the other linear TTL effects, e.g., by the piston effect.

B.1.2 Longitudinal Shifts of the Detector

In this section, I will evaluate the TTL effect induced by intentional displacements of the detector analytically. My derivation applies to the case of a jittering reference frame as well as the case of a jittering mirror.

Let the incident angles of the beams interfering at the shifted detector be given by $\varphi_{m,r}$. The detector shift of Δx_{PD} in longitudinal direction, i.e. along the sensitive axis, changes the OPD of both beams to

$$\text{OPD}' = \text{OPD} - \Delta x_{\text{PD}} \left(\frac{1}{\cos(\varphi_m)} - \frac{1}{\cos(\varphi_r)} \right). \quad (\text{B.17})$$

Assuming a static detector displacement and investigating the variation of the length signal due to the tilts of the measurement beam, this gives

$$\text{OPD}' \approx \text{OPD} - \frac{1}{2} \Delta x_{\text{PD}} \varphi_m^2. \quad (\text{B.18})$$

Additionally to the OPD, the beam walk is affected by longitudinal detector shifts. We find

$$y'_{im} = y_{im} + \Delta x_{\text{PD}} \tan(\varphi_m) \approx y_{im} + \Delta x_{\text{PD}} \varphi_m, \quad (\text{B.19})$$

$$y'_{ir} = y_{ir} + \Delta x_{\text{PD}} \tan(\varphi_r) \approx y_{ir} + \Delta x_{\text{PD}} \varphi_r. \quad (\text{B.20})$$

For the ideal case of two identical beams interfering at a large single element diode (Eq. (5.58)), we further find that the changes in the total LPS cancel except a reference beam angle dependent term, i.e.

$$\text{LPS}' \approx \left(\text{OPD} - \frac{1}{2} \Delta x_{\text{PD}} \varphi_m^2 \right) + \left(\text{LPS}_{\text{ng}} + \frac{1}{2} \Delta x_{\text{PD}} \varphi_m^2 - \Delta x \varphi_m \varphi_r \right) \quad (\text{B.21})$$

$$= \text{LPS} - \Delta x_{\text{PD}} \varphi_m \varphi_r. \quad (\text{B.22})$$

In summary, a longitudinal shift of the detector will add linear TTL coupling in all setups where the reference beam does not hit the detector at normal incidence. Additionally, we find second-order TTL coupling in cases, where the OPD and non-geometric LPS term do not cancel, e.g., for non-identical beams.

Note that these findings hold only for the application of the LPF signal definition. It has been shown in [39, 43] that longitudinal shifts add second-order TTL coupling when having QPDs and applying the AP signal definition. Therefore, it can be used to counteract TTL coupling of different origins.

B.2 Intuitive Approach: Signal Cancellation for Identical Beams

I have analytically proven in Sec. 5.2 that for two identical beams with one rotated around a point along the shared beam axis, i.e. with a longitudinal offset from the point of detection, the LPS cancels. In this section, I present an intuitive explanation for the vanishing TTL coupling [P3]. Since this approach applies to the lever arm effect as well as the receiver jitter with a longitudinal offset of the centre of rotation, I will assume here general beam tilts φ_m . My intuitive approach is departed in two steps. At first, I will show that the amplitude profile of the interfering beams is plane-symmetric around the centre of both beams' points of incidence. In the second step, I will examine the local phase differences. We find them to be antisymmetric around the same centre. Since the amplitude profile scales the phase differences, the latter will cancel out in the full interferometric readout.

B.2.1 Symmetry of the Amplitude Profile

I assume the setup depicted in Fig. B.2: The measurement beam (red) rotates around a pivot along its propagation axis. The distance from the point of detection to the centre of rotation is d_{long} . It is defined as negative if the beam passes the centre of rotation before impinging at the detector, and positive otherwise. This offset generates a beam walk along the detector surface when the beam rotates by φ_m . Hence the measurement beam's point of detection varies by (compare Eq. (5.64) for $d_{\text{lat}} = 0$)

$$y_{im} \approx d_{\text{long}} \varphi_m, \quad (\text{B.23})$$

while the reference beam stays constant, i.e. $y_{ir} = 0$. The radial distances of the beams in the detector coordinate system are then

$$r_m^2 = (y - y_{im})^2 \cos^2(\varphi_m) + z^2 \approx y^2(1 - \varphi_m^2) - 2y d_{\text{long}} \varphi_m + d_{\text{long}}^2 \varphi_m^2 + z^2 \quad (\text{B.24})$$

$$r_r^2 = y^2 + z^2. \quad (\text{B.25})$$

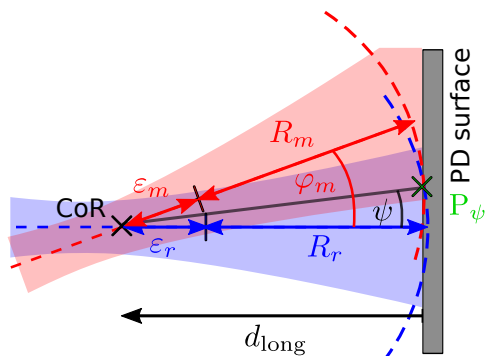


Figure B.2: Illustration of the measurement's (red) and reference's (blue) beam properties when their wavefront hits the point of interest P_ψ . This is the point at the detector a ray would hit that is rotated by an angle ψ with respect to the reference beam. The distance from the detector surface to the centre of rotation is d_{long} , i.e. negative in this figure. The radii of curvature of the wavefronts intersecting the point of interest are $R_{m,r}$. Correspondingly, $\varepsilon_{m,r}$ are defined as the distance between the centre of rotation and the beams centres of curvature.

I apply the same coordinate transformation to the beams' longitudinal coordinates, i.e.

$$x_m = x_0 + \frac{1}{2} d_{\text{long}} \varphi_m^2 - y \varphi_m, \quad (\text{B.26})$$

$$x_r = x_0, \quad (\text{B.27})$$

where x_0 denotes the distance from waist of a non-tilted beam at the detector. I substitute these into the amplitude of the interfering beams (compare derivation in Sec. 3.2.1)

$$A(y, z) = 2E_0^2 \frac{w_0^2}{w(x_m)w(x_r)} \exp \left[\frac{-r_m^2}{w(x_m)^2} + \frac{-r_r^2}{w(x_r)^2} \right]. \quad (\text{B.28})$$

We find that

$$A(-y + y_c, z) \approx A(y + y_c, z). \quad (\text{B.29})$$

with the y -coordinate

$$y_c = \frac{d_{\text{long}}}{2} \quad (\text{B.30})$$

defining the centre between the two points of incidence. Hence the amplitude profile is symmetric around the plane through this centre.

B.2.2 Cancellation of the Phase Differences

In this subsection, I examine the local phase differences at the detector surface. For simplification, I will only investigate the phase differences in the two-dimensional plane in which I will apply the rotation of the beam. This is valid in a small angle approximation: we see a constant phase difference between the two beams in the projection to the orthogonal plane. In this two-dimensional investigation, I will show that the phase difference at the centre point between the points of incidence is zero. Moreover, the local phase differences are antisymmetric around this centre. Therefore, I study the differences at an arbitrary point P_ψ on the detector surface, which is defined as the point the axis of a beam that is tilted by an angle ψ with respect to the reference beam would hit, see Fig. B.2. The absolute distance between the centre of rotation and this point is

$$|\vec{p}_\psi - \vec{p}_{\text{CoR}}| = |d_{\text{long}} \sec(\psi)| \approx |d_{\text{long}} (1 + \psi^2)| \quad (\text{B.31})$$

and for the offset on the detector with respect to the nominal point of detection we find

$$y_{i\psi} = d_{\text{long}} \tan(\psi) \approx d_{\text{long}} \psi. \quad (\text{B.32})$$

Both beams propagate a certain additional distance $\delta_{m,r}$ until their wavefronts hit this point.

In the following, I will derive these $\delta_{m,r}$ from geometric properties. Therefore, I present three equalities related to $\delta_{m,r}$ and solve the corresponding system of equations for these lengths.

Let $R_{m,r}$ define the radii of curvature of the beams crossing the point of interest. The centres of wavefront curvature do not necessarily coincide with the centre of rotation. Hence I define $\varepsilon_{m,r}$ as the distance from the centre of rotation to the centres of curvature, as illustrated in Fig. B.2. Depending on the setup, the $\varepsilon_{m,r}$ can be positive or negative. Both beams travel a different path length than the propagation distance in the nominal, non-tilted case until their wavefronts intersect the point of interest P_ψ . I account for these path length differences by $\delta_{m,r}$. Hence the sum of the radii of curvature $R_{m,r}$ and the auxiliary length $\varepsilon_{m,r}$ equal the difference between

the longitudinal distance between the detector surface and the centre of rotation d_{long} and the distance of interest $\delta_{m,r}$,

$$R_{m,r} + \varepsilon_{m,r} = -d_{\text{long}} + \delta_{m,r}. \quad (\text{B.33})$$

Due to my sign convention, d_{long} is negative in this equation.

As the distance from waist also changes in dependence on the investigated point by $\delta_{m,r}$, i.e.

$$x_{m,r} = x_0 + \delta_{m,r}, \quad (\text{B.34})$$

I determine the radii of curvature accordingly,

$$R_{m,r} = (x_0 + \delta_{m,r}) \left(1 + \left(\frac{x_R}{x_0 + \delta_{m,r}} \right)^2 \right). \quad (\text{B.35})$$

For further simplifications, I assume that $\delta_{m,r}$ is small, which is valid for common setups and the small angle approximation. Thus, I can expand $R_{m,r}$ in $\delta_{m,r}$ to

$$R_{m,r} \approx R_0 + \delta_{m,r} \left(2 - \frac{R_0}{x_0} \right). \quad (\text{B.36})$$

I define x_0 and R_0 as the nominal distance from waist and radius of curvature, i.e. the value we respectively get for a nominal beam when its axis hits the detector surface.

From trigonometric relationships, I derive a third set of equations. The centres of rotation and wavefront curvature, and the point of interest form a triangle for the measurement and the reference beam respectively. With the law of cosines it follows

$$\begin{aligned} R_m^2 &= \varepsilon_m^2 + (d_{\text{long}} \sec(\psi))^2 - 2d_{\text{long}} \varepsilon_m \sec(\psi) \cos(\varphi_m - \psi) \\ R_r^2 &= \varepsilon_r^2 + (d_{\text{long}} \sec(\psi))^2 - 2d_{\text{long}} \varepsilon_r \sec(\psi) \cos(\psi) \\ &= \varepsilon_r^2 + (d_{\text{long}} \sec(\psi))^2 - 2d_{\text{long}} \varepsilon_r \end{aligned} \quad (\text{B.37})$$

Given the set of equations (B.33), (B.36) and (B.37), I solve this system of equations for $\delta_{m,r}$ and find

$$\delta_m(\psi) \approx \frac{d_{\text{long}}}{2} (\varphi_m^2 - 2\varphi_m\psi) + \frac{d_{\text{long}}^2}{2R_0} (\varphi_m - \psi)^2, \quad (\text{B.38})$$

$$\delta_r(\psi) \approx \frac{d_{\text{long}}^2}{2R_0} \psi^2. \quad (\text{B.39})$$

First, I will show now that the local phase difference $\delta_m - \delta_r$ at the centre between the two points of incidence is zero. Assuming a small tilt angle φ_m , $\psi = \varphi_m/2$ defines in a good approximation that centre. I insert that angle in Eqs. (B.38) and (B.39) and find

$$\delta_m(\varphi_m/2) - \delta_r(\varphi_m/2) \approx \left(0 + \frac{d_{\text{long}}^2}{2R_0} \frac{\varphi_m^2}{4} \right) - \left(\frac{d_{\text{long}}^2}{2R_0} \frac{\varphi_m^2}{4} \right) = 0, \quad (\text{B.40})$$

which proves my claim. This was also expected for symmetry reasons since the wavefronts intersecting along the bisecting line from the centre of rotation to the defined centre point belong to beams having propagated the same distance.

Further, I will show that the phase differences cancel each other symmetrically around that centre. This holds if for arbitrary (but small) ψ the following equation holds:

$$[\delta_m(\psi) - \delta_r(\psi)] + [\delta_m(\varphi_m - \psi) - \delta_r(\varphi_m - \psi)] = 0. \quad (\text{B.41})$$

In fact, we find

$$\begin{aligned}
 & [\delta_m(\psi) - \delta_r(\psi)] + [\delta_m(\varphi_m - \psi) - \delta_r(\varphi_m - \psi)] \\
 &= \left[\frac{d_{\text{long}}(d_{\text{long}} - R_0)}{2R_0} (\varphi_m^2 - 2\varphi_m\psi) \right] + \left[\frac{d_{\text{long}}(d_{\text{long}} - R_0)}{2R_0} (-\varphi_m^2 + 2\varphi_m\psi) \right] \\
 &= 0
 \end{aligned} \tag{B.42}$$

proving the statement.

B.2.3 Summarising the findings

In summary, I have first shown that the intensity profile of the interfering beams is symmetric with respect to the plane through the centre between the two centres of incidence. Second, the phase differences are antisymmetric around that point. Since any two points arranged symmetrically around that centre (defined by $\psi = \varphi_m/2$) are weighted equally by the intensity, they all cancel each other. A measured LPS would hence also become zero.

B.3 Tilt-Dependency of the Beam Parameters

When describing the non-geometric TTL effects in Sec. 5.2, I neglected the tilt-dependency of the distance from waist x_m , i.e.

$$x_m(\varphi_m) = x_m(\varphi_m = 0) + \text{OPD}. \tag{B.43}$$

While these length changes were neglected in the ikx_m -term in order to distinguish between the geometric and non-geometric effects, I further removed the tilt-dependency for simplification when inserting the distance from waist into the radius of curvature $R(x_b)$, the waist size $w(x_b)$ and the Gouy phase $\zeta(x_b)$ functions. Here I validate this choice.

For a complete examination, I consider two beams with unequal beam parameters and beam offsets on the detector surface. In Sec. 5.2.1, I derived for this case the non-geometric LPS (5.60), i.e. $\text{LPS}_{\text{ng}}[x_m(\varphi_m = 0)]$. Including the tilt-dependency (B.43), Eq. (5.60) extends to

$$\begin{aligned}
 \text{LPS}_{\text{ng}} &\approx \text{LPS}_{\text{ng}}[x_m(\varphi_m = 0)] \\
 &+ \text{OPD} \left\{ \left[\frac{(y_{im} - y_{ir})^2 [(x_{Rm} + x_{Rr})^2 - (x_m - x_r)^2]}{2[(x_{Rm} + x_{Rr})^2 + (x_m - x_r)^2]^2} \right] \right. \\
 &\quad \left. + \left[\frac{(y_{im} - y_{ir}) [(x_{Rm} + x_{Rr})^2 x_m - (x_{Rm}^2 - x_{Rr}^2)(x_m - x_r) - (x_m - x_r)^2 x_r] \varphi_m}{[(x_{Rm} + x_{Rr})^2 + (x_m - x_r)^2]^2} \right] \right\} \\
 &+ \text{OPD}^2 \left\{ \left[\frac{(y_{im} - y_{ir})^2 [-3(x_{Rm} + x_{Rr})^2 + (x_m - x_r)^2] (x_m - x_r)}{[(x_{Rm} + x_{Rr})^2 + (x_m - x_r)^2]^3} \right] \right\},
 \end{aligned} \tag{B.44}$$

whereby the OPD is a series expression in φ_m up to second-order.

We see that a tilt-dependency of the distance from waist x_m does not only add higher-order terms to the non-geometric LPS. However, all added terms are small in interferometers. We find two terms with the multiplicand $(y_{im} - y_{ir})^2$. In order to receive a significant signal, the distance between both beams' points of detection must be small. Having this value squared and

multiplied with the considerable small OPD makes these terms negligible. Further, we encounter a product of the OPD, the difference between the points of detection, the incoming angles φ_m and the fraction of beam parameters. The first three named parameters are small, also making this term negligible.

In summary, it is $LPS_{ng} \approx LPS_{ng}[x_m(\varphi_m = 0)]$. It was therefore valid to neglect the beam tilt dependency of the measurement beam's distance from waist in Sec. 5.2.

Appendix C

Code: Derivation of Analytical TTL Formulas for LPF

The analytical TTL equations gain more complexity, the more components and dimensions the investigated setup has. This is visible in the case of LPF. Therefore, I implemented the relevant characteristics of the beams and components of the setup in Mathematica. Built on this, I derived the OPDs originating from the different TTL effects and the corresponding beam walk on the detector.

C.1 Derivation of Optical Path Length Differences and Beam Walk

I establish first the rotation matrices and direction vectors that are used to define the beams and relevant components in Sec. C.1.1. These are then used in Sec. C.1.2 to derive the OPD and the beam walk due to the lever arm, piston and transmissive components' effect.

To describe the rotations of the components, not only rotation matrices but also rotation transformations (i.e. for the piston effect) must be applied.

Definition C.1 Rotation Matrices

Definition of the rotation matrices:

$$\mathbf{M}_{\text{yaw}}(\alpha) = \begin{pmatrix} \cos(\alpha) & -\sin(\alpha) & 0 \\ \sin(\alpha) & \cos(\alpha) & 0 \\ 0 & 0 & 1 \end{pmatrix} \quad \mathbf{M}_{\text{pitch}}(\alpha) = \begin{pmatrix} \cos(\alpha) & 0 & \sin(\alpha) \\ 0 & 1 & 0 \\ -\sin(\alpha) & 0 & \cos(\alpha) \end{pmatrix}$$

Rotations around a certain point \mathbf{p} are applied by a rotation transformation (RT) function:

$$\mathbf{RT}_i(\alpha, \mathbf{p}) = \begin{bmatrix} \mathbf{M}_i(\alpha) & \mathbf{p} - \mathbf{M}_i(\alpha)\mathbf{p} \\ \mathbf{0} & 1 \end{bmatrix} \quad \text{for } i \in \{\text{yaw}, \text{pitch}\}$$

I further define a vector whose orientation is given in propagation angles, as are the incoming beams. This general vector representation can be used to define general surfaces, which we will need in Sec. C.1.1.

Definition C.2 Direction Vectors

Definition of a vector of length d with propagation angles $\alpha_{\text{pitch}}, \alpha_{\text{yaw}}$:

$$\mathbf{q}(d, \alpha_{\text{yaw}}, \alpha_{\text{pitch}}) = \frac{d}{\sqrt{\cos(\alpha_{\text{pitch}})^2 + \cos(\alpha_{\text{yaw}})^2 \sin(\alpha_{\text{pitch}})^2}} \begin{pmatrix} \cos(\alpha_{\text{yaw}}) \cos(\alpha_{\text{pitch}}) \\ \sin(\alpha_{\text{yaw}}) \cos(\alpha_{\text{pitch}}) \\ \cos(\alpha_{\text{yaw}}) \sin(\alpha_{\text{pitch}}) \end{pmatrix}$$

I use \mathbf{q} to define two special cases:

$$\mathbf{p}(d) = \mathbf{q}(d, 0, 0) = \begin{pmatrix} d \\ 0 \\ 0 \end{pmatrix} \quad \mathbf{SF}(y, z) = \mathbf{q}\left(y, \frac{\pi}{2}, 0\right) + \mathbf{q}\left(z, 0, \frac{\pi}{2}\right) = \begin{pmatrix} 0 \\ y \\ z \end{pmatrix}$$

C.1.1 Definition of Beams and Components

In the derivation, I am not interested in the absolute position of the components since I will only need their relative position to other investigated components. Therefore, I define here only their surfaces and surface normal vectors.

Most interesting for the computation are the test masses. In LPF they do not only rotate around their centre of mass but also around the rotation centre of the satellite. I account for both in the definition of the surface and normal vector properties.

Definition C.3 Test Masses in LPF

Centres of rotation with respect to points of reflection at TMs. The subindex denotes the object whose centre of mass defines the centre rotation:

$$\mathbf{p}_{\text{TM},i} = - \begin{pmatrix} d_{\text{longTM},i} \\ d_{\text{latTM},i} \\ d_{\text{vertTM},i} \end{pmatrix} \quad \mathbf{p}_{\text{OB},i} = - \begin{pmatrix} d_{\text{longOB},i} \\ d_{\text{latOB},i} \\ d_{\text{vertOB},i} \end{pmatrix} \quad \text{for } i \in \{1, 2\}$$

Rotated reflective mass surfaces:

$$\begin{bmatrix} \mathbf{TM}_{\text{surf},i} \\ 1 \end{bmatrix} = \mathbf{RT}_{\text{pitch}}(\eta_{\text{ob}}, \mathbf{p}_{\text{OB},i}) \mathbf{RT}_{\text{pitch}}(\eta_i, \mathbf{p}_{\text{TM},i}) \mathbf{RT}_{\text{yaw}}(\varphi_{\text{ob}}, \mathbf{p}_{\text{OB},i}) \mathbf{RT}_i(\varphi_i, \mathbf{p}_{\text{TM},i}) \begin{bmatrix} \mathbf{SF}(y_{\text{tm}}, z_{\text{tm}}) \\ 1 \end{bmatrix}$$

Normal vector of the test mass' reflective surface pointing away from its centre:

$$\mathbf{TM}_{\text{nv},i} = \mathbf{M}_{\text{pitch}}(\eta_i - \eta_{\text{ob}}) \mathbf{M}_{\text{yaw}}(\varphi_i - \varphi_{\text{ob}}) \mathbf{p}(-1^i)$$

Next I define the windows, which have the same properties each except for the orientation of their normal vectors.

Definition C.4 Windows

Window surfaces: $\mathbf{WIN}_{\text{surf}}(t_{\text{tc}}) = \mathbf{q}(t_{\text{tc}}, 0, 0) + \mathbf{SF}(y_{\text{win}}, z_{\text{win}})$

Window normal vector: $\mathbf{WIN}_{\text{nv},i} = \mathbf{q}(-1^i, 0, 0)$

In terms of the photodiode, I only need its surface orientation given at a certain distance in the

nominal beam direction.

Definition C.5 Photodiode

Position and surface of the photodiode:

$$\mathbf{PD}(d, \beta_y, \beta_z, \varphi_{\text{PD}}) = \mathbf{q}(-d, -\beta_y, -\beta_z) + \mathbf{M}_{\text{yaw}}(\varphi_{\text{PD}}) \begin{pmatrix} y_{\text{PD}} \tan(\beta_y) + z_{\text{PD}} \tan(\beta_z) \\ y_{\text{PD}} \\ z_{\text{PD}} \end{pmatrix}$$

Having defined all relevant components, I compute the directions of the beams before and after the test mass reflections. The directions of the reflected beams depend on the alignment of the test mass surfaces.

Definition C.6 Beam Directions

Incoming beam at TM1: $\mathbf{b}_{\text{in1}} = \mathbf{q}(1, \beta_{y1}, \beta_z)$
 Beam reflected at TM1: $\mathbf{b}_{\text{refl1}} = \mathbf{b}_{\text{in1}} - 2(\mathbf{b}_{\text{in1}} \cdot \mathbf{TM}_{\text{nv1}}) \mathbf{TM}_{\text{nv1}}$
 Incoming beam at TM2: $\mathbf{b}_{\text{in2}} = \mathbf{M}_{\text{yaw}}(\beta_{y2} + \beta_{y1}) \mathbf{b}_{\text{refl1}}$
 Beam reflected at TM2: $\mathbf{b}_{\text{refl2}} = \mathbf{b}_{\text{in2}} - 2(\mathbf{b}_{\text{in2}} \cdot \mathbf{TM}_{\text{nv2}}) \mathbf{TM}_{\text{nv2}}$

I derive the directions of the beams within the windows applying the three-dimensional convention of Snell's law (5.37).

Definition C.7 Beam in Window

Snell's three-dimensional law applied to the refraction at the windows onboard LPF.

$$\mathbf{b}_{\text{tc}}(\mathbf{b}_{\text{vac}}, \mathbf{WIN}_{\text{nv}}) = \frac{1}{n_{\text{tc}}} \mathbf{b}_{\text{vac}} - \left(\sqrt{1 - \frac{1}{n_{\text{tc}}^2} \left[1 - (\mathbf{b}_{\text{vac}} \cdot \mathbf{WIN}_{\text{nv}})^2 \right]} + \frac{\mathbf{b}_{\text{vac}} \cdot \mathbf{WIN}_{\text{nv}}}{n_{\text{tc}}} \right) \mathbf{WIN}_{\text{nv}}$$

Beam refracting WIN1: $\mathbf{b}_{\text{tc1}} = \mathbf{b}_{\text{tc}}(\mathbf{b}_{\text{refl1}}, \mathbf{WIN1}_{\text{nv}})$
 Beam refracting WIN2 the first time: $\mathbf{b}_{\text{tc2A}} = \mathbf{b}_{\text{tc}}(\mathbf{b}_{\text{in2}}, \mathbf{WIN2}_{\text{nv}})$
 Beam refracting WIN2 the second time: $\mathbf{b}_{\text{tc2B}} = \mathbf{b}_{\text{tc}}(\mathbf{b}_{\text{refl2}}, \mathbf{WIN2}_{\text{nv}})$

C.1.2 The TTL Effects

In LPF we encounter lever arm and piston effects originating from both test masses. Moreover, the beam refracts at windows three times after the first reflection at a test mass: once at the first window and then before and after the TM2-reflection at the second window. All these contribute to the full TTL effect, which I consider for LPF.

In this section, I explain how to derive the three-dimensional equations for these effects using the software Mathematica. Thereby, I make use of the definitions of the components and beam direction in Sec. C.1.1. The points and distances I compute in the following algorithms rely on the theory discussed in Sec. 5.1.

First, I derive the geometric lever arm effect and its corresponding beam walk. Within this derivation, I neglect the windows along the beam path.

Algorithm C.1 Lever Arm Effect

1. Computation of the beam's propagation distance from TM1 to TM2:

Start point: $\mathbf{s}_{\text{start}} = -d_{\text{lever1}} \mathbf{b}_{\text{in2}} |_{\varphi_{\text{ob}}=0, \eta_{\text{ob}}=0, \varphi_1=0, \eta_1=0}$ TM2 surface: $\mathbf{TM2}_{\text{lever}} = \mathbf{TM}_{\text{surf2}} |_{\mathbf{p}_{\text{OB2}}=0, \mathbf{p}_{\text{TM2}}=0}$ **sol1 = Solve** $\mathbf{s}_{\text{start}} + x \mathbf{b}_{\text{in2}} = \mathbf{TM2}_{\text{lever}}$ **for** $\{x, y_{\text{tm}}, z_{\text{tm}}\}$

2. Computation of the distance from the reflection point to the photodiode:

Start point: $\mathbf{s}_{\text{refl}} = \mathbf{TM2}_{\text{lever}} |_{\text{sol1}}$ **sol2 = Solve** $\mathbf{s}_{\text{refl}} + x \mathbf{b}_{\text{refl2}} = \mathbf{PD}(d_{\text{lever2}}, \beta_{y2}, \beta_z, \varphi_{\text{PD}})$ **for** $\{x, y_{\text{PD}}, z_{\text{PD}}\}$

3. Sum up to the full lever arm effect:

OPD_{lever} = $(x|_{\text{sol1}} - d_{\text{lever1}}) + (x|_{\text{sol2}} - d_{\text{lever2}})$ $y_{\text{im,lever}} = y_{\text{PD}} |_{\text{sol2}}$ $z_{\text{im,lever}} = z_{\text{PD}} |_{\text{sol2}}$

Here and later on, the notation $A|_b$ defines that the conditions b are inserted in A .

For the piston effect, I derive the effect of both test mass rotations independently and sum the results up in the end.

Algorithm C.2 Piston Effect

1. Derivation of the point $\mathbf{r}=(x_{\text{refl}}, y_{\text{refl}}, z_{\text{refl}})$ where the beam hits the tilted surface:

$$\mathbf{sol0}, i = \mathbf{Solve} \quad \mathbf{TM}_{\text{surf},i} = \mathbf{r} \quad \&\& \quad \mathbf{r}_m/\mathbf{b}_{\text{in},i,m} = \mathbf{r}_n/\mathbf{b}_{\text{in},i,n} \quad \mathbf{for} \quad \{\mathbf{r}, y_{\text{tm}}, z_{\text{tm}}\}$$
 With numbers $i \in \{1, 2\}$ for the test mass and $m, n \in \{1, 2, 3\}$ for the vector entry.
2. Piston effect of the first test mass:
 - (a) Derivation of the path the beam propagates additionally to the nominal case until it hits TM1 (can be negative):

$$\mathbf{sol1a} = \mathbf{Solve} \quad x \mathbf{b}_{\text{in1}} = \mathbf{r}|_{\mathbf{sol1a}} \quad \mathbf{for} \quad x$$
 - (b) Definition of the orientation of the TM2 surface with respect to the beam reflected at TM1:

$$\mathbf{TM2}_{\text{refl1}} = \mathbf{M}_{\text{yaw}}(-\beta_{y2} - \beta_{y1}) \mathbf{TM}_{\text{surf2}}|_{\mathbf{p}_{\text{OB2}}=0, \mathbf{p}_{\text{TM2}}=0}$$
 - (c) Derivation of the path length the beam propagates from its reflection point at TM1 $\mathbf{r}|_{\mathbf{sol1a}}$ to a surface $\mathbf{TM2}_{\text{refl1}}$ that intersects the nominal point of reflection at TM1:

$$\mathbf{sol1b} = \mathbf{Solve} \quad \mathbf{r}|_{\mathbf{sol1a}} + x \mathbf{b}_{\text{refl1}} = \mathbf{TM2}_{\text{refl1}} \quad \mathbf{for} \quad \{x, y_{\text{tm}}, z_{\text{tm}}\}$$
 - (d) Derive the path length the beam propagates from its offset reflection point at TM2 $\mathbf{TM2}_{\text{surf}}|_{\mathbf{sol1b}}$ to a detector surface that intersects the nominal point of reflection at TM2:

$$\mathbf{sol1c} = \mathbf{Solve} \quad \mathbf{TM2}_{\text{surf}}|_{\mathbf{sol1b}} + x \mathbf{b}_{\text{refl2}} = \mathbf{PD}(0, \beta_{y2}, \beta_z, \varphi_{\text{PD}}) \quad \mathbf{for} \quad \{x, y_{\text{PD}}, z_{\text{PD}}\}$$
3. Piston effect of the second test mass (neglecting all TTL effects originating from TM1):
 - (a) Derivation of the path length the beam propagates additionally to the nominal case until it hits TM2 (can be negative):

$$\mathbf{sol2a} = \mathbf{Solve} \quad x \mathbf{b}_{\text{in2}} = \mathbf{r}|_{\mathbf{sol2a}} \quad \mathbf{for} \quad x$$
 - (b) Derivation of the path length the beam propagates from its reflection point at TM2 to a detector surface that intersects the nominal point of reflection at TM2:

$$\mathbf{sol2b} = \mathbf{Solve} \quad \mathbf{r}|_{\mathbf{sol2a}} + x \mathbf{b}_{\text{refl2}} = \mathbf{PD}(0, \beta_{y2}, \beta_z, \varphi_{\text{PD}}) \quad \mathbf{for} \quad \{x, y_{\text{PD}}, z_{\text{PD}}\}$$
4. Sum up to the piston effect:

$$\begin{aligned} \text{OPD}_{\text{piston}} &= x|_{\mathbf{sol1a}} + x|_{\mathbf{sol1b}} + x|_{\mathbf{sol1c}} + x|_{\mathbf{sol2a}} + x|_{\mathbf{sol2b}} \\ y_{\text{im,piston}} &= y_{\text{PD}}|_{\mathbf{sol1c}} + y_{\text{PD}}|_{\mathbf{sol2b}} \\ z_{\text{im,piston}} &= z_{\text{PD}}|_{\mathbf{sol1c}} + z_{\text{PD}}|_{\mathbf{sol2b}} \end{aligned}$$

Next, I derive the TTL effects of all three mirror refractions. For the first two, I also include the additional contribution of the shifted reflection point at the second test mass. The solution I get from the following formalism provides the additional OPDs and beam walks on the second test mass as well as on the detector, which we would measure, when adding this windows to the setup. In LPF however, the nominal OPD and beam walks are measured beforehand and alter the reference path length, the piston effect of the second test mass, and the static beam offsets on the QPD. Thus, I have to subtract the constant terms of these three properties in the following algorithms each.

Algorithm C.3 Transmission through first Window

1. Definition of the path length the beam would propagate through the window assuming a refractive index of 1:

$$\text{solVac} = \text{Solve } x \mathbf{b}_{\text{refl1}} = \text{WIN}_{\text{surf}}(-t_{\text{tc}}) \quad \text{for } \{x, y_{\text{win}}, z_{\text{win}}\}$$

2. Definition of the path length the beam propagates through the actual window:

$$\text{solWin} = \text{Solve } x \mathbf{b}_{\text{tc1}} = \text{WIN}_{\text{surf}}(-t_{\text{tc}}) \quad \text{for } \{x, y_{\text{win}}, z_{\text{win}}\}$$

3. Derivation of the path length the beam propagates from its point of emission $\text{WIN}_{\text{surf}}|_{\text{solWin}}$ to a surface $\text{TM2}_{\text{refl1}}$ that intersects the point of emission in vacuum $\text{WIN}_{\text{surf}}|_{\text{solVac}}$:

$$\text{solTM} = \text{Solve } \text{WIN}_{\text{surf}}(0)|_{\text{solWin}} + x \mathbf{b}_{\text{refl1}} = \text{WIN}_{\text{surf}}(0)|_{\text{solVac}} + \text{TM2}_{\text{refl1}} \\ \text{for } \{x, y_{\text{tm}}, z_{\text{tm}}\}$$

4. Derivation of the path length the beam propagates from its offset reflection point at TM2 $\text{TM2}_{\text{surf}}|_{\text{solTM}}$ to a detector surface that intersects the nominal point of reflection at TM2:

$$\text{solPD} = \text{Solve } \text{TM2}_{\text{surf}}|_{\text{solTM}} + x \mathbf{b}_{\text{refl2}} = \text{PD}(0, \beta_{y2}, \beta_z, \varphi_{\text{PD}}) \quad \text{for } \{x, y_{\text{PD}}, z_{\text{PD}}\}$$

5. Set solution together to the effect of the first window:

$$\begin{aligned} \text{OPD}_{\text{tc1}} &= n_{\text{tc}} x|_{\text{solWin}} - x|_{\text{solVac}} + x|_{\text{solTM}} + x|_{\text{solPD}} \\ y_{\text{im,tc1}} &= y_{\text{PD}}|_{\text{solPD}} \\ z_{\text{im,tc1}} &= z_{\text{PD}}|_{\text{solPD}} \end{aligned}$$

Algorithm C.4 First Transmission through second Window

1. Definition of the path length the beam would propagate through the window assuming a refractive index of 1:

$$\text{solVac} = \text{Solve } x \mathbf{b}_{\text{in2}} = \text{WIN}_{\text{surf}}(-t_{\text{tc}}) \quad \text{for } \{x, y_{\text{win}}, z_{\text{win}}\}$$

2. Definition of the path length the beam propagates through the actual window:

$$\text{solWin} = \text{Solve } x \mathbf{b}_{\text{tc2A}} = \text{WIN}_{\text{surf}}(-t_{\text{tc}}) \quad \text{for } \{x, y_{\text{win}}, z_{\text{win}}\}$$

3. Derivation of the path length the beam propagates from its point of emission $\text{WIN}_{\text{surf}}|_{\text{solWin}}$ to a surface $\text{TM2}_{\text{lever}}$ that intersects the point of emission in vacuum $\text{WIN}_{\text{surf}}|_{\text{solVac}}$:

$$\text{solTM} = \text{Solve } \text{WIN}_{\text{surf}}(0)|_{\text{solWin}} + x \mathbf{b}_{\text{in2}} = \text{WIN}_{\text{surf}}(0)|_{\text{solVac}} + \text{TM2}_{\text{lever}} \\ \text{for } \{x, y_{\text{tm}}, z_{\text{tm}}\}$$

4. Derivation of the path length the beam propagates from its offset reflection point at TM2 $\text{TM2}_{\text{surf}}|_{\text{solTM}}$ to a detector surface that intersects the nominal point of reflection at TM2:

$$\text{solPD} = \text{Solve } \text{TM2}_{\text{surf}}|_{\text{solTM}} + x \mathbf{b}_{\text{refl2}} = \text{PD}(0, \beta_{y2}, \beta_z, \varphi_{\text{PD}}) \quad \text{for } \{x, y_{\text{PD}}, z_{\text{PD}}\}$$

5. Set solutions together to the effect of the first refraction at the second window:

$$\begin{aligned} \text{OPD}_{\text{tc2A}} &= n_{\text{tc}} x|_{\text{solWin}} - x|_{\text{solVac}} + x|_{\text{solTM}} + x|_{\text{solPD}} \\ y_{\text{im,tc2A}} &= y_{\text{PD}}|_{\text{solPD}} \\ z_{\text{im,tc2A}} &= z_{\text{PD}}|_{\text{solPD}} \end{aligned}$$

Algorithm C.5 Second Transmission through second Window

1. Definition of the path length the beam would propagate through the window assuming a refractive index of 1:

$$\text{solVac} = \text{Solve } x \mathbf{b}_{\text{refl}2} = \text{WIN}_{\text{surf}}(t_{\text{tc}}) \quad \text{for } \{x, y_{\text{win}}, z_{\text{win}}\}$$

2. Definition of the path length the beam propagates through the actual window:

$$\text{solWin} = \text{Solve } x \mathbf{b}_{\text{tc}2B} = \text{WIN}_{\text{surf}}(t_{\text{tc}}) \quad \text{for } \{x, y_{\text{win}}, z_{\text{win}}\}$$

3. Derivation of the path length the beam propagates from its point of emission $\text{WIN}_{\text{surf}}|_{\text{solWin}}$ to a detector surface that intersects the point of emission in vacuum $\text{WIN}_{\text{surf}}|_{\text{solVac}}$:

$$\text{solPD} = \text{Solve } \text{WIN}_{\text{surf}}(0)|_{\text{solWin}} + x \mathbf{b}_{\text{refl}2} = \text{WIN}_{\text{surf}}(0)|_{\text{solVac}} + \text{PD}(0, \beta_{y2}, \beta_z, \varphi_{\text{PD}}) \\ \text{for } \{x, y_{\text{PD}}, z_{\text{PD}}\}$$

4. Set solutions together to the effect of the second refraction at the second window:

$$\begin{aligned} \text{OPD}_{\text{tc}2B} &= n_{\text{tc}} x|_{\text{solWin}} - x|_{\text{solVac}} + x|_{\text{solPD}} \\ y_{\text{im},\text{tc}2B} &= y_{\text{PD}}|_{\text{solPD}} \\ z_{\text{im},\text{tc}2B} &= z_{\text{PD}}|_{\text{solPD}} \end{aligned}$$

To encounter the full effect of the windows in LPF, we have to add up the single window effects.

Algorithm C.6 The Full Window Effect

Sum contributors up to the full window effect:

$$\begin{aligned} \text{OPD}_{\text{tc}} &= \text{OPD}_{\text{tc}1} + \text{OPD}_{\text{tc}A} + \text{OPD}_{\text{tc}2B} \\ y_{\text{im},\text{tc}} &= y_{\text{im},\text{tc}1} + y_{\text{im},\text{tc}2A} + y_{\text{im},\text{tc}2B} \\ z_{\text{im},\text{tc}} &= z_{\text{im},\text{tc}1} + z_{\text{im},\text{tc}2A} + z_{\text{im},\text{tc}2B} \end{aligned}$$

C.2 Derivation of the Non-Geometric Longitudinal Path Length Signal

The longitudinal path length signal was derived following the algorithm in Sec. 5.2. Thereby, the angular alignment of the measurement beam at the detector depends on the differential rotation angle of the two test masses but not the S/C rotation which cancels out after the second test mass reflection. The beam walk of the measurement beam was derived as described in Sec. C.1. Furthermore, a QPD was used in LPF.

C.3 LISA Pathfinder Optical Parameters

The LPF parameters included in the full analytical TTL model for LPF are summarised in Tab. C.1. They have been extracted from a LPF setup, which had been implemented in IfoCAD by Gudrun Wanner and rely on the setup presented in [TN5].

param.	LPF value	description
k	$5.91 \cdot 10^6 \text{ m}^{-1}$	wave number of the beams
β_{y1}	-0.0785 rad	tilt of incoming beam at TM1 (propagation angle in xy -plane)
β_{y2}	0.0786 rad	tilt of incoming beam at TM2 (propagation angle in xy -plane)
β_z	-20.0 μrad	tilt of incoming beam at TM1 (propagation angle in xz -plane)
d_{lever1}	0.356 m	lever arm from PoR at TM1 to PoR at TM2 neglecting the windows
d_{lever2}	0.143 m	lever arm from PoR at TM2 to PD12A neglecting the windows
φ_{01}	7.98 μrad	nominal yaw rotation of TM1
φ_{02}	-60.7 μrad	nominal yaw rotation of TM2
η_{01}	13.0 μrad	nominal pitch rotation of TM1
η_{02}	0.355 μrad	nominal pitch rotation of TM2
d_{longTM1}	-0.023 m	longitudinal distance between initial PoR and CoR of TM1
d_{longTM2}	-0.023 m	longitudinal distance between initial PoR and CoR of TM2
d_{latTM1}	-6.37 μm	lateral distance between initial PoR and CoR of TM1
d_{latTM2}	15.8 μm	lateral distance between initial PoR and CoR of TM2
d_{vertTM1}	3.42 μm	vertical distance between initial PoR and CoR of TM1
d_{vertTM2}	10.5 μm	vertical distance between initial PoR and CoR of TM2
d_{longOB1}	0.188 m	longitudinal distance between initial PoR at TM1 and CoR of OB
d_{longOB2}	0.188 m	longitudinal distance between initial PoR at TM2 and CoR of OB
d_{latOB1}	-6.37 μm	lateral distance between initial PoR at TM1 and CoR of OB
d_{latOB2}	15.8 μm	lateral distance between initial PoR at TM2 and CoR of OB
d_{vertOB1}	3.42 μm	vertical distance between initial PoR at TM1 and CoR of OB
d_{vertOB2}	10.5 μm	vertical distance between initial PoR at TM2 and CoR of OB
t_{tc1}	6.05 mm	thickness of WIN1
t_{tc2}	6.05 mm	thickness of WIN2
n_{tc1}	1.61	reflection index of WIN1
n_{tc2}	1.61	reflection index of WIN2
D_{PD}	45 μm	slit width of PD12A
y_{im0}	-1.34 μm	nominal horizontal measurement beam offset at PD12A
z_{im0}	13.3 μm	nominal vertical measurement beam offset at PD12A
y_{ir}	-2.12 μm	horizontal reference beam offset at PD12A
z_{ir}	-2.26 μm	vertical reference beam offset at PD12A
φ_{PD}	-165 μrad	yaw angle between surface normal of PD12A and negative initial beam direction
η_{PD}	-20 μrad	pitch angle between surface normal of PD12A and negative initial beam direction (equals β_z)
φ_r	125 μrad	incoming yaw angle of reference beam at PD12A
η_r	7 μrad	incoming pitch angle of reference beam at PD12A
x_{Rm}	0.867 m	Rayleigh range of measurement beam
x_{Rr}	0.738 m	Rayleigh range of reference beam
x_m	0.519 m	distance from waist of measurement beam at PD12A
x_r	0.594 m	distance from waist of reference beam at PD12A

Table C.1: Nominal parameters describing the LPF setup, which are extracted from the three-dimensional LPF model in IfoCAD [Credit: Gudrun Wanner]. The indices 1 and 2 indicate the test mass or window of reference. All beam tilts are defined with respect to the axis of a fictitious beam of normal incidence.

Appendix D

LISA Pathfinder Data Analysis

D.1 The Long Cross-Talk Experiment

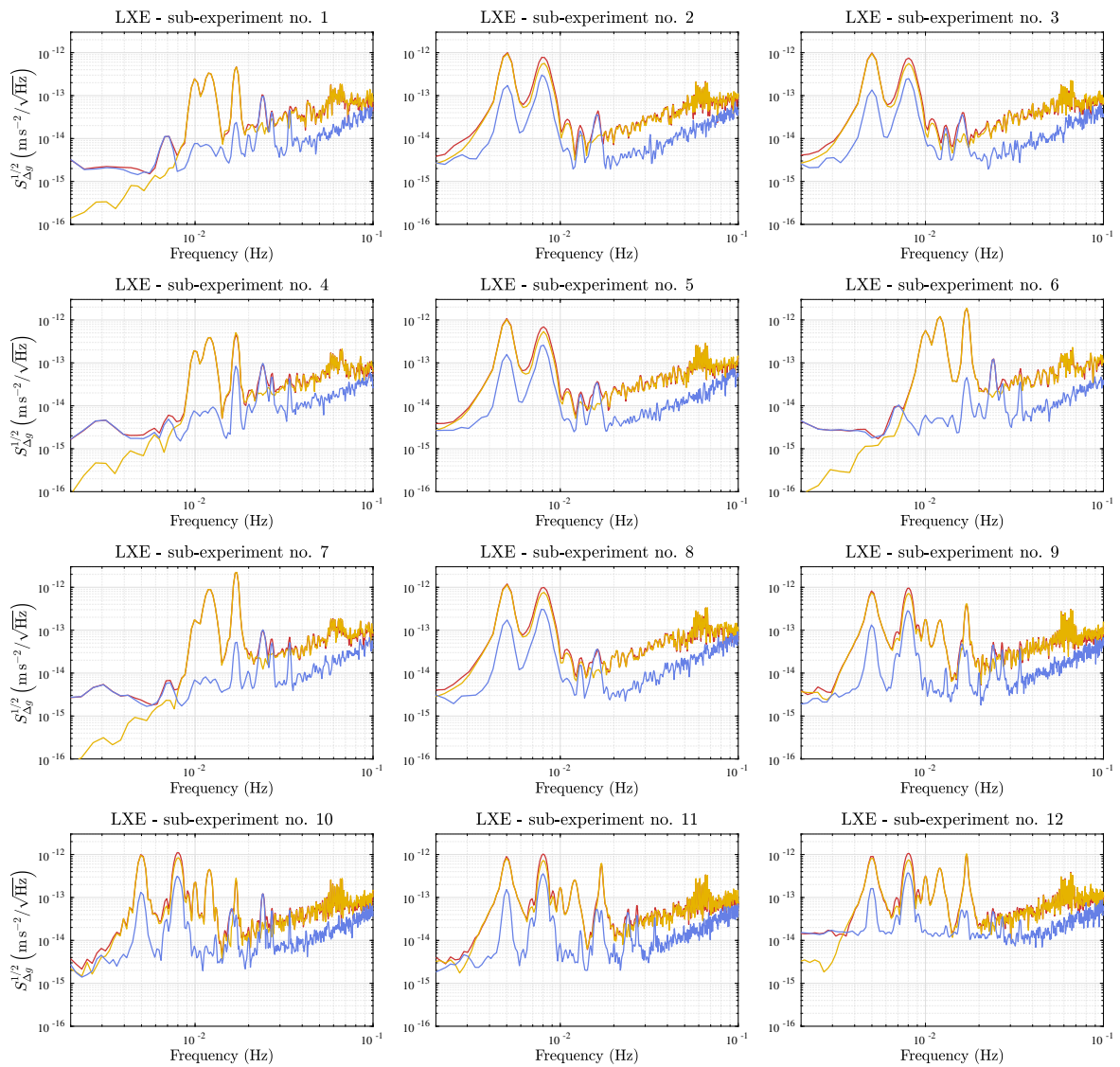


Figure D.1: Performance of the fit model during the twelve sub-experiments of the LXE. Red curve: ASD of the measured Δg with subtracted inertial forces. Yellow curve: ASD of the fit model. Blue curve: ASD of the residual after the subtraction of the fit model from the data.

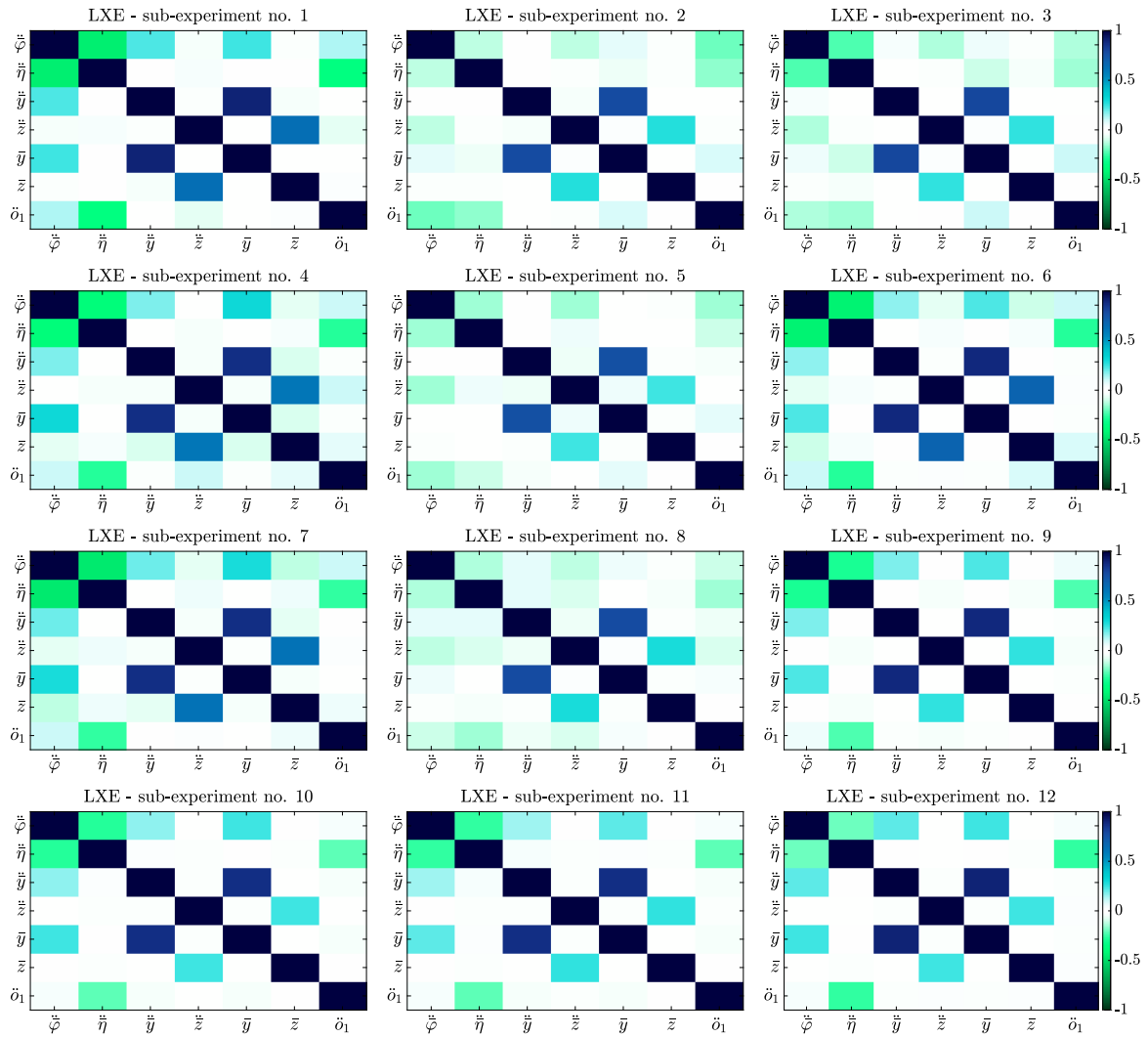


Figure D.2: Correlations in the fit model during all sub-experiments of the LXE. The darker the color, the stronger is the correlation between the quantities. The correlation is always 1 at the diagonal axis.

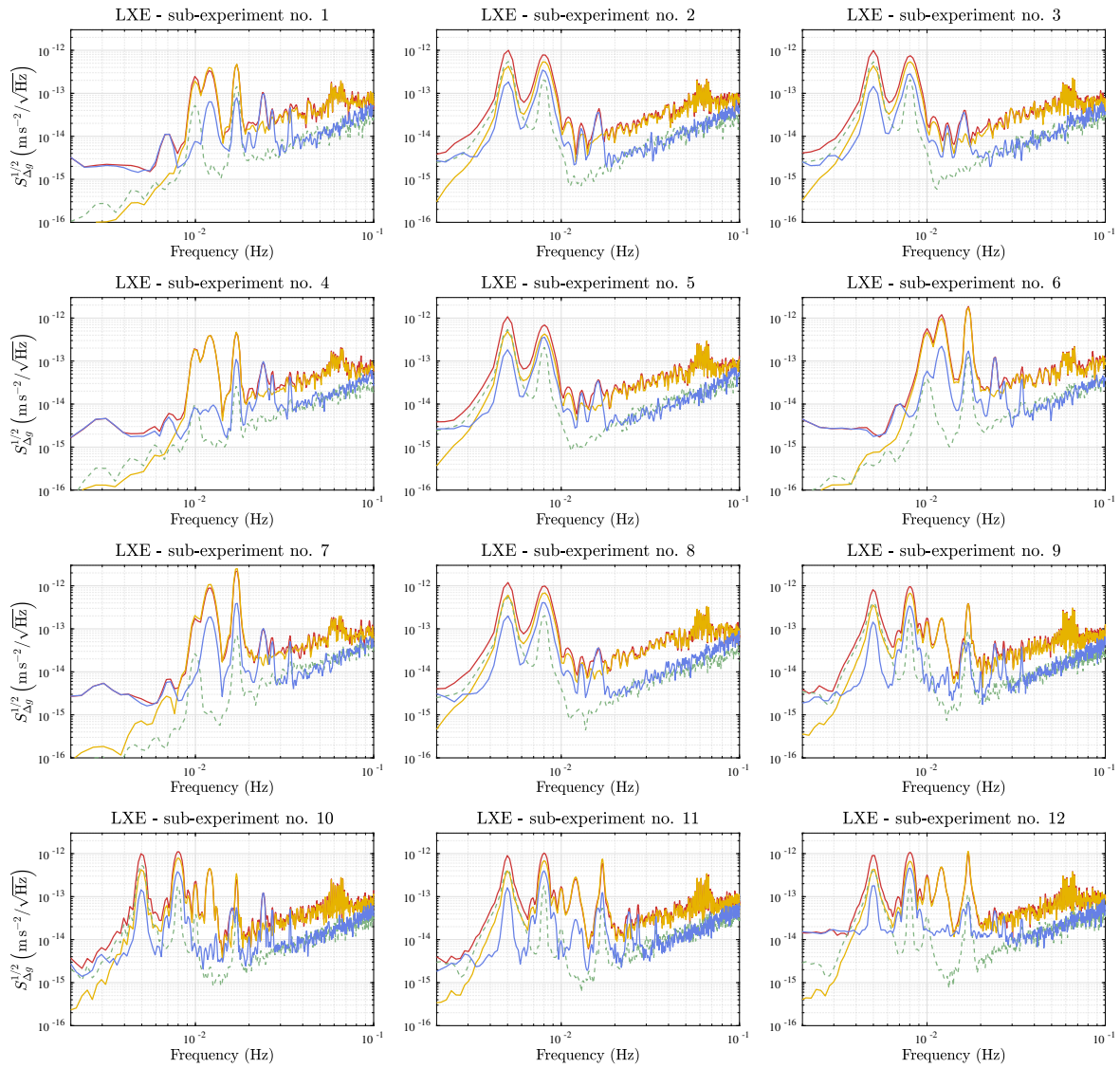


Figure D.3: Performance of the analytical model during the twelve sub-experiments of the LXE. Red curve: ASD of the measured Δg with subtracted inertial forces. Yellow curve: ASD of the analytical model. Dashed green curve: ASD of the stiffness terms and \ddot{o}_1 contribution fitted to the difference of the measured Δg and the analytical model. Blue curve: ASD of the residual after subtracting the analytical and additionally fitted terms from the measurement.

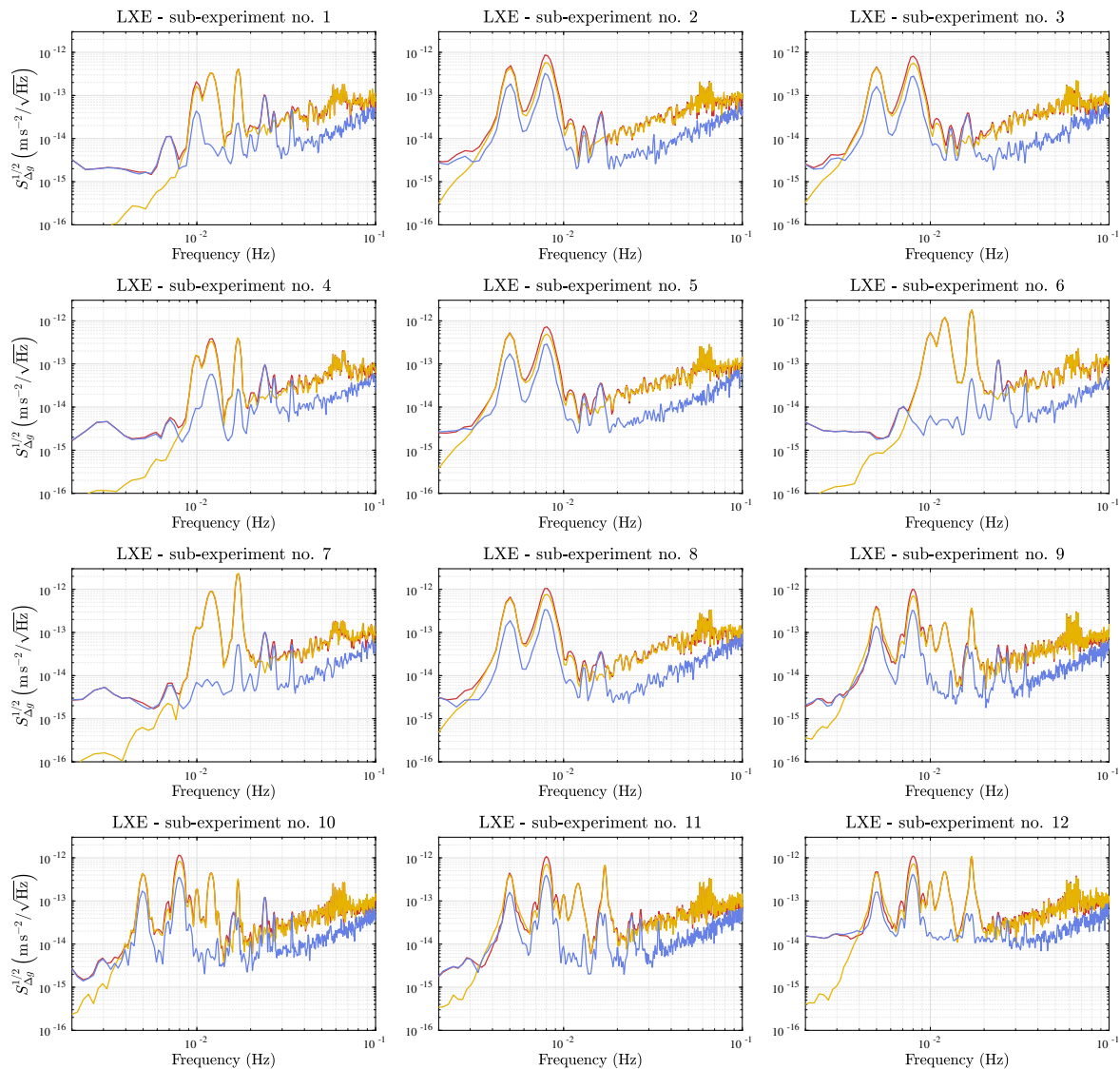


Figure D.4: Performance of the fit model without the stiffness terms during the twelve sub-experiments of the LXE. Red curve: ASD of the measured Δg with subtracted inertial forces and subtracted stiffnesses (with the same mean coefficients in all sub-experiments). Yellow curve: ASD of the fitted model. Blue curve: ASD of the residual after the subtraction of the fit model from the measurement.

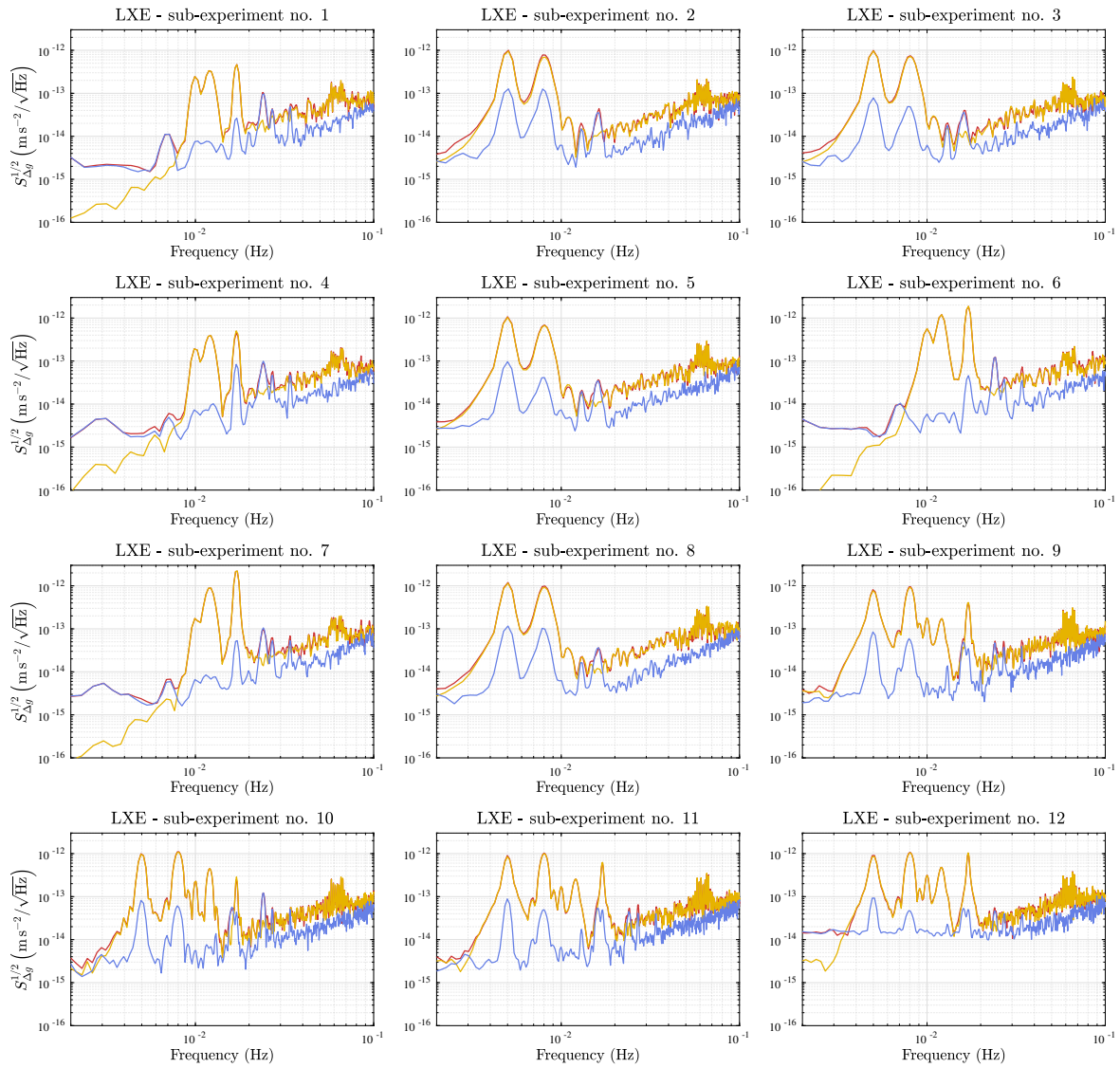


Figure D.5: Performance of the fit model without the contribution of residual longitudinal S/C accelerations during the twelve sub-experiments of the LXE. Red curve: ASD of the measured Δg with subtracted inertial forces. Yellow curve: ASD of the fitted model. Blue curve: ASD of the residual after the subtraction of the fit model from the measurement.

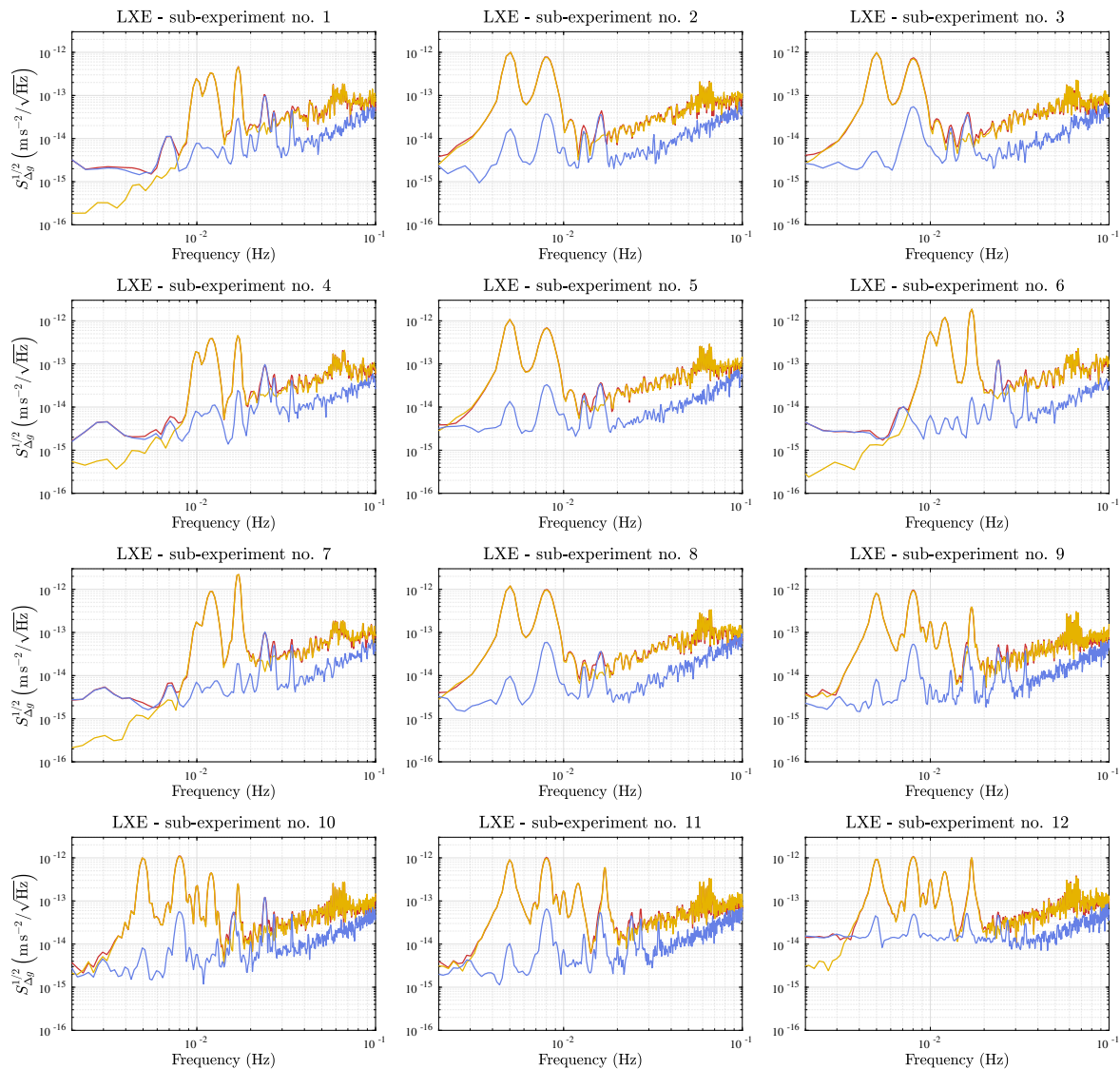


Figure D.6: Performance of the fit model additionally including angular stiffness terms during the twelve sub-experiments of the LXE. Red curve: ASD of the measured Δg with subtracted inertial forces. Yellow curve: ASD of the fitted model. Blue curve: ASD of the residual after the subtraction of the fit model from the measurement.

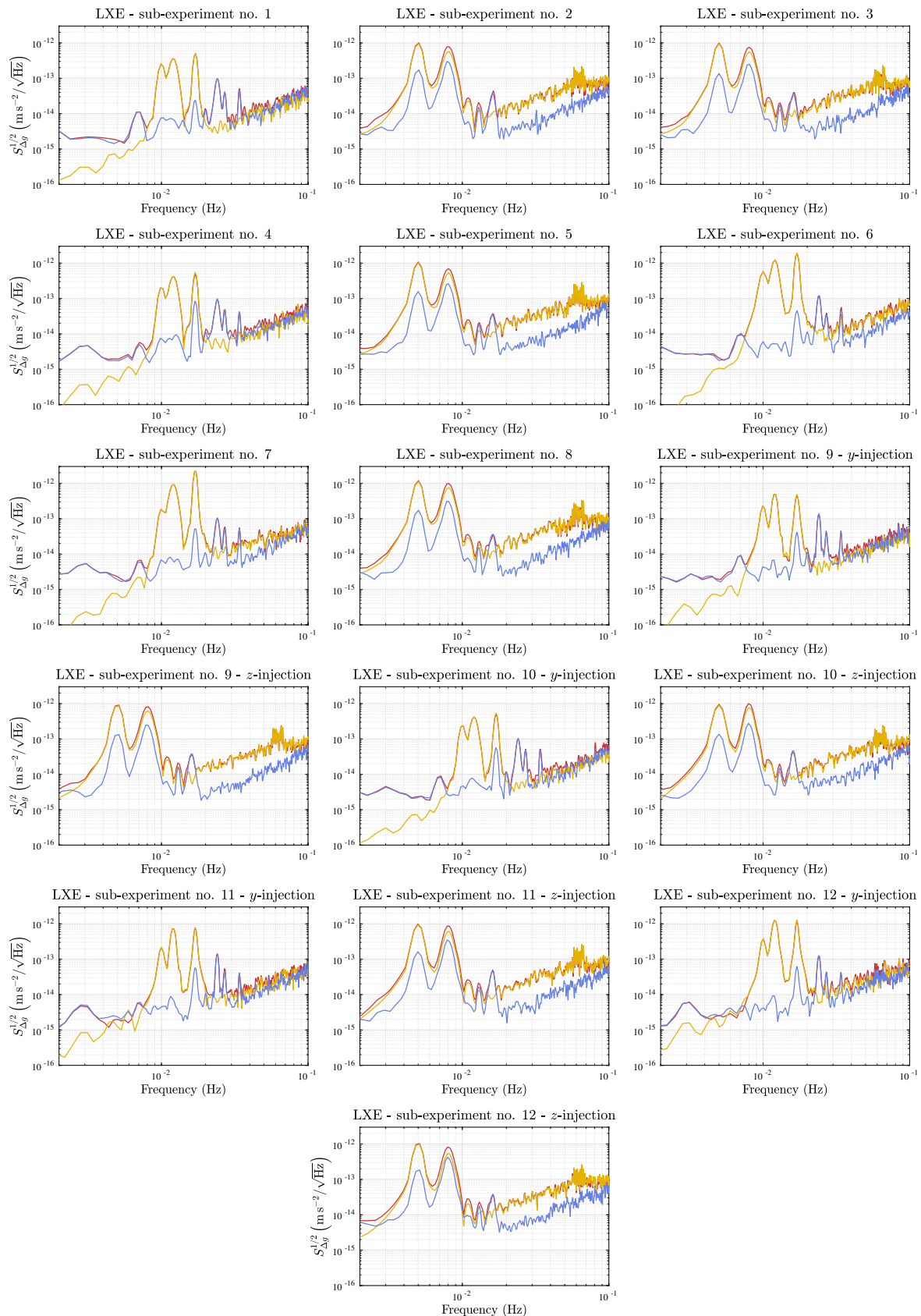


Figure D.7: Performance of the fit model adapted for experiments with y - and z -injections during the twelve sub-experiments of the LXE. Red curve: ASD of the measured Δg with subtracted inertial forces, corrected further for the mean fitted cross-acceleration coupling terms in the plane orthogonal to the performed injections. Yellow curve: ASD of the model fitted to the adapted measurement. Blue curve: ASD of the residual after the subtraction of the fit model from the adapted measurement.

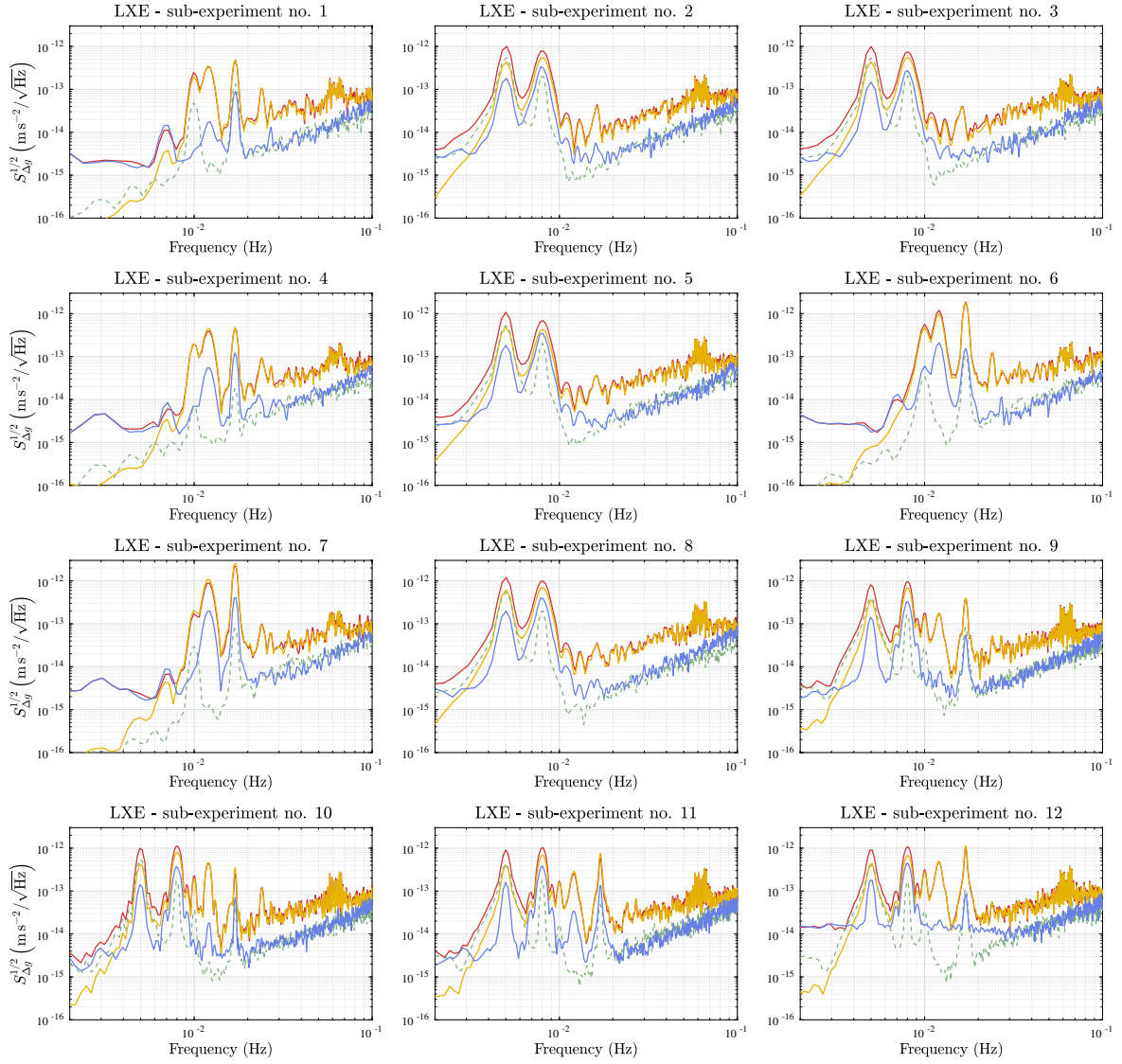


Figure D.8: Performance of the second-order analytical model during the twelve sub-experiments of the LXE. Red curve: ASD of the measured Δg with subtracted inertial forces. Yellow curve: ASD of the second-order analytical model. Dashed green curve: ASD of the stiffness and the \ddot{o}_1 contribution fitted to the difference of the measured Δg and the analytical model. Blue curve: ASD of the residual after subtraction the analytical and additionally fitted terms from the measurement.

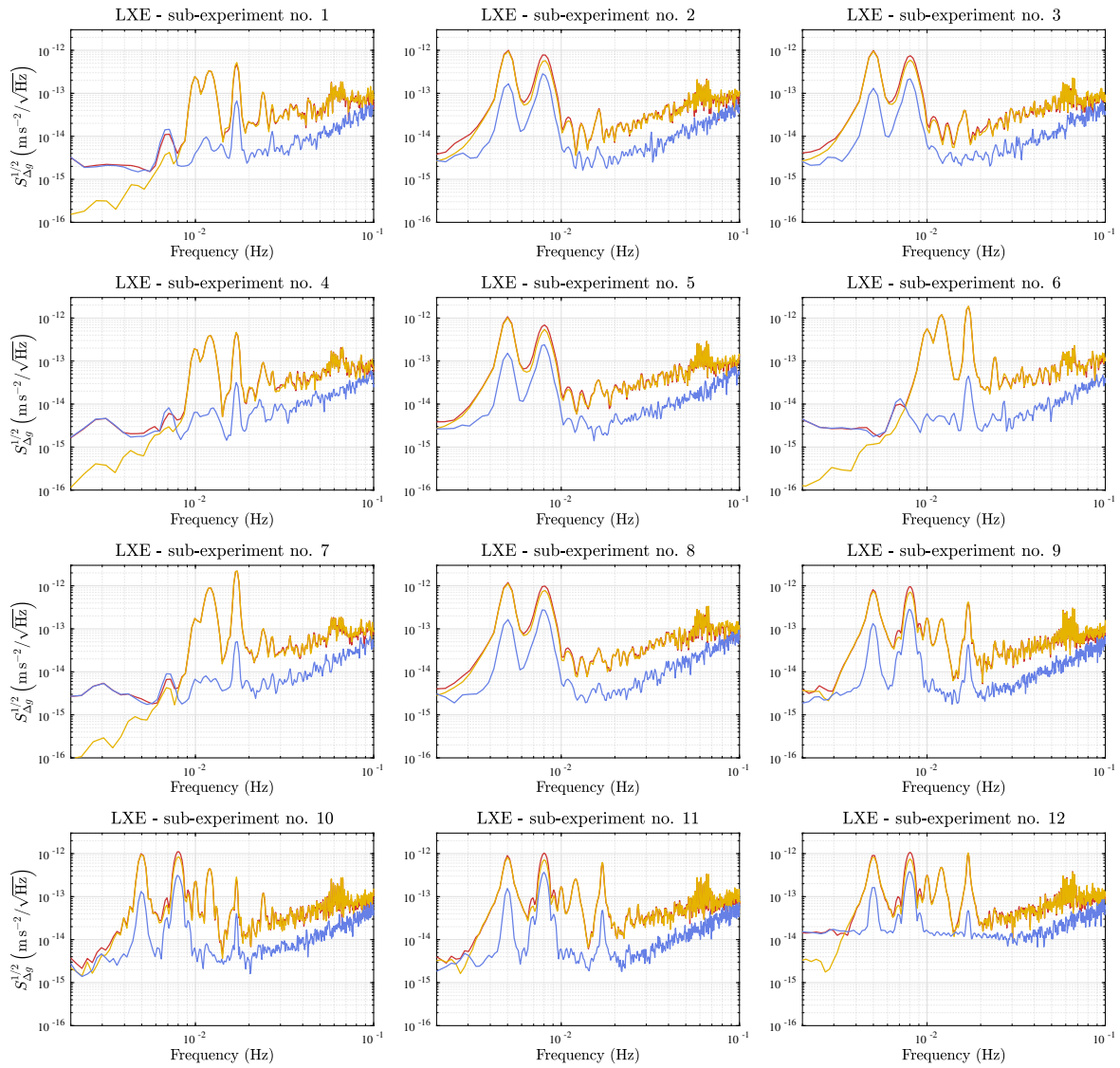


Figure D.9: Performance of the second-order fit model during the twelve sub-experiments of the LXE. Red curve: ASD of the measured Δg with subtracted inertial forces. Yellow curve: ASD of the second-order fit model. Blue curve: ASD of the residual of the subtraction of the fit model from the Δg measurement.

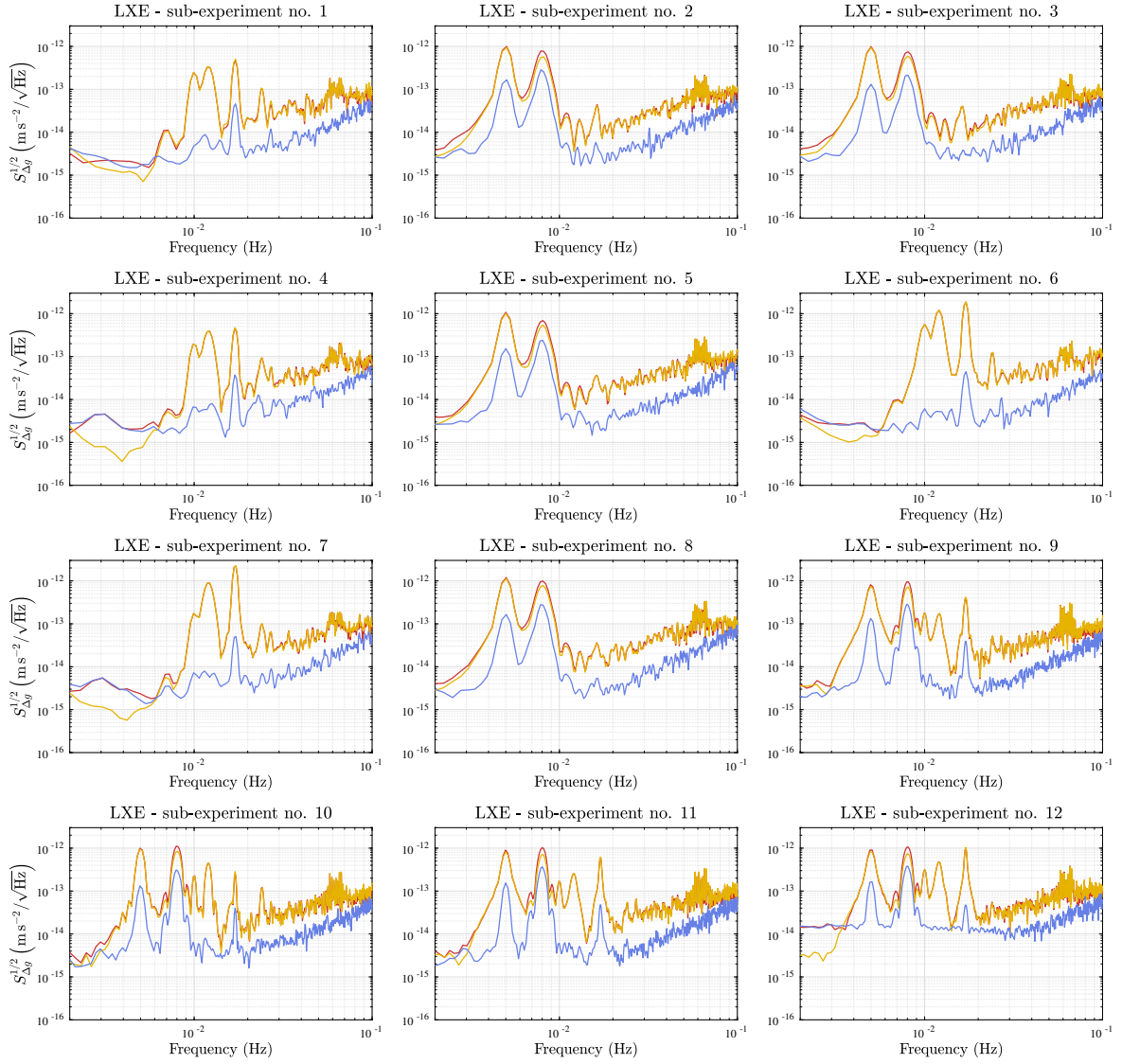


Figure D.10: Performance of the second-order fit model with two angular coefficients each during the twelve sub-experiments of the LXE. Red curve: ASD of the measured Δg with subtracted inertial forces. Yellow curve: ASD of the second-order fit model. Blue curve: ASD of the residual of the subtraction of the fit model from the Δg measurement.

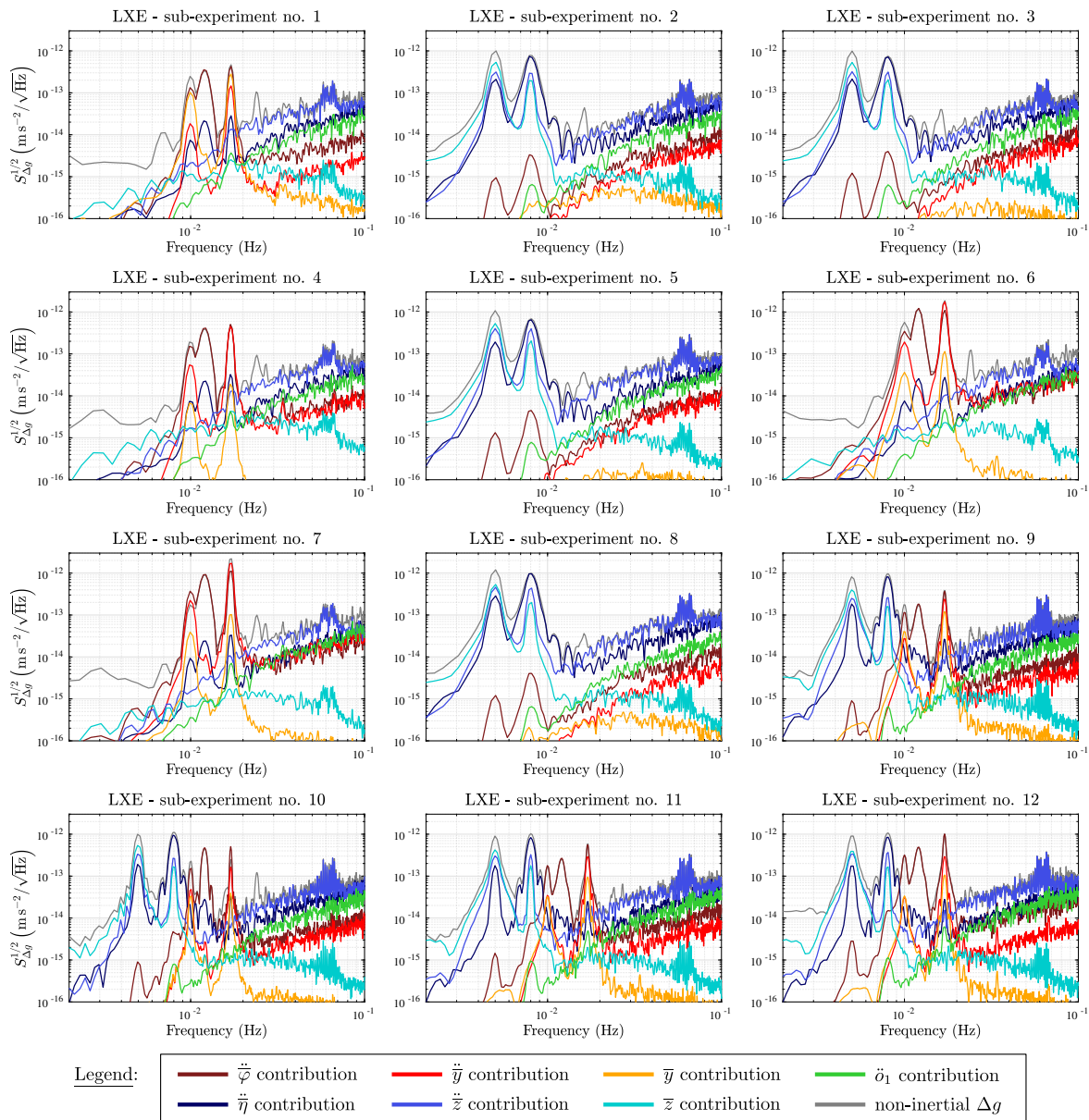


Figure D.11: Contribution of the cross-coupling terms to the measured Δg in the sub-experiments of the LXE. The noise at the injection frequencies depends on the terms in the respective plane. The acceleration \ddot{z} causes the noise at higher frequencies in all sub-experiments.

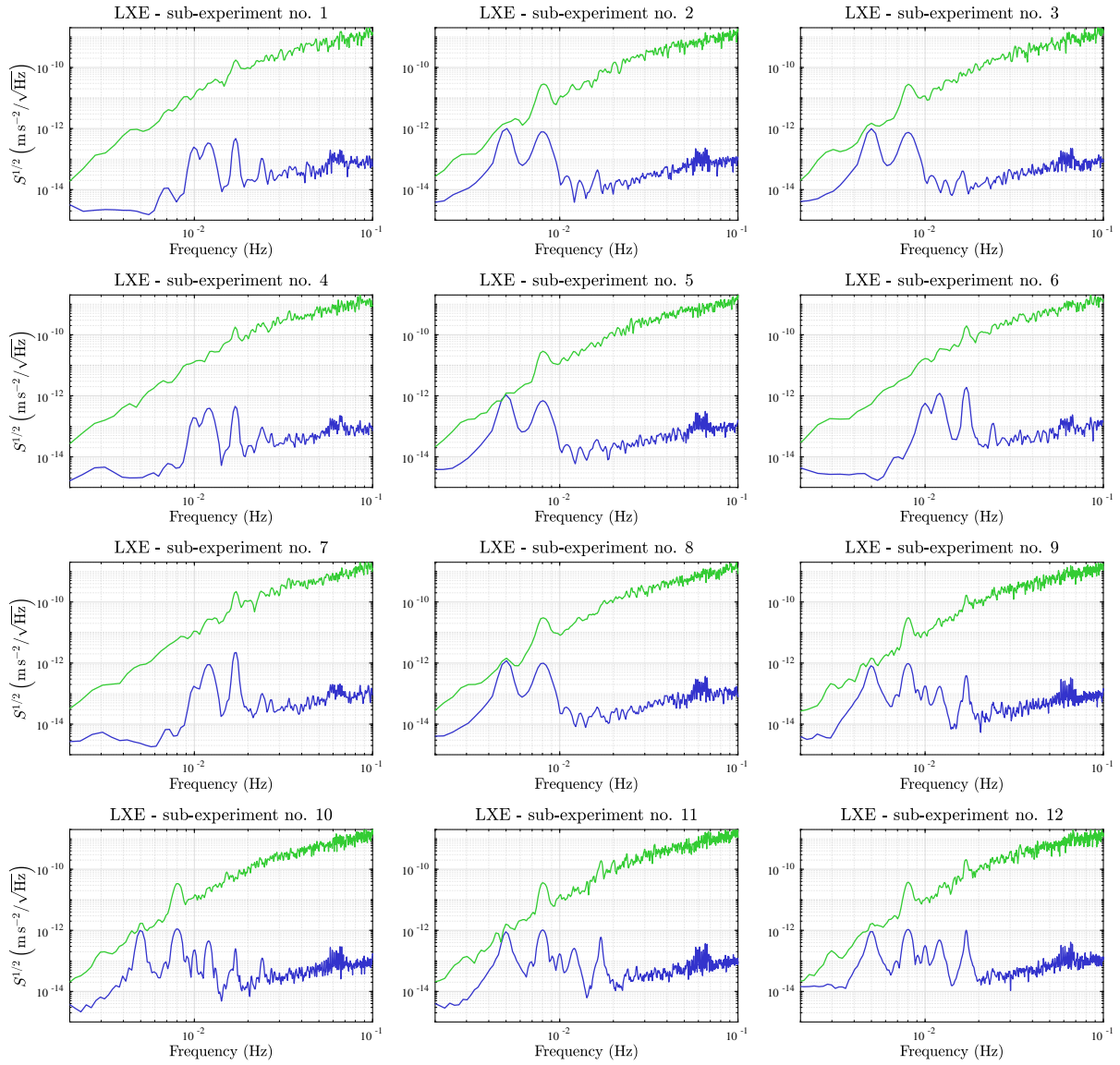


Figure D.12: The ASDs of the non-inertial Δg (blue) and the accelerations \ddot{o}_1 measured by the x1-interferometer (green). The injections applied to the first test mass are partially also visible in the o_1 -readout.

D.2 Long-Term Analysis

#	run index	start time	end time
1	6	21.03.2016 02:00	26.03.2016 08:00
2	9	04.04.2016 00:00	14.04.2016 08:00
3	12	26.04.2016 08:00	28.04.2016 08:00
4	13	01.05.2016 08:05	02.05.2016 23:55
5	16	13.05.2016 08:30	14.05.2016 08:00
6	17	16.05.2016 00:00	19.05.2016 05:00
7	31	06.06.2016 11:05	09.06.2016 08:00
8	39	19.06.2016 13:00	24.06.2016 08:00
9	40	10.07.2016 08:40	11.07.2016 09:55
10	41	11.07.2016 11:40	12.07.2016 09:55
11	42	17.07.2016 22:00	20.07.2016 06:00
12	43	24.07.2016 13:00	30.07.2016 00:00
13	44	31.07.2016 11:40	02.08.2016 06:00
14	45	07.08.2016 10:20	08.08.2016 04:20
15	53	19.09.2016 02:32	21.09.2016 13:00
16	53	21.09.2016 13:45	22.09.2016 06:00
17	54	28.09.2016 13:35	01.10.2016 08:00
18	56	05.10.2016 17:25	07.10.2016 00:49
19	56	07.10.2016 02:15	08.10.2016 07:50
20	58	07.11.2016 21:30	12.11.2016 08:00
21	59	16.11.2016 11:05	26.11.2016 08:00
22	61	26.12.2016 08:00	13.01.2017 19:58
23	63	27.01.2017 18:45	28.01.2017 08:00
24	64	02.02.2017 07:55	02.02.2017 20:20
25	66	13.02.2017 14:30	03.02.2017 21:50:19
26	67	09.03.2017 19:20	14.03.2017 09:40
27	68	14.03.2017 09:00	17.03.2017 00:30
28	70	01.05.2017 20:00	03.05.2017 18:27
29	71	03.05.2017 23:30	09.05.2017 14:00
30	72	10.05.2017 11:11:20	12.05.2017 12:02:07
31	73	12.05.2017 12:02:07	15.05.2017 08:00:59
32	74	18.05.2017 18:24:46	23.05.2017 02:00
33	75	28.05.2017 13:41	05.06.2017 15:04:40
34	76	08.06.2017 12:00:45	17.06.2017 02:56
35	78	22.06.2017 00:55	24.06.2017 20:00
36	80	15.07.2017 00:50	17.07.2017 13:45

Table D.1: Timespans with very low actuation used in this work for the fit of the TTL coupling coefficients (long-term analysis) and the corresponding LPF run index. Times are given in UTC.

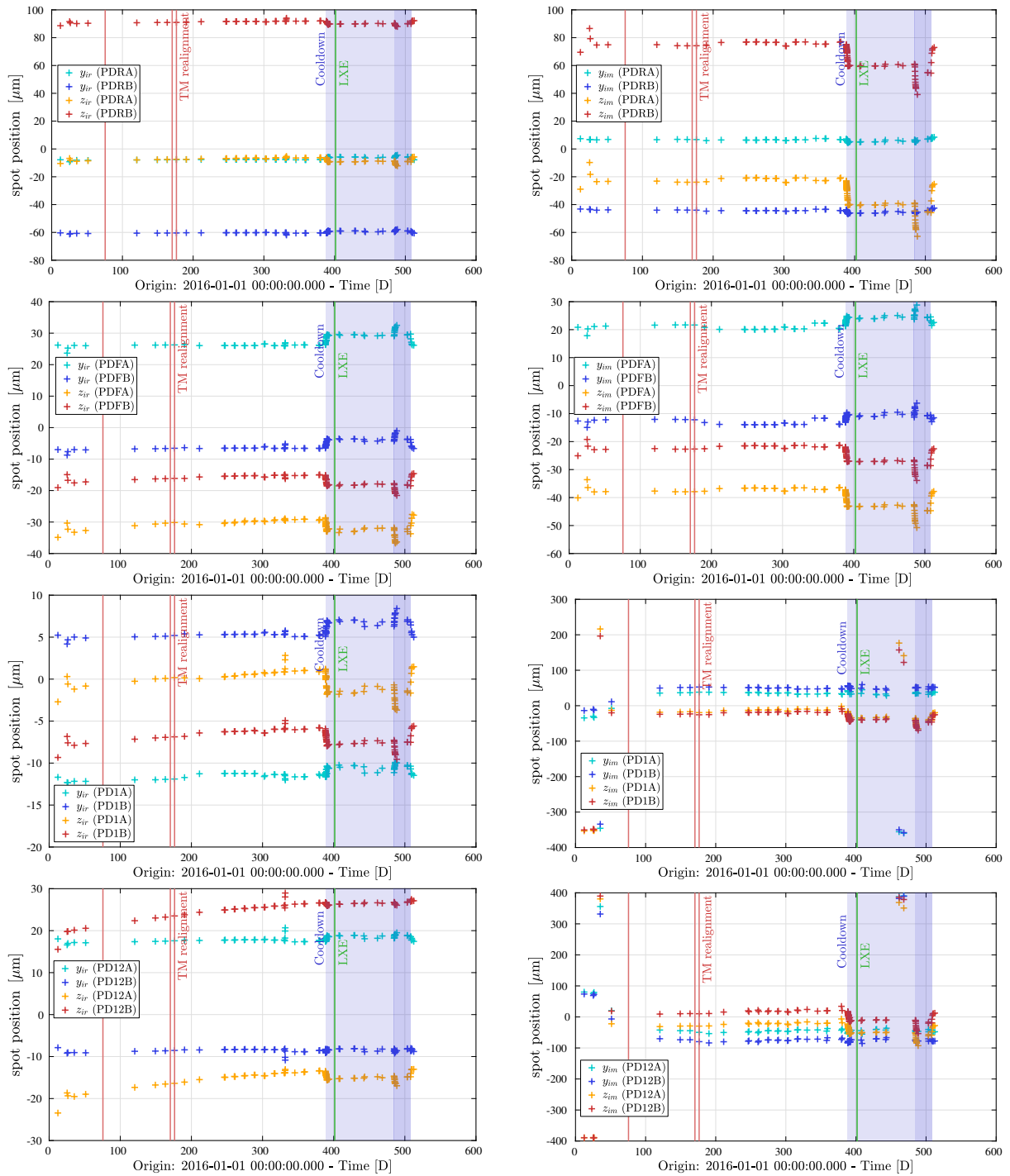


Figure D.13: Spot positions of both beams for the entire LPF mission. Shown are the positions at the A- and B-diodes of all interferometers.

Bibliography

- [1] J Aasi, B P Abbott, R Abbott, T Abbott, M R Abernathy, K Ackley, C Adams, T Adams, P Addesso, R X Adhikari, et al. Advanced LIGO. *Class. Quantum Grav.*, 32(7):074001, 2015.
- [2] A. Buikema, C. Cahillane, G. L. Mansell, C. D. Blair, R. Abbott, C. Adams, R. X. Adhikari, A. Ananyeva, S. Appert, K. Arai, et al. Sensitivity and performance of the Advanced LIGO detectors in the third observing run. *Phys. Rev. D*, 102:062003, 2020.
- [3] F Acernese, M Agathos, K Agatsuma, D Aisa, N Allemandou, A Allocca, J Amarni, P Astone, G Balestri, G Ballardin, et al. Advanced Virgo: a second-generation interferometric gravitational wave detector. *Class. Quantum Grav.*, 32(2):024001, 2014.
- [4] Catherine Nguyen for the Virgo Collaboration. Status of the Advanced Virgo gravitational-wave detector, 2021.
- [5] B. P. Abbott, R. Abbott, T. D. Abbott, M. R. Abernathy, F. Acernese, K. Ackley, C. Adams, T. Adams, P. Addesso, R. X. Adhikari, et al. Observation of gravitational waves from a binary black hole merger. *Phys. Rev. Lett.*, 116:061102, 2016.
- [6] M Punturo, M Abernathy, F Acernese, B Allen, N Andersson, K Arun, F Barone, B Barr, M Barsuglia, M Beker, et al. The einstein telescope: a third-generation gravitational wave observatory. *Class. Quantum Grav.*, 27(19):194002, 2010.
- [7] S Dwyer, D Sigg, S W Ballmer, L Barsotti, N Mavalvala, and M Evans. Gravitational wave detector with cosmological reach. *Phys. Rev. D*, 91:082001, 2015.
- [8] D Reitze, R X Adhikari, S Ballmer, B Barish, L Barsotti, G Billingsley, D A Brown, Y Chen, D Coyne, R Eisenstein, et al. Cosmic Explorer: The U.S. contribution to gravitational-wave astronomy beyond LIGO, 2019.
- [9] P. Amaro-Seoane, H. Audley, S. Babak, J. Baker, E. Barausse, P. Bender, E. Berti, P. Binetruy, M. Born, D. Bortoluzzi, et al. Laser Interferometer Space Antenna. *ArXiv e-prints*, 2017.
- [10] O Jennrich. LISA technology and instrumentation. *Class. Quantum Grav.*, 26(15):153001, 2009.
- [11] M Armano, H Audley, G Auger, JT Baird, M Bassan, P Binetruy, M Born, D Bortoluzzi, N Brandt, M Caleno, et al. Sub-femto-g free fall for space-based gravitational wave observatories: LISA Pathfinder results. *Phys. Rev. Lett.*, 116(23):231101, 2016.
- [12] Massimo Tinto and Sanjeev V. Dhurandhar. Time-delay interferometry. *Living Rev. Relativ.*, 24(1), 2020.

- [13] Massimo Tinto and Olaf Hartwig. Time-delay interferometry and clock-noise calibration. *Phys. Rev. D*, 98:042003, 2018.
- [14] Olaf Hartwig and Jean-Baptiste Bayle. Clock-jitter reduction in LISA time-delay interferometry combinations. *Phys. Rev. D*, 103:123027, 2021.
- [15] M Armano, M Benedetti, J Bogenstahl, D Bortoluzzi, P Bosetti, N Brandt, A Cavalleri, G Ciani, I Cristofolini, A M Cruise, et al. LISA Pathfinder: the experiment and the route to LISA. *Class. Quantum Grav.*, 26(9):094001, 2009.
- [16] M Armano, H Audley, G Auger, J Baird, P Binetruy, M Born, D Bortoluzzi, N Brandt, A Bursi, M Caleno, et al. The LISA Pathfinder mission. *J. Phys. Conf. Ser.*, 610:012005, 2015.
- [17] M. Armano, H. Audley, J. Baird, P. Binetruy, M. Born, D. Bortoluzzi, E. Castelli, A. Cavalleri, A. Cesarini, A. M. Cruise, et al. Calibrating the system dynamics of LISA Pathfinder. *Phys. Rev. D*, 97:122002, 2018.
- [18] M Armano, H Audley, J Baird, P Binetruy, M Born, D Bortoluzzi, E Castelli, A Cavalleri, A Cesarini, A M Cruise, et al. Temperature stability in the sub-milliHertz band with LISA Pathfinder. *Monthly Notices of the Royal Astronomical Society*, 486(3):3368–3379, 2019.
- [19] M. Armano, H. Audley, J. Baird, P. Binetruy, M. Born, D. Bortoluzzi, E. Castelli, A. Cavalleri, A. Cesarini, A. M. Cruise, et al. Beyond the required LISA free-fall performance: New LISA Pathfinder results down to 20 μHz . *Phys. Rev. Lett.*, 120:061101, 2018.
- [20] M. Armano, H. Audley, J. Baird, P. Binetruy, M. Born, D. Bortoluzzi, E. Castelli, A. Cavalleri, A. Cesarini, A. M. Cruise, et al. LISA Pathfinder, 2019.
- [21] G Heinzel, V Wand, A García, O Jennrich, C Braxmaier, D Robertson, K Middleton, D Hoyland, A Rüdiger, R Schilling, et al. The LTP interferometer and phasemeter. *Class. Quantum Grav.*, 21(5):S581–S587, 2004.
- [22] A Schleicher, T Ziegler, R Schubert, N Brandt, P Bergner, U Johann, W Fichter, and J Grzymisch. In-orbit performance of the LISA Pathfinder drag-free and attitude control system. *CEAS Space Journal*, 10:471–485, 2018.
- [23] K. Abich, A. Abramovici, B. Amparan, A. Baatzsch, B. B. Okihiro, D. C. Barr, M. P. Bize, C. Bogan, C. Braxmaier, M. J. Burke, et al. In-orbit performance of the GRACE Follow-On laser ranging interferometer. *Phys. Rev. Lett.*, 123:031101, 2019.
- [24] BS Sheard, G Heinzel, K Danzmann, DA Shaddock, WM Klipstein, and WM Folkner. Inter-satellite laser ranging instrument for the GRACE Follow-On mission. *J. Geod.*, 86(12):1083–1095, 2012.
- [25] Karan Jani and Abraham Loeb. Gravitational-wave lunar observatory for cosmology. *J. Cosmol. Astropart. Phys.*, 2021(06):044, 2021.
- [26] J Luo, L-S Chen, H-Z Duan, Y-G Gong, S Hu, J Ji, Q Liu, J Mei, V Milyukov, M Sazhin, et al. TianQin: a space-borne gravitational wave detector. *Class. Quantum Grav.*, 33(3):035010, 2016.
- [27] Wen-Rui Hu and Yue-Liang Wu. The Taiji Program in Space for gravitational wave physics and the nature of gravity. *Natl. Sci. Rev.*, 4(5):685–686, 2017.
- [28] W-H Ruan, C Liu, Z-K Guo, Y-L Wu, and R-G Cai. The LISA–Taiji network. *Nature Astronomy*, 4:108–109, 2020.

- [29] Yungui Gong, Jun Luo, and Bin Wang. Concepts and status of Chinese space gravitational wave detection projects. *Nature Astronomy*, 5:881–889, 2021.
- [30] S Kawamura, T Nakamura, M Ando, N Seto, K Tsubono, K Numata, R Takahashi, S Nagano, T Ishikawa, M Musha, et al. The japanese space gravitational wave antenna—DECIGO. *Class. Quantum Grav.*, 23(8):S125–S131, 2006.
- [31] S Kawamura, M Ando, N Seto, S Sato, T Nakamura, K Tsubono, N Kanda, T Tanaka, J Yokoyama, et al. The japanese space gravitational wave antenna: DECIGO. *Class. Quantum Grav.*, 28(9):094011, 2011.
- [32] S Sato, S Kawamura, M Ando, T Nakamura, K Tsubono, A Araya, I Funaki, K Ioka, N Kanda, S Moriwaki, et al. The status of DECIGO. *J. Phys. Conf. Ser.*, 840:012010, 2017.
- [33] G Wanner, G Heinzl, E Kochkina, C Mahrtdt, B Sheard, S Schuster, and K Danzmann. Methods for simulating the readout of lengths and angles in laser interferometers with gaussian beams. *Opt. Commun.*, 285(24):4831–4839, 2012.
- [34] Gudrun Wanner and Gerhard Heinzl. Analytical description of interference between two misaligned and mismatched complete gaussian beams. *Appl. Opt.*, 53(14):3043–3048, 2014.
- [35] Gudrun Wanner. *Complex optical systems in space: numerical modelling of the heterodyne interferometry of LISA Pathfinder and LISA*. PhD thesis, Leibniz Universität Hannover, 2010.
- [36] G Wanner, S Schuster, M Tröbs, and G Heinzl. A brief comparison of optical path-length difference and various definitions for the interferometric phase. *J. Phys. Conf. Ser.*, 610:012043, 2015.
- [37] Sönke Schuster. *Tilt-to-length coupling and diffraction aspects in satellite interferometry*. PhD thesis, Leibniz Universität Hannover, 2017.
- [38] E Morrison, B Meers, D Robertson, and H Ward. Automatic alignment of optical interferometers. *Appl. Opt.*, 33(22), 1994.
- [39] M Tröbs, S Schuster, M Lieser, M Zwetz, M Chwalla, K Danzmann, G Fernández Barránco, E D Fitzsimons, O Gerberding, G Heinzl, et al. Reducing tilt-to-length coupling for the LISA test mass interferometer. *Class. Quantum Grav.*, 35(10):105001, 2018.
- [40] C P Sasso, G Mana, and S Mottini. Coupling of wavefront errors and jitter in the LISA interferometer: far-field propagation. *Class. Quantum Grav.*, 35(18):185013, 2018.
- [41] C P Sasso, G Mana, and S Mottini. Coupling of wavefront errors and pointing jitter in the LISA interferometer: misalignment of the interfering wavefronts. *Class. Quantum Grav.*, 35(24):245002, 2018.
- [42] H Wegener, V Müller, G Heinzl, and M Misfeldt. Tilt-to-length coupling in the GRACE Follow-On laser ranging interferometer. *J. Spacecr. Rockets*, 57(6):1362–1372, 2020.
- [43] M. Chwalla, K. Danzmann, M. Dovalé Álvarez, J.J. Esteban Delgado, G. Fernández Barranco, E. Fitzsimons, O. Gerberding, G. Heinzl, C.J. Killow, M. Lieser, et al. Optical suppression of tilt-to-length coupling in the LISA long-arm interferometer. *Phys. Rev. Applied*, 14:014030, 2020.
- [44] S Schuster, G Wanner, M Tröbs, and G Heinzl. Vanishing tilt-to-length coupling for a singular case in two-beam laser interferometers with gaussian beams. *Appl. Opt.*, 54(5):1010–1014, 2015.

- [45] Gudrun Wanner, Nikolaos Karnesis, and the LISA Pathfinder collaboration. Preliminary results on the suppression of sensing cross-talk in LISA Pathfinder. *J. Phys. Conf. Ser.*, 840(1):012043, 2017.
- [46] S Schuster, M Tröbs, G Wanner, and G Heinzel. Experimental demonstration of reduced tilt-to-length coupling by a two-lens imaging system. *Opt. Express*, 24(10):10466–10475, 2016.
- [47] G. Anderson, J. Anderson, M. Anderson, G. Aveni, D. Bame, P. Barela, K. Blackman, A. Carmain, L. Chen, M. Cherng, et al. Experimental results from the ST7 mission on LISA Pathfinder. *Phys. Rev. D*, 98, 2018.
- [48] Andrew S. Glassner, editor. *An Introduction to Ray Tracing*. Academic Press Ltd., GBR, 1989.
- [49] R Giusteri, S Paczkowski, M Hewitson, N Karnesis, and E D Fitzsimons. Post-processing subtraction of tilt-to-length noise in LISA. *Submitted to Phys. Rev. D*, 2022.
- [50] Z Wang, T Yu, Y Zhao, Z Luo, W Sha, C Fang, Y Wang, S Wang, K Qi, Y Wang, and X Xu. Research on telescope TTL coupling noise in intersatellite laser interferometry. *Photonic Sens.*, 2019.
- [51] Y Zhao, Z Wang, Y Li, C Fang, H Liu, and H Gao. Method to remove tilt-to-length coupling caused by interference of flat-top beam and gaussian beam. *Appl. Sci.*, 9(19), 2019.
- [52] Ya Z, Jia S, Chao F, Heshan L, Zhi W, and Ziren L. Tilt-to-length noise coupled by wavefront errors in the interfering beams for the space measurement of gravitational waves. *Opt. Express*, 28(17):25545–25561, 2020.
- [53] M. Armano, H. Audley, J. Baird, P. Binetruy, M. Born, D. Bortoluzzi, E. Castelli, A. Cavalleri, A. Cesarini, A. M. Cruise, et al. LISA Pathfinder micronewton cold gas thrusters: In-flight characterization. *Phys. Rev. D*, 99:122003, 2019.
- [54] Albert-Einstein-Institute. IfoCAD. Accessed Febr. 8, 2022 [Online].
- [55] E Kochkina, G Heinzel, G Wanner, V Müller, C Mahrardt, B Sheard, S Schuster, and K Danzmann. Simulating and optimizing laser interferometers. *9th LISA Symposium*, pages 291–292, 2013.
- [56] C Killow, E Fitzsimons, M Perreux-Lloyd, D Robertson, H Ward, and J Bogenstahl. Optical fiber couplers for precision spaceborne metrology. *Appl. Opt.*, 55(10):2724–2731, 2016.
- [57] Marie-Sophie Hartig, Gudrun Wanner, and Nikos Karnesis. Optical crosstalk (tilt-to-length etc.) in LISA Pathfinder. Presented at the LISA Pathfinder Mission Accomplished conference, Trento, Italy, 2018.
- [58] Larissa Tevlin. Comparison of an analytical and fitted model describing Tilt To Length coupling in LISA Pathfinder. Praxisprojekt, FH Aachen University of Applied Sciences, 2021.
- [59] Larissa Tevlin. Refining the LISA Pathfinder Tilt-To-Length Analysis: A Study of Correlations. B.S. Thesis, FH Aachen University of Applied Sciences, 2021.
- [60] K. Danzmann, G. Heinzel, M. Hewitson, J. Reiche, M. Tröbs, G. Wanner, M. Born, H. Audley, N. Karnesis, A. Wittchen, S. Paczkowski, B. Kaune, and L. Wissel. *LPF Final Report for the German Contribution to the Nominal Mission*. Max-Planck-Institut für Gravitationsphysik, Albert-Einstein-Institut, Teilinstitut Hannover, 2018.

- [61] David Robertson. LPF Beam Position Measurements. What we learned. Presented at the LISA Pathfinder Mission Accomplished conference, Trento, Italy, 2018.
- [62] David Robertson. Private communications, 2022.
- [63] M Nofrarias, A F García Marín, A Lobo, G Heinzl, J Ramos-Castro, J Sanjuán, and K Danzmann. Thermal diagnostic of the optical window on board LISA Pathfinder. *Class. Quantum Grav.*, 24(20):5103–5121, 2007.
- [64] Johanna Bogenstahl. *Interferometry for the space mission LISA Pathfinder*. PhD thesis, University of Glasgow, 2010.
- [65] D I Robertson, E D Fitzsimons, C J Killow, M Perreur-Lloyd, H Ward, J Bryant, A M Cruise, G Dixon, D Hoyland, D Smith, and J Bogenstahl. Construction and testing of the optical bench for LISA Pathfinder. *Class. Quantum Grav.*, 30(8):085006, 2013.
- [66] B. Tapley, S. Bettadpur, J.C. Ries, P. Thompson, and M. Watkins. GRACE measurements of mass variability in the Earth system. *Science (New York, N.Y.)*, 305:503–5, 2004.
- [67] B. Tapley, J.C. Ries, S. Bettadpur, C. DP, M. Cheng, F. Condi, B. Gunter, Z. Kang, P. Nagel, Pastor, et al. GGM02 - an improved Earth gravity field model from GRACE. *J. Geod.*, 79:467–478, 2005.

Project Documents

- [TN1] U. Denskat, R. Gerndt, G. Link, and U. Johann. Phasemeter processing and laser control. Technical Report S2-ASD-RS-3018, ASD, 09 2009.
- [TN2] M. Dave, R. García Álvarez, and G. Wanner. Tilt-to-length coupling in LISA: IfoCAD simulation results. Technical Report LISA-AEI-INST-TN-009_i0.1_IfoCADResultsOnTTL, AEI, 11 2021.
- [TN3] E. Fitzsimons. LISA tilt-to-length and optical alignment analysis. Technical Report LISA-UKOB-INST-TN-004, UKOB, 12 2020.
- [TN4] M. Hewitson, E. Fitzsimons, J. Martino, R. Giusteri, and S. Paczkowski. Mitigation concept for tilt-to-length coupling in LISA. Technical Report LISA-LCST-INST-RP-001, LCST, 09 2021.
- [TN5] D. Robertson. 3OB "As Built" OptoCAD Model. Technical Report S2-UGL-TN-3045, University of Glasgow, 07 2016.

Complete List of Publications

- [P1] M Armano, H Audley, J Baird, P Binetruy, M Born, D Bortoluzzi, N Brandt, E Castelli, A Cavalleri, ... M-S. Hartig, ... , et al. Sensor noise in LISA Pathfinder: An extensive in-flight review of the angular and longitudinal interferometric measurement system. *In preparation*, 2022.
- [P2] Marie-Sophie Hartig, Sönke Schuster, Gerhard Heinzl, and Gudrun Wanner. Non-geometric tilt-to-length coupling in precision interferometry: mechanisms and analytical descriptions. *In preparation*, 2022.
- [P3] Marie-Sophie Hartig, Sönke Schuster, and Gudrun Wanner. Geometric tilt-to-length coupling in precision interferometry: mechanisms and analytical descriptions. *Journal of Optics*, 24(6):065601, 2022.
- [P4] Pau Amaro-Seoane, Lea Bischof, Jonathan J. Carter, Marie-Sophie Hartig, and Dennis Wilken. LION: laser interferometer on the moon. *Class. Quantum Grav.*, 38(12):125008, 2021.
- [P5] M. Armano, H. Audley, J. Baird, P. Binetruy, M. Born, D. Bortoluzzi, N. Brandt, E. Castelli, A. Cavalleri, ... M-S. Hartig, ... , et al. Sensor noise in LISA Pathfinder: In-flight performance of the optical test mass readout. *Phys. Rev. Lett.*, 126:131103, 2021.
- [P6] Marie-Sophie Hartig. Approximation of gaussian curvature by the angular defect: An error analysis. *Math. Comput. Appl.*, 26(1), 2021.
- [P7] D. Bortoluzzi, D. Vignotto, A. Zambotti, M. Armano, H. Audley, J. Baird, P. Binetruy, M. Born, E. Castelli, ... M-S. Hartig, ... , et al. In-flight testing of the injection of the LISA Pathfinder test mass into a geodesic. *Adv. Space Res.*, 67(1):504–520, 2021.
- [P8] M Armano, H Audley, J Baird, P Binetruy, M Born, D Bortoluzzi, E Castelli, A Cavalleri, A Cesarini, ... M-S. Hartig, ... , et al. Spacecraft and interplanetary contributions to the magnetic environment on-board LISA Pathfinder. *Mon. Notices Royal Astron. Soc.*, 494(2):3014–3027, 2020.
- [P9] M. Armano, H. Audley, J. Baird, M. Born, D. Bortoluzzi, N. Cardines, E. Castelli, A. Cavalleri, A. Cesarini, ... M-S. Hartig, ... , et al. Analysis of the accuracy of actuation electronics in the laser interferometer space antenna pathfinder. *Rev. Sci. Instrum.*, 91(4):045003, 2020.
- [P10] H. Audley, M. Born, K. Danzmann, M.S. Hartig, G. Heinzl, M. Hewitson, N. Karnesis, B. Kaune, S. Paczkowski, J. Reiche, et al. *LISA Pathfinder Mission Extension Report for the German Contribution*. Max-Planck-Institut für Gravitationsphysik, Albert-Einstein-Institut, Teilinstitut Hannover, 2020.

- [P11] M. Armano, H. Audley, J. Baird, P. Binetruy, M. Born, D. Bortoluzzi, E. Castelli, A. Cavalleri, A. Cesarini, ... M-S. Hartig, ... , et al. Novel methods to measure the gravitational constant in space. *Phys. Rev. D*, 100:062003, 2019.
- [P12] M. Armano, H. Audley, J. Baird, P. Binetruy, M. Born, D. Bortoluzzi, E. Castelli, A. Cavalleri, A. Cesarini, ... M-S. Hartig, ... , et al. LISA Pathfinder performance confirmed in an open-loop configuration: Results from the free-fall actuation mode. *Phys. Rev. Lett.*, 123:111101, 2019.

Acknowledgements

First of all, I would like to thank Prof. Dr. Karsten Danzmann for creating the positive atmosphere at our institute and sharing the enthusiasm about space-based gravitational wave missions. I remember that I was very impressed in my first year as PhD student that you seem to know the names of every member of the AEI. I also appreciate that you joined every IMPRS lecture week and were particularly interested in the mission proposals we came up with in the end of this series.

Furthermore, I would like to thank my supervisor Prof. Dr. Gerhard Heinzel. Despite the rapid growth of our group in the last years and your immense workload, your office door was always open. Also, you are constantly interested in the well-being of every group member, creating a very collegial atmosphere. I am very happy to have you as a referee for my thesis.

A warm thank you goes out to Prof. Dr. Guido Müller and Dr. David Robertson for unhesitatingly agreeing to referee my work as well. I am not sure if you were aware of the numerous equations awaiting you in this manuscript, and I hope you made it safely through it. I would further like to thank Prof. Dr. Klemens Hammerer for being the head of my defence talk.

An exceptional thank you goes out to Dr. Gudrun Wanner for all the time and overtime you spend supervising my work, arguing about formulations in the papers and proofreading the full manuscript of my thesis. During the last four years, I really liked the mixture of having the freedom in my daily working routine as well as someone who sharpens the focus of my work at appropriate times. Also, you always had an ear for any other concerns.

The last two years have been marked by the analysis of the LPF data. This simply would not have been possible without the support of Dr. Nikos Karnesis. Thank you for all the meetings, in which you patiently explained how the experiments in LPF were designed, how the TTL subtraction was performed and how your codes work. Thank you also for all the discussions about the results found along this journey.

This data analysis was also highly supported by Larissa Tevlin. Thank you for sharing the adventure of digging into LTPDA and the LXE data. You rock!

In terms of the LTPDA, I definitely owe Lennart Wissel something for the uncounted hours you spent explaining its functionalities to me and finding the obvious bugs in my codes. Also, the MATLAB generated figures in this thesis would probably look worse without your tutorial.

I would furthermore like to thank my former colleagues Dr. Sönke Schuster and Dr. Nils Brause for your support with the simulation library IfoCAD and Axel Schnitger for his introduction to git. I always tried hard not to delete things.

A huge thank you to all the proofreaders of my thesis, namely (in alphabetical order) Ana, Gudrun, Jonathan, Kevin, Lea, Lennart, Malte, Martin S., Megha, Sarah, Victor and Yong, and everyone who discussed my questions with me in the writing process.

In particular, I would like to thank Dr. Martin Hewitson for discussing mysteries in the LPF data, Dr. David Robertson for insights into the LPF optical system stability and Dr. Sarah Paczkowski, Dr. Roberta Giusteri and Dr. Ewan Fitzsimons for further information regarding the TTL coupling analysis in LISA.

Despite I missed the LPF mission itself, as was always a great joy to work with the (decreasing) LPF team at the AEI. Amongst others, I have good memories of the – sometimes very exciting – hat productions. Thank you for introducing me to heat shrinkable tubings and teaching me how to solder.

Many thanks to the LION crew around Jonathan Carter, Lea Bischof and Dennis Wilken. Working together on our paper about a laser interferometer on the moon was an awesome experience. Hear the universe roar!

I am very thankful for the great infrastructure at the AEI and for having competent personnel at critical positions that made it possible for me to focus on scientific work. In these terms, I would like to emphasise two women. Thank you, Kirsten Labove, for just making everything happen! And thank you, dear ‘Promodrachen’ Birgit Ohlendorf, for the competent organisation of everything concerning the official side of my doctorate.

Life in and around the institute would not have been the same without YOU, dear colleague. I always enjoyed having lunch with you or a short chat in the corridor or the tea kitchen. I am pleased to be your office mate. We were the best Christmas party organisation team! Also, the IMPRS lecture weeks, conferences, and any after-work event would not have been that much fun without you. Particularly, I am honoured to be your football teammate (and for some time in the past also your captain). Go AEI!

I would like to thank Anastasia Gaponik for all your support in the final phase of my thesis. Thank you for our endless phone calls!

Last but not least, I would like to thank my family for everything. Due to you, I was always able to follow my own plans. Needless to say that without I would not sit here, writing these lines. Danke!

“Mathematical science shows what is. It is the language of unseen relations between things. But to use and apply that language, we must be able to fully to appreciate, to feel, to seize the unseen, the unconscious.”

– Ada Lovelace

Curriculum Vitae

Personal Information

Full Name	Marie-Sophie Dorothee Hartig
Date of Birth	05. June 1992
Place of Birth	Lüneburg, Germany

Education

01/2018 - present	PhD candidate in Physics Max-Planck-Institute for Gravitational Physics (Albert-Einstein-Institute) and Institute for Gravitational Physics, Leibniz Universität Hannover, Germany
10/2015 - 09/2017	M.Sc. in Mathematics Friedrich-Schiller-University, Jena, Germany
10/2011 - 09/2015	B.Sc. in Mathematics Friedrich-Schiller-University, Jena, Germany
09/2013 - 12/2013	B.Sc. in Mathematics, Study Abroad University of Eastern Finland, Joensuu, Finland
07/2011	Abitur Gymnasium Johanneum, Lüneburg, Germany